Wake Vortex Assessment of Lidar Measurements Employing Large Eddy Simulations and Machine Learning

Wirbelschleppencharakterisierung von Lidar-Messungen mit Grobstruktursimulationen und maschinellem Lernen

Von der Fakultät für Maschinenwesen der Rheinisch-Westfälischen Technischen Hochschule Aachen zur Erlangung des akademischen Grades eines Doktors der Ingenieurwissenschaften genehmigte Dissertation

vorgelegt von

Niklas Louis Wartha

Berichter: **Univ.-Prof. Dr.-Ing. Eike Stumpf**
apl. Prof. Dr.-Ing. habil. Christian Breitsamter

Tag der mündlichen Prüfung: 3. März 2026

Diese Dissertation ist auf den Internetseiten der Universitätsbibliothek online verfügbar.

Wake Vortex Assessment of Lidar Measurements Employing Large Eddy Simulations and Machine Learning

Niklas Louis Wartha



München, 2026

Abstract

Coherent flow structures such as aircraft wake vortices may pose a hazard to follower aircraft potentially subjecting them to severe rolling moments. Particularly in their final approach towards the runway such disturbances may prove consequential. The characterization of wake vortices generated by leading aircraft therefore constitutes a decisive element for ensuring safe and efficient airport runway operation. Light detection and ranging (lidar) instruments are most frequently employed for undertaking measurements of wake vortices. The one-dimensionality of the measured velocity field necessitates processing algorithms with large-scale assumptions to determine the position and strength of wake vortices within. The accuracy of available algorithms, such as the radial velocity (RV) method, is so far not known, in particular for turbulent atmospheric cases.

The lack of a ground truth in field measurements motivates this thesis to simulate lidars within high-fidelity Reynolds-Averaged Navier-Stokes and Large Eddy Simulation (LES) aircraft landing runs. Wake vortices are simulated from their generation behind a detailed aircraft geometry to their decay, with known position and strength. Lidar simulations within the LES, LES Lidar Simulators (LLS) including lidar parameters and characteristics, allow wake vortex processing algorithms to be assessed. Realistic modeling of both the complex wake vortex flow and the lidar instrument has not been done previously. This thesis determines the RV method to overestimate the strength of wake vortices by 4 %, while dislocating them by 6 %. The RV method is particularly inaccurate in ground proximity, as it lacks the modeling of image vortices. Efficiently processing extensive data amounts or characterizing wake vortices in fast-time, for dynamic aircraft separations at airports, is not accommodated with available lidar processing algorithms. Herein, a novel Machine Learning (ML) pipeline is developed for individual wake vortex characterizations, enabling fast-time, reliable, and accurate characterizations (at least as accurate as the RV method) with no bias or undesirable wall effects. For the first time, LES data are employed for training ML models and evaluating field measurements. This enables the processing of field measurement datasets that lack labeled field measurements for training. The necessity for lidar simulations to include atmospheric noise and measurement noise, abbreviated as $\mathrm{LLS_n}$, is determined. $\mathrm{LLS_n}$-trained ML pipelines detect over 90 % of hazardous wake vortices in representative field measurements. This is on a par with the reliability of field-measurement-trained ML pipelines, suggesting that trustworthy wake vortex processing is achievable using simulated lidars when the expected measurement setup, aircraft categories, and atmospheric conditions are considered.

Zusammenfassung

Kohärente Strömungsstrukturen, zum Beispiel von Flugzeugen erzeugte Wirbelschleppen, können insbesondere im Landeanflug gefährliche Rollmomente auf folgende Flugzeuge ausüben. Die Charakterisierung von Wirbelschleppen ist daher ein entscheidendes Element, um den Landebahnbetrieb unter Gewährleistung der Sicherheit effizienter zu gestalten. Messungen von Wirbelschleppen werden meist mit Lidar-Instrumenten (Light Detection and Ranging) durchgeführt. Das gemessene eindimensionale Geschwindigkeitsfeld erfordert zur Bestimmung von Wirbelschleppenposition und -stärke Algorithmen mit weitreichenden Annahmen. Die Genauigkeit dieser Algorithmen, wie die radiale Geschwindigkeitsmethode (RV-Methode), ist bisher wenig erforscht, insbesondere für Fälle mit turbulenter Atmosphäre. Eine fehlende Grundwahrheit durch Feldmessungen legt die Generierung und Nutzung von simulierten Lidar-Daten nahe.

In dieser Arbeit werden erstmals realistische Simulationen von Lidar-Daten und Wirbelschleppen im Landeanflug kombiniert. Hierbei werden die Wirbelschleppen mittels hochpräzisen Reynolds-gemittelten Navier-Stokes-Gleichungen und Grobstruktursimulationen (LES) berechnet und mit virtuellen Lidar-Instrumenten vermessen. Deren Position und Stärke kann in den Simulationen genau bestimmt werden. Die LES-Lidar-Simulatoren (LLS) ermöglichen die Bewertung von Algorithmen zur Wirbelschleppencharakterisierung. Es wird gezeigt, dass die RV-Methode die Wirbelstärke um 4 % überschätzt und die Wirbelposition um 6 % versetzt. Nicht modellierte Spiegelwirbel führen zu einer höheren Ungenauigkeit in Bodennähe. Die Verarbeitung von großen Datenmengen und Implementierung von dynamischen Flugzeugseparationen benötigt eine schnelle Wirbelcharakterisierung. Bestehende Algorithmen ermöglichen dies nicht. Daher wird hier eine neuartige maschinelle Lern-Pipeline (ML-Pipeline) vorgestellt. Die Genauigkeit der RV-Methode wird hierbei übertroffen. Unerwünschte Bias- oder Wandeffekte treten nicht auf. Erstmals werden Feldmessungen mit einer auf LES-Daten trainierten ML-Pipeline ausgewertet. Dies erlaubt die Verarbeitung verschiedener Feldmessungsdatensätze, auch wenn kein annotierter Feldmessungsdatensatz für das Training verfügbar ist. Die Berücksichtigung von Atmosphären- und Messrauschen in der Lidar-Simulation (LLS_n) erweist sich als essenziell für die Wirbelerkennung. LLS_n-trainierte ML-Pipelines detektieren über 90 % der gefährlichen Wirbelschleppen in repräsentativen Feldmessungen - vergleichbar mit den von Feldmessungen trainierten ML-Pipelines. Dies zeigt, dass eine zuverlässige Wirbelschleppenprozessierung mit simulierten Lidar-Daten erreichbar ist, wenn die zu erwartende Messanordnung, die Flugzeugkategorien und die atmosphärischen Bedingungen simuliert werden.

Disclaimer

This thesis was conducted at the German Aerospace Center's (DLR) Institute of Atmospheric Physics in Oberpfaffenhofen, starting in September 2021. Since then, numerous publications have emerged from the author's work, which in great parts cover the content of this thesis. Significant parts from the following publications may reappear in this thesis:

– (Wartha et al., 2023): **Wartha, N.**, Stephan, A., and Holzäpfel, F.: Investigating errors of wake vortex retrievals using high fidelity lidar simulations, AIAA AVIATION 2023 Forum, DOI: 10.2514/6.2023-3679, 2023.

Contributions: The co-authors Anton Stephan and Frank Holzäpfel were responsible for the supervision of primary author Niklas Wartha, providing thorough feedback.

– (Stephan et al., 2023): Stephan, A., Rotshteyn, G., **Wartha, N.**, Holzäpfel, F., Petross, N., and Stietz, L.: Artificial neural networks for individual tracking and characterization of wake vortices in lidar measurements, AIAA AVIATION 2023 Forum, DOI: 10.2514/6.2023-3682, 2023.

Contributions: The machine learning pipeline introduced was developed by Lars Stietz under the supervision of Niklas Wartha, the concept and implementation of the projection method was conducted by Anton Stephan and Gregory Rotshteyn, with assistance from Nicolas Petross. Frank Holzäpfel and Niklas Wartha were involved in theoretical discussions about the projection method.

– (Wartha et al., 2025a): **Wartha, N.**, Stephan, A., and Holzäpfel, F.: Assessment of a Wake Vortex Retrieval Method Using Large-Eddy Simulations and a Lidar Simulator, Journal of Atmospheric and Oceanic Technology, 42(3), 233-251, DOI: 10.1175/JTECH-D-24-0093.1, 2025.

Contributions: The co-authors Anton Stephan and Frank Holzäpfel were responsible for the supervision of primary author Niklas Wartha, providing thorough feedback.

– (Wartha et al., 2025c): **Wartha, N.**, Stephan, A., and Holzäpfel, F.: Wake vortex lidar measurement processing with large-eddy simulations and machine learning, Optics Express, 33(12), 26473-26498, DOI: 10.1364/oe.562553, 2025.

Contributions: The co-authors Anton Stephan and Frank Holzäpfel were responsible for the supervision of primary author Niklas Wartha, providing thorough feedback.

– (Qu et al., 2025): Qu, Z., Yuan, S., Färber, M., Brennfleck, M., **Wartha, N.**, and Stephan, A.: Explainable lidar 3D point cloud segmentation and clustering for detecting airplane-generated wind turbulence, 31st ACM SIGKDD Conference on Knowledge Discovery and Data Mining V.1, 2504–2513, DOI: 10.1145/3690624.3709436, 2025.

Contributions: The colleagues Zhan Qu, Shuzhou Yuan, Michael Färber, and Marius Brennfleck were responsible for the development of the dynamic graph convolutional neural network. Niklas Wartha and Anton Stephan conceptually assisted the development and provided the necessary datasets.

Additionally, during 2022 the master's thesis authored by Lars Stietz from the University of Hamburg was supervised, contents not previously published in any of the above publications may also appear in his thesis:

– (Stietz, 2022): Stietz, L.: Artificial neural networks for individual tracking and characterization of wake vortices in lidar measurements, University of Hamburg, `https://elib.dlr.de/189820/`, 2022.

Contributions: Lars Stietz designed and implemented the ML pipeline as part of the thesis at hand. Niklas Wartha supervised his work, deeply involved in the conceptual design, strategic decisions, and theoretical discussions. Niklas Wartha provided thorough feedback throughout.

The lidar simulator datasets produced throughout this thesis (LLS and LLS_n) as well as the labels by the Large Eddy Simulation wake vortex tracking algorithm and the Radial Velocity method are available at:

– (Wartha et al., 2025b): **Wartha, N.**, Stephan, A., and Holzäpfel, F.: Virtual RHI lidar scans retrieved in high-fidelity wake vortex simulations of landing aircraft under turbulent crosswind conditions - LES Lidar Simulator (LLS), Zenodo, DOI: 10.5281/zenodo.12085034, 2025.

Contributions: The co-authors Anton Stephan and Frank Holzäpfel were responsible for the supervision of primary author Niklas Wartha, providing thorough feedback.

Additional talks (not published) were given on material covered in this thesis. Niklas Wartha presented the ML pipeline at AI4Aerospace 2023 in Paris, France as well as at a DGLR workshop in Garching, Germany. Anton Stephan also presented the ML pipeline at the FLY AI Forum 2025 in Brussels, Belgium and talked about the herein presented ML pipeline dataset composition studies at MADEAI 2025 in Porto, Portugal.

This thesis uses the Ludwig Maximilian University of Munich thesis template built by Robert Dahlke and Sigmund Stintzing. The Institute of Aerospace Systems, RWTH Aachen University logo can be found at `ilr.rwth-aachen.de`. Schematic figures presented in this thesis were produced employing the LaTeX-package TikZ. To a limited extent (for efficiency and effectivity purposes) their production was assisted by OpenAI's ChatGBT. These include: Figs. 2.5, 2.11, 3.5, 3.11, 3.21. Concepts, ideas, and content are all the author's own work (unless stated otherwise).

Table of Contents

Abstract **v**

Zusammenfassung **vii**

Table of Contents **xiii**

1 Introduction **1**
1.1 Motivation 1
1.2 State-of-the-Art Wake Vortex Processing 5
1.3 Aims and Objectives of the Thesis 8
1.4 Outline of the Thesis 12

2 Fundamental Principles **13**
2.1 Wake Vortices 13
2.1.1 Phases and Evolution 17
2.1.2 External Influences on Wake Vortex Progression 19
2.1.3 Vortex Models 22
2.1.4 Wake Vortex Characterization Parameters 25
2.2 Lidar Measurements for Wake Vortices 27
2.2.1 Lidar Types 27
2.2.2 Wake Vortex Measurement Overview 28
2.2.3 Backscatter Retrieval 30
2.2.4 LOS Velocity Processing 32

3 Methods **35**
3.1 Numerical Simulations of Wake Vortices 35
3.1.1 Large Eddy Simulation Code 36
3.1.2 Wake Vortex Simulations 37
3.1.3 Extension to Landing Aircraft 41
3.1.4 Computational Domain 42
3.1.5 Crosswind Pre-Simulations 44
3.2 LES Lidar Simulators 47
3.2.1 LOS Velocity Retrieval 47

3.2.2 LES Lidar Simulator Without Noise (LLS) . . . 49
3.2.3 LES Lidar Simulator With Noise (LLS_n) . . . 51
3.3 Dataset Families . . . 54
3.3.1 Field Measurements (FMs) . . . 54
3.3.2 LES Lidar Simulators (LLS_n and LLS) . . . 59
3.4 Wake Vortex Characterization . . . 62
3.4.1 Simulation Tracking Algorithm . . . 62
3.4.2 Radial Velocity (RV) Method . . . 63
3.4.3 Machine Learning Pipeline . . . 64

4 Results **83**
4.1 Numerical Wake Vortex Simulations . . . 83
4.1.1 Reproduction of Wake Vortex Evolution Phases . . . 83
4.1.2 Simulated Wake Vortex Trajectories . . . 85
4.2 LES Lidar Simulations . . . 90
4.2.1 Spatial Factors . . . 90
4.2.2 Temporal Factors . . . 94
4.2.3 Comparison of the Lidar Simulator Types: LLS and LLS_n . . . 94
4.3 Accuracy of Lidar Processing Algorithms . . . 96
4.3.1 Radial Velocity Method . . . 96
4.3.2 Machine Learning Pipeline . . . 107
4.4 Field Measurement Processing using LES Lidar Simulations and ML . . . 111
4.4.1 Wake Vortex Detection . . . 111
4.4.2 Wake Vortex Characterization . . . 118
4.5 Increased ML Pipeline Accuracy with Ground Truth Labels . . . 123
4.6 ML Pipeline Dataset Composition Studies . . . 125
4.6.1 Number of Training Scans . . . 127
4.6.2 Hybrid Training Subsets . . . 127
4.6.3 Tuning Towards Additional Lidar Setups . . . 129

5 Conclusions and Outlook **133**

A Derivation of the Range Gate Weighting Function **139**

B Estimation of the LOS Velocity Without Noise **141**

C Derivation of the Midpoint Rule for the LOS Velocity Estimation **143**

List of Acronyms **145**

List of Abbreviations **149**

List of Symbols **158**

List of Figures 162

List of Tables 164

Bibliography 183

Acknowledgments 185

Chapter 1

Introduction

1.1 Motivation

The overarching motivation of this thesis is to ensure safe, economically viable, and sustainable aircraft operations at airports. Particularly the final approach and landing phases of an aircraft constitute critical situations, with low speed and immediate ground vicinity. Handling and counteracting abrupt disturbances, such as atmospheric gusts, is a serious challenge for pilots, frequently resulting in necessary go-around maneuvers (Hallock and Holzäpfel, 2018). Furthermore, the glide path of aircraft during final approach and landing is commonly shared between aircraft, thus coherent flow structures generated by leading aircraft may further increase the risk of encountering a disturbance. The most prominent physical phenomenon resulting from leading aircraft are wake vortices, trailing vortices generated by all airborne vehicles producing aerodynamic lift. Although encounters with wake vortices may occur also during other flight phases, such as cruise (Hoogstraten et al., 2015) or take-off and departure (Holzäpfel et al., 2009b), the probability and involved safety risk is significantly higher for aircraft in final approach and landing phases (Rossow and James, 2000; Gerz et al., 2002). Both the heading and size of a follower aircraft affect its interaction with wake vortices generated by the leading aircraft. If the heading and size are comparable, a rolling moment is exerted onto the follower aircraft, with the magnitude depending on the ratio between the generator and follower aircraft size/mass (Rossow and James, 2000). Additionally, wake vortices generated by landing aircraft may pose a hazard to other emerging air vehicles, such as air taxis, which for logistical reasons may have vertiports installed in runway vicinity.

High frequency aircraft arrival sequencing along the glide path, leading to closely spaced aircraft, increase vortex encounter risks. Simultaneously air traffic growth demands the throughput of runways to be increased. EUROCONTROL (2025) expects that already in 2025 pre-COVID-19-pandemic air traffic levels are reached in Europe. With further growth as well as current regulations and airport infrastructure, EUROCONTROL (2024) anticipates a capacity gap of 1.1 million flights by 2050 (7 % of the total demand). Thus, there are competing interests and stakeholders, including airport operators, authorities,

airlines, passengers, and wider society. Approaches aiming to reduce the hazard posed by wake vortices and, at a minimum, preserve current safety standard, while increasing runway throughput include: dynamically regulating the separation between landing aircraft, active/passive flow control, and ground modifications underneath the aircraft glide path.

Wake vortex aircraft separations are routine in airport operations, complementing the standard Minimum Radar Separation (MRS), nowadays typically spanning 2.5 nautical miles (nm). The majority of airports operate under International Civil Aviation Organization (ICAO) standards following Table 1.1, where wake vortex separations depend on the Maximum Take-Off Mass (MTOM) of the involved aircraft types. Growing air travel demand has exhausted this categorization from the 1970s (with the addition of the Super category for the Airbus A388 in the 2000s), leading wake vortex separations to be a bottleneck for airport runway capacity (Gerz et al., 2002; ICAO, 2008).

Table 1.1: ICAO wake vortex (distance-based) separation minima. Light: MTOM $\leq$ 7 tons, Medium: 7 tons $<$ MTOM $\leq$ 136 tons, Heavy: 136 tons $<$ MTOM, except the Airbus A388: MTOM = 560 tons, considered a Super. (Rooseleer, 2024)

Generator ICAO aircraft category	Follower ICAO aircraft category	Separation [nm]
Super	Heavy	6
Super	Medium	7
Super	Light	8
Heavy	Heavy	4
Heavy	Medium	5
Heavy	Light	6
Medium	Light	5

Gerz et al. (2002) note the over-conservative nature of the ICAO separations. Alternative aircraft separation schemes have been suggested and in-part already implemented. These include time-based separations (De Visscher et al., 2020) operative at London Heathrow Airport (Morris et al., 2013) and the joint effort RECAT-EU by EUROCONTROL as well as the European Union Aviation Safety Agency (EASA). A comparable program has been introduced by the Federal Aviation Administration (FAA). The RECAT-EU program is divided into three phases, aiming to shift from a MTOM-based system to a vortex-strength-based system (Cheng et al., 2016): RECAT-I re-categorizes the four ICAO aircraft categories into six new categories (CAT-A to CAT-F, see Table 1.2 for categories relevant to commercial aviation), where alongside their aircraft mass also speed, wing characteristics, and the exerted rolling moment onto a follower aircraft is considered. Numerous airports around the world have commenced to implement RECAT-I separation minima provided in Table 1.3 (FAA, 2014; Ministère de la Transition Écologique et Solidaire, 2018; NATS, 2018). RECAT-II extends generator-follower pairs to individual aircraft types, and RECAT-III aims to consider prevailing atmospheric conditions for wake vortex trajectories at runways and therefore dynamically adjusting minimum aircraft separations.

Table 1.2: RECAT-EU aircraft categories sorted by aircraft types. The provided list is non-exhaustive, with the focus on common operative commercial fixed-wing Airbus and Boeing aircraft and commercial airport relevant categories. Where possible aircraft families are listed instead of individual types. EUROCONTROL and Isambert (2022) provide a full list.

Lower Medium	Upper Medium	Lower Heavy	Upper Heavy	Super Heavy
E	D	C	B	A
Boeing 717	Airbus A320	Airbus A310	Airbus A330	Airbus A388
Boeing 737 Classic	Airbus A220	Boeing 757	Airbus A340	
	Boeing 737 NG	Boeing 767	Airbus A350	
	Boeing 737 MAX		Boeing 747	
			Boeing 777	
			Boeing 787	

Table 1.3: RECAT-EU wake vortex separation minima including aircraft categories relevant for commercial airport operations. Distance-based separation minima [nm], for details and time-based separation minima see Rooseleer (2024). Empty cells dictate MRS.

Generator ↓ / Follower →	E	D	C	B	A
E	-	-	-	-	-
D	-	-	-	-	-
C	4	3	3	-	-
B	5	4	4	3	-
A	6	5	5	4	3

In the past, several flow control initiatives have been studied. Depending on the particular objective the approaches differ (Breitsamter, 2007, chap. 6): geometries such as flaps, fins, or spoilers may be modified in order to generate turbulence, leading to the broadening of the vorticity field, a larger vortex core, and lower tangential velocities. The resulting low peak vorticity vortices reduce the rolling moment induced onto follower aircraft. This approach is called passive flow control. Alternatively, active flow control for instance employs oscillating flaps, generating an oscillating wake in order to trigger three-dimensional instabilities which cause premature wake vortex decay. Numerical simulations (Stumpf, 2005) and experiments (Coustols et al., 2003; Breitsamter, 2007; Ehlers et al., 2015) have thoroughly investigated the potential of flow control. However in recent years, flow control efforts lessened given challenges with reliability.

Modifications of the ground below the aircraft glide path aim to trigger secondary vortices emerging from the installed obstacles, rather than modifying the aircraft generated wake vortices. The interaction of the primary and secondary vortices causes premature wake vortex decay. Both numerical simulations (Stephan et al., 2014) and field experiments (Holzäpfel et al., 2016a; Holzäpfel et al., 2021) have demonstrated the potential of this approach.

Regardless of the undertaking, the majority of undertakings need, at a very minimum, to be validated or also monitored with costly and time-consuming field measurements. Wake vortex measurements in the critical airport area for landing aircraft have in recent years focused on light detection and ranging (lidar) instruments, either on-board the aircraft, measuring forwards, such that hazardous coherent structures can be identified in the flight path (Darracq et al., 2000; Schmitt et al., 2007; Hirschberger, 2013; Fezans et al., 2017), or on the ground, placed besides the aircraft glide path towards the runway (see Fig. 1.1) as Köpp et al. (1991); Köpp (1994) first thoroughly analyzed. On-ground lidar measurements contain one-dimensional velocity information along the laser Line-Of-Sight (LOS) (to or away from the lidar), capturing two-dimensional scans of Range-Height Indicator (RHI) type. In order to evaluate the potential hazard posed to an aircraft by a wake vortex, it must be characterized by its position and strength. The one-dimensionality of the flow field information necessitates a processing algorithm for computing the wake vortex characterization parameters reliably, accurately, automatically, and in fast-time. The requirements emerge from two common applications in wake vortex science, the processing of elaborative campaign datasets, as well as the fast-time surveillance of wake vortex hazard in the glide path region of runways for a Wake Vortex Advisory System (WVAS) or enabling dynamic pair-wise wake vortex separations as suggested by RECAT-EU.



Figure 1.1: Photo of a Vaisala WINDCUBE® 200s lidar measuring at Vienna Airport in 2019 (left) and animation of a measuring on-ground lidar (right). The red line represents the lidar laser beam and LOS. Copyright by Frank Holzäpfel and DLR (2006), respectively.

1.2 State-of-the-Art Wake Vortex Processing

Determining wake vortex characteristics from lidar measurements is an active field of research since just before the turn of the millennium. Algorithms for this purpose can be separated into two main categories, physical algorithms, based on modeling the measured velocity field or extracting characteristics from the velocity field and data-driven algorithms, based on labeled datasets consisting of wake vortex lidar scans and the associated characteristics of wake vortices within each scan.

First physical algorithms strongly focused on kinematic assumptions, such as tangential vortex velocities or the downdraft between a vortex pair, in order to estimate the position and strength of wake vortices (Hannon et al., 1997; Holzäpfel et al., 2003). Frehlich and Sharman (2005) introduced a maximum likelihood algorithm, comparing spectral lidar data to analytical vortex models, however their algorithm requires prior knowledge of the wake vortex generating aircraft type and focuses on the wake vortex pair collectively, as common for these earlier algorithms. Later publications suggested improvements to the spectral modeling, for instance for processing lidar scans measured under non-ideal conditions (Yoshikawa and Matayoshi, 2017). Further noteworthy wake vortex characterization processing algorithms published include Kaikwong and Pakwai (2017); Gao et al. (2018); Shen et al. (2020); Li et al. (2020), for some of which practical tools have been developed (Lai et al., 2010; Jacob et al., 2011, 2013, 2015). A major disadvantage of most physical lidar processing algorithms constitutes the estimation of a vortex core radius, which may lead to estimate adulterations of vortex characteristics. Stephan et al. (2023) recently suggested a combined physical and data-driven lidar processing algorithm, the Projection Method (PM). While it is still under investigation, the PM elegantly determines the core radius of a vortex prior to estimating its strength, while also providing a quality metric for the fit vortex model. The most popular and widely adapted purely physical algorithms include the Velocity Envelope (VE) and Radial Velocity (RV) methods.

Brockman et al. (1999) first mentioned the VE method, where the signal returning to the lidar, the backscatter signal, is Fourier transformed to the frequency domain and normalized with a mean noise component before power spectrum thresholds obtain minimum and maximum LOS velocity envelopes belonging to the spectrum peak and the tangential velocities of a vortex (Banakh and Smalikho, 2013; Köpp et al., 2004). Köpp et al. (2005) estimate vortex characterization Root Mean Squared Error (RMSE) values as 4.5 m in the vertical vortex axis direction, 6.5 m in the horizontal vortex axis direction, and 13 m^2 s^{-1} for the circulation (representing vortex strength and defined as the integration of velocity along a curve enclosing the vortex center) by comparing results of two lidar types. The downsides of the VE method include the high lidar Signal-to-Noise Ratio (SNR) requirement, reflecting the power content of the echo signal (signal of interest) with respect to the atmospheric and instrument noise content, as well as the high number of iterations required for obtaining correct power spectrum thresholds (Banakh and Smalikho, 2013, chap. 5). Wassaf et al. (2011) presented enhancements of the VE method using a dynamic power spectrum threshold. Later, Hallermeyer et al. (2016) suggested a combination of the VE method for finding the wake vortex position and the maximum likelihood method

for estimating the circulation of the wake vortices. Dolfi-Bouteyre et al. (2008) developed a practical tool employing the VE method.

In recent years, the laser wavelength of lidars has been decreased from 2-µm to 1.5-µm, increasing the laser pulse repetition frequency and thus the measurement accuracy significantly in low SNR scenarios (Smalikho et al., 2015). Since the VE method struggles with low SNR lidar measurements, Smalikho et al. (2015) established the RV method. In summary, the RV method employs a LOS-velocity-based functional in order to locate the vortex centers. Afterwards, the vortex strength is estimated by fitting analytical vortex models to the measured velocity field. Theoretical estimates of the Euclidean distance RMSE and circulation RMSE are 1.0 m and 10.3 to 21.0 $m^2\ s^{-1}$, respectively (Smalikho et al., 2015; Smalikho, 2019). Several field studies have been conducted with the RV method (Thobois and Cariou, 2017; Holzäpfel et al., 2021). Recently, Smalikho (2019) introduced an enhanced RV method, taking into account the ground effect and significantly increasing the accuracy of wake vortices in ground vicinity. Furthermore, Wu et al. (2019) studied a hybrid algorithm of the RV and VE methods.

Physical processing algorithms for characterizing wake vortices in 1.5-µm lidar scans, such as the RV method, have so far not been able to deliver fast-time and automatic evaluation. With the rise in Machine Learning (ML) popularity, for example in real-time video analysis, numerous new data-driven processing algorithms have been suggested, with the goal of achieving fast-time wake vortex processing. ML-based methods can handle vast data amounts efficiently, particularly in combination with Graphics Processing Units (GPUs). Such ML processing algorithms in the context of a WVAS can be considered an assistance to human system according to the EASA guidelines (Soudain, 2024). The majority of the data-driven processing algorithms are based on Artificial Neural Networks (ANNs), a ML type ideal for large datasets and learning non-linear input-output relationships.

To the author's knowledge, Pan et al. (2019b) initiated ML studies on wake vortex processing in RHI lidar scans using the popular Convolutional Neural Network (CNN) architecture AlexNet, built to recognize the entire wake of an aircraft. Out of all processed lidar scans containing wake vortices, 91 % scans were correctly classified as wake vortex lidar scans. In the same year, Pan et al. (2019a) achieved an accuracy of 94 % for the same task by employing the third version of the popular object detection network You Only Look Once (YOLO). Ai et al. (2021) proposed a further framework for wake vortex identification, relying on a CNN-based Long Short-Term Memory (Hochreiter and Schmidhuber, 1997) architecture, popular for handling temporal information. Besides the velocity fields captured by the lidar instrument, they include additional information (aircraft position, scan sequence) as inputs. Moreover, networks by the visual geometry group (Simonyan and Zisserman, 2014), attention-based ANNs, and residual ANNs were investigated (Pan et al., 2022a,b; Deng et al., 2024). In particular, Pan et al. (2022a) achieve a wake detection accuracy of above 99 %. Besides ANNs, also alternative ML methods have been investigated, for instance Support Vector Machines (Pan et al., 2020), a robust alternative to ANNs for smaller datasets. Also random forest algorithms (ensemble of decision trees) were investigated for entire aircraft wake recognition (Leng et al., 2021; Pan et al., 2022c), reaching an accuracy of 95 %. The data-driven processing algorithm by Duan et al.

(2023) can differentiate whether individual counter-rotating vortices are close together or far apart. Baranov and Resnick (2021) performed first individual wake vortex position estimations using CNNs. Qu et al. (2025) conducted similar work using dynamic graph CNNs. However, for data-driven processing algorithms to compete with physical algorithms, not only the existence of wake vortices but individual wake vortex characteristics need to be estimated.

Wartha et al. (2022) were the first to fully characterize individual wake vortices, i.e., their two dimensional wake vortex position and strength (circulation), by employing straightforward CNNs. The primary downside of their method is the requirement for each observed lidar scan to contain a wake vortex pair, lidar scans containing more or fewer wake vortices cannot be processed. Furthermore, all vortex characteristics are estimated by separate CNN models, including the two-dimensional vortex position. It follows that their approach still lacks in accuracy and robustness compared to the state-of-the-art physical processing algorithms, despite providing promising results. Particularly, the characterization accuracy of the vortex position strongly varies with the investigated measurement scenario. The minimum median wake vortex position characterization error is 11 m Euclidean distance between the labeled vortex center and the estimated vortex center, and the minimum circulation characterization RMSE is 36 m^2 s^{-1} (Wartha et al., 2022). However, the processing of wake vortex lidar scans is automatic and fast-time capable, the characterization of wake vortices within a single lidar scan is executed in approximately 0.2 s on a consumer-level central processing unit.

Although data-driven processing algorithms for characterizing wake vortices in lidar scans have improved their accuracy and scope throughout the years, two issues remain:

- The supervised nature of ML algorithms requires a physical processing algorithm to label the data employed for training the ML models, modifying parameters in the model, and allowing them to learn wake vortex patterns. The physical algorithms carry inherent errors, hindering the ML models to obtain higher wake vortex detection reliability and characterization accuracy. For the data-driven processing algorithms this signifies that accuracy evaluations for field measurements are in comparison to the physical processing algorithm employed for labeling the data. In other words, the data-driven processing algorithms mimic the physical algorithm instead of independently learning the ground truth of wake vortex position and circulation.

- The generalizability is unknown, i.e., how well a ML model trained on one dataset can process data from a different dataset. It is not desirable to require a physical algorithm labeled dataset for training ML models with every new measurement campaign or lidar setup.

Therefore, means are required for delivering wide-ranging datasets with highly accurate labels. To date, no universally applicable, accurate, fast-time, and automatic processing algorithm is available for characterizing wake vortices within lidar measurements.

1.3 Aims and Objectives of the Thesis

From the current state of wake vortex characterization processing of lidar measurements discussed in the above section, the following four open research questions arise. This thesis aims to answer these employing and developing novel methods. Below lists the contributions of the present thesis in the field of wake vortex retrievals using lidar instruments.

What are the accuracies and limitations of wake vortex characterization algorithms for lidar measurements?

The true error bounds of established processing algorithms for wake vortex processing of lidar measurements are unknown, given that the lack of a reliable ground truth in field measurements cannot be obtained with conventional measurement instruments. Documented error bounds have so far been established via theoretical or numerical studies (Frehlich and Sharman, 2005; Köpp et al., 2005; Smalikho et al., 2015; Smalikho, 2019). Experimentally obtained error bounds rely on cross-validation with alternative measuring equipment (Köpp et al., 2005), equally not representing the ground truth. Thus, the true accuracy, particularly under turbulent atmospheric conditions largely remains an open question.

The accuracy of the processing algorithms must be determined for trustworthy knowledge to be produced. Thus, a first aim of this thesis is to assess the accuracy of lidar processing algorithms for practical applications. The corresponding objective is the generation of realistic lidar simulations in Large Eddy Simulations (LESs) from aircraft in their final approach. The ground truth wake vortex characteristics, position and strength, can be determined to a high-level of accuracy within the three-dimensional parameter space of the LES domain.

The simulation of atmospheric measurement instruments for wake vortex research is no new approach, since the 1970s studies have been pushed forward (Thomson and Meng, 1976). First specific lidar simulations were performed by purely focusing on the backscatter to the instrument. For instance, Rye (1990) assumed white noise and random backscatter spectra. Salamitou et al. (1995) investigated the ability to analyze different atmospheric conditions, altering the backscatter spectra accordingly. Subsequently, Frehlich (1997) analyzed the effect of the atmospheric condition on the lidar performance. Studies of wake vortex lidar simulations can be split into two groups, forward oriented lidar on-board aircraft and ground-based lidar in order to investigate wake vortex behavior in ground proximity, with the present thesis focusing on the latter. To the author's knowledge, Holzäpfel et al. (2003) first mentioned Navier-Stokes based numerical simulations in the context of wake vortices and lidar simulations. In their work, the authors simulated wake vortices with numerical simulations initialized by a counter-rotating analytical Lamb-Oseen (Lamb, 1932) vortex pair and a separate aircraft generated multi-vortex system. The lidar simulations concentrated on kinematic and geometry aspects, neglecting filtering and SNR characteristics of lidar instruments. Frehlich and Sharman (2005) continued work on analytical vortex pairs, with the extended focus on the lidar operations, including lidar parameters such as range gate, angular scanning rate, laser wavelength, and pulse

duration. Even a turbulent wind is included in their simulations. Afterwards, the usage of lidar simulations in LES gained traction. For instance, Wassaf et al. (2011); Jacob et al. (2015) included lidar simulators featuring scanning, processing, and aerosol (air particle) scattering parameters within the LES.

To this day, wake vortex lidar simulations either focus on sophisticated lidar simulations or the high-fidelity modeling of the physical wake vortex phenomenon. Most studies focus on the former (Lugan, 2016; Gao et al., 2018, 2019; Li et al., 2020; Wei et al., 2024), rarely the fidelity of the numerical wake vortex simulation is prioritized (Stephan et al., 2019a).

Lai et al. (2010); Jacob et al. (2011); Lai et al. (2011) previously proposed the simulation of lidar scans for assessing lidar processing algorithms. They evaluated the wake vortex position and circulation characterization accuracy of the Lockheed Martin Coherent Technologies wake vortex processing algorithm [based on Hannon and Thomson (1994); Hannon et al. (1997); Rye and Hardesty (1994); Frehlich and Sharman (2005); Constant et al. (1994)] using a lidar simulator and LESs. Out-of-ground and partly in-ground wake vortex scenarios, as well as crosswinds and turbulent scenarios were investigated. However, they only sparsely disclosed details on the sophistication of the lidar simulator and the underlying LESs. Entirely comprehending and reconstructing their method is not possible. Additionally, the wake vortices observed by the simulated lidars, claimed to be of realistic detail, emerge either from analytical vortex models or individual slices of LESs for instance from a Boeing 747 aircraft. The measurement of a typical RHI lidar scan consists of multiple LOS, which cannot be measured instantaneously and instead takes up to several seconds (depending on the lidar setup). Usage of a single LES timestep for generating simulated lidar scans therefore entirely neglects temporal averaging inherent to wake vortex measurements; a key aspect for descending/ascending wake vortices (Smalikho, 2019). Furthermore, the degree of detail of the simulated aircraft in the LESs is unknown, however it is understood that the simulation of the in-ground effect is restricted to aircraft flying at constant low altitude - the descent and touchdown of the aircraft are not simulated.

This thesis elevates the sophistication of both the LESs for the landing scenario of aircraft and the lidar simulator in order to increase traceability and establish high-principled algorithm error bounds. It aims to minimize compromises in both simulation aspects. High-fidelity hybrid landing numerical simulations for an Airbus A340 aircraft are performed at multiple levels of turbulent crosswind magnitude. The hybrid numerical simulations consist of a Reynolds-Averaged Navier-Stokes (RANS) simulation for capturing the wake vortex generation close to the aircraft correctly, whereas LES is used to simulate all evolution stages of wake vortices. Stephan et al. (2014) demonstrated that the realistic simulation of the aircraft descent and touchdown has a significant impact on the evolution, coherency, and trajectory of the generated wake vortices for instance due to so-called end effects. With both the lidar and wake vortices in the landing scenario being simulated at realistic level of detail, the accuracy of processing algorithms can be estimated reliably. Note that two types of lidar simulators are studied throughout this thesis, one ideal LES Lidar Simulator (LLS) for low/no noise conditions (high SNR) based on Robey and Lundquist (2022), and a realistic $\mathrm{LLS_n}$ also simulating high noise conditions (low SNR) following Stephan et al.

(2019b). In the present thesis, the evaluation of the processing algorithms, including the physical RV method, is performed using the lidar simulator for low noise conditions. Thus, error bounds presented in this work can be considered benevolent or upper accuracy limits.

How can ML realize reliable, accurate, and rapid wake vortex characterizations?

A second aim of this thesis is to enable universally applicable, reliable, accurate, rapid, and automatic wake vortex processing of lidar measurements in order to allow a fast-time lidar-based monitoring system as part of a WVAS or efficient campaign dataset processing. The objective is to present a data-driven lidar processing algorithm based on an object detection ML framework, named the ML pipeline. Individual wake vortex characterization, position (in two dimensions) and strength (in terms of the circulation), is realized. It has previously been established that data-driven processing algorithms may enable fast-time and automatic lidar scan processing, however they still lack high reliability and high accuracy, as well as wake vortex independent characterization.

The ML pipeline suggested in this thesis solves this by first employing an object detection ML model, allowing to detect any number of wake vortices in lidar scans, followed by two regression CNNs, similar to the architecture suggested by Wartha et al. (2022), which individually process wake vortex cut-outs previously detected. The ML pipeline promises a wide and universally applicable strategy for characterizing wake vortices in lidar measurements. In order to verify the ML pipeline working, reliability, and accuracy, three different dataset families are employed in this thesis: field measurements from Vienna Airport with labeling by the original RV method (Holzäpfel et al., 2021) and the two aforementioned types of lidar simulators (LLS and $\mathrm{LLS_n}$). Guidelines provided by the EASA include consideration on trustworthiness, ensuring learning, explainability (how are results reached), and safety risk mitigation (Soudain, 2024). In general, an operative lidar monitoring system employing the ML pipeline within a WVAS complies with the cross-checking guideline for trustworthiness and safety risk mitigation.

To what extent can simulated data replace measurement data for training ML models?

Generalizability, the potential of a ML model to successfully evaluate previously unseen lidar data, which may comprise data originating from different measurement setups, configurations, and overall scenarios, may not naturally be assumed for the ML pipeline. Furthermore, labeled field measurement datasets are rare. If unavailable, obtaining such labeled dataset is a costly and time-consuming process. The aim of this thesis is to establish measurement independent ML pipeline models capable of processing field measurements accurately. The subsequent objective is to employ simulated lidar scans (LLS and $\mathrm{LLS_n}$) for training ML frameworks such as the ML pipeline, providing a generalization approach.

Wei et al. (2024) previously trained a ML model with lidar simulations. However, rather than employing high-fidelity LES of landing aircraft, they realized wake vortex evolutions via analytical vortices and the probabilistic two-phase wake vortex decay model (P2P)

(Holzäpfel, 2003). Furthermore, their studies focused on low instrument/atmospheric noise, not suitable for modern 1.5-µm lidars (as established in Section 1.2). This thesis puts a particular focus on characterizing wake vortices in noisy and turbulent lidar measurements. By comparing both lidar simulators (LLS and LLS_n), this thesis reveals the importance of simulating both a realistic lidar and realistic wake vortices in ground proximity for processing field measurements using simulated lidar data.

Generalizability of the ML pipeline is realized by modeling specific measurement setups and atmospheric conditions representing the investigated field measurements. Successful processing of field measurements using a ML pipeline trained on simulated lidar scans indirectly implies the realism of the LLS and LLS_n, as well as the numerical wake vortex simulations, verifying their suitability for the assessment of lidar processing algorithms (the first research question of this thesis). Beyond wake vortices, similar simulations and approaches may thus be successful for other atmospheric phenomena.

Can the provision of ground truth data help improve the accuracy of lidar processing algorithms?

As a direct consequence of the previous objective, training the ML pipeline with simulated lidar data, this thesis aims to understand whether data labeled with the ground truth, instead of physical processing algorithms such as the RV method, can reduce errors of data-driven processing algorithms, i.e., the ML pipeline. The associated objective is to train the ML pipeline with ground truth labels instead of the RV method (which carries an error itself). Additional lidar scans with ground truth labels are employed to compare the two approaches. In supervised ML, where patterns from input data are learned, reliable and accurate labels for the input data are essential. Errors inherent to the labels may result in false and inappropriate training of the ML models. Thus, data labels representing the ground truth are expected to increase reliability and accuracy of trained ML pipelines.

This thesis has no access to ground truth wake vortex characteristics from field measurements, therefore evaluating whether a ML pipeline trained with ground truth labels can outperform a ML pipeline trained with RV method labels using field measurements is not possible (the processing comparison of field measurements is always to the RV method labels). Instead, the research question can partially be answered by comparing LLS_n-labeled and field-measurement-labeled ML pipelines on lidar simulation data. ML models trained and tested on data emerging from the same dataset family are expected to outperform ML models trained on data originating from an alternative dataset family and may thus obliterate results. Nonetheless, potential benefits of ground truth labels can be identified. Further investigations are necessary in the future, in particular a ground truth for field measurements could be established for instance with particle image velocimetry experiments.

1.4 Outline of the Thesis

This thesis is divided into five chapters, the introduction (**Chapter 1)** above outlined the relevance of wake vortices in airport vicinity. Measurements of wake vortices and their processing are motivated and justified. An overview of the current state-of-the-art processing algorithms is provided, leading to the raised research questions. Resulting aims and objectives guide the remainder of this thesis.

Chapter 2 introduces elementary physical aspects, providing a broader context of concepts relevant for this thesis. Section 2.1 defines wake vortices and details their generation to decay. Furthermore, aspects influencing the evolution of wake vortices are covered, in particular ground obstacles and atmospheric conditions. Frequently employed analytical vortex models are introduced and compared. Fundamental wake vortex parameters are detailed. Section 2.2 describes lidar principles, including underlying concepts, functions, and implications for ground-based wake vortex measurements.

Chapter 3 covers all methods employed and developed in this thesis. Section 3.1 details hybrid (RANS-LES) numerical simulations of landing aircraft, which allow studying realistic wake vortex evolutions from their generation to their complete decay. The initialization of turbulent crosswinds is described. Section 3.2 introduces two lidar simulator types (LLS and $\mathrm{LLS_n}$), both build on an underlying LOS velocity retrieval operating simultaneously with the landing aircraft simulations. Two differing post-processing methods of obtained LOS velocity fields, comprising the two lidar simulator types, are explained. The three considered dataset families are provided in Section 3.3: field measurements from a Vienna Airport campaign, LLS, and $\mathrm{LLS_n}$. Finally, three lidar processing algorithms for wake vortex characterization are outlined in Section 3.4: retrieval within the LES, the legacy RV method, and the ML pipeline.

Chapter 4 is separated into six results sections. The purpose of Section 4.1 is to manifest the validity of the RANS-LES runs. The influence of the turbulent crosswinds on the vortex evolution is a particular focus. Section 4.2 verifies the presence of spatial and temporal averaging aspects of lidars in the simulations. In addition, the two lidar simulators are compared, establishing the appropriate application of both. In Section 4.3 the first two research questions of this thesis are answered by evaluating the characterization accuracy of both the RV method as well as the ML pipeline. Section 4.4 provides a response to the third research question, lidar field measurements are evaluated using a ML pipeline trained on lidar simulations, establishing essential simulation components necessary for successful field measurement processing. Section 4.5 addresses the fourth research question and demonstrates the advantage of training the ML pipeline with labels close to the ground truth. Finally, hybrid training subsets (field measurement and $\mathrm{LLS_n}$ scans) for training ML pipelines are investigated in Section 4.6. The generalizability of the ML pipeline to new lidar positions is investigated and improved.

Chapter 5 provides a summary of the developed methods, study findings, and contributions by this thesis to the field of wake vortex retrievals using lidar measurements. This thesis ends with an outlook offering recommendations for improvements and future studies.

Chapter 2

Fundamental Principles

2.1 Wake Vortices

The following sections deliver a comprehensive picture of wake vortices, what they are, how they are generated and develop in time, as well as in what manner their development is influenced by external factors such as walls or atmospheric effects. Wake vortices constitute a vortex type generated by aircraft as a direct consequence of lift generation. The below commences with describing a general vortex and is in great parts, unless stated otherwise, recapitulated from Saffman (1992); Anderson (1984).

A vortex in a three-dimensional space $\boldsymbol{x} = [x,\, y,\, z]$ can be understood as a collection of rotating fluid particles around a common center (Lugt, 1983, chap. 2). Mathematically this fluid rotation can be described with the curl of the velocity field $\boldsymbol{V} = [u,\, v,\, w]$,

$$\boldsymbol{\omega}\left(\boldsymbol{x},\, t\right) \equiv \nabla \times \boldsymbol{V} = \left[\frac{\partial w}{\partial y} - \frac{\partial v}{\partial z},\, \frac{\partial u}{\partial z} - \frac{\partial w}{\partial x},\, \frac{\partial v}{\partial x} - \frac{\partial u}{\partial y}\right] = \left[\omega_x,\, \omega_y,\, \omega_z\right]. \tag{2.1}$$

The strength of a vortex can be determined by the integration of the velocity along a curve C enclosing the vortex center. Through Stokes' theorem the circulation equally represents the integral over the vorticity within the C-enclosed area A, resulting in

$$\Gamma := \oint_C \boldsymbol{V} \cdot d\boldsymbol{s} = \int_A \boldsymbol{\omega} \cdot \boldsymbol{n}\, dA, \tag{2.2}$$

with $\boldsymbol{n}$ representing the normal unit vector to the surface. In this thesis the terms strength and circulation are treated as synonyms in the context of vortices.

With wake vortices constituting a product of aircraft lift generation, the below summarizes mechanisms and theories involved. For an inviscid and incompressible flow, Lanchester (1907) first described the generation of lift by an airfoil, the cross-section of a wing, with the superposition of a potential and a rotational flow. Kutta (1902); Joukowski (1906) derived the corresponding mathematical formulation, nowadays known as the Kutta-Joukowski theorem. They associate the rotational flow around the airfoil with the circulation, such that for an infinitely spanning wing the lift per unit span reads

$$l = \rho_\infty U_\infty \Gamma, \tag{2.3}$$

where ρ_∞ represents the fluid density and U_∞ represents the freestream velocity (Anderson, 1984, chap. 4). The definition of circulation from Eq. (2.2) allows an infinite number of curves to encompass the airfoil, affecting the computed circulation and thus lift. In practice, the so-called Kutta condition dictates that for lift production, the fluid flow must leave the trailing edge of an airfoil in a smooth manner (a stagnation point is found at the trailing edge) (Anderson, 1984, chap. 4), revealing an unique circulation and thus lift magnitude for an airfoil at a particular angle of attack to the flow.

Building on the above, Prandtl (1918b, 1919) formulated first practical aerodynamic theories for modeling finite wings. He argued that a wing of finite span B can be modeled using a so-called bound vortex, which rotates the vortex line into the flow at the wingtips, at $y = -B/2$ and $y = B/2$ ($y = 0$ at the lateral center of the wing). This is formally known as the horseshoe vortex theory illustrated in Fig. 2.1 (Lugt, 1983, chap. 4). In reality these trailing vortices form as a result of the pressure difference developing between the lower and upper sides of the wing due to the airfoil camber and/or angle of attack, where over- and underpressure prevail, respectively. As an act of balancing pressure, the overpressure forces the flow laterally outward, causing the trailing vortex circulation senses shown in Fig. 2.1.

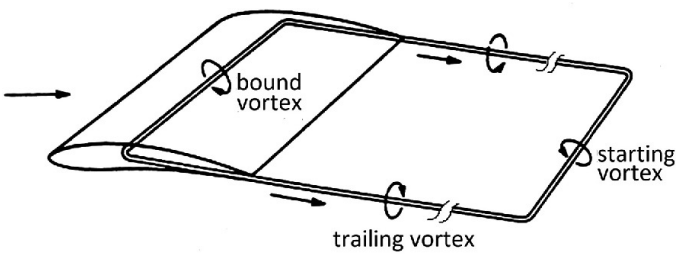

Figure 2.1: Schematic of the closed vortex ring system, constituting the bound vortex, the trailing vortices, and the starting vortex, for modeling a finite wing. With permission of 2021 Springer-Verlag GmbH Germany, part of Springer Nature, from Hirschel et al. (2021); permission conveyed through Copyright Clearance Center, Inc.

Assuming a limiting case line vortex with vorticity $\boldsymbol{\omega} = \Gamma\delta(n)\delta(b)\boldsymbol{s}$, where δ denotes the Dirac delta function, $\boldsymbol{s}$ denotes the tangent vector along the line, and both n and b represent the normal and bi-normal coordinates, respectively (Saffman, 1992, chap. 2), to represent a trailing vortex, the velocity induced at point $\boldsymbol{x}$, distance $\boldsymbol{r}$ from the line, reads

$$\boldsymbol{V}(\boldsymbol{x}) = \frac{\Gamma}{4\pi}\int \frac{d\boldsymbol{s}\times\boldsymbol{r}}{|\boldsymbol{r}|^3}, \tag{2.4}$$

named the Biot-Savart law. Lamb (1932, chap. 7) deduced that a counter-rotating pair of equal strength vortices and separation b induce each other a propagation speed of

$$\boldsymbol{V} = \frac{\Gamma}{4\pi(b/2)}. \tag{2.5}$$

A more realistic finite wing model is achieved not only with a single horseshoe vortex, but with the superposition of numerous horseshoe vortices with varying bound vortex lengths (Anderson, 1984, chap. 5). A bound vortex with the same circulation along its length results in approaching an infinite induced velocity towards $y = -B/2$ and $y = B/2$. Instead, superposing multiple horseshoe vortices allows for modeling a realistic circulation distribution in span direction of the wing, where the union of superposed bound vortices is referred to as the lifting-line (Anderson, 1984, chap. 5). The total lift force produced by the wing is thus (Anderson, 1984, chap. 5)

$$L = \rho_\infty U_\infty \int_{-B/2}^{B/2} \Gamma(y)\, dy. \tag{2.6}$$

The lift coefficient for a wing with planform area S is defined as

$$C_L = \frac{2L}{\rho_\infty U_\infty^2 S}. \tag{2.7}$$

In the limiting case of an infinite number of superposed horseshoe vortices, no circulation and a finite induced velocity at the wingtips is possible. The maximum circulation is found at the root of the wing, thus named the root circulation Γ_0. The horseshoe vortices and the lateral fluid motion along the wing generate a vortex sheet behind the trailing edge of the wing, which ultimately rolls up to the trailing wake vortices of strength Γ_0 each, as sketched in Fig. 2.2. The downward velocity acting on the lifting line by the vortex sheet is termed the downwash. Note that unless explicitly indicated, the circulation sense is not given with a circulation value in this thesis i.e., $|\Gamma| = \Gamma$. According to the third law of Helmholtz (1858) the trailing vortices cannot end freely in space, which leads to the so-called starting vortex (see Fig. 2.1), generated as the wing starts to move, to close the vortex ring (Lugt, 1983, chap. 4).

The downwash alters the incident flow at the wing (Anderson, 1984, chap. 5). The geometric angle of attack, representing the angle between the airfoil chord line and the freestream flow direction, is reduced by the induced angle of attack $\alpha_i = \tan^{-1}(w/U_\infty)$, giving the effective angle of attack (w gives the magnitude of the downwash velocity at the lifting line). The wing thus produces lift L perpendicular to the immediate incident flow ($\nparallel U_\infty$). According to the induced angle of attack this produces two force components: the conventional lift force (perpendicular to U_∞) and a so-called induced drag component $D_i = L\sin(\alpha_i)$ parallel to U_∞ (Kundu and Cohen, 2002, chap. 14).

The induced drag is minimized with an elliptic circulation distribution,

$$\Gamma(y) = \Gamma_0 \sqrt{1 - \left(\frac{2y}{B}\right)^2}, \tag{2.8}$$

and is frequently employed for modeling purposes (Kundu and Cohen, 2002, chap. 14). Also the lift distribution $l(y)$ is elliptic, while the lift coefficient distribution $C_l(y)$ is constant for the same airfoil across the entire span of an untwisted wing with an elliptic planform (these conditions rarely exist) (Anderson, 1984, chap. 5).

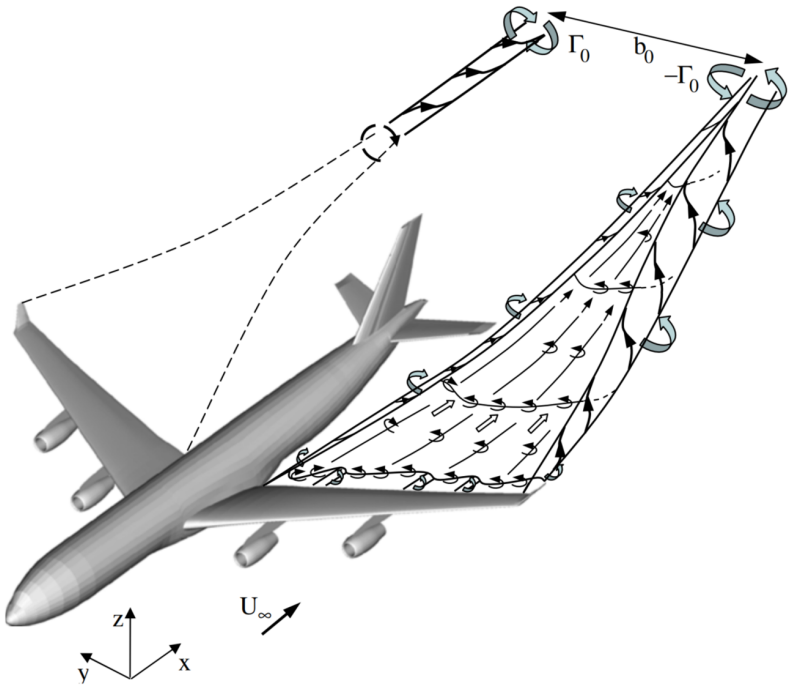

Figure 2.2: Schematic of a detaching vortex sheet from the wing and rolling up to trailing wake vortices. With permission of 2010 Elsevier Ltd., from Breitsamter (2011); permission conveyed through Copyright Clearance Center, Inc.

An unique characteristic of an elliptic circulation and lift distribution is the constant downwash along the wingspan. The root circulation for a wing with an elliptical lift distribution reads (Gerz et al., 2002)

$$\Gamma_0 = \frac{2C_L U_\infty B}{\pi\Lambda} = \frac{Mg}{\rho_\infty b_0 U_\infty}, \tag{2.9}$$

where $\Lambda := B^2/S$ is the defined as the wing aspect ratio and

$$b_0 = \frac{\pi}{4}B, \tag{2.10}$$

is the initial wake vortex pair separation of the fully rolled up pair (see Fig. 2.2). In steady flight, the aircraft weight, the product of its mass M and the gravitational acceleration $g = 9.81$ m s^{-2}, equal the lift produced by the aircraft.

Employing Γ_0, b_0, and Eq. (2.4) describes the initial descent speed of wake vortices for a wing with elliptical circulation distribution (Gerz et al., 2002),

$$w_0 = \frac{\Gamma_0}{2\pi b_0}. \tag{2.11}$$

This mutual velocity induction by the counter-rotating trailing vortices leads the pair, which is approximately fully rolled up ten wingspans behind the aircraft (Breitsamter,

2007, chap. 2), to descend a distance b_0 in the characteristic time,

$$t_0 = \frac{b_0}{w_0}. \tag{2.12}$$

The elliptical lift distribution assumption (typically representing an overestimated spanwise load factor) may substantial under- and overestimate w_0 and t_0, respectively. The vorticity unit scale amounts to (Gerz et al., 2002)

$$\omega_0 = \frac{1}{t_0}. \tag{2.13}$$

The forgoing parameters, Γ_0, b_0, w_0, t_0, ω_0, are employed for normalizing circulation magnitude, length, velocity, vortex age, and vorticity in this thesis (with the elliptical lift distribution assumption), allowing aircraft type and flight state independent analyses. Values normalized throughout this thesis are marked with an asterisk (*).

Note that primarily aircraft in high-lift configuration are considered in this thesis, their spanwise circulation and lift distributions deviate from the elliptical assumption (Breitsamter, 2007, chap. 2). Larger spanwise load factors $s = b_0/B$ (than $s = \pi/4$ found for the elliptical lift distribution) may be observed for landing aircraft in high-lift configuration (also smaller s may be observed), resulting in marginally lower Γ_0 and larger b_0 (Holzäpfel et al., 2022; Brown and Holzäpfel, 2025). In cruise, Brown and Holzäpfel (2025) find the initial wake vortex pair separation to be 15 % and 17 % smaller than expected by the elliptical lift distribution for Airbus and Boeing aircraft, respectively. Given that $t_0 \propto s^3$ and $w_0 \propto s^{-2}$, key wake vortex parameters of Airbus aircraft may be adulterated by approximately 40 % (Brown and Holzäpfel, 2024).

2.1.1 Phases and Evolution

Above it has been established that wake vortices are a consequence of finite geometry belonging to flying aircraft, with the pressure disparity on top and below the wing resulting in flow curving around the wingtips and along the trailing edge, ensuing in a vortex sheet rolling up into trailing vortices. The evolution of the trailing vortices, from their generation to their decay can be divided into four phases for cruise: the near-field, the extended near-field, the far-field, and finally the decay. The following descriptions are based on formulations by Breitsamter (2007, chap. 2), unless stated otherwise.

Near-Field

The near-field is generally located at $2x/B = \mathcal{O}(1)$, containing the generation and immediate advance of the vortex sheet detaching from the trailing edge of the wing. Note that the pressure difference between the top and bottom wing surfaces results not only in the roll up of the vortex sheet at the aircraft wingtips, but also at additional finite surfaces, particularly relevant in high-lift wing configurations (Stumpf, 2005; Stephan et al., 2019a). The precise shape and size of the wake vortices is dependent on the spanwise circulation

and lift distribution, influenced by factors including the wing sweep and wingtip geometry. The latter is frequently varied between aircraft generations, for example by installing winglets, allowing the increase of the effective wing aspect ratio (see above) and thus a reduced lift-induced drag.

Extended Near-Field

The extended near-field is generally located at $x/B \leq 10$. Completely developed wake vortices, commonly referred to as rolled up wake vortices, mark the ending of the extended near-field. The roll up of the vortex sheet ends is driven by self induction. As demonstrated in numerical simulations for a high-lift configuration aircraft (Stumpf, 2005), the various co- and counter-rotating wing-related wake vortices merge during this phase - primarily made up of the flaptip and wingtip wake vortices. Vortex regions of varying vorticity interact, causing the stretching of the co-rotating pair and secondary vortices wrap around the primary wake vortices (interaction of wingtip and flaptip vortices). This fluid exchange of the two primary co-rotating wake vortices results in a merging of the two co-rotating vortices into a single primary vortex of larger core size. Further, weaker wake vortices, caused for instance by the engines and landing gear of the aircraft, may not join this main wake vortex, and may instead descend downwards relative to the main vortex pair (Stephan et al., 2019a). The hazard by such secondary aircraft wake vortices to follower aircraft is minimal. Wake vortices are defined to be fully rolled up when their circulation corresponds to the theoretical root circulation Γ_0. At this point, the centers of the main counter-rotating wake vortex pair are separated by the distance b_0. Flight experiments find b_0-values of $0.66B$, $0.67B$, and $0.65B$ for Airbus A380-800, Airbus A350-900, and Boeing 747-400, respectively (Brown and Holzäpfel, 2025). Delisi et al. (2013) report similar values for Heavy aircraft, while b_0-values measured for Medium aircraft (such as Airbus A319 and Airbus A320) nearly match those computed with the elliptical lift distribution assumption (ICAO aircraft categories).

Far-Field

The far-field is generally located at $10 \leq x/B \leq 100$. Significant lengths behind the aircraft only show minor wake topology and strength developments. Solely a minor increase in the vortex cores is observed.

Decay

The decay region is generally located at $x/B > 100$ (although particularity a highly turbulent atmosphere can lead to a premature decay onset). The aforementioned mutual velocity induction is also the driver for the long wavelength Crow instability (Crow, 1970; Crow and Bate, 1976) initiated by any small disturbances and in numerical simulations usually by a sinusoidal disturbance in the vortex trajectories. Elliptical deformations of the outer vortex streamlines result due to the mutually-induced center-focused stagnation points,

which also lead to vortex core deformations. For the counter-rotating vortex pair of equivalent magnitude a fluctuation axis inclination of ± 45 deg with respect to the horizontal is observed (Breitsamter, 2007, chap. 5). Note that depending on the particular conditions also further short and medium scale instabilities may prevail. Altogether these mechanisms result in a significant loss of vortex coherency. Thereafter the trajectory deflection grows exponentially, eventually causing the counter-rotating wake vortex pair to interact across the symmetry plane, significantly speeding up the decay process (at T^*_{onset}). Finally, the vortex filaments link, resulting in vortex rings, and eventually their complete dissipation. The simplified schematic in Fig. 2.3 divides the decay of wake vortices into a slow turbulent diffusion phase and a rapid decay of vortex circulation (Gerz et al., 2002). In practice, the decay of wake vortices depends on the prevailing atmospheric conditions. Proctor et al. (2010); Holzäpfel et al. (2010) also find one-phase and three-phase wake vortex decays, with the latter prevailing under low turbulence and neutral stratification conditions.

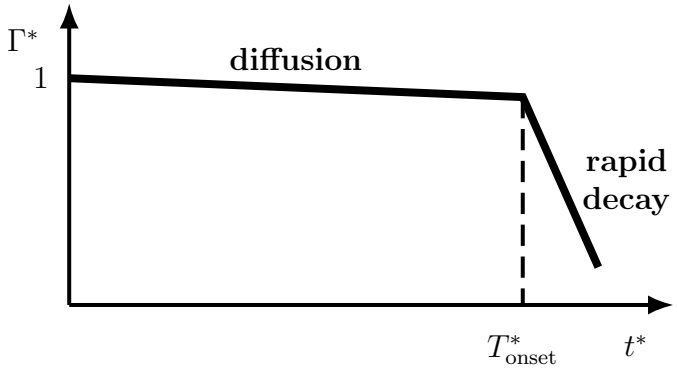

Figure 2.3: Simplified schematic of the two-phase counter-rotating wake vortex pair decay in terms of normalized vortex circulation and age. After Gerz et al. (2002).

2.1.2 External Influences on Wake Vortex Progression

The evolution and trajectory of a wake vortex pair, as well as its strength development, significantly differ when conditioned by factors external to the aircraft. Particularly the vicinity to walls, in the form of the ground and objects placed on the ground, as well as the prevailing atmospheric scenario alter the evolution of a wake vortex pair. Unfavorable combinations can lead to extended vortex lifetimes and consequently higher wake vortex encounter risk for follower aircraft.

Ground Influence

Aircraft in ground vicinity experience altered flight characteristics. Aircraft ground effects, first studied by Prandtl (1918a); Wieselberger (1922), have a significant impact on the stability and the trim state of an aircraft. For example, the wing downwash is hampered, reducing the induced angle of attack and therefore altering the generated lift and drag

(Staufenbiel and Schlichting, 1988). At the same time, a significant pressure increase occurs between the lower wing surface and the ground (known as the wing-in-ground effect), resulting in a lift increase - a phase referred to as flare (Stephan et al., 2014; Staufenbiel and Schlichting, 1988; Lange and Moore, 1980). These altered handling characteristics require piloting inputs, ensuring continued safe flight by the aircraft (Etkin, 1972, chap. 7).

Wake vortices are also affected by the ground, the relevant in-ground effect is defined to initiate below an altitude of one initial vortex separation (b_0) (Proctor et al., 2000). Out of ground proximity, mutual velocity induction of the counter-rotating wake vortex pair causes a pure downward motion (neglecting further atmospheric effects, which are mentioned below). Inviscid theory demands vortices in the proximity to a horizontal wall to additionally transport in the lateral direction; in order to satisfy the kinematic boundary condition of no vertical velocity, vortices overall follow an asymptotic altitude (Saffman, 1992, chap. 7). This in-ground effect can be modeled using image vortices (also called mirror vortices), which are placed on the imaginary opposite side of the wall and are of opposing circulation sense but equivalent magnitude to the descending wake vortices (see Fig. 2.4). An initially descending counter-rotating vortex pair thus forms symmetric outwards-oriented hyperbolic trajectories. In practice however, shortly after the lateral vortex transport, an additional vertical velocity component is experienced by the vortices (Harvey and Perry, 1971). Below an altitude of $1.5b_0$, the descending vortex pair provokes a viscous boundary / vorticity layer via induced cross-flow onto the ground (Robins et al., 2001). As the vorticies approach the ground further, the adverse pressure gradient within the boundary layer grows, eventually causing secondary vortices of opposite circulation sense to separate and detach from the boundary layer (gray vortices in Fig. 2.5) (Doligalski et al., 1994). Thus, the altered wake vortex trajectories are reasoned by their interaction with the produced secondary vortices. Each wake vortex receives an associated secondary vortex, forming counter-rotating vortex pairs, also subject to short wavelength elliptic instabilities and as a result shortening the lifetime of the wake vortices.

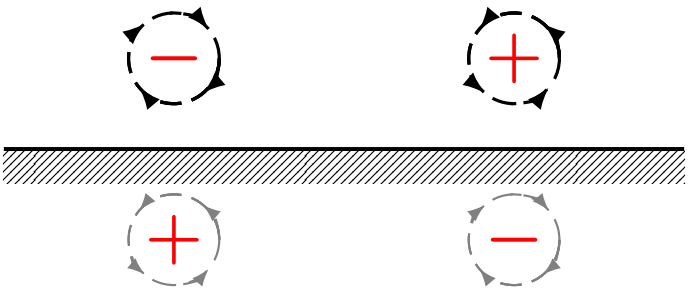

Figure 2.4: Counter-rotating vortex pair above a wall in black color, image vortices of the equal circulation, but opposite circulation sense are given in gray color.

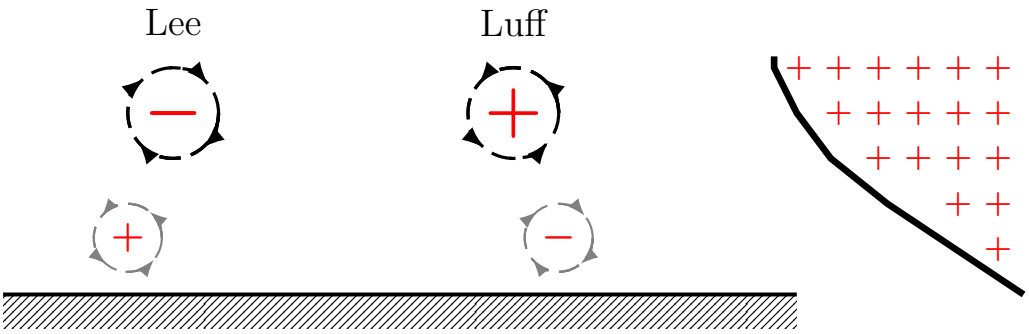

Figure 2.5: Wake vortex pair (black) in ground vicinity generating secondary vortices (gray) which shed-off the induced boundary layer. On the right a logarithmic crosswind is sketched. Signs indicate the vorticity sense. After Stephan et al. (2013a).

Complex terrain or objects on the ground may alter wake vortex development further. For example a tree ensemble, or alternative obstacles have shown to lead to severe vortex rebounds (Holzäpfel et al., 2002) given the smaller separation between a wall and the vortex, and further wind shear generated (Holzäpfel and Steen, 2007). Recently it has been suggested to intentionally alter the ground profile underneath the glide path of approaching aircraft at airports to trigger premature vortex decay and reduce the vortex lifetime. Last decade a patent (DE 10 2011 010 147.0 for Germany, international patents followed) was filed for accelerating wake vortex decay in airport vicinity with a modification of the ground. The refined Plate Line concept has been numerically simulated (Stephan et al., 2013a, 2014) and experimentally validated (Holzäpfel et al., 2016a; Holzäpfel et al., 2021) (see Fig. 2.6 left), reaching technology readiness level 7 and prototype status in 2023 (see Fig. 2.6 right) (Jung, 2023). A patent license was issued to the Lattix® Production AB in the same year.



Figure 2.6: Experimental Plate Line below the glide path of landing aircraft at Vienna Airport in 2019 (left) and the permanent plate design exhibit at the German Aerospace Center (DLR) in Oberpfaffenhofen, Germany (right). Copyright by Frank Holzäpfel.

According to Holzäpfel et al. (2021) the placement of plates in a line can reduce the lifetime of wake vortices by 22 % to 37 % for Airbus A320 and Boeing 777-200 (also known as B772), respectively. This amounts to a 50 % reduction of wake vortex circulation generated by a Heavy aircraft for a Medium follower aircraft (ICAO aircraft categories). Consequently, the RECAT-EU minimum separations could be reduced further (Holzäpfel et al., 2022; Koloschin et al., 2025).

Atmosphere

In quiescent atmosphere, the evolution of wake vortices in ground proximity is influenced by the vortex-induced boundary layer and geometry on the ground. Turbulent crosswinds, forming shear flows, influence the evolution of wake vortices in ground proximity with accelerated vortex decay and asymmetric trajectories (Holzäpfel and Steen, 2007). Both the primary wake vortices and the secondary vortices, detaching from the viscous boundary layer, are affected by a prevailing crosswind (see Fig. 2.5). Depending on the crosswind strength, the generation of the secondary vortex resulting from the descend of the luff (upwind) vortex is delayed or even suppressed, in comparison to the secondary vortex generated by the descending lee (downwind) vortex, where the opposite occurs. In fact, Holzäpfel and Steen (2007) identify a crosswind of $0.5w_0$ to be most critical in the airport runway context [confirmed by Stephan et al. (2013a); Holzäpfel et al. (2016b)]. Such crosswind compensates the vortex-induced lateral propagation speed, resulting from the vortex-boundary interaction, allowing the luff vortex to hover over the runway for a significant period of time.

Out-of-ground, further atmospheric effects, such as ambient turbulence and stratification may contribute significantly to the evolution of wake vortices. For instance, stable stratification decelerates the vortex descend and may even cause a similar rebound as observed for a viscous boundary layer, due to developing baroclinic vorticity (Holzäpfel and Gerz, 1999). However, in ground vicinity these atmospheric effects play a minor role in comparison to the boundary layer interaction (Holzäpfel and Steen, 2007). Solely a premature vortex linking with the ground may result (Proctor et al., 2000).

2.1.3 Vortex Models

Wake vortices can be modeled in multiple ways. Vortex models extend from the inviscid potential vortex and typically focus on a quasi two-dimensional flow using the tangential velocity component in cylindrical coordinate system, with x as the axis, r as the radial coordinate, and θ as the azimuthal angle (see Fig. 2.7). The following partly reproduces descriptions by Breitsamter (2007, chap. 2).

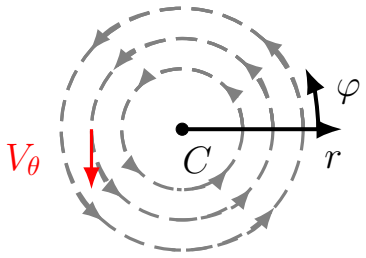

Figure 2.7: Cylindrical coordinate system of a vortex located at C.

Potential Vortex

The potential vortex establishes the foundation of most vortex models. It forms the solution to an incompressible, inviscid, and irrotational flow (Anderson, 1984, chap. 3). The velocity (purely tangential, V_θ) along each streamline is constant. The velocity distribution of a potential vortex in cylindrical coordinates is

$$V_x = 0,\ V_r = 0,\ V_\theta = \frac{\Gamma_0}{2\pi r}, \tag{2.14}$$

indicating an inverse relationship between the radius r and V_θ ($V_\theta \propto 1/r$). All following vortex models share the same velocity components V_x and V_r.

In practice, the potential vortex is not met as it suggests infinite velocity magnitude at its center. Analytical models therefore include viscous considerations in their model, with the inner part of a vortex representing the vortex core. The core flow can be modeled as the rotation of a solid body of radius r_c, defined by the maximum tangential velocity of the vortex $V_{\theta,\max}$. Various analytical vortex models represent the physics under different assumptions, ultimately aiming to blend the viscous core flow with the potential vortex flow. Popular analytical vortex models are the Rankine (R), Lamb-Oseen (LO), and Burnham-Hallock (BH) vortices compared by their tangential velocity profiles in Fig. 2.8 (with V_θ^0 representing the tangential velocity of the potential vortex at r_c set for the other vortex models). Additionally, the potential vortex (P) is plotted. Evidently, a Rankine vortex follows the potential vortex for $r > r_c$, resulting in unphysical maximum tangential velocities. The Lamb-Oseen and Burnham-Hallock vortices smoothly blend the rotating solid body and the potential vortex. Nonetheless, Hallock and Holzäpfel (2018) conclude that no universal V_θ-profile is known for a wake vortex. They argue that the V_θ-profile transforms as the wake vortex evolves and on average the Burnham-Hallock vortex represents an adequate compromise. The exact V_θ-profile depends on both the Reynolds number and vortex age, affecting both peak velocity and vorticity (Stumpf, 2003; Hallock and Holzäpfel, 2018).

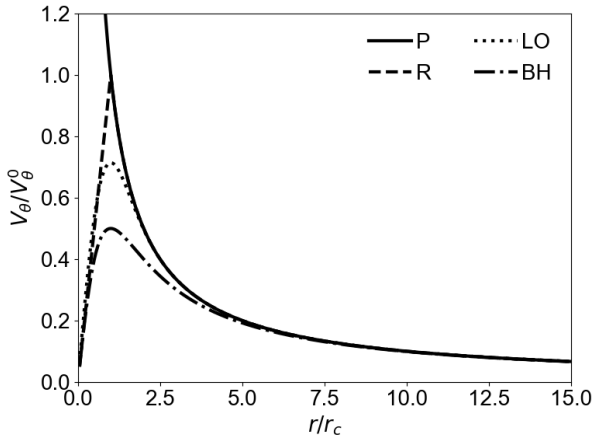

Figure 2.8: Normalized tangential velocity (V_θ) profiles with respect to the core-radius-normalized vortex radius of the potential (P), Rankine (R), Lamb-Oseen (LO), and Burnham-Hallock (BH) vortex models. The normalization is performed using the core radius and the potential vortex tangential velocity at the core radius.

Rankine Vortex

Strictly speaking, the Rankine vortex model does not model a viscous vortex core. Instead, a solid body rotation (ω_x is constant) at $r \leq r_c$ and potential vortex flow ($\omega_x = 0$) at $r > r_c$ is defined (Breitsamter, 2007, chap. 2),

$$V_\theta = \begin{cases} (\Gamma_0/2\pi r_c)\,(r/r_c)\,, & r \leq r_c, \\ \Gamma_0/2\pi r, & r > r_c, \end{cases} \tag{2.15}$$

resulting in a linear increase in tangential velocity with the vortex radius, until reaching the vortex core radius, from where the potential vortex is considered.

Lamb-Oseen Vortex

Lamb (1932) first mentioned this analytical vortex model, constituting an exact solution to the Navier-Stokes equations (mathematical representation of fluid flow in the form of mass, momentum, and energy conservation), thus considering viscosity ν and a smooth transition between the vortex core and the potential vortex,

$$V_\theta = \frac{\Gamma_0}{2\pi r}\left\{1 - \exp\left[-\left(\frac{r^2}{4\nu t}\right)\right]\right\}. \tag{2.16}$$

The diffusion of the vortex core with time is given by $dr_c^2/dt = 5.0257\nu$ (Breitsamter, 2007, chap. 2), leading to

$$V_\theta = \frac{\Gamma_0}{2\pi r}\left\{1 - \exp\left[-1.2526\left(\frac{r}{r_c}\right)^2\right]\right\}. \tag{2.17}$$

Burnham-Hallock Vortex

Burnham and Hallock (1982) consider both the solid body rotation of the vortex core and a well-defined root circulation (Burnham and Hallock, 2013). Their vortex model defines r_c by both the maximum V_θ as well as $\Gamma(r = r_c) = \Gamma_0/2$, resulting in

$$V_\theta = \frac{\Gamma_0}{2\pi r} \frac{r^2}{r^2 + r_c^2}. \tag{2.18}$$

This thesis assesses the RV method (see Section 3.4.2) which employs Burnham-Hallock vortices for characterizing the strength of wake vortices from lidar measurements. Limitations of this approach are discussed in Section 4.3.1.

2.1.4 Wake Vortex Characterization Parameters

Parameters which are commonly employed for characterizing wake vortices and a counter-rotating wake vortex pair are summarized in this section. Section 2.1.1 described the generation of the primary wake vortex pair as the merged result of numerous vortices shed off the aircraft geometry. In theory, the two counter-rotating wake vortices have the same strength but different signs, i.e., $\Gamma_1 = -\Gamma_2$ and $|\Gamma_1| = |\Gamma_2|$. As shown in Fig. 2.2, the fully rolled up wake vortices each have an absolute circulation of Γ_0. Throughout their evolution, each wake vortex is characterized by their position and circulation (strength), with Fig. 2.9 giving a schematic overview of involved parameters for a counter-rotating vortex pair, made up of a starboard (Str) vortex and a port (Prt) vortex.

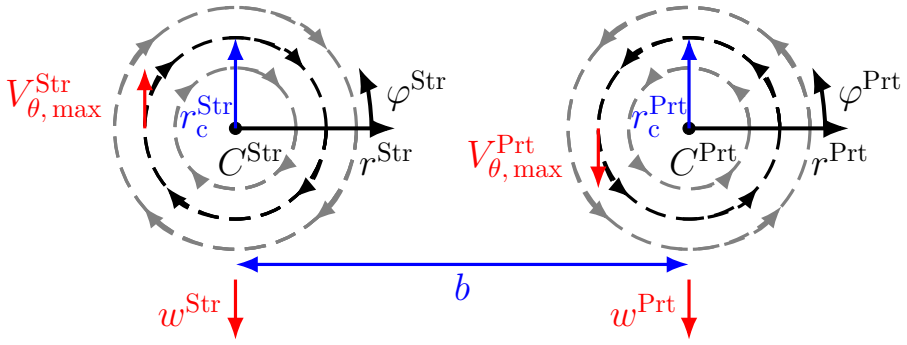

Figure 2.9: Schematic of a counter-rotating analytical vortex pair. Black circles represent the vortex core.

The position of a vortex in a flow field can be determined by several measures, one common approach is computing the centroids over a half-plane. In the case of a vortex within the yz-plane, the vortex center is found at (Gerz et al., 2002),

$$\bar{y}_C = \frac{1}{\Gamma} \int_{-\infty}^{\infty} \int_{0}^{\infty} y \omega_x dy dz, \tag{2.19}$$

$$\bar{z}_C = \frac{1}{\Gamma} \int_{-\infty}^{\infty} \int_{0}^{\infty} z\omega_x dy dz. \tag{2.20}$$

The determinable circulation of aircraft wake vortices is dependent on the area considered [see Eq. (2.2)], while the root circulation Γ_0 would encompass the entire vorticity belonging to the isolated wake vortex in an infinitely large area. In practice, it is common to employ an averaged circulation parameter such as

$$\Gamma_{5-15} = 0.1 \int_{5\text{ m}}^{15\text{ m}} \Gamma(r) dr, \tag{2.21}$$

describing the averaged circulation over radii 5 m to 15 m from the vortex center. Such averaged circulation, and particularly Γ_{5-15}, is useful for omitting measurement outliers (Gerz et al., 2002) and recommended for wake vortex encounter analysis (Hinton and Tatnall, 1997). Given its widespread usage in literature, note that Γ_{5-15} is synonymous with circulation in this thesis, unless explicitly stated otherwise. Restricting the analysis of the vortices to this particular radius spectrum emerges from research of large aircraft, causing inferior reliability for the analysis of wake vortices generated by smaller aircraft (Breitsamter, 2011). Both Hinton and Tatnall (1997) and Holzäpfel et al. (2003) describe a circulation overestimation just below 20 % for Medium aircraft such as the Airbus A320 (ICAO aircraft categories), while aircraft with $b_0 > 40$ m can expect an overestimation well below 10 % when employing vertically viewing lidars. The overestimation of wake vortex strength estimation with Γ_{5-15} reduces significantly when employing oblique viewing lidars (as is the case in this thesis) (Holzäpfel et al., 2003).

Furthermore, a hazard analysis for a follower aircraft (index f) can be conducted. Typically, such analysis involves quantifying the rolling moment induced by the potentially hazardous wake vortex onto the aircraft,

$$M_{L,f} = \frac{1}{2} \rho_\infty U_{\infty,f}^2 \int_{-B/2}^{B/2} C_{l,f} \left[y, \alpha_f (y) \right] c_f (y)\, y dy, \tag{2.22}$$

where U_∞ can be interpreted as the True Air Speed (TAS), c is the airfoil chord length, y is the position along the aircraft's wing, and $C_{l,f} \left[y, \alpha_f (y) \right] = C_{l_\alpha,f} \tan^{-1} \left[w(y)/U_\infty \right]$ is the local airfoil lift coefficient with $C_{l_\alpha} = \partial C_l / \partial \alpha_f$ and the local airflow w (Breitsamter, 2007, chap. 2). Thus, local airflow and wake vortices induce rolling moments onto aircraft by varying w. Note that moments are denoted with an M in this thesis. Straightforwardly, the roll moment coefficient with respect to the wingspan reads

$$C_{M_L} = \frac{2 M_L}{\rho_\infty U_\infty^2 S B}. \tag{2.23}$$

Small aircraft flying into the center of a vortex experience larger rolling moments than aircraft with a larger wingspan. For smaller aircraft, the higher velocities prevailing near the vortex core are induced at the outer parts of the wing (large lever arm), leading to an overproportional contribution to the vortex-induced rolling moment. For larger aircraft,

the outer parts of the wing (large lever arm) are subject to lower velocities, while the higher velocities prevailing near the vortex core are paired with a small lever arm. Wake vortex encounters are therefore particularly hazardous for smaller aircraft flying behind larger aircraft (which generate stronger wake vortices).

It is therefore necessary to evaluate whether follower aircraft are able to counteract the vortex-induced rolling moment via the roll control potential,

$$R_C := \left| \frac{\delta_c C_{L_p}}{C_{M_L,f}} \right| = \left| \frac{C_{M_L,c}}{C_{M_L,f}} \right|, \tag{2.24}$$

where δ_c represents the deflection of a control surface, C_{L_p} is the roll damping coefficient (exception to the thesis' notation to allow neat equation display, the rolling moment is simply L, not M_L), $C_{M_L,f}$ denotes the wake-induced rolling moment coefficient and $C_{M_L,c}$ denotes the rolling moment coefficient by control surface deflection (Breitsamter, 2007, chap. 2). If $R_C \geq 1$ the wake vortex induced rolling moment can be counteracted to return to stable flight. This may also be expressed as the Roll Control Ratio (RCR) (Hahn et al., 2004),

$$RCR := \left| \frac{\delta_C^{\text{req}}}{\delta_C^{\max}} \right|, \tag{2.25}$$

where superscripts denote the required (req) and the maximum (max) aileron deflections. These parameters are used in the concept of Simplified Hazard Area Prediction (SHAPe) (Hahn et al., 2004) to define hazardous regions in the wake of a generating aircraft, as well as safety separations.

2.2 Lidar Measurements for Wake Vortices

Measuring velocity fields in the lower troposphere is conducted with measurement devices built for the scales one aims to observe. Previously employed instruments include sound based sonic detection and ranging (sodar), radio based Doppler radio detection and ranging (radar) (based on radio waves), and light amplification by stimulated emission of radiation (laser) based Doppler lidar instruments (Banakh and Smalikho, 2013). Wake vortices represent relatively small-scale phenomena in the atmosphere, necessitating the short wavelength of a laser beam. Only in highly noisy atmospheric conditions, for instance in the presence of fog or rain, radars are beneficial over lidars at the wake vortex scale (Kovalev, 2019). This thesis focuses on clean air conditions and thus lidars are investigated. Below recapitulates Banakh and Smalikho (2013, chaps. 1 and 2) to summarize the most fundamental and relevant lidar principles for this thesis (unless stated otherwise).

2.2.1 Lidar Types

Multiple categories of lidars exist, most modern lidars for atmospheric measurements are Coherent Doppler Lidars (CDLs), implying their ability to measure both the amplitude and

the phase of a signal instead of solely the energy content (Kingston, 1977). In that way a relatively weak signal in a noisy atmosphere suffices for realizing high accuracy LOS velocity measurements (Banakh and Smalikho, 2013; Gimmestag and Roberts, 2023). Indeed, CDLs with respective processing algorithms are considered the most efficient instruments for studying wake vortices in the atmosphere (Banakh and Smalikho, 2013, chap. 5). Two types of CDLs exist:

- **Continuous wave CDL (cw-CDL)**: A continuous laser beam is emitted. It focuses on a particular point in space using a single sensing volume, within which the atmosphere is assumed steady in time - limiting the velocity accuracy (Cariou and Boquet, 2011). This is particularly a trade-off for a larger focal distance, which also increases the sensing volumes such that wake vortices can be observed (Banakh and Smalikho, 2013, chap. 5).

- **Pulsed Coherent Doppler Lidar (PCDL)**: Individual pulse beams (or simply pulses) of laser are emitted. It uses multiple sensing volumes along a LOS and is focused on delivering a high spatial (and velocity) resolution, dramatically simplifying the processing of the return signal, the backscatter signal, to the lidar device, and allowing long durations of wake vortex observation (Mikkelsen, 2009; Köpp et al., 2004; Cariou and Boquet, 2011).

PCDLs are suggested as part of a WVAS (see Fig. 1.1 left) (Holzäpfel et al., 2009a) and were employed at the most recent wake vortex measurement campaigns, for instance the Vienna Airport campaign (Holzäpfel et al., 2021). As a result, this thesis concentrates on the PCDL operation and is used interchangeably with lidar herein.

2.2.2 Wake Vortex Measurement Overview

LOS velocity information is retrieved from the atmosphere using a lidar by considering two fundamental aspects covered below:

1. The interaction of the emitted pulsed laser beam with aerosols.

2. The backscatter signal returning to the lidar must be processed and decoded.

The most common ground lidar configuration for wake vortex measurements in runway vicinity is the RHI configuration sketched in Fig. 2.10 with two coordinate systems, a Cartesian coordinate system $[x', y', z']$ and a spherical coordinate system $[r, \varphi, \theta]$, where O represents the origin (lidar position). This thesis assumes the azimuth angle $\theta = 0$ deg i.e., perpendicular to the wake vortex pair, sketched as Str and Prt vortices relative to the aircraft flying out of the page.

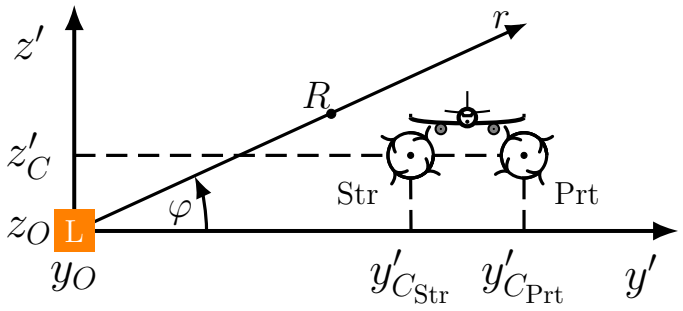

Figure 2.10: Schematic of a lidar (L) performing a RHI scan. The Str and Prt wake vortices are captured. The lidar laser beam is given by the solid black line. Adapted from Wartha et al. (2022)©.

The lidar (L), located next to the glide path at (x_O, y_O, z_O), emits laser beam pulses along a LOS of elevation angle φ, which interact with aerosols in the atmosphere. The shape of a pulse emitted is assumed Gaussian (Banakh and Smalikho, 2013, chap. 1),

$$g(s) = \frac{1}{\Delta p\sqrt{\pi}} \exp\left(-\frac{s^2}{\Delta p^2}\right), \tag{2.26}$$

where $\Delta p = c\sigma_P/2$ denotes the spatial pulse width defined by the e^{-1} intensity level with respect to the maximum intensity (σ_P is the temporal pulse width) and $c = 0.3$ m ns^{-1} denotes the speed of light in air. An alternative temporal pulse width frequently used is the Full-Width at Half Maximum (FWHM),

$$\tau_P = 2\sigma_P\sqrt{\log 2}, \tag{2.27}$$

which considers the power drop to the half maximum level from the peak (spatial: $\Delta r = c\tau_P/2$). The aerosols scatter light back to the receiver of the lidar, arriving at the lidar as an intensity-time signal. By transforming the time signal into the frequency domain, the emitted reference (ref) signal frequency f_{ref} and received (rec) signal frequency f_{rec} (also referred to as the first spectral moment of the received signal) can be employed for determining the LOS velocity via the Doppler relation (Banakh and Smalikho, 2013, chap. 2),

$$V_r = \frac{\lambda(f_{\mathrm{rec}} - f_{\mathrm{ref}})}{2}, \tag{2.28}$$

with λ denoting the laser wavelength. The LOS velocities from different positions R along the LOS are differentiated by considering the time-of-flight of laser pulses. For RHI lidar scans the elevation angle continuously changes at a predetermined scanning rate ω_S between a minimal and maximal elevation angle φ_- and φ_+, respectively. A positive and negative scanning rate correspond to elevation angle increase, $+\varphi \equiv t_{\varphi_-} < t_{\varphi_+}$, or decrease $-\varphi \equiv t_{\varphi_+} < t_{\varphi_-}$ during the scan.

The process repeats until the LOS sweep from φ_- to φ_+ (or vice versa) has been covered. Figure 2.11 provides a schematic of the process with discrete elevation angles φ_k. A total of K elevation angles and J ranges (distances R from the lidar), spaced by $d\varphi$ and dR, respectively, are considered. Thus, the LOS velocity is desired at (R_j, φ_k) pairs.

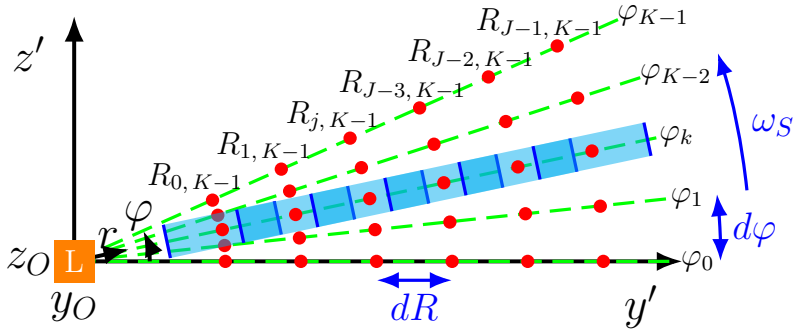

Figure 2.11: Schematic of a RHI scan with LOSs, measurement points, and range gates. Red dots represent locations for which the LOS velocity is estimated along the LOS (green dashed lines). Overlapping range gate windows are drawn for φ_k in blue color (the window width is exaggerated for visibility). Adapted from Wartha et al. (2025c)©.

2.2.3 Backscatter Retrieval

In reality, lidar instruments cannot realize point measurements of LOS velocities as implied by the red dots in Fig. 2.11. Individual laser pulses simultaneously interact with multiple aerosols, which are also distributed in an unpredictable manner at $(r_{i'}, \boldsymbol{\rho}_{i'})$, with $\boldsymbol{\rho} = [x'', y'']$ defining the beam cross-section, in the spherical lidar coordinate system. Instead, sensing volumes and range gates, which mark atmosphere volumes along the LOS with the centers (R_j, φ_k), are considered. Range gates are predefined lengths $\Delta R = cT_W/2$ (T_W represents the temporal range gate), depicted in Fig. 2.11 as blue windows. The thickness of the laser beam is exaggerated for visibility purposes, in fact it is common practice to neglect the perpendicular direction to the laser beam for estimating LOS velocities (Banakh and Smalikho, 2013, chap. 1).

Furthermore, the light scattered back to the lidar, the backscatter signal, consists of two components, the echo signal Z_S, which describes the component of interest i.e., movement of the aerosols, and an atmospheric background noise signal component Z_N including disturbances such as instrument noise, surrounding light/radiation sources, condensation, fog, smoke, hard targets, cosmic noise and many more (Banakh and Smalikho, 2013; Menzies and Hardesty, 1989; Doviak and Zrnić, 1993), giving

$$Z(t) = Z_S(t) + Z_N(t). \tag{2.29}$$

The intensity of the echo signal is proportional to a backscatter coefficient β_π determined by the aerosol concentration, size, and backscatter cross-section as well as the pulse energy E_P

(Banakh and Smalikho, 2013, chap. 1). An echo signal with a high intensity is desirable for accurate LOS velocity measurements. The SNR is defined as the ratio of the mean echo signal power (associated with Z_S) to the mean noise power (associated with Z_N) over a particular frequency band (Banakh and Smalikho, 2013, chap. 1). In this thesis the frequency band considered is $B_f = 50$ MHz in accordance with Stephan et al. (2019b). The LOS velocity associated with a range gate can be determined using Eq. (2.28) by transferring the echo signal to the frequency domain. In the case when $Z_N(t) \approx 0$ i.e., SNR $>> 1$, the signal is Fourier transformed for N_a pulses (in ideal conditions $N_a = 1$), measuring $Z_S(t, n)$ arrays,

$$S(f) = \frac{1}{N_a} \sum_{n=1}^{N_a} \left| \int_{-\infty}^{\infty} W(t) Z_S(t, n) \exp(-2\pi j f t) dt \right|^2 , \tag{2.30}$$

where the normalized complex echo signal for a PCDL is given by (Banakh and Smalikho, 2013, chap. 1)

$$Z_S(t) = \frac{\lambda}{\pi a_0^2} \sqrt{\frac{2\eta E_p}{h\nu B_0 \sqrt{\pi} \sigma_P}} \sum_{i'=0}^{I'-1} \alpha_{i'} \exp\left[-\frac{(t - 2r_{i'}/c)}{2\sigma_P^2} + j\psi_{i'} + 2\pi j \frac{2V_r(r_{i'})}{\lambda} t \right] \times I_{\mathbf{PN}}\left(r_{i'}, \boldsymbol{\rho}_{i'}, t\right), \tag{2.31}$$

where the contributions from each aerosol can be divided in I' sub-signals with amplitude $\alpha_{i'}$, I_{PN} gives the normalized intensity of the laser beam with a radius a_0 (at intensity level e^{-1}), $h\nu$ gives the photon energy with Planck's constant and the photon's frequency ν, η gives the quantum efficiency (the probability of an electron capturing a photon), $j = \sqrt{-1}$, and V_r is the particular aerosol LOS velocity responsible for $f_{\mathrm{rec}} \neq f_{\mathrm{ref}}$. Possible f_{rec} within bandwidth B_0 are considered.

Besides the background noise mentioned above, a second source of noise can be defined as aerosol noise (atmospheric fluctuations). It is a consequence of turbulent velocity fluctuations within range gates, causing different aerosols to move in various magnitudes and directions with respect to the lidar LOS. Furthermore, the aerosol distribution in combination with various aerosol sizes and shapes, lead to unpredictable refractions and therefore contributions from sub-signals (Robey and Lundquist, 2022). Due to the two types of noise, the PCDLs cannot rely on the backscatter of a single pulse and instead employ pulse accumulation, where the power spectra of N_a pulses are averaged (accumulated). The accumulated power spectrum aims to neutralize random noise components of individual pulses and delivers f_{rec} using methods introduced in Section 2.2.4 (strictly speaking $\bar{f}_{\mathrm{rec}}$).

Each laser pulse P_n travels through a range gate and interacts with aerosols therein, as well as partly thereout (as a result of pulse travel and width relative to the range gate size). Indeed, since wake vortices represent coherent small-scale structures in the lower troposphere, employed range gate windows are typically smaller than the laser pulse width (both range gate size and pulse width are subject to hardware limitations). As a result, a

sensing volume can be defined by (Banakh and Smalikho, 2013, chap. 2)

$$\Delta z = \int_{-\infty}^{+\infty} \frac{Q_S(s)}{Q_S(0)} ds = Q_S^{-1}(0), \tag{2.32}$$

where Q_S is the spatial resolution function representing the weighting function of spatial averaging over the sensing volume, also referred to as Range Gate Weighting Function (RWF) in this thesis. Using the definition of a pulse from Eq. (2.26) and the summarizing the range gate profile via an indicator function,

$$W(s) = \begin{cases} 1/\Delta R, & |s| \leq \Delta R/2, \\ 0, & |s| > \Delta R/2, \end{cases} \tag{2.33}$$

the RWF is obtained from their convolution (Robey and Lundquist, 2022),

$$Q_S(s') = \int_{-\infty}^{+\infty} g(s'-s) W(s) ds. \tag{2.34}$$

Substitution of Eqs. (2.26) and (2.33) gives the RWF as

$$Q_S(s') = \frac{1}{cT_W} \left[\operatorname{erf}\left(\frac{2s'/c + T_W/2}{\sigma_P} \right) - \operatorname{erf}\left(\frac{2s'/c - T_W/2}{\sigma_P} \right) \right], \tag{2.35}$$

with the standard error function,

$$\operatorname{erf}(x) := \frac{2}{\sqrt{\pi}} \int_0^x \exp\left(-\xi^2\right) d\xi. \tag{2.36}$$

The full derivation is provided in Appendix A. Substitution of Eq. (2.35) into Eq. (2.32) allows the longitudinal sensing volume length to be computed by the formulation

$$\Delta z = \frac{\Delta R}{\operatorname{erf}\left[\Delta R / \left(c\sigma_P\right)\right]}. \tag{2.37}$$

On top of the previously discussed instrument noise, environmental influences, as well as aerosol noise, a further factor influencing the SNR is the focal range. With lidar instruments representing optical measurement devices, optical considerations are of importance. Therefore, every lidar is optimized for a particular focal range from the instrument, achieving the highest SNR at that range. Ideally, the focal range is set to where the phenomenon of interest is located, however lidar placement and hardware may hinder an ideal focal range. The SNR is therefore not equal throughout a RHI lidar scan.

2.2.4 LOS Velocity Processing

The LOS velocity associated with a single range gate window is processed by analyzing the Doppler power spectrum, which is given by

$$S_D\left(f; R_j, \varphi_k\right) = S\left(f; R_j, \varphi_k\right) - S_N\left(f; \varphi_k\right), \tag{2.38}$$

where S is the result of the Fourier transform of the backscatter signal received by the lidar [see Eq. (2.30)]. An example spectrum is given in Fig. 2.12. It is not possible to separately determine the echo and noise signals from Eq. (2.29), therefore it is common practice to estimate the background noise signal by measuring a backscatter signal at a distance far from the considered phenomenon, where the echo signal is negligible, and thus $Z \approx Z_N$. With Eq. (2.30) and substituting Z_N for Z_S, the noise power spectrum S_N is estimated.

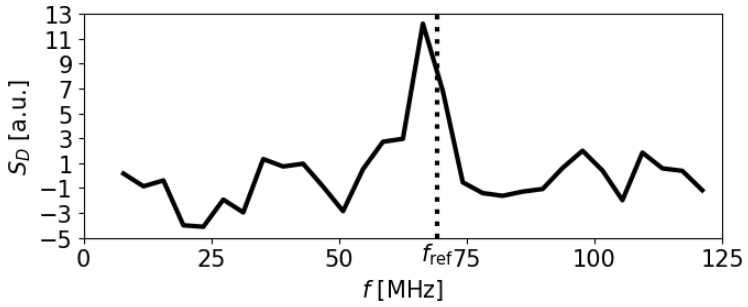

Figure 2.12: Example Doppler power spectrum of a range gate along a lidar LOS with the reference frequency f_{ref}. The spectrum uses an arbitrary unit (a.u.).

Two main methods for determining f_{rec} from the Doppler power spectrum exist, determining the peak or center of gravity of S_D. Given the condition SNR $>>$ 1 and negligible aerosol noise (signal fluctuations), it is sufficient to consider a single laser pulse i.e., $N_a = 1$. In this case, the center of gravity coincides with the peak of the spectrum. Thus, a straightforward center of gravity computation of S_D (or simply S) determines f_{rec} accurately. Under the same assumptions the transformation to the frequency domain can be escaped entirely. Determining the LOS velocity can be achieved by solely considering the linear low-pass spatial filter from the RWF and the individual aerosol LOS velocities corresponding to a range gate (Banakh and Smalikho, 2013, 1997, chap. 2),

$$\bar{V}_r(R_{j,k}) = \int_{-\infty}^{+\infty} Q_S(s) V_r(R_{j,k} + s) ds. \tag{2.39}$$

A derivation of the above is provided in Appendix B.

When realistic (low) SNRs are considered and aerosol noise is not negligible, nonlinear low-pass spatial filtering occurs, causing the center of gravity and peak of the power spectrum to differ. Stephan et al. (2019b) determined that the peak of the power spectrum delivers a significantly more accurate f_{rec} and thus LOS velocity estimate. Transformation to the frequency domain cannot be escaped in the low SNR case.

Chapter 3

Methods

3.1 Numerical Simulations of Wake Vortices

As a foundation for simulated lidar measurements this thesis relies on high-fidelity landing simulations from a RECAT-EU CAT-B aircraft, namely an Airbus A340 (equivalent to Airbus A343 or simply Airbus A340 in this thesis). While this four-engined aircraft type is no longer in production, the popular two-engined Airbus A350 features a comparable root circulation. This thesis simulates the flow around the aircraft geometry with through-flow nacelles, with the jet exhaust not modeled. Stephan et al. (2018) found that including the jet exhaust in aircraft simulations can delay the decay of the primary wake vortices. Through-flow nacelles can be considered analogous to engines running at idle - an acceptable assumption given the low thrust level of landing aircraft. Under such setting, Stephan et al. (2019a) showed that engines generate secondary vortices which rapidly descend (and rebound), with minimal influence on the primary wake vortices emerging from the flaptips and wingtips. The increased number of secondary vortices generated by a four-engined aircraft in comparison to a two-engined aircraft is therefore not expected to alter the decay of the primary wake vortices significantly during the final approach and landing phases. Simulations from the Airbus A340 are therefore assumed representative also for modern (two-engined) aircraft.

A hybrid approach, consisting of RANS solution fields actively swept through a LES domain, is employed. One-directional information exchange from the RANS simulation to the LES is realized. Misaka et al. (2015) first implemented this approach for horizontal flight, and Stephan et al. (2014) adapted it for the landing scenario. It elegantly circumvents the high computational cost of a fine-structured LES, as required in regions of complex geometry, by solving the flow around the immediate aircraft geometry via the compressible German Aerospace Center (DLR) in-house RANS code TAU (Schwamborn et al., 2006). Despite temporal averaging of the turbulent wake vortex roll up process, Stumpf (2005) showed that RANS simulations are highly capable of capturing the flow around complex geometries such as an aircraft. However, it is necessary for the development of realistic wake vortices to accurately simulate the atmosphere, which is possible by employing LES

(Holzäpfel et al., 2001; Misaka et al., 2012b). Overall, this approach allows the simulation of wake vortices from their generation to their complete decay in the final approach and landing phases. As visualized with Fig. 3.1, first a hybrid wake initialization simulation is performed, followed by a continuing LES-only run enduring several minutes. Note that Misaka et al. (2015); Stephan (2014); Stephan et al. (2014) previously studied the hybrid numerical simulations and particularly the landing scenario, the following sections therefore recapitulate significant parts of their works. Also significant parts from Wartha et al. (2025a) are covered in this section.

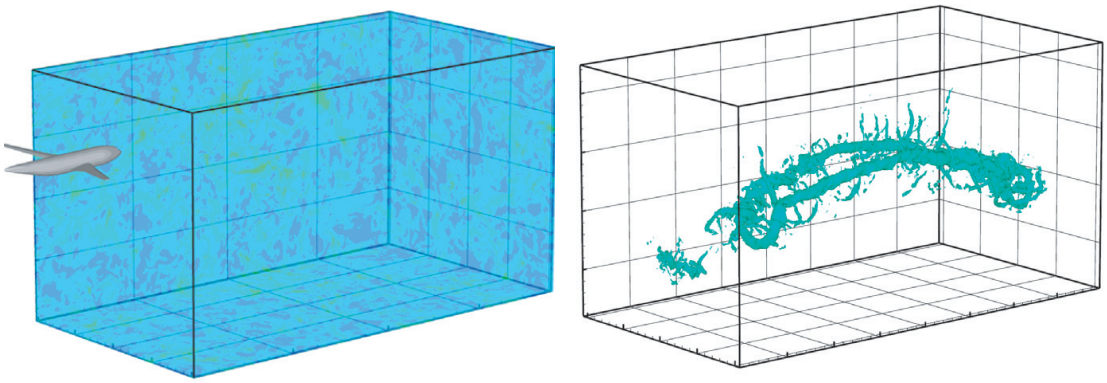

Figure 3.1: Schematic of the hybrid aircraft numerical simulation approach in horizontal flight. In a first step (left) the wake of the aircraft is initialized by sweeping the aircraft geometry through the LES domain which can be set-up with a specific atmospheric condition as illustrated, covering several seconds. The wake development in time (right) follows in a second step and allows for the simulation of the aircraft wake for several minutes. From Misaka et al. (2012a); reprinted by permission of the American Institute of Aeronautics and Astronautics, Inc.

3.1.1 Large Eddy Simulation Code

This thesis employs the incompressible Navier-Stokes equations solver Multi Grid Large Eddy Turbulence (MGLET) developed by Manhart (2004) and colleagues at the Technical University of Munich. Dufresne et al. (2005); Misaka et al. (2010) concluded that MGLET solves the momentum and continuity equations physically accurate for wake vortex flows. In comparison to alternative incompressible Navier-Stokes solvers, MGLET favorably conserves the total kinetic energy during the wake vortex evolution. The momentum and continuity equations in Einstein (summation) notation are respectively given by,

$$\frac{\partial u_i}{\partial t} + \frac{\partial (u_i u_j)}{\partial x_j} = -\frac{1}{\rho_\infty}\frac{\partial p'}{\partial x_i} + \frac{\partial}{\partial x_j}\left[(\nu + \nu_t) 2 S_{ij}\right], \tag{3.1}$$

$$\frac{\partial u_j}{\partial x_j} = 0, \tag{3.2}$$

where u and x give the velocity and spatial components, respectively, for the spatial directions (i, $j = 1, 2, 3$), $\rho_\infty = 1.2$ kg m^{-3} represents the constant air density, $p' = p - p_0$ gives the pressure deviation from a reference state denoted by p_0, $S_{ij} = (\partial u_i/\partial x_j + \partial u_j/\partial x_i)/2$ gives the strain rate tensor, and the total kinematic viscosity is given by the sum of the kinematic viscosity $\nu = \mu/\rho_\infty = 1.5 \times 10^{-5}$ m^2 s^{-1} (with the dynamic viscosity μ) and the eddy viscosity ν_t defined using the Lagrangian dynamic subgrid-scale model (Meneveau et al., 1996), capable of capturing the laminar flow within a vortex core, while also allowing external turbulent flow (Misaka et al., 2012b).

The Navier-Stokes solver in its applied version is of fourth-order accuracy employing a finite volume compact scheme (Kobayashi, 1999; Hokpunna and Manhart, 2010). The computational domain is split up for parallelization purposes. The parallel solution of the tridiagonal system of the compact scheme (the only non-zero matrix elements are located along the main diagonal, the subdiagonal, and the supradiagonal) is realized via the efficient split-interface algorithm by Hokpunna (2009). Misaka et al. (2012b) detail the pressure solver based on a velocity-pressure iteration approach by Hirt and Cook (1972). Time integration is performed by a third-order Runge-Kutta time integration scheme (Williamson, 1980).

3.1.2 Wake Vortex Simulations

The one-directional coupling of the RANS solutions and the LES has been introduced by Misaka et al. (2015), with recapitulations of their work in this section. Their approach can be considered the numerical equivalent of a catapult wind tunnel or towing tank experiment (Coton, 1998; Stephan et al., 2013b). The RANS simulations for a long range aircraft model, similar to a scale 1 : 27 Airbus A340 in high-lift configuration, have been performed prior to this thesis for the EU AWIATOR project (Keye, 2011) and provided by Stefan Melber from the Institute of Aerodynamics and Flow Technology at DLR Braunschweig. They were carried out on a fine unstructured grid displayed in Fig. 3.2 with refinements in the wingtip vortex and the flaptip vortex regions, as well as the fuselage (not all refinements are visible). The vorticity distribution of the Airbus A340 RANS simulation is given in Fig. 3.3, with blue color giving the axial vorticity in the clockwise sense and red color giving the axial vorticity in the counter-clockwise sense. Misaka et al. (2015) note that immediately behind the trailing edge of the main wing a highly complex flow structure, with numerous individual vortices, develops. By the time the flow reaches the tailplane primarily the vortices generated by the wingtip, engine, flaptip, and the fuselage-wing junction prevail. From the aforementioned vortices, all but the fuselage-wing junction vortex rotate in the counter-clockwise sense. According to Misaka et al. (2015), the outlier fuselage-wing vortex quickly decays as a result of the turbulent wake generated in immediate vicinity to the aircraft fuselage. The tailplane itself contributes only marginally to the vorticity distribution aft the aircraft.

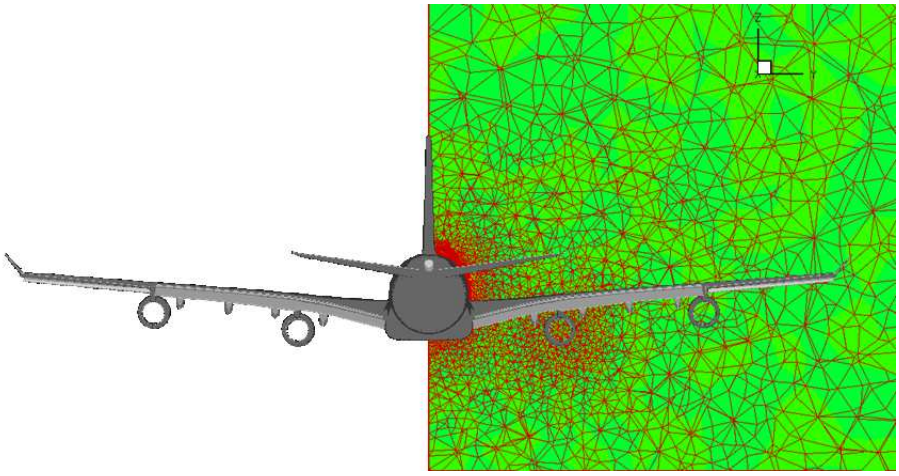

Figure 3.2: The unstructured RANS grid in flow direction for the Airbus A340 aircraft model in high-lift configuration by Stefan Melber. With permission of Stephan (2014).

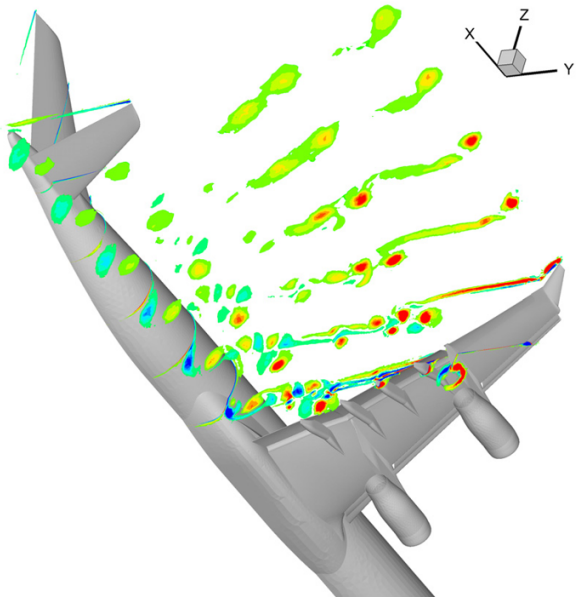

Figure 3.3: Axial vorticity distribution around the Airbus A340 in a RANS simulation. Blue and red color represent clockwise and counter-clockwise rotations, respectively. From Misaka et al. (2013); reprinted by permission of the American Institute of Aeronautics and Astronautics, Inc.

This thesis aims to simulate lidar measurements with realistic wake vortex lidar configurations, thus the RANS flow fields must be scaled to realistic Airbus A340 dimensions such that appropriate vortex circulation values are obtained. Table 3.1 provides characteristics of the 1 : 27 aircraft model and the Airbus A340-300. As a result, RANS flow field dimensions are scaled-up by a factor of 27 and RANS flow field velocities are scaled-

up by a factor of 3. Indeed, this scaling artificially yields a Mean Aerodynamic Chord (MAC) based Reynolds number of the same order as documented for a real Airbus A340-300 (Breitsamter, 2007, chap. 2, Table 2.1). The underlying wake vortex parameters for the numerical simulations in this thesis are provided in Table 3.2 relying on the 1 : 1 modeling values from Table 3.1 and the elliptical lift distribution assumption, given that in ground proximity b_0 is not explicitly defined and thus cannot be determined directly from the simulation [see Fig. 8 by Stephan et al. (2014)].

Table 3.1: RANS simulation parameters in high-lift configuration. The 1 : 27 values have been documented by Stephan et al. (2014) and the Airbus A340-300 values have been documented by Breitsamter (2007).

Parameter	Symbol	Unit	1 : 27	1 : 1	Airbus A340-300
Wingspan	B	m	2.236	60.372	60.3
Wing aspect ratio	Λ	-	9.3	9.3	10.1
Freestream velocity	U_∞	m s^{-1}	25	75	75
Lift coefficient	C_L	-	1.4	1.4	1.527

Table 3.2: Normalization parameters for the 1 : 1 numerical simulation setup from Table 3.1. References to the corresponding equations are provided.

Parameter	Symbol	Unit	Equation	Value
Initial/root circulation	Γ_0	m^2 s^{-1}	(2.9)	433.9
Initial vortex spacing	b_0	m	(2.10)	47.4
Initial vortex descend velocity	w_0	m s^{-1}	(2.11)	1.5
Characteristic time	t_0	s	(2.12)	32.6
Vorticity unit	ω_0	s^{-1}	(2.13)	0.03

The artificial increase in Reynolds number may deliver flow solutions differing from an authentic aircraft landing at this Reynolds number. Slightly varying vortex radii, which vortex theory suggests to adulterate vortex strength (Zierep, 1992, chap. 2), and less detailed secondary vortices detaching e.g., from flaps and slats may result (the RANS resolution is $[dx, dy, dz]_{\mathrm{LES}}/2$ with values from Section 3.1.4). Lidars inherently mollify high velocities and steep gradients of measured atmospheric velocity fields. This low-pass filter characteristic itself overestimates the size of vortex cores and reduces the impact of adulterated secondary vortices (lidar scans in Fig. 4.10 neatly detail the visibility or lack of secondary structures, particularly in comparison to point measurements). Furthermore, the employed numerical scheme i.e., the dissipation and subgrid-scale model, and the resolution of the vortices are primarily responsible for an adulterated aircraft wake in the simulations. Thus, the effect caused by the implemented RANS-field scaling is considered relatively less significant.

RANS-LES Interface

The necessary transition of the RANS and LES flow fields is visualized in Fig. 3.4 and performed via,

$$\boldsymbol{V} = f\,(y,\,\alpha,\,\beta)\,\boldsymbol{V}_{\mathrm{LES}} + (1 - f\,(y,\,\alpha,\,\beta)\,\boldsymbol{V}_{\mathrm{RANS}}, \tag{3.3}$$

where the transition function,

$$f(y,\alpha,\beta) := \frac{1}{2}\left[\tanh\alpha\left(\frac{y}{\beta} - \frac{\beta}{y}\right) + 1.0\right], \tag{3.4}$$

containing the slope α and wall-distance β, represents the weighting between the two flow fields. In this thesis, $\alpha^* = 0.02$ and $\beta^* = 0.08$, corresponding to Misaka et al. (2015); Stephan (2014). The RANS solutions represent a forcing term within the Navier-Stokes equations solved by the LES. This approach corresponds well with a fortified solution algorithm (Fujii, 1995) or data assimilation nudging technique (Kalnay, 2003, chap. 5) (Misaka et al., 2015).

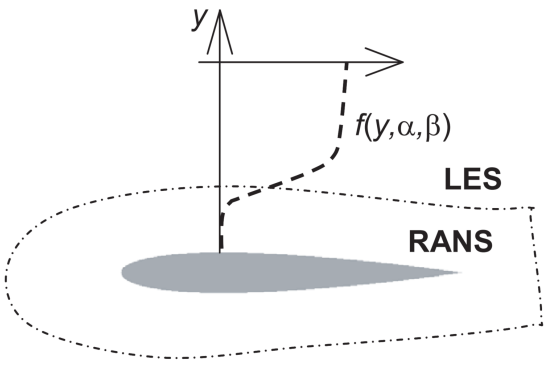

Figure 3.4: Signature weighting function combining the RANS and the LES flow fields. From Misaka et al. (2012a); reprinted by permission of the American Institute of Aeronautics and Astronautics, Inc.

The LES is performed with a structured Cartesian mesh, necessitating an interpolation (chosen as linear) of the RANS solution onto the LES mesh. With the RANS solution swept through the LES domain, the RANS mesh must be finer than the LES mesh; here, $[dx,\,dy,\,dz]_{\mathrm{LES}} = 2 \times [dx,\,dy,\,dz]_{\mathrm{RANS}}$. This allows the horizontal aircraft movement to be realized with the shift in dx_{RANS}. Two steady RANS solutions, also called frames, at different points in time are necessary to complete one dx_{LES}. With that, the LES timestep reads

$$dt = \frac{dx_{\mathrm{RANS}}}{U_\infty}. \tag{3.5}$$

Once the wake has been initialized to its full extent the RANS flow field is completely removed as a forcing term from the LES-solved Navier-Stokes equations and effectively continued as a pure LES run.

3.1.3 Extension to Landing Aircraft

The final approach and landing phases of an aircraft are of most concern when considering the hazard from wake vortex encounters. Therefore, Stephan et al. (2014); Stephan (2014) extended the hybrid numerical simulations for wake vortices to the final approach and landing phases. The following recapitulates the main properties of their developments.

An adaption has to be made to the interaction of the steady RANS flow fields and the LES flow field. The descent of an approaching aircraft is realized with a shift in dx_{RANS} and dz_{RANS}. The required RANS frame number depends on the desired glide path angle γ and must be handled with a set of RANS frames employed in an alternating fashion i.e., in total $2n$ RANS frames are required. This necessitates the k-th frame to be shifted by $k dx_{\mathrm{RANS}}$ in horizontal direction and $(k/n)\, dz_{\mathrm{RANS}}$ downwards, implying a movement of $n dx_{\mathrm{LES}}$ in horizontal direction and dz_{LES} downwards. For fixed aspect ratio of the grid, the number of RANS frames dictates the glide path angle flown,

$$\gamma = \arctan\left(\frac{dx_{\mathrm{LES}}}{n\ dz_{\mathrm{LES}}}\right). \tag{3.6}$$

The FAA (2023) aeronautical information manual states 3 deg as the typical glide path angle of commercial aircraft towards a runway. This thesis considers $n = 16$, giving $\gamma = 3.6$ deg for an equidistant mesh. Accordingly, the LES timestep must be adjusted [cf. Eq. (3.5) for horizontal flight] such that the inflow to the RANS solutions remains valid, that is,

$$dt = \frac{0.5dx}{U_\infty}\sqrt{1 + \frac{1}{16^2}}, \tag{3.7}$$

with the factor 0.5 such that the Courant–Friedrichs–Lewy (CFL) number, relating the speed of information travel, timestep, and the mesh spacing, ensures stable numerical simulation i.e.,

$$\mathrm{CFL} = \frac{|\boldsymbol{V}|\ dt}{dx} \leq 1. \tag{3.8}$$

Consequently, the number of RANS frames is doubled to 32. Furthermore, the aircraft is at a constant pitch angle of $\theta = 5.5$ deg throughout the simulation.

Section 2.1.2 discussed the effect of ground vicinity for aircraft. The hybrid simulation considers the aircraft in-ground effect by adjusting the weighting function of the RANS-LES interface. As the aircraft approaches the ground β in Eq. (3.3) is gradually reduced. Furthermore, the touchdown of the aircraft is modeled by gradually fading the RANS forcing term in the LES-solved Navier-Stokes equations, corresponding to the lift reduction experienced by aircraft at touchdown.

3.1.4 Computational Domain

The computational domain of the LES is sketched in Fig. 3.5 and set to $X^* = 23.3$, $Y^* = 11.7$, and $Z^* = 2.9$ in flight, spanwise, and vertical directions, respectively. Additionally the LES coordinate system $[x,\ y,\ z]_{\mathrm{LES}}$ is positioned. For clarity the LES coordinates system may also be referred to as directly $[x,\ y,\ z]$ in this thesis. The computational domain dimensions enable the capture of the complete wake vortex trajectory while attempting to avoid significant interactions with the lateral and top domain boundaries in the quiescent atmosphere. Both measurements and simulations support these dimensions: Holzäpfel and Steen (2007) observe a maximum vortex rebound of $2.5b_0$ altitude at Frankfurt Airport, instead Holzäpfel et al. (2016b) find a maximum altitude of $2.0b_0$ in numerical simulations even including crosswind. For lateral wake vortex transport Holzäpfel and Kladetzke (2011) derive over 1500 m (without restriction in flight height and crosswind magnitudes) in measurements and $3.3b_0$ in quiescent atmosphere simulations (Stephan et al., 2014).

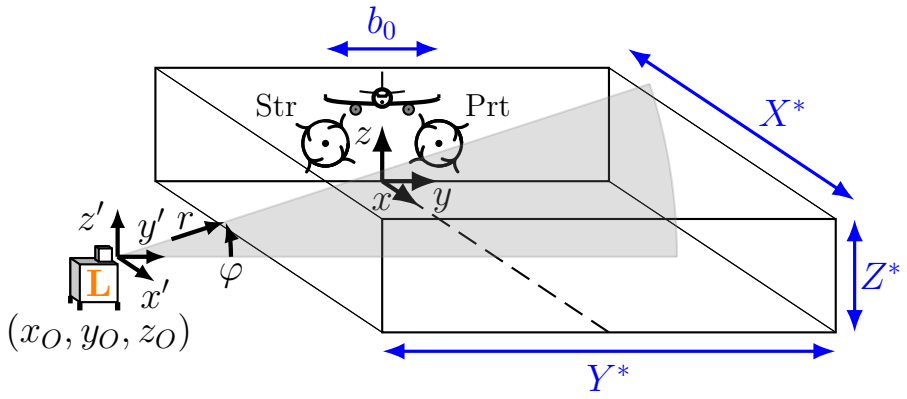

Figure 3.5: Schematic of a virtual Lidar (L) setup with respect to the LES computational domain. The lidar measures a RHI scan (gray) with Str and Prt vortices. Adapted from Wartha et al. (2025c)©.

The uniform LES mesh is spaced equally in all three spatial dimensions, $dx^*_{\mathrm{LES}} = dy^*_{\mathrm{LES}} = dz^*_{\mathrm{LES}} = 0.011$. The fine spacing is chosen to resolve wake vortex cores with a minimum of six grid points corresponding to a vortex core radius of under $r^*_c = 0.03$ ($r_c = 1.35$ m). This resolution has proven suitable (Stephan et al., 2014).

This thesis considers two time parameters, differing in their initialization:

1. $\boldsymbol{t}$: The vortex age initialized with the aircraft passing the respective lidar measurement plane in flight direction.

2. $\boldsymbol{t_L}$: Time initialized with the touchdown of the aircraft, enabling the comparison of wake vortices measured by lidars at different positions in the LES domain.

Reference LES domain positions and times include the position of the aircraft as it enters the front of the domain $x^* = 0$, the corresponding aircraft altitude $z^* = 1.0$, and the corresponding time with respect to touchdown $t^*_L = -0.33$. The aircraft touchdown position

is located at $x^* = 16.5$. Depending on the simulated atmospheric condition, in this thesis limited to turbulent crosswinds, the aircraft is moved laterally into the crosswind. Thus, in quiescent atmosphere the aircraft glide path is located at $y^* = 0$. Instead, when crosswind is simulated the glide path is moved to $y^* = 2.8$, allowing longer vortex tracking.

The numerical simulations are wall-modeled LES, in order to reduce the number of degrees of freedom while still allowing high Reynolds number investigations and the physical accurate simulation of turbulent wake vortex decay (Stephan, 2014). The Grötzbach-Schumann wall model (Grötzbach, 1987) based on the logarithmic law is employed, locally modeling the wall shear stress τ_w; an appropriate approach for the multi-vortex system generated by aircraft close to the ground (Stephan, 2014). The logarithmic law is modeled based on a half-channel flow of width δ [see for example Kundu and Cohen (2002, chap. 13)]. The velocity tangential at a node close to the ground $\hat{z}$, within the logarithmic regime, is given by

$$u_{\tan}(\hat{z}) = \frac{\mathrm{Re}_\tau \nu}{\delta}\left[\frac{1}{\kappa}\log\left(\frac{\hat{z}\mathrm{Re}_\tau}{\delta}\right) + B\right], \tag{3.9}$$

where $\mathrm{Re}_\tau = (u_\tau \delta)/\nu$ denotes the intrinsic Reynolds number with u_τ representing the wall friction velocity, $\kappa = 0.4$ is the von Kármán constant (Baumert, 2013), and $B = 5.5$ (Sagaut, 2001; Stephan, 2014). Adherence to the general logarithmic turbulent profile from Moser et al. (1999) is proven in Section 3.1.5 with Fig. 3.7 for turbulent crosswinds.

The LES boundary conditions employed are non-slip and free-slip on the bottom (ground) and top boundaries, respectively, as required by the half-channel flow description. Lateral boundaries feature the periodic condition, common for LES of wake vortices, as they facilitate the implementation of atmospheric phenomena (Misaka et al., 2012b). Furthermore, Misaka et al. (2012b); Stephan et al. (2014) established that initial disturbances from the sudden RANS forcing and the initial aircraft wake can be treated efficiently with periodic boundary conditions when the aircraft is initialized in the back part of the LES domain (see Fig. 3.6). Shortly after LES start-up, the aircraft enters the front of the domain, such that the LES solution can be manipulated. In the back of the domain the trailing vortices end freely in space, however according to the third law of Helmholtz (1858) this is not possible. Thus, the front slice of the domain is extended into the back part of the domain and closed in a horseshoe fashion as depicted in Fig. 3.6. This closure suggested by Stephan et al. (2014) replaces the originally produced start-up wake and corresponds to a vortex ring which may result when vortex filaments are subject to the Crow instability. Moreover, it delays the ultimately expected unphysical vortex filament linking with the bottom wall. The linking produces strong vertical vortex filament components, which travel into the front part of the domain and lead to unphysical wake vortex motion.

Computational resources for the Airbus A340 landing simulation are 4096 cores split onto 171 nodes at the Leibniz Rechenzentrum (LRZ) SuperMUC-NG supercomputer.

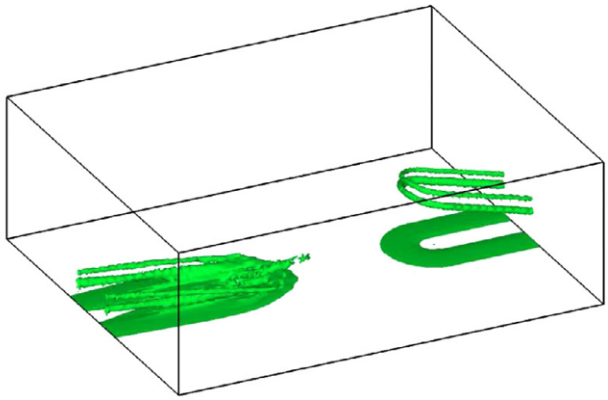

Figure 3.6: Horseshoe closure of the wake vortex filaments at LES start-up. With permission of 2014 Elsevier Inc., from Stephan et al. (2014); permission conveyed through Copyright Clearance Center, Inc.

3.1.5 Crosswind Pre-Simulations

It has been established in Section 2.1.2 that wake vortex generation in ground proximity and under crosswind conditions can result in the unfavorable scenario of a prevailing luff wake vortex in the runway corridor, presenting a hazard to follower aircraft. This thesis simulates four crosswind magnitudes relevant for wake vortex hazard studies of the format $\chi \times w_0$, where χ represents a factor and the respective crosswind speed is attained at an altitude of b_0 above the ground [the corresponding Beaufort wind scale condition, see for instance Huler (2007), is given in brackets using w_0 from Table 3.2]:

- $\boldsymbol{\chi = 0.0}$ [0.00 m s^{-1} $\approx$ 0.0 knots, *calm air*]: This quiescent atmosphere scenario acts as a reference case in this thesis.

- $\boldsymbol{\chi = 0.5}$ [0.73 m s^{-1} $\approx$ 1.4 knots, *light air*]: Section 2.1.2 established this crosswind magnitude to be explicitly hazardous, providing ideal conditions for the luff wake vortex to remain in the runway corridor for a significant period of time.

- $\boldsymbol{\chi = 1.0}$ [1.46 m s^{-1} $\approx$ 2.8 knots, *significant light air*]: Most wake vortex encounters at London Heathrow airport are recorded for crosswind of this magnitude (Critchley and Foot, 1991), therefore considered particularly operationally relevant.

- $\boldsymbol{\chi = 2.0}$ [2.92 m s^{-1} $\approx$ 5.6 knots, *light breeze*]: This crosswind magnitude represents a case with substantial turbulence and is considered the upper limit of relevant crosswind magnitudes. Wake vortex encounters with stronger crosswinds are highly unlikely, as even luff vortices rapidly advect out of the runway corridor.

Turbulent crosswind cases require pre-simulations prior to the wake initialization. These are conduced on a computational domain of length $X^*/4$ with 512 cores split onto 16 nodes on the LRZ SuperMUC-NG supercomputer. Afterwards the flow field is periodically

extended to match the LES domain length of the wake initialization. Stephan (2014); Stephan et al. (2017) previously described and implemented the pre-simulations approach, below key steps are reproduced. The general approach remains to model a classic half-channel flow (Kundu and Cohen, 2002, chap. 13). A pressure gradient dp/dy is imposed in the LES domain, allowing a logarithmic wind profile to develop in the vertical direction (z). Note that a landing aircraft undergoes a descent, the wind speed thus cannot be set to the desired wind speed at every vortex initialization height. Additionally, velocity fluctuations are initialized using the von Kármán wind turbulence model (von Kármán, 1937). The pre-simulation is complete once characteristic wall streaks establish and the mean vertical velocity profile $\langle v^+ \rangle = \bar{v}/u_\tau$ agrees with results from Moser et al. (1999), where $u_\tau = \sqrt{\bar{\tau}_w/\rho_\infty}$ represents the spanwise wall friction velocity with $\bar{\tau}_w = -\left(d\bar{p}/dy\right)\delta$, $z^+ = \left(z u_\tau\right)/\nu = \mathrm{Re}_\tau z/\delta$ gives the non-dimensional height, and $\langle\rangle$ refers to spatial averaging in crosswind direction.

In the incompressible LES runs the viscosity ν is fixed, it follows that the pressure gradient or Re_τ dictates the wind profile. From the Grötzbach-Schumann wall model (Grötzbach, 1987) the necessary pressure gradient to achieve $\chi \times w_0$ at altitude b_0,

$$\bar{v}\left(b_0\right) = \chi \times w_0 = \frac{\mathrm{Re}_\tau \nu}{\delta}\left[\frac{1}{\kappa}\log\left(\frac{b_0\ \mathrm{Re}_\tau}{\delta}\right) + B\right], \tag{3.10}$$

is solved using several iterations of Newton's method. The summarized initialized velocity field therefore reads

$$v^+\left(z^+\right) = \begin{cases} z^+, & z^+ \leq 11.635, \\ \log z^+/\kappa + B, & z^+ > 11.635, \end{cases} \tag{3.11}$$

including the viscous sublayer and logarithmic sublayer of a boundary layer (Kundu and Cohen, 2002, chap. 13). The resulting wind initializations are given in Table 3.3. Figure 3.7(a) evidences a strong agreement with the logarithmic turbulent profile from Moser et al. (1999) for all three crosswind magnitudes, only a minor underestimation of $\langle v^+ \rangle$ is observed. For the $2.0w_0$ crosswind a larger fluctuation at low z^+ can be observed, which is a direct consequence of the increased pressure gradient in the imposed boundary layer and resulting detaching vorticity streaks. The higher turbulence at higher crosswind speeds represented by the Root Mean Square (RMS) velocity fluctuations $[u_{\mathrm{RMS}}, v_{\mathrm{RMS}}, w_{\mathrm{RMS}}]^+$ in Fig. 3.7(b) supports this argument. Overall, Fig. 3.7 indicates that the wind profile diverges from the logarithmic profile when approaching the free-slip top boundary of the LES domain. As discussed in Section 3.1.4, the chosen LES domain height restricts the wake vortices from nearing the top boundary. Since the aircraft descends with progression through the LES domain, the wind statistics are considered appropriate.

Table 3.3: Turbulent crosswind specifications in terms of imposed pressure gradient and intrinsic Reynolds number for viscosity $\nu = 1.5 \times 10^{-5}$ m^2 s^{-1} and half-channel width $\delta = Z$. LES timestep and sideslip angle into the wind are also provided.

Crosswind at $z^* = 1$	dp/dy $\times 10^{-5}$ [Nm^{-3}]	Re_τ
$0.5w_0$	0.41	201 217
$1.0w_0$	1.51	383 852
$2.0w_0$	5.50	733 721

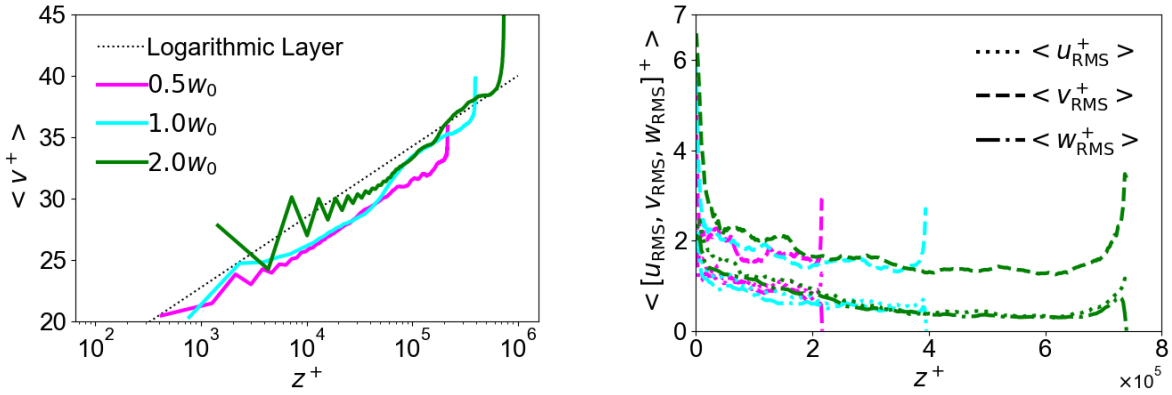

(a) Mean wind velocity profile $< v^+ >$. The dashed line gives the expected profile.

(b) Mean RMS fluctuations of all velocity components $[u_{\mathrm{RMS}}, v_{\mathrm{RMS}}, w_{\mathrm{RMS}}]^+$.

Figure 3.7: Turbulent wind statistics initialized in LESs with respect to distance above the ground z^+ of fully developed crosswinds for three strengths $\chi \times w_0$. Adapted from Wartha et al. (2025a)©.

With the modifications of the atmospheric conditions in the LES, also the RANS solution requires modifications. The approaching aircraft landing under crosswind conditions requires a sideslip angle into the wind, countering the induced lateral velocity by the wind and ensuring touchdown on the runway tarmac. The sideslip angle β_{ss} is found from trigonometry and maintaining the TAS,

$$\beta_{\mathrm{ss}} = \arcsin \frac{\chi w_0}{U_\infty}. \tag{3.12}$$

In order to ensure a correct RANS-LES flow interface, the ground speed must be reduced accordingly. Therefore, the LES timestep is modified [cf. Eq. (3.7)],

$$dt = \frac{0.5dx}{U_\infty \cos \beta_{\mathrm{ss}}} \sqrt{1 + \frac{1}{16^2}}. \tag{3.13}$$

3.2 LES Lidar Simulators

This thesis places virtual lidar instruments within the above detailed high-fidelity wake vortex simulations of landing aircraft. Lidar simulations are split into two steps:

1. LOS velocities are retrieved from the LES described in Section 3.1. Hereby, the lidar scanning rate is responsible for temporal averaging inherent to lidar.

2. The obtained LOS velocity fields are post-processed to represent spatial averaging inherent to lidar and may include atmospheric and instrument noise.

Indeed two types of LES lidar simulators are investigated in this thesis:

- **LLS**: Idealized type assuming SNR >> 1, based on Robey and Lundquist (2022).

- **LLS$_\mathbf{n}$**: Practical type with realistic noise, based on Stephan et al. (2019b).

The two LES lidar simulator types (together also referred to as LLSs) share the first simulation step, namely the retrieval of the LOS velocities from the LES. This section in large parts follows descriptions by Wartha et al. (2025a,c).

3.2.1 LOS Velocity Retrieval

Computing LOS velocities from LESs necessitates careful treatment of both spatial and temporal aspects. In a LES the flow velocity vector $\mathbf{V} = [u, v, w]$ is computed at every node and LES timestep dt. In reality the LOS elevation angle of a lidar performing RHI measurements continuously rises or descends according to the scanning rate. For the LLSs discrete elevation angles are assumed, giving the lidar timestep dt' in accordance with the scanning rate. A RHI lidar scan thus consists of LOSs captured at different points in time, ensuring modeling of temporal averaging and distortions. Particularly in the context of descending/ascending wake vortices this may lead to the misinterpretation of their strength (Smalikho, 2019), therefore constituting an essential component of the herein described dynamic LES velocity retrieval. Since laser pulses travel at the speed of light, the LOS velocities along an individual LOS are assumed to be instantaneously captured. Generally, the LES timestep is significantly smaller than the lidar timestep i.e., $dt << dt'$, such that temporal nearest-neighbor interpolation is employed to select relevant LES timesteps for the recording of LOS velocities.

The large LES domain from Section 3.1 enables wake vortices to be tracked for significant periods of time, from their generation to their decay, even under turbulent crosswind conditions. However, in field measurements lidars are frequently placed at lateral distances far from the glide path, such that the domain dimensions do not suffice for directly retrieving all required velocity vectors $\mathbf{V}$. The scenario is described by introducing fields $0 - 5$ in Fig. 3.8.

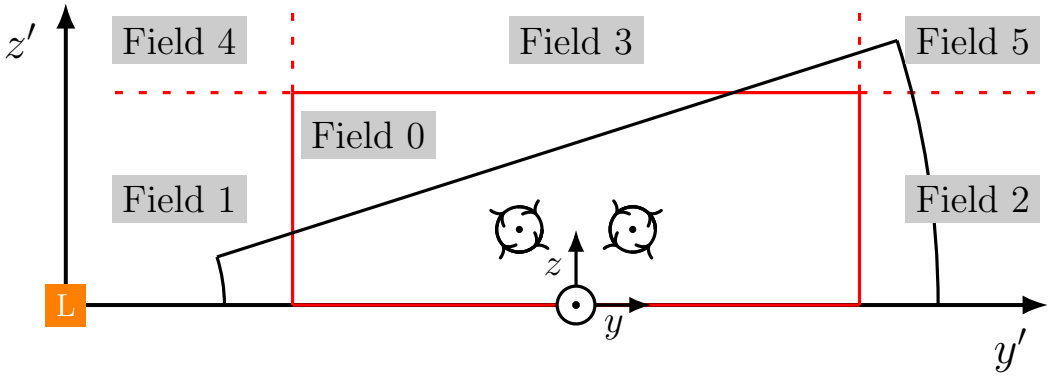

Figure 3.8: Schematic of the padding method for simulated lidar measurements with respect to the lidar and LES coordinate systems. In red the LES domain is drawn, in black the measurement window, covering the RHI scan, of the lidar is given. Field 0 represents the region where velocities can be retrieved from the LES domain. Fields 1 to 5 represent regions where flow field padding is applied. Adapted from Wartha et al. (2025a)©.

Instead of further increasing the LES domain, a straightforward padding method is introduced - an appropriate approach considering that wake vortices are typically unexpected in these peripheral regions of RHI lidar scans. The following rules apply for obtaining velocity vectors $\mathbf{V}$ at desired locations within and outwith the LES domain:

- In general, bilinear interpolation is employed for velocities in-between nodes. Required velocities outwith the LES domain utilize the boundary velocity values of the LES domain. Furthermore, in order to avoid the potential stimulation of large velocity magnitudes, which the padding may extend for uncontrollable and unphysical lengths, a weighting factor of decreasing magnitude with increasing distance to the LES domain boundary is applied.
- **Field 0**: $\mathbf{V}$ is directly retrieved from the LES.
- **Fields 1 and 2**: $\mathbf{V}$ is retrieved from the closer lateral boundary in the domain (y_- or y_+) at the desired vertical z-component.
- **Field 3**: $\mathbf{V}$ is retrieved from the upper boundary in the domain (z_+) at the desired lateral y-component.
- **Fields 4 and 5**: $\mathbf{V}$ is retrieved from (y_-, z_+) and (y_+, z_+), respectively.

With lidar instruments strictly oriented perpendicular to the runway i.e., $y \parallel y'$ (see Fig. 3.5), the velocity component u can be disregarded for computing the LOS velocity. Finally, by projecting the obtained velocity components onto the respective LOS unit direction vector $\mathbf{e}$, a LOS velocity for a single aerosol is obtained with

$$V_r = \mathbf{e} \cdot \mathbf{V} = v \cos\varphi + w \sin\varphi. \tag{3.14}$$

While the performance optimization of the LLSs within MGLET is not the focus of this thesis, below documents the increase in wall time caused by their operation. The comparison is conducted to the plain MGLET operation for the crosswind pre-simulations from Section 3.1.5 with an initialized $0.5w_0$ crosswind and equivalent computational resources (512 cores split onto 16 nodes) on the LRZ SuperMUC-NG supercomputer. Various simulations are run with different numbers of initialized LLSs (N_{LLS}). Each LES is run for $N_{dt} = 1000$ LES timesteps, Fig. 3.9 summarizes the results. A low number of initialized LLSs does not affect the wall time T of the LES significantly in comparison to the reference wall time T_{ref} for the plain MGLET ($N_{\mathrm{LLS}} = 0$). Only at high amounts of initialized LLS the wall time increase significantly as a result of negative scaling effects. The wall time for all N_{dt} LES timesteps can be approximated by $T \approx 0.002N_{\mathrm{LLS}}^2 - 0.01N_{\mathrm{LLS}} + T_{\mathrm{ref}}$ for the tested simulation set-up.

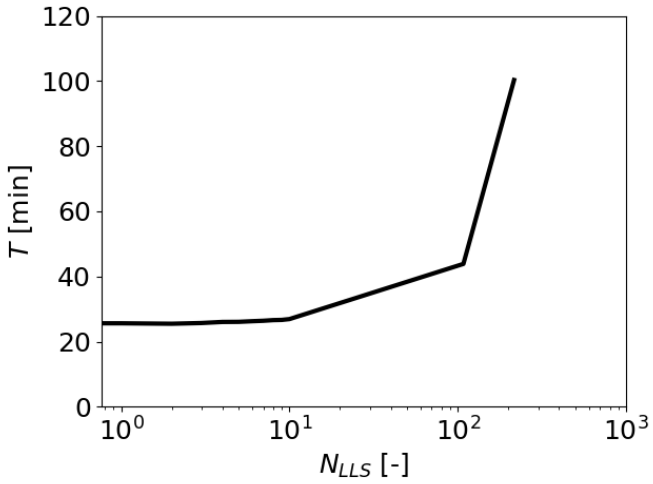

Figure 3.9: Influence of LLSs on the LES computational time for 1000 timesteps with respect to the number of initialized LLSs within MGLET with constant domain size and computational resources.

3.2.2 LES Lidar Simulator Without Noise (LLS)

This section details the idealized lidar simulator valid when SNR >> 1 i.e., the instrument noise (aerosol scattering inconsistencies and further atmospheric background noise) is considered negligible. This LLS represents an ideal case suggested by Robey and Lundquist (2022), with their method recapitulated below.

Section 2.2.4 established that given the above conditions, the LOS velocity for a range gate can be found via Eq. (2.39) i.e., by the convolution of the RWF and aerosol velocities. Robey and Lundquist (2022) suggest to skip the simulation of a backscatter signal altogether, as it corresponds to the idealized spatial averaging case, where the center of gravity and peak of the backscatter power spectrum coincide. For the numerical implementation

of Eq. (2.39), the bounds of the integral must be set and a discretization implemented. The nodes used to approximate the integral are bound by $[-\hat{R}, +\hat{R}]$, where $\hat{R} = 30$ m. As shown in Fig. 3.10, the transformation to a finite integral,

$$\bar{V}_r(R_{j,k}) \approx \int_{-\hat{R}}^{+\hat{R}} Q_S(s) V_r(R_{j,k} + s) ds, \tag{3.15}$$

is tenable, with negligible contributions by the RWF tails $|s| > \hat{R}$ (red areas) in comparison to $|s| \leq \hat{R}$ (gray area). The integral is estimated by using the quadrature formulation (Robey and Lundquist, 2022),

$$\bar{V}_r(R_{j,k}) \approx \sum_{i'}^{I'} \frac{h_{i'} Q_S(s_{i'})}{\sum_n^{I'} h_n Q_S(s_n)} V_r(R_{j,k} + s_{i'}), \tag{3.16}$$

where I' aerosols spaced by $h = 1$ m surround $R_{j,k}$ on the LOS with elevation angle φ_k. Figure 3.10 also provides a visual representation of aerosols, blue symbols, considered for computing $\bar{V}_r$. Note that the derivation and assumptions of this quadrature formulation are discussed in Appendix C.

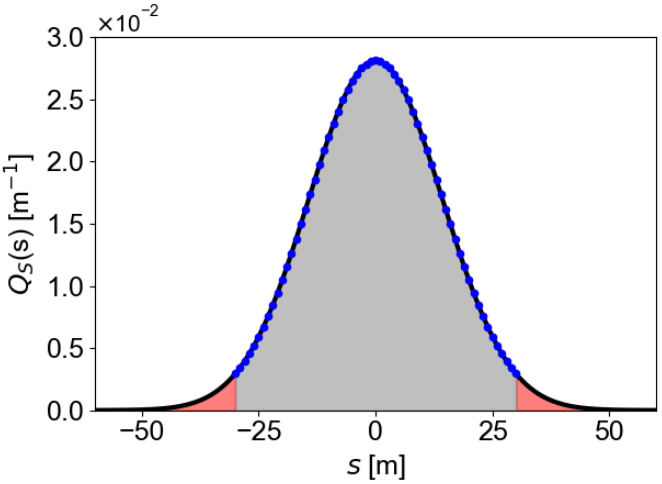

Figure 3.10: Range Gate Weighting Function distribution (RWF) with blue symbols representing contributions from aerosols. Shaded in gray is the effectively considered integral. Shaded in red are not considered contributions.

3.2.3 LES Lidar Simulator With Noise ($\mathbf{LLS_n}$)

In contrast to the LLS above, this section models PCDLs with realistic SNR values and aerosol noise. In this case, the center of gravity and peak of the backscatter power spectrum do not coincide. Thus, the backscatter must be transformed to the frequency domain for accurately computing the LOS velocity via the backscatter power spectrum peak. The method described below follows ideas by Stephan et al. (2019b) in significant parts, which itself focuses on the Vaisala (formerly Leosphere) WINDCUBE® 200s PCDL. Alterations to Stephan et al. (2019b) are indicated where necessary and have previously been described by Wartha et al. (2025c). In general, theoretical and continuous elements from Section 2.2 are transferred into practical and discrete representations.

For a single snapshot in time a simplified representation of a pulse traveling through a range gate is depicted in Fig. 3.11. The pulse is placed in the center of the range gate window $R_{j,k}$ (text in red color). As part of an analog-to-digital conversion process, lidars sample the received backscatter signal with time interval $\delta t = 1/B_0$ ($\delta R = c\delta t/2$ in space). The transmission bandwidth $B_0 = 250$ MHz is double the Nyquist frequency (125 MHz). In the single sided power spectrum, the observed frequency maximum corresponds to the Nyquist frequency and is divided into $L = 32$ spectral channels, dictating $I = 2L$ sampling points. Throughout the signal sampling process, the pulse travels through the range gate window, as manifested by the convolution for the RWF [see Eq. (2.34)]. Thus, I' distinct aerosols located along the longitudinal sensing volume are activated with various pulse intensities (black dots in Fig. 3.11). Red circles represent the sample points, with the filled red dot representing the location along the LOS φ_k shown in Fig. 2.11. In this model $I = I'$, thus the LOS aerosol spacing $h = \delta R$.

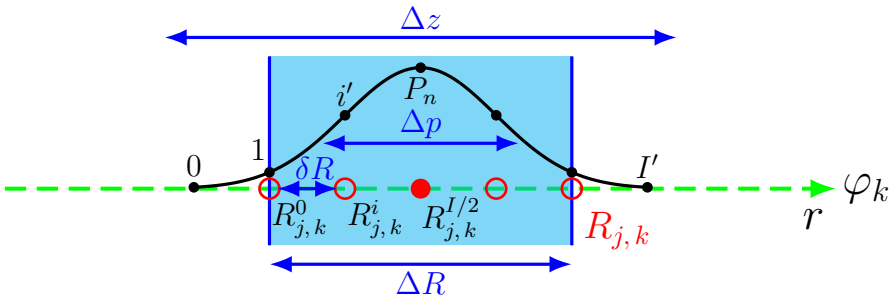

Figure 3.11: Schematic of an emitted laser pulse traveling through a range gate window. The blue shaded area represents the range gate window for estimating the LOS velocity at $R_{j,k}$ along LOS φ_k. Red circles are sampling points. The laser pulse is modeled of Gaussian shape. Black dots along the pulse represent individual aerosol sub-signal weightings. Adapted from Wartha et al. (2025c)©.

The complex backscatter signal received by a lidar was previously described by Eq. (2.29). For a single pulse P_n at a sampling time t_i the backscatter can be modeled by

$$Z\left(t_i; n\right) = \mathcal{R}\{Z_S\left(t_i; n\right)\} + Z_N\left(t_i; n\right), \tag{3.17}$$

producing a real number. In contrast to real lidar, where coherent pulse, range, and backscatter matching is realized using the magnitude and phase information of the backscatter, the real component of the backscatter suffices for a lidar model where laser pulses are not emitted, but only their backscatter simulated. The background noise Z_N is modeled by a pseudo-random parameter $\varepsilon_1(i)$, distinct for each sample and pulse, assuming a Gaussian probability density function with a mean of zero and unit variance [suggested by Banakh and Smalikho (2013, chap. 2)]. The model echo signal $Z_S(t_i; n)$ for the WINDCUBE® 200s,

$$Z_S(t_i; n) = \sqrt{\mathrm{SNR}\frac{2B_f}{B_0}\frac{\delta R}{\sqrt{\pi}\Delta p}}\sum_{i'=0}^{I'-1}\zeta(i+i'; n)\, g(i') \times \exp\left\{2\pi j t_i\left[f_{\mathrm{ref}} + \frac{2}{\lambda}V_r\left(R_{j+i'}, \varphi_k\right)\right]\right\}, \tag{3.18}$$

contains all main components, pulse energy, contribution by each sub-signal, and the sub-signal itself, previously discussed for the general case [cf. Eq. (2.31) in Section 2.2.3]. Differences prevail for modeling reasons, including the direct inclusion of $\mathrm{SNR} = \eta P_S/(h\nu B_0)$ with the signal power P_S (Banakh and Smalikho, 1997), the frequency band B_f, and the aerosol noise modeled by ζ. Furthermore, components associated with coherent detection are not required for modelling the backscatter.

Analogous to the LLS method, the $\mathrm{LLS_n}$ employs a Gaussian pulse shape. Compared to Eq. (2.26), Stephan et al. (2019b) propose normalization and scaling adjustments for the emitted pulse by the WINDCUBE® 200s, giving

$$g(i') = \exp\left\{-\frac{\left[(i' - I'/2)\,\delta R/\Delta p\right]^2}{2}\right\}. \tag{3.19}$$

The aerosol noise is modeled by $\zeta(i+i'; n) = \Psi\left[\varepsilon_2(i+i'; n) + j\varepsilon_3(i+i'; n)\right]$, and adapted from Stephan et al. (2019b). Again, ε_2 and ε_3 represent pseudo-random parameters given by a Gaussian probability density function with a mean of one and unit variance (distinct for each sample and aerosol). This thesis introduces an additional empirically determined factor Ψ, constituting a power scaling parameter allowing the SNR value input in Eq. (3.18) to be retrieved from the modeled backscatter signal. The difference in the aerosol noise formulation compared to suggestions by Stephan et al. (2019b) stems from two origins:

1. The practical SNR computation may vary between processing algorithms. Field measurements from Vienna Airport campaign (see Section 3.3.1) consider

$$\mathrm{SNR}\left(R_j, \varphi_k\right) = \frac{\sum_{f_-}^{f_+} S_D\left(f_l; R_j, \varphi_k\right)}{\sum_{f_-}^{f_+} S_N\left(f_l; \varphi_k\right)}, \tag{3.20}$$

   where $f_\pm = f_{\mathrm{ref}} \pm B_f/2$, and the spectra S_D and S_N are defined below (Banakh and Smalikho, 2013, chap. 2).

2. Unlike Stephan et al. (2019b), the $\mathrm{LLS_n}$ considers all laser pulses to be centered within the range gate window at every sampling point. Therefore, the LOS velocities V_r of the I' aerosols are obtained at

$$R\left(j+i'\right) = R_j + \left(i' - I'/2\right)\delta R. \tag{3.21}$$

The simplification is implemented for computational efficiency purposes, as it allows to share velocity computations along LOSs. The high number of pulses used by a PCDL for averaging the signal are on average centered in the range gate window, justifying this approach. The obtained $\bar{V}_r$ is not affected by this assumption, however the echo signal may be too strong, which can be corrected by the above introduced scalar Ψ.

For input-output SNR matching of the Vienna campaign data, $\Psi = 0.2124/\sqrt{2}$ is empirically determined, with a particular focus on matching the focal range ($\approx$ 500 m) and the denominator representing the magnitude of the unity variance of ε_2 and ε_3.

Overall, the backscatter signal for a particular range gate is modeled with Eq. (3.17) for all I sample points. In order to retrieve $\bar{V}_r$ associated with that range gate, the backscatter is transferred to the frequency domain using the Fast Fourier Transform,

$$S\left(f_l; R_j, \varphi_k\right) = \frac{1}{N_a}\sum_{n=1}^{N_a}\left|\sum_{i=0}^{I-1} W\left(i\delta t\right) Z\left(i\delta t - T_W/2\right)\exp\left(-2\pi j\frac{li}{I}\right)\right|^2, \tag{3.22}$$

with a corresponding rectangular temporal range gate profile ,

$$W(t) = \begin{cases} 1, & t \le T_W, \\ 0, & t > T_W, \end{cases} \tag{3.23}$$

which also considers the numerical implementation. Note that with the specified aerosol number of 64 and the sampling time, not all aerosols are activated by the indicator function.

Finally, Eq. (2.28) is employed for obtaining the averaged LOS velocity estimate for a particular range gate $\bar{V}_r\left(R_j, \varphi_k\right)$. The averaged f_{rec} is determined via the peak of the Doppler spectrum S_D [see Eq. (2.38)]. Thus, Eq. (3.22) is used twice, once to compute the spectrum S associated with the modeled backscatter, and once to compute the noise spectrum S_N, modeled as a pure noise signal. The associated time signal is defined by $Z'_N\left(t_i\right) = \varepsilon_4$, where ε_4 is defined analogous to ε_1. From the pulse repetition frequency f_P and the scanning rate ω_S (given in Table 3.4), a pulse accumulation of $N_a = 1000$ pulses can be determined.

The width of a spectral channel (or frequency resolution) can be computed as $\Delta f = B_0/I = 3.90625$ MHz. According to the Doppler relation this corresponds to a velocity resolution $\Delta V \approx 3$ m s^{-1}. In order to increase the velocity resolution Fourier interpolation is employed. Each spectral channel is subdivided into $L' = 128$ channels, in total producing $\Delta f = B_0/(IL') = 0.03052$ MHz. This corresponds to $\Delta V \approx 0.0235$ m s^{-1}.

Table 3.4: Settings of the WINDCUBE® 200s lidar. Adapted from Wartha et al. (2025c)©.

Parameter	Symbol	Unit	Value
Laser wavelength	λ	µm	1.543
Pulse energy	E_P	µJ	50
FWHM pulse width	τ_P	ns	200
Pulse repetition frequency	f_P	kHz	20
Pulses for accumulation	N_a	-	1000
Reference beam frequency	f_{ref}	MHz	69.3
Bandwidth	B_0	MHz	250
Temporal range gate	T_W	ns	140
Sensing volume length	Δz	m	35.6
Spectral channels count for $0 - 125$ MHz	L	-	32
Elevation angle resolution	$d\varphi$	deg	0.2
Scanning rate	ω_S	deg s^{-1}	4
Lidar timestep	dt'	s	0.05
Range gate spacing	dR	m	3

3.3 Dataset Families

Throughout this thesis three dataset families consisting of RHI lidar scans are employed: field measurements from a campaign at Vienna Airport (Holzäpfel et al., 2021), and two types of LES lidar simulator (LLS and LLS_n) (Wartha et al., 2025a,c,b). All three dataset families represent wake vortex RHI lidar scans for the Vaisala (formerly Leosphere) WINDCUBE® 200s PCDL pictured in Fig. 3.12. Settings used for wake vortex measurements are given in Table 3.4, further specifications for the various dataset families are provided below. All three dataset families are divided into subsets for training, validating, and testing the ML models in an approximate $80 : 10 : 10$ split. These are necessary for ML purposes, ensuring an independent and unbiased analysis. The lidar scans consist of wake vortex evolutions, namely at least one wake vortex is present. Dataset descriptions in this section may in parts include descriptions by Wartha et al. (2025c).

3.3.1 Field Measurements (FMs)

From May to November 2019 a comprehensive wake vortex measurement campaign was conducted by DLR at Vienna Airport with the lidar instrumentation setup given in Fig. 3.13. Holzäpfel et al. (2021) provide full details of the campaign, relevant aspects are recapitulated in this section. The original purpose of the campaign was the investigation of the effectiveness of the Plate Line concept (see Fig. 2.6 left). Red dashes represent the plates in Fig. 3.13 and are each sized 4.5×9.0 m^2 in height and width, respectively.



Figure 3.12: Vaisala WINDCUBE® 200s at Vienna Airport in 2019 on the airfield (left) with a close-up of the scanning head (right). Copyright by Frank Holzäpfel.

The evolution of wake vortices generated by approaching aircraft was tracked employing lidar measurements from five lidar positions (L1 to L5 in Fig. 3.13) starboard of the glide path towards runway 16. Per aircraft overflight (landing aircraft) up to three lidar positions were occupied with measuring WINDCUBE® 200s lidars, providing multiple vortex evolutions per landing and allowing various flow phenomena to be captured. The median aircraft altitudes at the measurement planes for L1 to L5 were determined by Mode S transponder data [secondary surveillance radar system (ICAO, 2004)] as 39.9, 45.0, 53.6, 64.3, 74.2 m, respectively, with a standard deviation of 4.2 m. The lidar positions as well as the configured elevation angle and range extents, minimum (−) and maximum (+) subscripts, are tabulated in Table 3.5. Besides 21 days of measurements with erected Plate Lines, further 45 days of reference measurements were conducted without Plate Lines. A total of 9473 overflights were recorded, of which only 5 % were processed using the characterization RV method, given the manual algorithm surveillance required and the consequential processing time of 5 to 10 s per lidar scan [1]. Further information regarding the RV method is given in Section 3.4.2. The processed overflights have been selected based on meteorological conditions (headwinds below 2 m s^{-1} and crosswinds below 1.5 m s^{-1}) and aircraft types. Mode S transponder data are employed for estimating the root circulation of landing aircraft as described in the appendix of Holzäpfel et al. (2022) [they estimate the aircraft mass according to Holzäpfel and Rotshteyn (2023), except for Austrian Airlines aircraft where the exact gross mass has been provided by Austrian Airlines] [2]. By assuming an elliptic lift distribution, all parameters used for normalizing field measurement values can be derived using Eqs. 2.10 to 2.13.

[1] The processing of field measurements was conducted by Anton Stephan and Grigory Rotshteyn.
[2] The estimations were conducted by the authors of Holzäpfel et al. (2022).

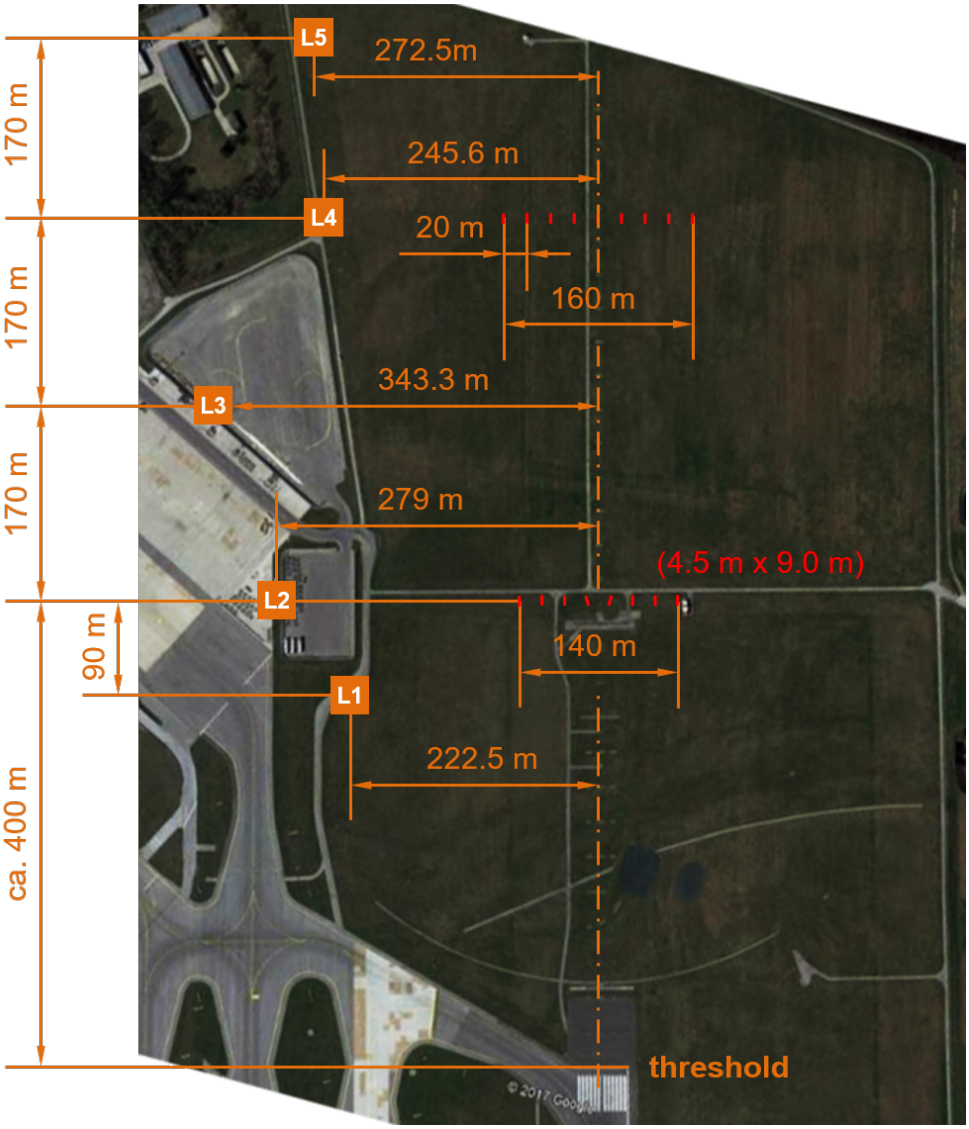

Figure 3.13: Positioning of lidar instruments L1 to L5 (orange boxes) and two Plate Lines (red dashes) at runway 16 of Vienna Airport (© Google 2017). The flight direction is from top to bottom. Adapted with permission of Holzäpfel et al. (2021).

Table 3.5: Lidar setup at Vienna Airport (field measurements). Lidar positions in flight direction are given with respect to the runway threshold (see Fig. 3.13) assumed at aircraft altitude of 50 ft ≈ 15 m (Holzäpfel et al., 2021). Adapted from Wartha et al. (2025c)©.

Parameter	Symbol	Unit	Value
Lidar position	-	-	(L1, L2, L3, L4, L5)
Min/max elevation angle	$[\varphi_-, \varphi_+]$	deg	$[0, 25]$, $[0, 20]$, $[0, 18]$, $[1, 28]$, $[0, 29]$
Min/max range gate	$[R_-, R_+]$	m	$[80, 530]$
x-position lidar	x_O	m	$(230, 140, -30, -200, -370)$
y-position lidar	y_O	m	$-(222.5, 279.0, 343.3, 245.6, 272.5)$
z-position lidar	z_O	m	$(1.0, 0.0, 1.0, -4.0, -6.0)$

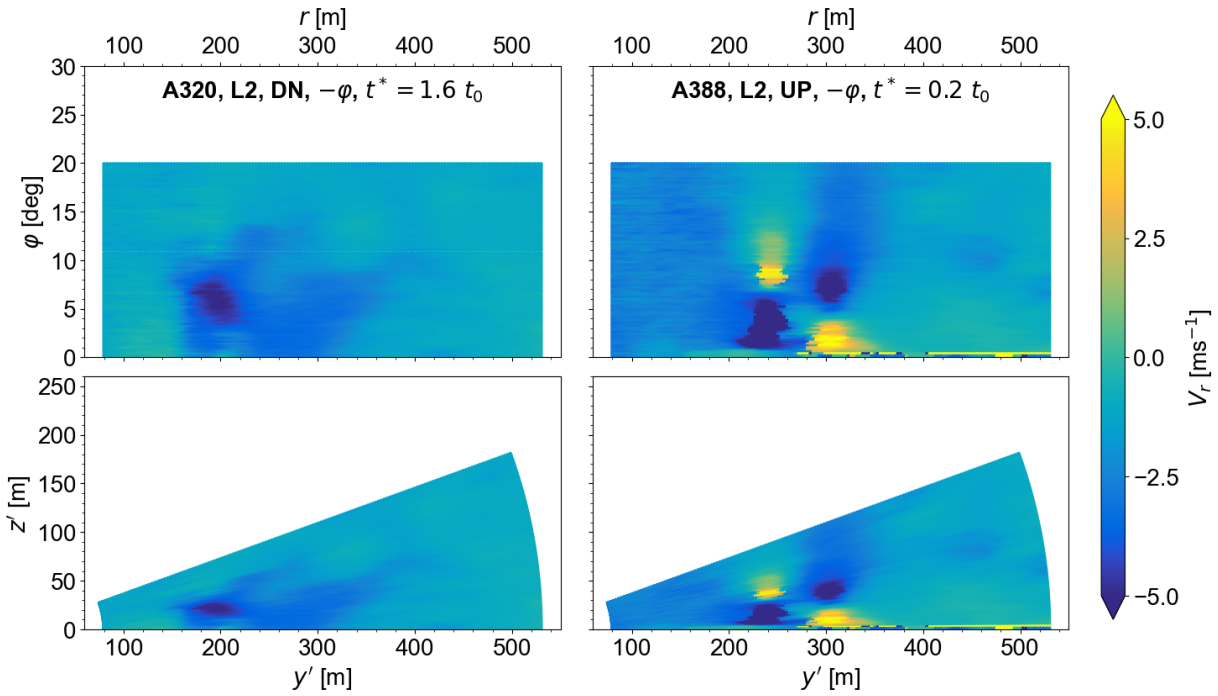

Figure 3.14: Example RHI lidar scans from Vienna Airport in spherical (top) and Cartesian (bottom) coordinate systems. The aircraft type, lidar position, Plate Line status (DN or UP), scan direction, vortex age are given, respectively.

The considered field measurement (FM) dataset family does not differentiate between lidar measurements conducted when the Plate Lines were erected or not in use. Stephan et al. (2023) has demonstrated the Plate Line status to have little impact on the characterization of wake vortices. Figure 3.14 displays two example lidar scans from Vienna Airport - each containing a vortex pair - in both the spherical (top) and Cartesian (bottom) coordinate systems. Figure 3.14 left features flat (DN) Plate Lines, while Fig. 3.14 right

features erected (UP) Plate Lines. Wake vortex pairs appear as two-dipole structures in lidar scans, where each dipole contains a patch of high positive LOS velocities and a patch of high negative LOS velocities. The disturbances at low elevation angle LOSs in Fig. 3.14 right can be directly associated with obstructing hard target plates delivering erroneous LOS velocities. These can be straightforwardly filtered prior to applying lidar processing algorithms. However, unlike in Fig. 3.14 left, the vortex pair can be identified well in this example.

The mean SNR distribution from the Vienna Airport campaign is visualized in Fig. 3.15. The lidar focal range of the measurement campaign was set at approximately 500 m, which can be identified straightforwardly with the highest available SNR values. Closer to the lidar SNR values decrease significantly. Furthermore, the boundary layer as well as the installed Plate Lines lead to a lower SNR at low altitudes.

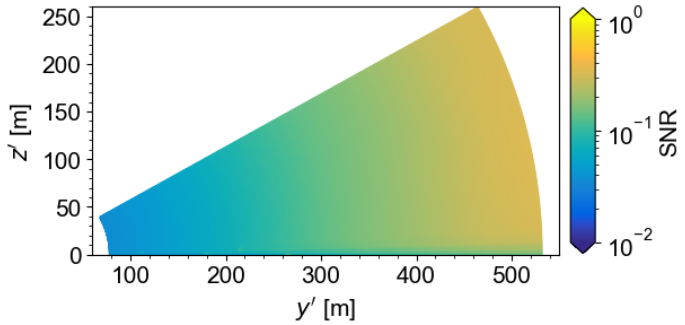

Figure 3.15: Mean SNR distribution of the field measurement dataset family, irrespective of lidar position at the 2019 Vienna Airport campaign.

The field measurement dataset family is split into 13 618 training, 1757 validation, and 1628 test lidar scans ($\approx 80 : 10 : 10$). RHI scans pertaining to one vortex evolution belong to the same subset, resulting in minor subset size differences. The vortex distributions with respect to vortex circulation (normalized and dimensionalized) and age for the training subset are given in Fig. 3.16 and emerge from lidar scan processing via the RV method. The distributions of the validation and test subsets are analogous, only the overall amount of vortices differs. Most vortices contained in the subset are young with $t^* \leq 4$, consequentially only few weak vortices are available. Furthermore, the majority of wake vortices have been generated by RECAT-EU CAT-D aircraft, with the Airbus A320 constituting the most common aircraft type at Vienna Airport during the measurement period. Figure 3.16 top right plots the vortex strength development with age in black. Even fully rolled up wake vortices rarely reach Γ_0, presumably since averaged Γ_{5-15} (covering only a disc around the vortex core) and estimated/assumed Γ_0 are defined according to different concepts.

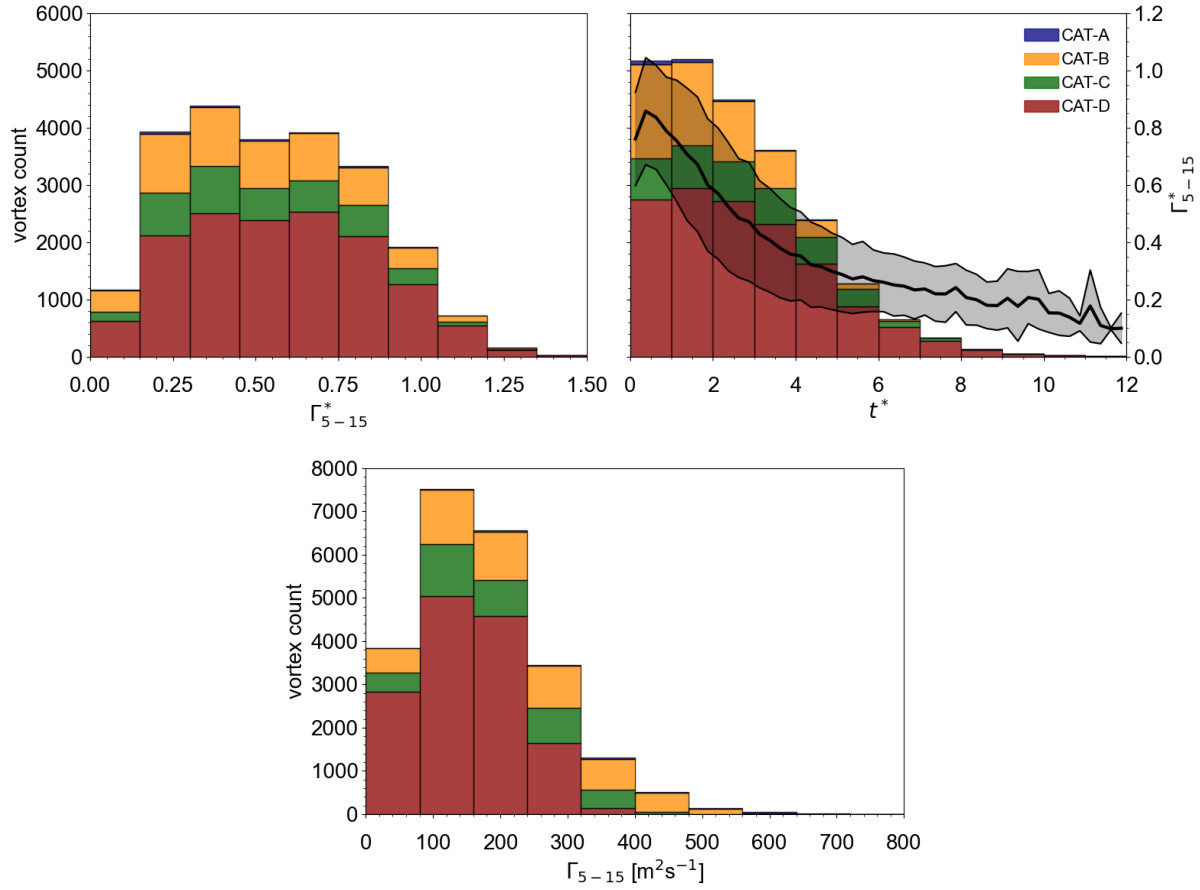

Figure 3.16: Distributions of absolute normalized/dimensional vortex circulation Γ^*_{5-15} (top left) and Γ_{5-15} (bottom), and vortex age t^* (top right) of the field measurement training subset. The temporal evolution of Γ^*_{5-15} is plotted with standard deviations on the right. RECAT-EU aircraft categories are given by color. (Wartha et al., 2025c)©

3.3.2 LES Lidar Simulators (LLS_n and LLS)

This section describes the two simulation dataset families, the LLS and the LLS_n dataset families. They represent separate dataset families, however with both relying on the same LES output, their underlying wake vortex statistics are equivalent.

The lidar placement within the LES computational domain is given in Table 3.6. Note that lateral lidar positions are with respect to the runway/glide path. Scanning range, elevation angles, and lidar positions are motivated by matching the Vienna Airport campaign (cf. Table 3.5). The Vienna Airport campaign only considered RHI lidar scans from the starboard side of the runway. The simulations also place virtual lidars on the port side of the virtual runway. By assuming mirror symmetry of the simulation about the glide path axis (virtual runway), scans recorded from the port side can be transformed to

further starboard virtual lidars, with the opposing atmospheric condition. This provides a computationally efficient way to obtain virtual lidar scans for both port and starboard crosswinds with one LES run. Additional virtual lidars are employed in order to generalize the analysis. Thus, for example the $\mathrm{LLS_n}$ subsets may be split into two sub-categories:

– $\mathbf{LLS_n^0}$: Scans modeling the field measurements (left of the semi-colon in Table 3.6).

– $\mathbf{LLS_n^+}$: Scans modeling additional lidar setups (right of the semi-colon in Table 3.6).

Note that $\left(\mathrm{LLS_n^0} \cap \mathrm{LLS_n^+}\right) \subset \mathrm{LLS_n}$ and $\left(\mathrm{LLS_n^0} \cap \mathrm{LLS_n^+}\right) = \emptyset$. Example $\mathrm{LLS_n^0}$ and $\mathrm{LLS_n^+}$ scans are given in Section 4.6.3, Fig. 4.39.

Table 3.6: Shared LLS and $\mathrm{LLS_n}$ parameters in the LES computational domain. There are 26 equidistant x_O^* positions, each with all possible y_O^* positions and the associated elevation angle spectrum. Normalizations are performed for the simulated Airbus A340. When the glide path and the lateral center of the LES domain do not coincide, the y^*-positions must be shifted with the glide path. (Wartha et al., 2025c)©

Parameter	Symbol	Unit	Idealized Vaisala WINDCUBE® 200s
Number of lidars	-	-	312
Elevation angle limits	$[\varphi_-, \varphi_+]$	deg	$[0, 20]$, $[0, 25]$, $[0, 18]$, $[0, 28]$, $[0, 29]$; $[0, 20]$
Range limits	$[R_-, R_+]$	m	$[80, 530]$; $[210, 660]$
x^*-position lidar	x_O^*	-	$[0.0, 17.1]$ with a spacing of 0.67
y^*-position lidar	y_O^*	-	$\pm(4.9, 5.9, 7.2, 5.2, 5.7; 10.0)$
z^*-position lidar	z_O^*	-	0

Both simulated dataset families, LLS and $\mathrm{LLS_n}$, are split into 14 250 training, 1859 validation, and 1570 test scans ($\approx 80 : 10 : 10$). RHI scans pertaining to one measurement plane along the LES x-axis belong to the same subset, resulting in minor subset size differences. The vortex distributions with respect to vortex circulation and age for the training subset are given in Fig. 3.17 and emerge from the LES using the tracking algorithm introduced in Section 3.4.1. As for the field measurements, the distributions of the validation and test subsets are analogous, only the overall amount of vortices differs. Most simulated vortices contained in the subset are young with $t^* \leq 4$, however less old and weak wake vortices are featured in comparison to the field measurement dataset family (cf. Fig. 3.16). As described in Section 3.1.4, the simulated Airbus A340 aircraft enters the LES domain at at an altitude of $b_0 = 47.4$ m, thus wake vortices are on average generated at a lower altitude in comparison to the field measurements (cf. Section 3.3.1). Holzäpfel et al. (2016a) previously corroborated that wake vortices decay significantly faster close to the ground. Therefore, less old wake vortices can be expected in the simulated dataset families in comparison to the field measurement dataset family. A comparison of the field measurement vortex distribution from Fig. 3.16 top right and the simulation vortex distribution from Fig. 3.17 right shows that the reduced vortex circulation during roll up

(left bin of the vortex age distributions) observed for the field measurements is not reproduced in the simulations. In general, the vortex circulation values obtained from the LES simulations exceed those experienced in the field measurements. It cannot be concluded which dataset represents vortex strength evolutions more accurately, given the differing processing algorithms.

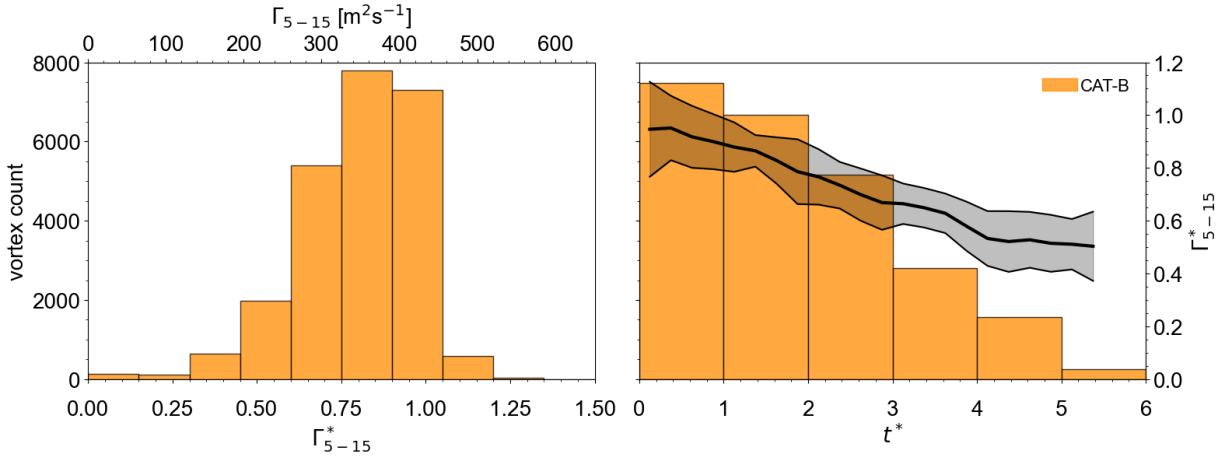

Figure 3.17: Distributions of absolute normalized/dimensional vortex circulation Γ^*_{5-15} and Γ_{5-15} (left) and the vortex age t^* (right) of the LLS and LLS$_n$ training subsets. The temporal evolution of Γ^*_{5-15} is plotted on the right with the respective standard deviations in black. (Wartha et al., 2025c)©

LLS$_n$ scans employ the mean SNR field from the field measurements (Fig. 3.15) in Eq. (3.18). The example LLS$_n$ scan in Fig. 3.18 reproduces the initialized SNR field well, solely regions of high velocity gradients are adulterated. An additional pseudo-random factor of unity mean and a variance of 1/4 is multiplied with the mean SNR field from the field measurements in order to differentiate lidar scans and construct a divers dataset.

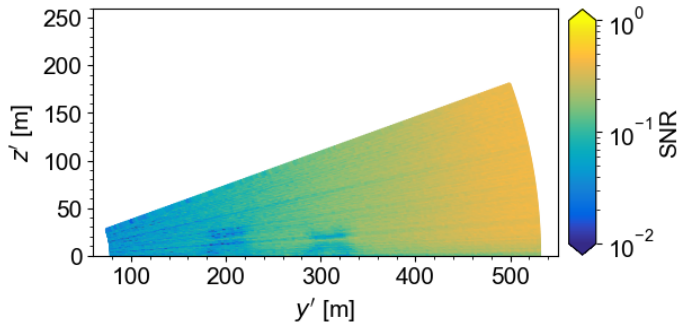

Figure 3.18: Example SNR distribution of a LLS$_n$ scan, resembling the SNR distribution of field measurements from Vienna Airport as seen in Fig. 3.15.

3.4 Wake Vortex Characterization

Determining the key characteristics of generated wake vortices for evaluating the potential hazard for follower aircraft, namely the position of the vortex core center and the circulation (i.e., strength) from which the vortex-induced rolling moment can be derived, is essential for safe and efficient aircraft operations. The available flow field information determines how and with what accuracy the aforementioned characteristics can be obtained. While single lidars are solely capable of measuring one-dimensional flow velocities, simulations provide high resolution three-dimensional flow field information.

Below introduces three lidar processing algorithms for wake vortex characterization:

- Section 3.4.1 details the LES tracking and characterizing algorithm.
- Section 3.4.2 describes the physical RV lidar processing method, given that the field measurements from Vienna Airport were processed using a 1.5-µm PCDL, for which the RV method has proven to outperform alternative physical lidar processing methods (Smalikho et al., 2015).
- Section 3.4.3 provides a novel data-driven lidar processing algorithm. The so-called ML pipeline is engineered for individual wake vortex detection and characterization.

3.4.1 Simulation Tracking Algorithm

Under the assumption of vortex filaments remaining horizontal in flight direction for a significant time period, Stephan (2014) suggests that a straightforward pressure-vorticity approach can be employed for determining the position of a wake vortex in LESs. The strength of more complex vortex filament structures, for instance with significant vertical or spanwise vorticity components, are underestimated and should be tracked with more sophisticated methods as suggested by Jeong and Hussain (1995); Hennemann (2010); Hennemann and Holzäpfel (2011). The most hazardous wake vortices are coherent, young, strong, and thus primarily horizontal. Such vortices can be detected reliably with the relative pressure p' and vorticity in flight direction ω_x. The extreme values (both positive and negative for the counter-rotating vortices) of $\omega_x \times p'$ provide the vortex center. The vorticity in flight direction is then employed for computing the circulation magnitude of the vortex. Spatial averaging in flight direction as well as temporal and spatial constraints are employed to ensure clean vortex tracking (Stephan, 2014). Furthermore, quantitative and qualitative checks, based on wake vortex trajectory and strength trends, omit apparent miss-identifications. Quantitative checks include surveillance of the vortex circulation sense, radical circulation magnitude drops, or generally extreme wake vortex circulation magnitudes and positions. Note that outliers and human errors cannot be ruled out entirely, only minimized, given the turbulent nature of the flow.

Results from this algorithm are considered the ground truth for LLS and LLS_n scans in this thesis. Both lidar scans and the LES tracking algorithm are limited to vertical flow field slices, thus relying on a ground truth algorithm which does not consider vortex tilt is considered acceptable. Nonetheless, potential vortex strength underestimations must be kept in mind during analyses.

3.4.2 Radial Velocity (RV) Method

It has been established in Section 1.2 that among available 1.5-µm PCDLs physical algorithms, the RV method is most suitable for wake vortex characterizations. This thesis focuses on the original RV method version (Smalikho et al., 2015), given its employment for analyzing the field measurements from Vienna Airport. Thus, RV method results constitute the ground truth for field measurement scans. Previously DLR implemented a practical tool via the graphical system design application LabVIEW (National Instruments). Note that this thesis does not aim to improve the RV method, rather it aims to reveal its limits and evaluate the reliability of findings from published studies. The following recapitulates the principle of the RV method as presented by Smalikho et al. (2015). The approach involves two parts: first the vortex center position is determined using the spherical coordinate system of a lidar, second the vortex circulation is estimated.

Determination of the vortex position is further separated into two steps. First, the range from the lidar instrument to the vortex center R_C is estimated by selecting the maximum of

$$D(R_j) = \sum_{k=0}^{K} \left[\bar{V}_r(R_j, \varphi_k)\right]^2, \tag{3.24}$$

which is plotted in Fig. 3.19 for a vortex pair. Equation 3.24 corresponds to finding the range with the highest LOS velocities across all elevation angles. Each peak of D corresponds to a vortex in the lidar scan.

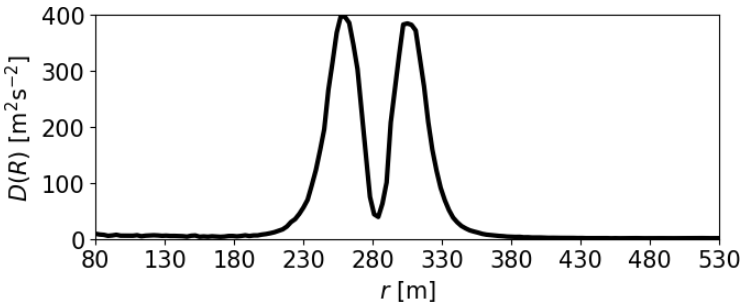

Figure 3.19: Example computation of the functional $D(R)$ for all distance from the lidar for an example lidar scan with a vortex pair. After Smalikho et al. (2015).

The corresponding elevation angle φ_C is determined by selecting the highest and lowest LOS velocities across all φ_k at the respective R_C, with which the mean value

$$\varphi_C = \frac{\varphi_{\max_k\left[\bar{V}_r(R_C,\varphi_k)\right]} + \varphi_{\min_k\left[\bar{V}_r(R_C,\varphi_k)\right]}}{2}, \tag{3.25}$$

is computed. The wake vortex circulation is estimated by minimizing the functional

$$G(\Gamma_n) = \sum_{k=0}^{K} \left[\bar{V}_r(R_{C,n},\varphi_k) - \widetilde{V}_r(R_{C,n},\varphi_k;\Gamma_{n=1},\Gamma_{n=2})\right]^2. \tag{3.26}$$

The located wake vortices are modeled via the analytical Burnham-Hallock vortex (Burnham and Hallock, 1982) with a fixed vortex core radius r_c for each aircraft type. For a vortex pair $n = 1, 2$, the circulations Γ_n are determined by iteratively minimizing the difference between the measured velocity field in vortex core vicinity $\bar{V}_r(R_{C,n},\varphi_k)$ and the modeled velocity field $\widetilde{V}_r(R_{C,n},\varphi_k;\Gamma_1,\Gamma_2)$. Values of Γ_{5-15} are obtained by modeling the Burnham-Hallock vortex for the determined root circulation and core radius.

Within the LabVIEW implementation of the RV method, the user can decide to include a so-called background scan (superscript B) which is subtracted from the wake vortex scan (superscript V) being analyzed. The average LOS velocity is computed in the background scan along each LOS and subtracted from the appropriate LOS velocities in the wake vortex scan, i.e.,

$$\bar{V}_r\left(R_j,\varphi_k\right) = \bar{V}_r^{\mathrm{V}}\left(R_j,\varphi_k\right) - \langle\bar{V}_r^{\mathrm{B}}\left(\varphi_k\right)\rangle. \tag{3.27}$$

A measured velocity field constitutes the sum of a background wind velocity field and a turbulent velocity field. In this thesis, the background velocity field is assumed a RHI lidar scan just before the wake vortex generating aircraft has passed the lidar measurement plane. Clearly, there is a temporal delay between the background scan and the wake vortex scan, thus primarily temporally constant atmospheric structures, such as crosswinds, can be captured and damped with this approach.

3.4.3 Machine Learning Pipeline

Employing ML for characterizing wake vortices in lidar measurements has gained traction just over half a decade ago (see Section 1.2). The majority of efforts focused on detecting wake vortices only, resulting in an estimation of the vortex position. However, evaluating the potential wake vortex encounter requires the characterization of both the vortex position and strength. Section 2.1.2 established that due to atmospheric conditions and lidar scan geometry, capture of the primary wake vortex pair is not certain [as Wartha et al. (2022) assume]. None, just one, or more than two vortices may be present in a captured RHI lidar scan. Therefore, it is essential for a processing algorithm to operate independently of an expected number of wake vortices in a lidar scan. Furthermore, universally applicable, reliable, accurate, rapid, and automatic wake vortex processing must be ensured to overcome obstacles of currently available lidar processing algorithms.

The suggested approach of this thesis is therefore to first identify wake vortices in a lidar scan using the popular object detection model YOLO, after which they are individually characterized by the position and circulation using regression CNNs. This framework is referred to as ML pipeline, with a schematic overview provided in Fig. 3.20. Arabic numbers outline the four steps involved, with Roman numbers indicating the ML steps. Stephan et al. (2023) previously introduced the ML pipeline, substantial parts are reiterated in this section [3]. This section therefore partly answers the second research question posed in this thesis. Further data-driven ML algorithms followed Stephan et al. (2023), such as a two stage CNN framework (Chu et al., 2024a,b) or analogous YOLO-based methods (Shen et al., 2023; Zhang et al., 2024). None of these approaches surpassed the capabilities and accuracy of the ML pipeline. Following a general overview of ANNs and the employed dataset notation, below addresses each ML pipeline step (1-4) in order.

Artificial Neural Networks Overview

ML steps in this thesis are based on ANNs. The following provides a brief overview of this supervised ML type. Details are available in for example Chollet (2018); Bishop (2006); Lindholm et al. (2022); Géron (2019). Supervised learning refers to tuning trainable parameters by mapping input data to known labels/targets (lbl) during an optimization process named training. In general labels are referred to as $\mathbf{y}_{\text{lbl}}$, in this thesis representing the two-dimensional vortex position and the vortex circulation. The input is represented by the LOS velocities of each lidar scan. ANNs have the goal to obtain a function f that models the relationship between the input $x \in \mathbb{R}$ and output parameter $y \in \mathbb{R}$ i.e., $y = f(x)$. Thus, ANNs are also called feedforward neural networks, as they process input data uni-directionally through a chain of operations. In the most simple form a so-called artificial neuron (McCulloch and Pitts, 1943) assumes a linear relationship,

$$y = wx + b, \tag{3.28}$$

where a weight $w \in \mathbb{R}$ and a bias $b \in \mathbb{R}$ represent the trainable parameters summarized by $\mathbf{p} \in \mathbb{R}$. An activation function $y_\alpha = \alpha(y)$ can be implemented to enable non-linear relationships or achieve a particular output format. For example the popular Rectified Linear unit (ReLu) activation function (Nair and Hinton, 2010) reads $\alpha(x) = \max(0,\, x)$. A single artificial neuron does not suffice for highly complex input-output relationships. When multiple artificial neurons are employed for the above task, a so-called dense layer is formed. Multiple layers can be placed one after another for furthering the complexity of f and allowing hierarchical features in the input data to be represented i.e., low-level and high-level features. Layer arrangements are referred to as architectures. In a dense layer, each artificial neuron is connected to all artificial neurons in the forgoing and following dense layer. Alternative weight arrangements allow different patters to be modeled by f, giving the rise to various ANN layer types.

[3] The ML pipeline was subject of a master's thesis by Lars Stietz (Stietz, 2022) under the supervision of Niklas Wartha.

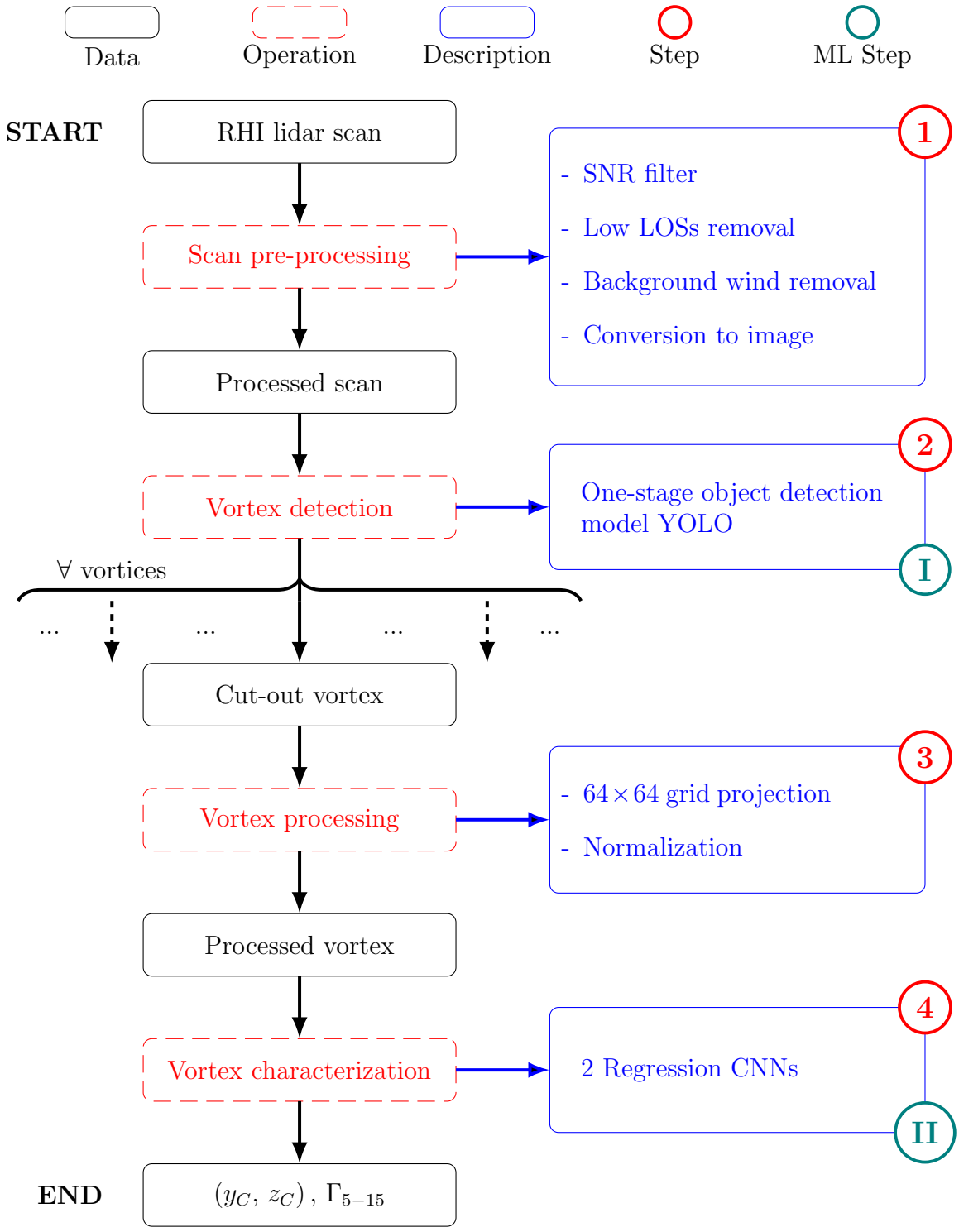

Figure 3.20: Schematic of the ML pipeline from the RHI lidar scan to the position and circulation of all detected vortices. Arabic and Roman numbers are used for overall and ML steps, respectively.

Computer vision tasks (image analysis) typically rely on convolutional layers (LeCun, 1989). Weights and biases are arranged into kernels (also sometimes called filters), representing weight grids of size $k \times k$ and a bias. A kernel can therefore represent two-dimensional patterns and recognize features within a so-called receptive field. Generally, a kernel $\boldsymbol{\kappa}$ is swept through the input, where the resonance of the kernel pattern with the input $\mathbf{x}$ is sampled, which can be represented as a convolution process with the layer output (Lindholm et al., 2022, chap. 6),

$$\mathbf{q}_{i,\,j} = \alpha \left(\sum_{n=0}^{k-1} \sum_{m=0}^{k-1} \mathbf{x}_{i+n,\,j+m} \boldsymbol{\kappa}_{n,\,m} \right), \tag{3.29}$$

also called a feature map. Convolutional layers are efficient, as they share weights across the input and are therefore also translation invariant - suitable for vortex analysis in a Cartesian coordinate system (unlike a spherical coordinate system). Employment of multiple kernels in a convolutional layer allows various features to be represented (Bishop, 2006, chap. 5). When an ANN consists of multiple convolutional layers, kernels in shallow layers recognize high-level features, kernels in deeper layer merge these to obtain low-level features. An ANN made up of multiple convolutional layers is termed a CNN. Parameters such as padding and stride, dictating the kernel movement along the input, are employed for controlling the data dimensions from one layer to the next.

Trainable parameters values are obtained by solving an optimization problem. The so-called loss function,

$$\mathcal{L}_{\text{MSE}} := \frac{1}{D} \sum_{d=1}^{D} \left(y_{\alpha}^{d} - y_{\alpha,\text{lbl}}^{d} \right)^2, \tag{3.30}$$

here in the form of the Mean Squared Error (MSE), must be minimized for all data instances D (Géron, 2019, chap. 4). In this thesis D represents the number of training lidar scans or wake vortices (depending on the ML step considered). The minimization problem is solved via an optimization algorithm (also known as optimizer), based on updating trainable parameters with a correction in the negative gradient direction (Bishop, 2006, chap. 5),

$$\mathbf{p}_t \leftarrow \mathbf{p}_{t-1} - \eta \nabla \mathcal{L} \left(\mathbf{p}_{t-1} \right), \tag{3.31}$$

where η represents the step size or learning rate, t denotes an optimization step, and

$$\nabla \mathcal{L} \left(\mathbf{p}_t \right) = \sum_{d=1}^{D} \nabla \mathcal{L}_d \left(\mathbf{p}_t \right). \tag{3.32}$$

Depending on the size of D it is common for a mini-batch size to be defined, allowing updates to the trainable parameters in a more frequent manner and enabling faster ANN training. The individual $\nabla \mathcal{L}_d \left(\mathbf{p} \right)$ is computed in a process called backpropagation (Rumelhart et al., 1985) and gives an understanding of how each trainable parameter contributes

to the loss i.e., $\partial\mathcal{L}/\partial p_{ji}$ (for the particular trainable parameter p_{ji}). Thus, it is strictly necessary for an activation function to be differentiable. Bishop (2006, chap. 5) provides extensive details on backpropagation. Specific formulas highly depend on the particular ANN architecture. In general, the chain rule is used to compute the contribution of a single trainable parameter to the overall loss.

Two further layers employed in this thesis are:

- **Maximum-pooling layers** (Jarrett et al., 2009): Similar to the convolutional layers they use a receptive field of size $k \times k$, however they contain no trainable parameters and instead restructure data. Within the receptive field the maximum value, the highest activation in a convolution feature map, is passed as the output.

- **Flatten layers**: They also restructure data and contain no trainable parameters. Multi-dimensional arrays are transformed to one-dimensional vectors.

Dataset Notation

Section 3.3 introduced three different dataset families, all of which are separately employed for training, validating, and testing the ML pipeline. However, cross evaluations i.e., employing different dataset families for training, validating, and testing, is equally explored. In order to keep track of the subsets used for training and testing of a particular ML pipeline, this thesis specifies the employed dataset families for training, validation, and testing subsets using the notation

$$\textit{trained on}\,(\textit{evaluated on})\,. \tag{3.33}$$

For example, *FM(LLS)* refers to the ML pipeline trained on field measurements (training subset) and processing/testing of LLS scans (test subset). The validation subset is not specifically mentioned, as it strictly employs the same dataset family as the training subset.

ML Pipeline Step 1: Lidar Scan and Label Pre-Processing

Data curation has the ability to strongly enhance ML performance, particularly computer vision tasks are greatly simplified by enabling the object of interest, the vortex in this thesis, to overshadow patterns not of interest [in compliance with EASA guidelines (Soudain, 2024)]. Studies for wake vortex pattern recognition in lidar scans have revealed that primarily velocities and gradients of high magnitude are utilized for identifying wake vortices. Wartha et al. (2022) tested multiple feature engineering techniques and compiled a list of suggested pre-processing steps. Their suggestions and additional pre-processing steps are employed in this thesis (Stietz, 2022):

1. **SNR filter**. Every LOS velocity contained in a RHI lidar scan has an associated SNR value. A threshold of $\mathrm{T_{SNR}} = 0.02$ ensures LOS velocities associated with a SNR value equal or lower to $\mathrm{T_{SNR}}$ are filtered.

2. **Measurements at low LOSs are neglected**. Lidar scans measuring close to the ground often contain erroneous data points, either from hitting hard targets (such as the Plate Lines, see Fig. 3.14 right) or from interactions with the boundary layer. Both effects may lead to very high magnitude LOS velocities, with the potential to overshadow the velocity pattern of the wake vortices. Thus, LOSs which result in an altitude of 7 m or lower at the glide path are neglected.

3. **Projection of LOS velocities onto an universal Cartesian grid using linear interpolation**. Most ML architectures necessitate instances of input data to be of equal size. It is particularly advantageous for CNNs with rectangular kernels to convolute over rectangular data instances. For RHI lidar scans the Cartesian format $[y', z']$ is preferred; it avoids unphysical scaling of wake vortices as perceived by RHI lidar scans in the spherical format $[r, \varphi]$. The universal grid is sized according to the the field measurements from Vienna Airport, $\left[y'_- = 70, y'_+ = 530\right] \times \left[z'_- = 0, z'_+ = 256\right]$ m, with the largest scans measured at lidar position L5 ($\varphi_+ = 29$ deg). Discretization into an equidistant grid $S \times S$ is schematically visualized in Fig. 3.21. Furthermore, $W_{\text{lid}} = y'_+ - y'_-$ and $H_{\text{lid}} = z'_+ - z'_-$ represent the Cartesian width and height of the lidar (lid) scan. Charette (2025) recommends objects for detection to exceed 16×16 pixels. Additionally, input dimensions must be multiples of 32 (Bochkovskiy, 2021) and images (im). Given that the Airbus A320 (or A20N) with $b_0 = 26.8$ m constitute the smallest aircraft considered in this thesis, the above conditions are fulfilled if $H_{\text{im}} = 256$ pixels (nodes) for the vertical dimension, corresponding to the z'-axis and $W_{\text{im}} = 448$ pixels (nodes) for the horizontal dimension, corresponding to the y'-axis. Correspondingly, $dz_{\text{im}} = 1$ m and $dy_{\text{im}} = 1.03$ m (Stietz, 2022). RHI lidar scans with fewer LOS employ nearest-neighbor interpolation.

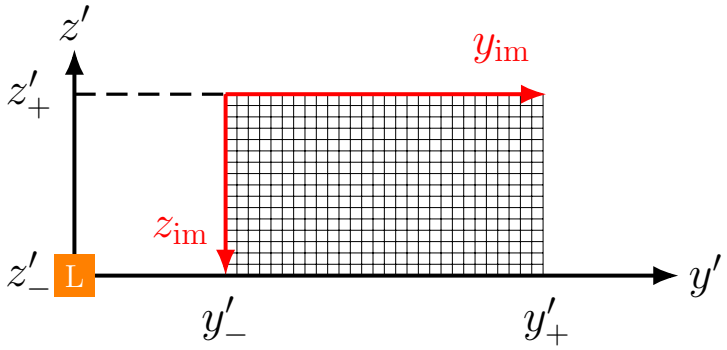

Figure 3.21: Schematic of a simplified universal Cartesian grid in the lidar coordinate system $[x', y', z']$ with minimum (subscript $-$) and maximum (subscript $+$) values sketched in black color. The coordinate system of an image $[y_{\text{im}}, z_{\text{im}}]$ is defined in red color.

4. **Subtraction of a background wind component from the measured lidar scan**. As for the RV method, the background wind component is captured by a lidar scan just before the aircraft overflight. This background wind scan is equally interpolated onto the above universal Cartesian grid. Given that a crosswind is a shear flow, rather than subtracting background velocities per LOS, the ML pipeline uses the universal Cartesian grid and subtracts the mean background wind along altitude z' (Stietz, 2022),

$$\bar{V}_r\left(y', z'\right) = \bar{V}_r^{\mathrm{V}}\left(y', z'\right) - \langle \bar{V}_r^{\mathrm{B}}\left(z'\right)\rangle. \tag{3.34}$$

5. **Further interpolation**. Remaining unavailable data point are filled in the nearest-neighbor fashion in the vertical direction and under the assumption of a vertical atmospheric stratification with $\langle \bar{V}_r\left(z'\right)\rangle$ in the horizontal direction.

6. **Conversion of measurements to an image**. LOS velocities of a lidar scan must undergo a conversion into pixel intensities for the first ML step (I). Considering the '.png' image data format (16-bit), it follows that the minimum and maximum LOS velocities of the training subset, interval $\left[\bar{V}_r^-,\, \bar{V}_r^+\right]$, are normalized to $[0,\, 2^{16}-1]$, employing min-max normalization as suggested by the EASA guidelines (Soudain, 2024). Subsequently, values are multiplied by $2^{16}-1$, giving

$$\bar{V}_r^{\mathrm{pixel}}\left(\bar{V}_r\right) = \frac{\bar{V}_r - \bar{V}_r^-}{\bar{V}_r^+ - \bar{V}_r^-}\left(2^{16}-1\right), \tag{3.35}$$

   for each LOS velocity $\bar{V}_r$ associated to an image pixel.

Object detection models such as YOLO make use of rectangular boxes, termed bounding boxes, for capturing the object of concern. Therefore, also the labels must be defined by bounding boxes, their size is chosen such that it contains the object to detect. Let a bounding box $\mathbf{BB}\left(x_{\mathrm{BB}},\, y_{\mathrm{BB}},\, w_{\mathrm{BB}},\, h_{\mathrm{BB}}\right)$ be defined by four spatial parameters, providing the horizontal position of the bounding box center in the input image, the vertical position of the bounding box center in the input image, the width of the bounding box, and the height of the bounding box, respectively. Labels in this thesis emerge from either the RV method for field measurements or the LES tracking algorithm for the LLSs. Both processing methods deliver the vortex center position $(y'_C,\, z'_C)$ and the circulation Γ_{5-15}. Thus coordinate system transformations are necessary to transform the labels to the image Cartesian coordinate system (see Fig. 3.21) (Stietz, 2022):

$$y_{\mathrm{im}} = \frac{y' - y'_{\mathrm{min}}}{W_{\mathrm{lid}}} W_{\mathrm{im}}, \quad z_{\mathrm{im}} = \frac{z'_{\mathrm{max}} - z'}{H_{\mathrm{lid}}} H_{\mathrm{im}}, \quad w_{\mathrm{im}} = \frac{w_{\mathrm{lid}}}{W_{\mathrm{lid}}} W_{\mathrm{im}}, \quad h_{\mathrm{im}} = \frac{h_{\mathrm{lid}}}{H_{\mathrm{lid}}} H_{\mathrm{im}}. \tag{3.36}$$

Bounding box labels in YOLO are normalized quantities with respect to the input image size, thus simplifying Eq. (3.36) to

$$y_{\mathrm{BB}}\left(y'_C\right) = \frac{y'_C - y'_{\mathrm{min}}}{W_{\mathrm{lid}}}, \quad z_{\mathrm{BB}}\left(z'_C\right) = \frac{z'_{\mathrm{max}} - z'_C}{H_{\mathrm{lid}}}, \quad w_{\mathrm{BB}} = \frac{b_0}{W_{\mathrm{lid}}}, \quad h_{\mathrm{BB}} = \frac{b_0}{H_{\mathrm{lid}}}, \tag{3.37}$$

where $h_{\text{lid}} = b_0$ and $w_{\text{lid}} = b_0$, in order to compensate for different aircraft sizes.

Throughout this section a lidar scan shown in Fig. 3.22 left undergoes the complete ML pipeline. This wake vortex scan belongs to a Boeing 787-900 overflight. The pre-processed lidar scan is shown in Fig. 3.22 right,

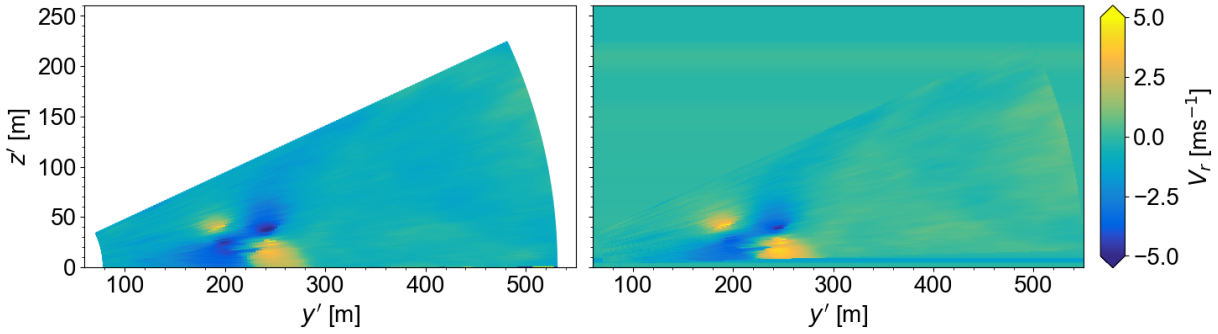

Figure 3.22: Example of the pre-processing performed for RHI lidar scans. The original RHI lidar scan (left) and the pre-processed lidar scan (right) are given (prior to converting the scans into image files).

ML Pipeline Step 2: Wake Vortex Detection with YOLO

The second step in the ML pipeline, the first ML step (I), consists of an one-stage object detection network. Object detection ML models determine the position of an object using bounding boxes, while simultaneously classifying it (Zhao et al., 2019), starboard and port vortices in the case of this thesis. They are the popular choice for a variety of video and image analysis applications. In the literature two types of object detection exist, one-stage object detection and two-stage object detection. The latter emerged first, according to Zhao et al. (2019) as a result of Region-based CNNs (R-CNNs) (Girshick et al., 2014), a region-proposal network, which rapidly developed into jointly optimizing the bounding boxes and classification via fast R-CNNs (Girshick, 2015), and further with faster R-CNNs (Ren et al., 2017) efficiently extracting features at several scales for efficiency benefits.

Despite high accuracy, two-stage object detectors share a main disadvantage, their inability to operate in fast-time, as the region proposal and classification tasks are separately trained and their pooling in the processing of data presents a bottleneck (Zhao et al., 2019). One-stage object detectors directly classify objects by mapping the input to bounding boxes without a separate region proposal step allowing significantly more efficient data processing and thus fast-time operation. The most popular one-stage object detection models are YOLO [first proposed by Redmon et al. (2016), several developments have been released since], RetinaNet (Lin et al., 2017), and Single Shot Multibox Detector (SSD) (Liu et al., 2016).

At time of release, Bochkovskiy et al. (2020) found YOLOv4 to offer the best compromise between processing speed and detection accuracy. Given that YOLO is a community driven project, throughout the course of this thesis other versions of YOLO have been

released. While some newer versions are focused on improving deployment characteristics of YOLO, such as YOLOv5 being python-based (Jocher et al., 2022), others have the objective to improve overall performance, such as YOLOv6 improving small object detection (Li et al., 2022). It is expected that some of these characteristics may improve accuracy and efficiency achieved in this thesis even further. YOLOv4 is nonetheless considered suitable for demonstrating the ML pipeline functionality (as well as advantages compared to alternative processing algorithms) and the performed wake vortex studies, particularly for comparing the different dataset families introduced in Section 3.3. Descriptions below recapitulate parts from Bochkovskiy et al. (2020) [4]. Unless stated otherwise, the remainder of this thesis refers to YOLOv4 as simply YOLO.

YOLO Architecture

A schematic representation of the YOLO architecture is given in Fig. 3.23. It follows the general object detector setup:

- A **backbone** learns high-level features from the input.
- A **head** is responsible for the final parameter estimation via learning low-level features i.e., estimating bounding boxes and associated object classes.
- A **neck** is employed. Given the high difference in feature scales, feature maps from different backbone layers are assembled. Paths between high-level and low-level allow the multi-scale features to interact efficiently (Bouraya and Belangour, 2021).

The backbone is a pre-trained CSPDarknet-53 (Wang et al., 2020), an update to YOLOv3's Darknet-53 (Redmon and Farhadi, 2018), made up of Cross Stage Partial (CSP) blocks illustrated in Fig. 3.24(a). In other words the backbone is made up of 53 convolutional layers with batch normalization (for stability) (Ioffe and Szegedy, 2015) and the mish activation function (comparable to ReLu while allowing some negative component) (Misra, 2019), abbreviated as Convolution Batch Mish (CBM) layers. Residual shortcuts (skipping layers), enable effective gradient learning during the backpropagation process (He et al., 2016). The first CBM layer of a CSP block has the purpose to down-sample the input via a stride of 2, after which two copies of the output from that layer are sent through two different paths: a single CBM layer and a chain of CBM layers, including N residual blocks. Each residual block is given in Fig. 3.24(b), representing further CBM layers and by-passed information. In this thesis the backbone has been pre-trained with the Common Objects in Context (COCO) dataset (Lin et al., 2014).

[4] YOLO was implemented via the GitHub library by Bochkovskiy (2021).

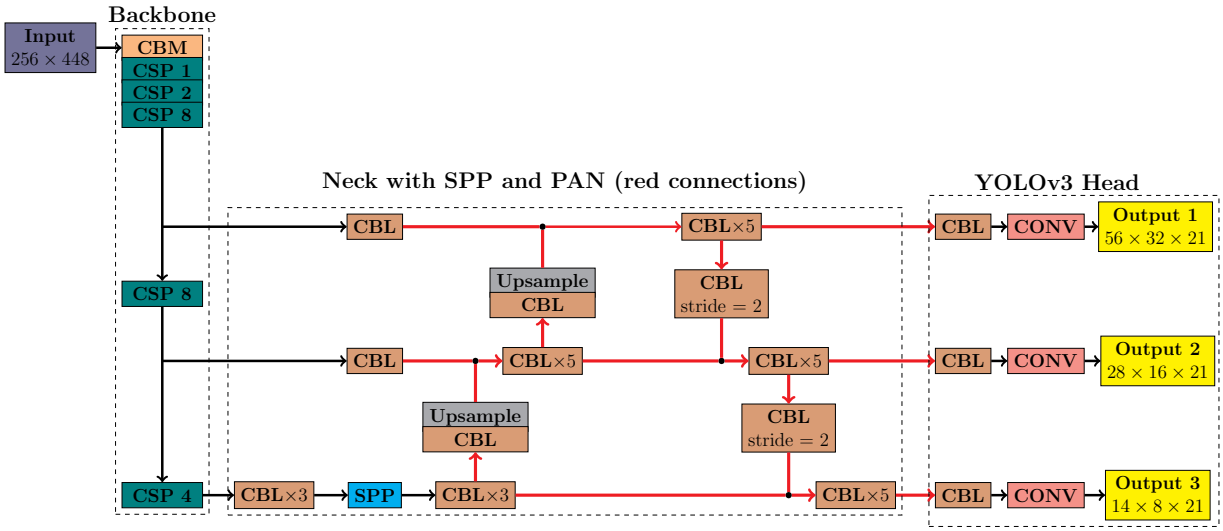

Figure 3.23: Schematic of the YOLOv4 architecture. Specifics on individual blocks are given in Fig. 3.24. Joining paths represent concatenated information. Splitting paths carry the same information further on all branches. Output tensors are given by $N \times M \times [A\ (4+1+2)]$, corresponding to 3 anchor boxes, the 4 bounding box offsets, the objectness prediction, and the two class predictions, respectively. With permission of Stephan et al. (2023).

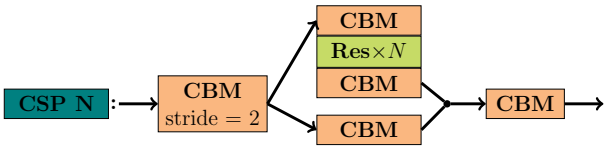

(a) Cross Stage Partial (CSP) block including N residual blocks (Res).



(b) Residual Block (Res) including Convolution Batch Mish (CBM) blocks.

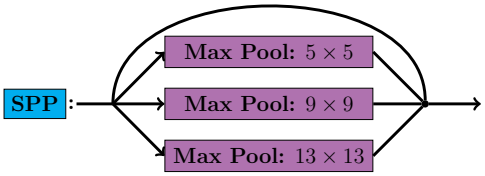

(c) Spatial Pyramid Pooling (SPP) block.

Figure 3.24: Schematics of individual YOLOv4 blocks. With permission of Stephan et al. (2023).

The neck is highly intertwined with the backbone, already prior to the penultimate CSP block, data are fed into the neck made up of Spatial Pyramid Pooling (SPP) (He et al., 2015) and a modified Path Aggregation Network (PAN) (Liu et al., 2018) using convolutional layer with batch normalization and the Leaky ReLu (LReLu) activation function (also comparable to ReLu while allowing some negative component) (Maas et al., 2013), abbreviated as Convolution Batch Leaky (CBL) layers. The SPP block illustrated in Fig. 3.24(c) provides YOLO a large receptive field via maximum-pooling layers of different scales for context information (Bochkovskiy et al., 2020). Instead, the PAN operation (red arrows in Fig. 3.23) combines features extracted at different network depths via up- and down-sampling (Liu et al., 2018).

The head of YOLOv4 is the same as for YOLOv3 (Redmon and Farhadi, 2018), with output estimations being made on three different scales (see Fig. 3.23), allowing vortices of different sizes to be detected. The head uses fixed anchor boxes with center (c_x, c_y), width p_w, and height p_h, illustrated in Fig. 3.25, to estimate possible bounding boxes - three at each scale, thus nine in total. The recommended standard anchor boxes are employed in this thesis. All nine anchor boxes are evaluated by each grid cell ($N \times M$ grids defined in the yellow boxes in Fig. 3.23), estimating an offset (t_x, t_y, t_w, t_h) from the anchor box, class, and objectness O. The objectness relates the Intersection over Union (IoU) of the labeled bounding box and the estimated (est) bounding box i.e.,

$$\text{IoU} := \frac{|\mathbf{BB}_{\text{est}} \cap \mathbf{BB}_{\text{lbl}}|}{|\mathbf{BB}_{\text{est}} \cup \mathbf{BB}_{\text{lbl}}|} \tag{3.38}$$

and the probability of any object class being contained in the estimated bounding box, i.e., $O(\mathbf{BB}) := \text{P}(\text{object})\,\text{IoU}(\mathbf{BB}_{est}, \mathbf{BB}_{lbl})$ (Redmon et al., 2016). YOLO estimates the objectness with t_O, equally a probability for each class is estimated with t^i_{class}, both using the logistic activation function $\sigma(x) = 1/[1 + exp(-x)]$. In summary, a bounding box is estimated using (Redmon and Farhadi, 2017),

$$b_x = \sigma(t_x) + c_x, \qquad b_y = \sigma(t_y) + c_y, \qquad b_w = p_w e^{t_w}, \qquad b_h = p_h e^{t_h}, \tag{3.39}$$

$$O(\mathbf{BB}) = \sigma(t_O), \qquad \text{P}(\text{class}_i) = \sigma(t^i_{\text{class}})\ i \in \{1, 2\}. \tag{3.40}$$

An overall YOLO-confidence for each estimation is determined by (Redmon et al., 2016),

$$\begin{aligned} C(\mathbf{BB}) &= \text{P}(\text{class}_i)\text{IoU}(\mathbf{BB}_{est}, \mathbf{BB}_{lbl}) \\ &= \text{P}(\text{class}_i|\text{object})\text{P}(\text{object})\,\text{IoU}(\mathbf{BB}_{est}, \mathbf{BB}_{lbl}). \end{aligned} \tag{3.41}$$

Given the number of estimated bounding boxes per image, some large objects, particularly close to image borders, may be detected by multiple bounding boxes. Greedy non-maximal suppression (Bodla et al., 2017) solves this issue by choosing the bounding box with the highest YOLO-confidence score and suppressing all other bounding boxes with an IoU > 0.231 (Bochkovskiy, 2021).

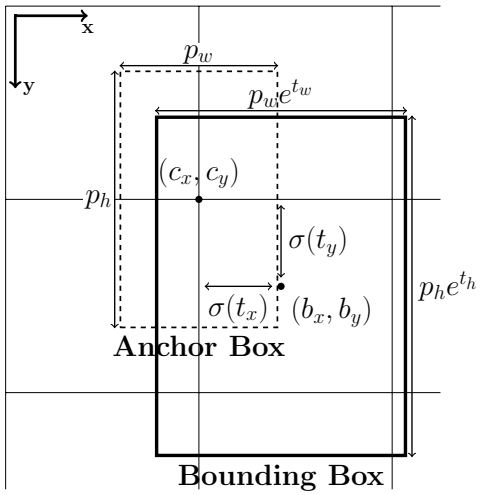

Figure 3.25: Schematic of the relationship between an anchor box and a bounding box estimation. After Redmon and Farhadi (2017). With permission of Stephan et al. (2023).

YOLO Loss Function

The YOLOv4 loss function constitutes three components (Redmon et al., 2016; Redmon and Farhadi, 2018; Bochkovskiy et al., 2020; Guo et al., 2021):

$$\mathcal{L} = \lambda_{\text{CIoU}}\mathcal{L}_{\text{CIoU}} + \lambda_{\text{class}}\mathcal{L}_{\text{class}} + \lambda_O\mathcal{L}_O, \tag{3.42}$$

with λ representing weighting factors:

– **Bounding box loss ($\boldsymbol{\mathcal{L}_{\text{CIoU}}}$)**: Complete IoU (CIoU) (Zheng et al., 2020) is employed, considering the distance between the estimated and labeled bounding box centers, the IoU, and aspect ratio, giving

$$\mathcal{L}_{\text{CIoU}}(\mathbf{BB}_{\text{est}}, \mathbf{BB}_{\text{lbl}}) = 1 - \text{IoU}(\mathbf{BB}_{\text{est}}, \mathbf{BB}_{\text{lbl}}) + \frac{(b_x - x_{\text{lbl}})^2 + (b_y - y_{\text{lbl}})^2}{c^2} + \alpha v, \tag{3.43}$$

where the consistency of aspect ratio is given by

$$v = \frac{4}{\pi^2}\left[\arctan\left(\frac{w_{\text{lbl}}}{h_{\text{lbl}}}\right) - \arctan\left(\frac{w_b}{h_b}\right)\right]^2, \tag{3.44}$$

c gives the diagonal of the smallest box enclosing $\mathbf{BB}_{\text{est}}$ and $\mathbf{BB}_{\text{lbl}}$ and α is a trade-off parameter defined as

$$\alpha = \frac{v}{(1 - \text{IoU}) + v}. \tag{3.45}$$

– **Class loss** ($\boldsymbol{\mathcal{L}_{\text{class}}}$): Binary-cross entropy loss is computed for each cell in the image grid and class,

$$\mathcal{L}_{\text{class}} = -\sum_{s=0}^{S\times S} \mathbb{1}_{sa}^{\text{object}} \sum_{\text{class}_i}^{\text{Str, Prt}} \{\mathrm{P}_{\text{lbl}}(\text{class}_i) \log[\mathrm{P}_{\text{est}}(\text{class}_i)] + [1-\mathrm{P}_{\text{lbl}}(\text{class}_i)] \log[1-\mathrm{P}_{\text{est}}(\text{class}_i)]\}, \tag{3.46}$$

where $\mathbb{1}_{sa}^{\text{object}}$ defines whether the object appears in the considered grid cell s (according to the label) and the a-th anchor box (of all A anchor boxes on the grid). Note that effectively $\mathrm{P}_{\text{lbl}}(\text{class}_i)$ can only be 0 or 1, as there is no ambiguity in the label.

– **Objectness loss** ($\boldsymbol{\mathcal{L}_{\mathrm{O}}}$): Equally binary-cross entropy loss is employed,

$$\mathcal{L}_O = -\sum_{s=0}^{S\times S}\sum_{a=0}^{A} \mathbb{1}_{sa}^{\text{object}} [O_{\text{lbl}}^s \log(O_{\text{est}}^s) + (1-O_{\text{lbl}}^s)\log(1-O_{\text{est}}^s)] - \lambda_{(\text{no object})} \sum_{s=0}^{S\times S}\sum_{a=0}^{A} \mathbb{1}_{sa}^{(\text{no object})} [O_{\text{lbl}}^s \log(O_{\text{est}}^s) + (1-O_{\text{lbl}}^s)\log(1-O_{\text{est}}^s)], \tag{3.47}$$

where also 'no object' components are included to balance positive and negative samples i.e., True Positives (TPs), False Positives (FPs), False Negatives (FNs), and True Negatives (TNs) (Redmon et al., 2016; Guo et al., 2021).

YOLO Evaluation Metrics

Object detection models such as YOLO utilize several accuracy metrics based on their estimated or missed bounding boxes. Thus vortices may be true positives, false positives, or false negatives with respect to the labeled bounding boxes. Two prominent metrics are,

$$\text{recall} := \frac{\mathrm{TP}}{\mathrm{TP}+\mathrm{FN}}, \qquad \text{precision} := \frac{\mathrm{TP}}{\mathrm{TP}+\mathrm{FP}}, \tag{3.48}$$

representing the rate of detected objects out of all labeled objects in a test dataset, and the rate of correctly detected objects (according to the labels) out of all detected objects, respectively (Lindholm et al., 2022, chap. 4). A YOLO-confidence threshold T_C and an IoU threshold $\mathrm{T}_{\mathrm{IoU}}$ are employed for defining true positive, false positive, or false negative vortices by YOLO.

Suitable threshold values are obtained with the mean Average Precision (mAP), which takes into account precision, recall, and the YOLO-confidence threshold. The mAP is determined for a particular IoU threshold and thus denoted mAP@$\mathrm{T}_{\mathrm{IoU}}$. It provides a first understanding of the YOLO accuracy. The mAP is the mean of the average precision of all classes, where the average precision is the area under the Precision-Recall Curve (PRC)

plotted in Fig. 3.26(a) for each class, giving an unified metric for recall and precision (Everingham et al., 2009). Here, $\mathrm{T_{IoU}} = 0.25$ is employed [see dashed line in Fig. 3.26(b)], given that both recall and precision feature very high values in that region. Along the PRC the YOLO-confidence threshold is varied as pictured with color. The optimum $\mathrm{T}_C = 0.25$ is marked with red in Fig. 3.26(a). However, for the wake vortex hazard recognition application, recall and precision should not be equally weighted. A low recall signifies a high number of false negatives, whereas a low precision signifies a high number of false positives. A conservative approach is chosen, favoring high recall rates over high precision rates. Potentially hazardous wake vortices are less likely to be missed, while the number of false alarms may be higher. Thus, $\mathrm{T}_C = 0.2$ is set throughout this thesis. Still, to reduce the number of false negatives the Euclidean distance (two-norm) between the bounding box centers of the label and YOLO-estimation,

$$D_C := \sqrt{\left(y_C^{\mathrm{est}} - y_C^{\mathrm{lbl}}\right)^2 + \left(z_C^{\mathrm{est}} - z_C^{\mathrm{lbl}}\right)^2}, \tag{3.49}$$

is computed afterwards. Only detections with $D_C < 42$ m are considered true positives, where the threshold emerges from the semi-diagonal of a bounding box with $w_{\mathrm{BB}} = 60$ m and $h_{\mathrm{BB}} = 60$ m (Wartha et al., 2025c). Additionally, if multiple vortices estimated by YOLO fulfill all above requirements, only the vortex estimate with the smallest D_C is considered a true positive.

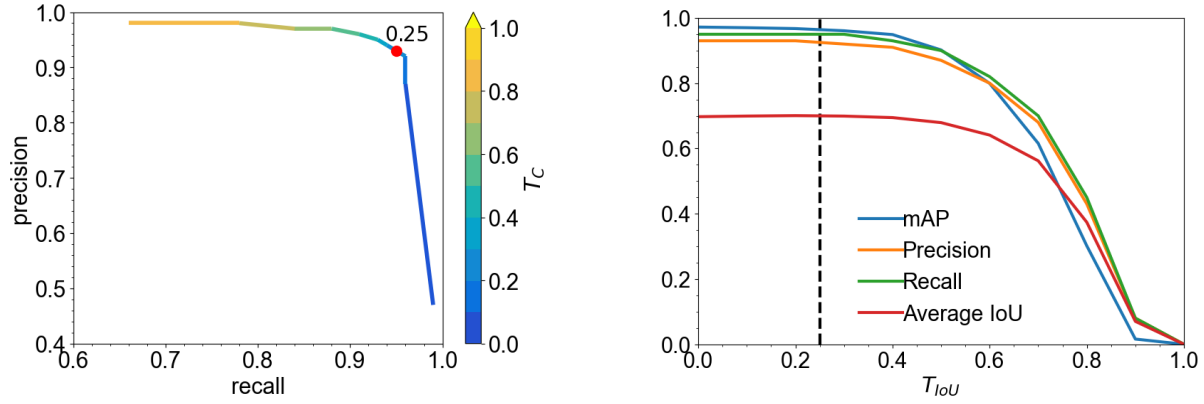

(a) Mean PRC of both classes for varying T_C at $\mathrm{T_{IoU}} = 0.25$. The optimum T_C is marked in red.

(b) Performance for varying $\mathrm{T_{IoU}}$ with the dashed line marking $\mathrm{T_{IoU}} = 0.25$.

Figure 3.26: Recall, precision, and mAP with respect to the IoU and YOLO-confidence thresholds. The ML pipeline case FM(FM) is considered. After Stephan et al. (2023).

Bochkovskiy (2021) recommended further settings for YOLOv4, including the learning rate and the mini-batch size of 64, which are adhered to throughout this thesis. The training of the YOLO models is conducted on the High-Performance-Data Analysis cluster KRATOS, employing an NVIDIA Tesla V100 GPU, for 235 epochs. An epoch signifies that each data instance belonging to the training subset has been considered. An exception is made when training with the LLS dataset family, in which case 101 epochs are

employed. Overfitting to the LLS training subset significantly deteriorates the accuracy on other dataset families (when testing on the LLS dataset family, the accuracy level remains comparable). Training times depend on the size of the training subset, for 13 618 lidar scans the training of 235 epochs takes approximately 20 hours, although cluster performance may vary depending on the parallel hardware utilization.

The YOLO-output for the pre-processed lidar scan from Fig. 3.22 right is given in Fig. 3.27. The classes and YOLO-confidence levels associated to the estimated bounding boxes are also provided. The center of the detected bounding box gives the position of the vortex center.

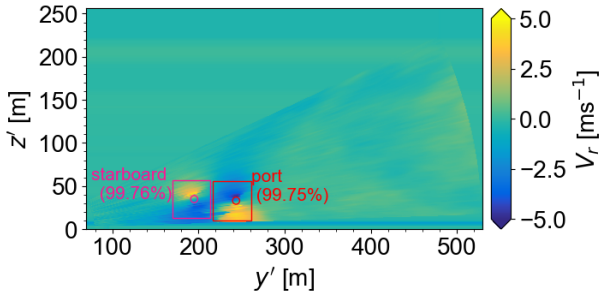

Figure 3.27: Example of YOLO-estimated bounding boxes with YOLO-confidence and class for the pre-processed lidar scan from Fig. 3.22 right. Pink color represents the starboard vortex, red color represents the port vortex. Circular symbols represent the labels provided by the RV method. (Wartha et al., 2025c)©

ML Pipeline Step 3: Processing of Detected Vortices

Bounding boxes of YOLO-detected vortices are not fixed in size, for further use in the ML pipeline these cut-outs of the LOS velocity field must be projected onto a grid of the same size. The chosen grid dimension is 64×64 pixels, where $dyy = dy_{\mathrm{im}}$ and $dzz = dz_{\mathrm{im}}$, spanning just above the initial vortex separation of the Airbus A380-800 ($b_0 = 62.7$ m, assuming an elliptical lift distribution) - the largest label bounding boxes of the field measurement dataset family. The grid employs a Cartesian coordinate system $[yy, zz]$. Obtained $\mathbf{BB}_{\mathrm{est}}$ are cut-out from their respective pre-processed RHI lidar scan. Bounding boxes of smaller dimension are padded on the edges with the mean LOS velocity of those contained in the bounding box, such that the bounding box is centered in the 64×64 grid. In the rare occasion when the bounding box exceeds the universal vortex grid, the outer edges are cropped accordingly. Note that vortex fields are clipped such that a LOS velocity of 20 m s^{-1} is the maximum (99 % of all field measurements are below this threshold), limiting LOS velocity outliers and avoiding unphysical gradients (Stietz, 2022).

Normalization of the LOS velocities is a second processing step. Processed vortices are normalized such that the vortex training subset has a mean LOS velocity of zero and a variance of unity, avoiding large LOS velocity differences and gradients, which may prevent ML models from converging (Chollet, 2018, chap. 4).

The above is performed for the training, validation, and test subsets. Note that also the training subset for the second ML step (II) consists of vortex bounding boxes previously estimated for the respective subset by YOLO. It ensures that training vortex fields are not placed perfectly central within the 64×64 grid and therefore the fourth step of the ML pipeline [ML step (II)], does not straightforwardly learn to place all vortices in the 64×64 grid center. Clearly, the regression CNNs are only trained with true positive wake vortices (both the label and YOLO have detected each wake vortex).

ML Pipeline Step 4: Regression Convolutional Neural Network

The purpose of this fourth pipeline step and second ML step (II) is to fine-tune the wake vortex position obtained from YOLO and determine the circulation of each wake vortex. The CNN architecture suggested by Wartha et al. (2022), and schematically described with Fig. 3.28, is employed for this task [5]. It has previously produced satisfactory results for processing wake vortices in RHI lidar scans. Only individual vortices from pipeline step three are evaluated, circumventing the main downside of Wartha et al. (2022) - detecting wake vortices. The CNN is based on four layer types: primarily convolutional layers ($k = 3$, stride of 2, zero-padding), maximum-pooling layers ($k = 2$, stride of 2) for dimensionality reduction (the output size is half of the input), a flatten layer for data transformation, and a final dense layer allowing a regression output. The combination of a convolutional layer followed by a maximum-pooling layer is referred to as a ConvPool block, of which four are employed. With increasing network depth and each ConvPool block, the number of kernels is doubled.

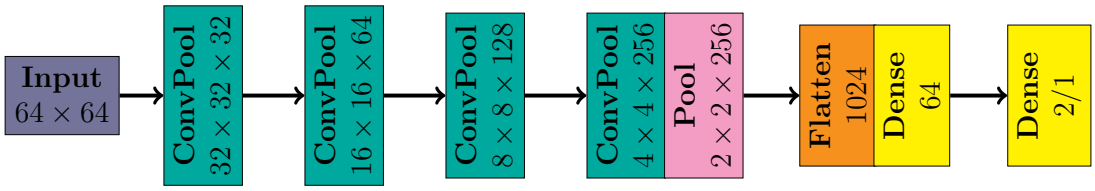

Figure 3.28: Regression CNN architecture for processing the vortex center position and vortex circulation for an individually cut-out vortex from a RHI lidar scan. Output dimensions are provided for each block/layer. ConvPool dimensions are a two dimensional grid (first two integers) and the number of feature maps (last integer). With permission of Stephan et al. (2023).

The ReLu activation function is chosen for all trainable layers, except the output dense layer. The loss function is the MSE. Adam (Kingma and Ba, 2014), an enhancement of the gradient descent method, is employed as the optimizer,

$$\mathbf{p}_t \leftarrow \mathbf{p}_{t-1} - \eta \frac{\hat{m}_t}{\sqrt{\hat{v}_t} + \epsilon}, \tag{3.50}$$

[5] The Python library Keras (Chollet et al., 2015) was employed for implementing the CNN.

where $\eta = 0.001$ and $\epsilon = 10^{-7}$ is a numerical stability factor,

$$\hat{v}_t = \frac{v_t}{1-\beta_2^t} \qquad \text{with} \qquad v_t = \beta_2 v_{t-1} + (1-\beta_2)\, g_t^2, \tag{3.51}$$

$$\hat{m}_t = \frac{m_t}{1-\beta_1^t} \qquad \text{with} \qquad m_t = \beta_1 m_{t-1} + (1-\beta_1)\, g_t, \tag{3.52}$$

provide an adaptive learning rate (β_1=0.9, $\beta_2 = 0.999$) using the first and second moments of the gradients,

$$g_t = \nabla_p \mathcal{L}_{\mathrm{MSE}}\left(\mathbf{p}_{t-1}\right), \tag{3.53}$$

to avoid local loss function minima. A mini-batch size of 128 is employed.

The output dimensions of the data are reflected in boxes of Fig. 3.28. For the ConvPool blocks the first two integers refer to the grid size, while the third integer gives the number of feature maps (kernels). Unlike Wartha et al. (2022), this thesis estimates the Cartesian vortex center position in one CNN. This approach is reflected by the output layer in Fig. 3.28, where the output dimension is two, giving (y'_C, z'_C), for the vortex center position CNN. For characterizing the circulation magnitude $|\Gamma_{5-15}|$, the CNN output dimension is one. The CNNs are thus built to characterize vortices of both circulation senses.

The training of the regression CNNs is conducted on KRATOS, employing a NVIDIA Tesla V100 GPU, until $\mathcal{L}_{\mathrm{MSE}}$ has not decreased for the validation subset in 30 epochs. On average training 23 000 vortices for 50 epochs takes approximately 0.5 hours.

The evaluation of the individual wake vortices detected by YOLO in Fig. 3.27 is illustrated with the respective position and circulation magnitude characterizations (crosses) in Fig. 3.29. The center of the pixel grid for each vortex can be considered the vortex center position estimation by YOLO, visibly the regression CNN fine-tunes that result with minor deviations from the bounding box center towards the labels (circles). Note that Wartha et al. (2022) previously presented explainability of this regression CNN architecture for wake vortex lidar scans [requested by the EASA guidelines (Soudain, 2024)]. They find the network to learn the dipole structure of vortices at different scales in the velocity field, which is predominantly driven by the ReLu activation function.

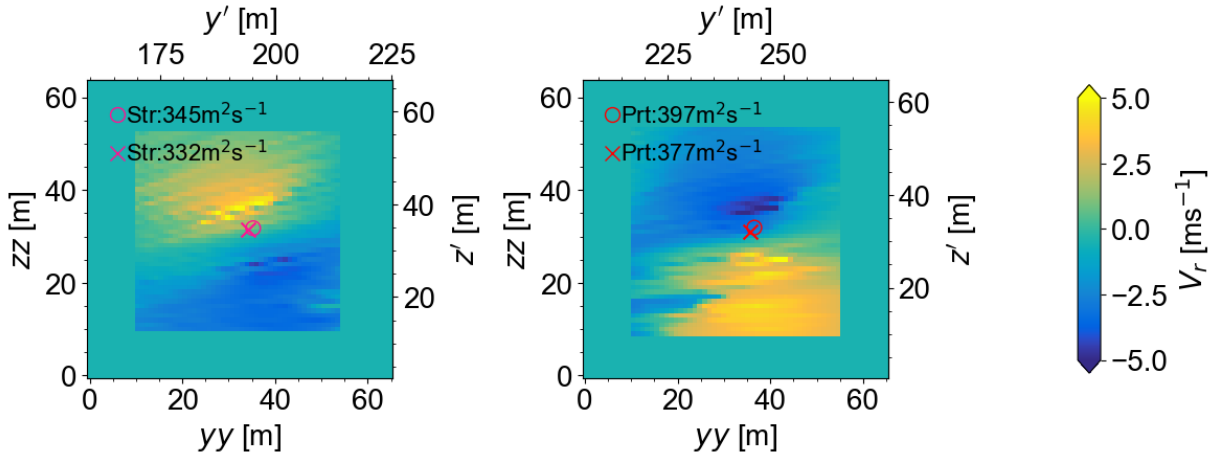

Figure 3.29: Example of the regression CNN characterizing the Str (left) and Prt (right) wake vortices previously detected by YOLO in Fig. 3.27 using the vortex position and circulation (legend). Circles represent the labels and crosses are CNN estimates. Adapted from Wartha et al. (2025c)©.

Chapter 4

Results

4.1 Numerical Wake Vortex Simulations

The purpose of this section is to present the obtained vortex evolutions from the numerical landing simulations for the Airbus A340 aircraft in high-lift configuration, describe the observable wake vortex phases and interactions, and finally detail the extent to which these simulations satisfy expected physical phenomena. The validity of the underlying LESs for all atmospheric conditions is demonstrated. These results build the foundation for the accepted ground truth, with respect to which wake vortex processing methods can be assessed and judged, as well as ML algorithms effectively trained. Wartha et al. (2025a) previously published great parts of this section.

4.1.1 Reproduction of Wake Vortex Evolution Phases

All four phases of wake vortex evolution in ground proximity, previously introduced for cruise in Section 2.1.1, are captured well by the RANS-LES landing simulations, with the first three displayed for the quiescent atmosphere case in Fig. 4.1. The near-field is marked by 'A' and showcases the highly complex wake generated by the aircraft. Several vortices detach from the geometry, with the expected dominance of the aircraft-generated flaptip and wingtip vortices in high-lift configuration evident in the extended near-field at 'B'. These two dominating vortex types merge in the far-field at 'C', also called the vortex phase, given that wake vortices are now fully rolled up. It can be seen that the flaptip vortices deliver the largest contribution to the rolled up primary wake vortex filaments.

The Airbus A340 and its generated wake vortices impose a high vorticity onto the ground (see Fig. 4.1), with increasing magnitude as the aircraft descends. The pressure increase in the wake-vortex-induced vorticity layer eventually leads to secondary vortices of opposite circulation sense to detach from the ground. As shown by the red arrow in Fig. 4.2, the positive streamwise vorticity counters the negative streamwise vorticity by the wake vortices. Therefore, a counter-rotating vortex pair is present on each aircraft side. These vortices approach one another, rapidly leading to their interaction (see Fig. 4.3). Therefore, wake vortices close to the ground experience accelerated decay.

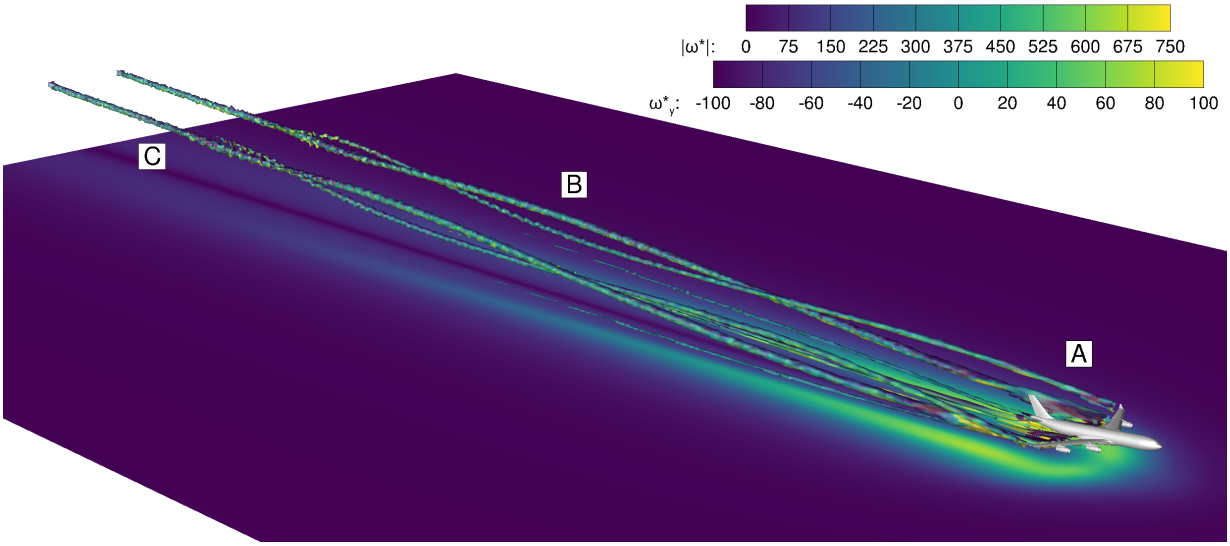

Figure 4.1: Airbus A340 landing at $t_L^* = -0.03$ and altitude $z^* = 0.05$ in quiescent atmosphere showcasing the complete wake vortex roll up to a counter-rotating pair. The iso-surface is given for $|\omega^*| = 300$ and colored by the spanwise vorticity ω_y^* to make vortex deformations apparent. The ground is colored by the overall vorticity magnitude $|\omega^*|$. (Wartha et al., 2025a)©

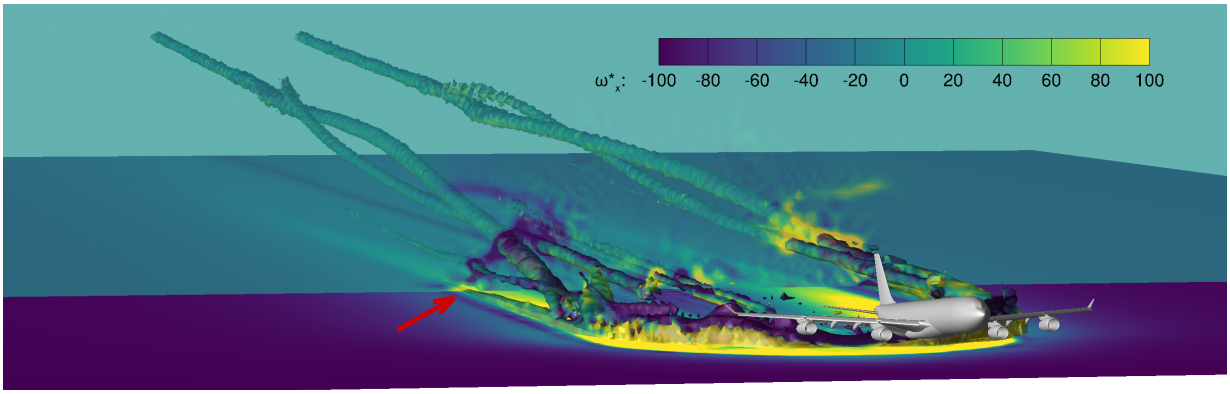

Figure 4.2: Airbus A340 landing showcasing detaching secondary vortices from the ground at $t_L^* = 0.02$ in quiescent atmosphere. The vertical slice is colored by the streamwise vorticity ω_x^*, all other settings are analogous to Fig. 4.1. (Wartha et al., 2025a)©

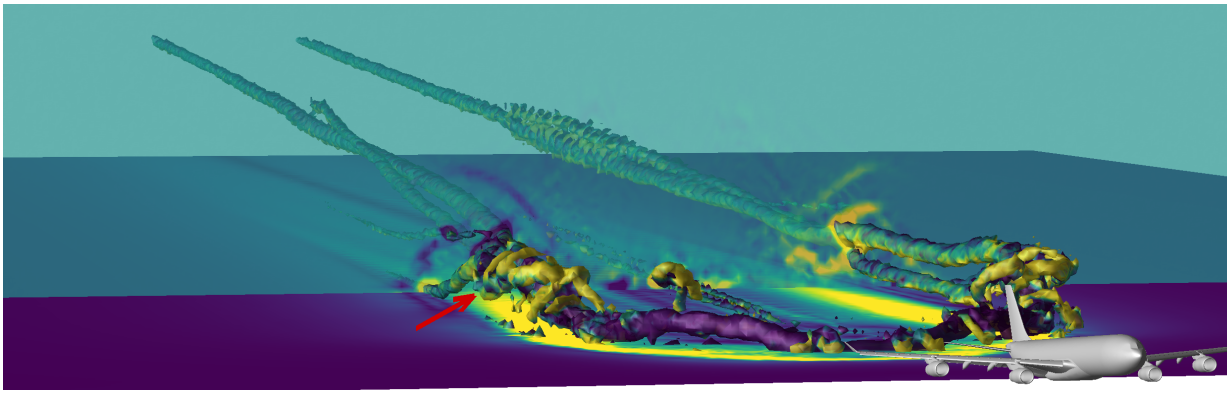

Figure 4.3: Airbus A340 landing with interacting secondary and wake vortices at $t_L^* = 0.05$ in quiescent atmosphere. Equal settings to Fig. 4.2. (Wartha et al., 2025a)©

4.1.2 Simulated Wake Vortex Trajectories

This section analyzes the wake vortex trajectories and strengths with respect to the flight direction x and the time t_L for four crosswind conditions using the LES tracking algorithm from Section 3.4.1. Spatial dimensions in the plots are limited by the LES domain.

The quiescent atmosphere vortex trajectories and strengths are plotted in Figs. 4.4 and 4.5 with ten cases each, five per vortex type [starboard (Str) and port (Prt)]. In Fig. 4.4 colors refer to different longitudinal positions in the LES domain (for example, 2Prt refers to the port vortex at $x^* = 2$). In Fig. 4.5 colors refer to different simulation times with respect to the aircraft touchdown (for example, 2Prt refers to the port vortex at $t_L^* = 2$). Trajectories from Stephan et al. (2014), which they show to strongly adhere to real flight data (see their Fig. 6), are neatly reproduced (see their Figs. 8-10). Thus, the validity of the herein performed setup adaptations (scaling and the relative computational domain size) and therefore the simulated vortex trajectories and strengths are confirmed for quiescent atmospheric conditions.

Prior to touchdown ($t_L^* < 0$) the wake vortex roll up process is captured, with the vortex circulation characterized significantly below Γ_0 in Fig. 4.4 bottom. Figure 4.5 captures the aircraft touchdown instant with the dark blue lines. At high vortex altitudes, the vortex circulation remains just below the expected Γ_0 magnitude (see Figure 4.5 bottom). Closer to the touchdown point ($x^* = 16.5$), with decreasing aircraft altitude, the LES-determined circulation steadily increases, even superseding Γ_0, which can be expected in immediate ground proximity (Stephan et al., 2014). The LES tracking algorithm is not applicable for characterizing wake vortices directly at or behind the touchdown point. The combination of near-field complexity and strong in-ground effects does not satisfy the algorithm's limiting conditions (minimal vortex tiling, curvature, etc.). High circulation fluctuations in Fig. 4.5 bottom underpin this argument. This behavior is linked to Helmholtz' vortex theorems, causing so-called end effects (Bao and Vollmers, 2005; Moet et al., 2005). These are triggered by a pressure difference within the center of the vortex filament and lead to axial flow, disturbances, and a rapid vortex filament breakdown (Stephan et al., 2014).

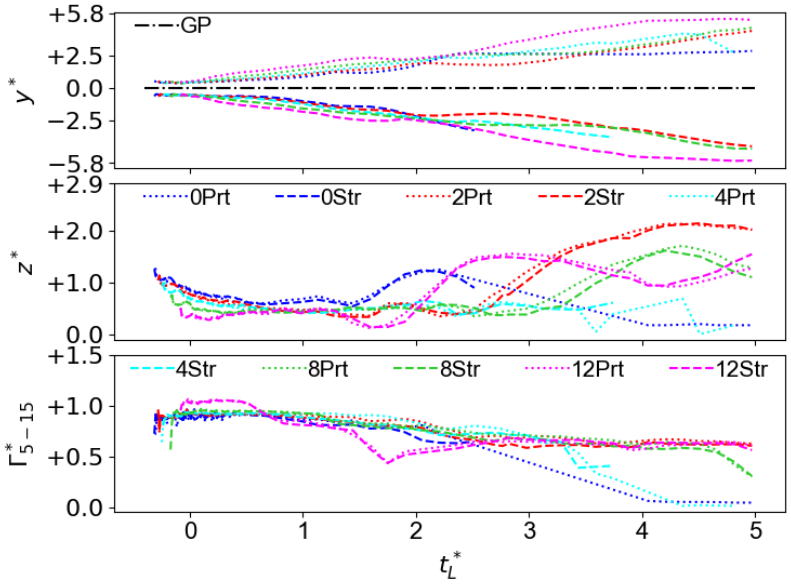

Figure 4.4: Temporal evolution of starboard (Str) and port (Prt) vortices, in terms of circulation Γ^*_{5-15}, lateral position y^*_C, and distance above the ground z^*_C, in quiescent atmosphere. Legend numbers refer to LES x^* positions. Plot limits represent the computational domain. The glide path (GP) of the aircraft is located at $y^* = 0$. Asynchronous termination of vortex tracking may arise when the tracking failed. (Wartha et al., 2025a)©

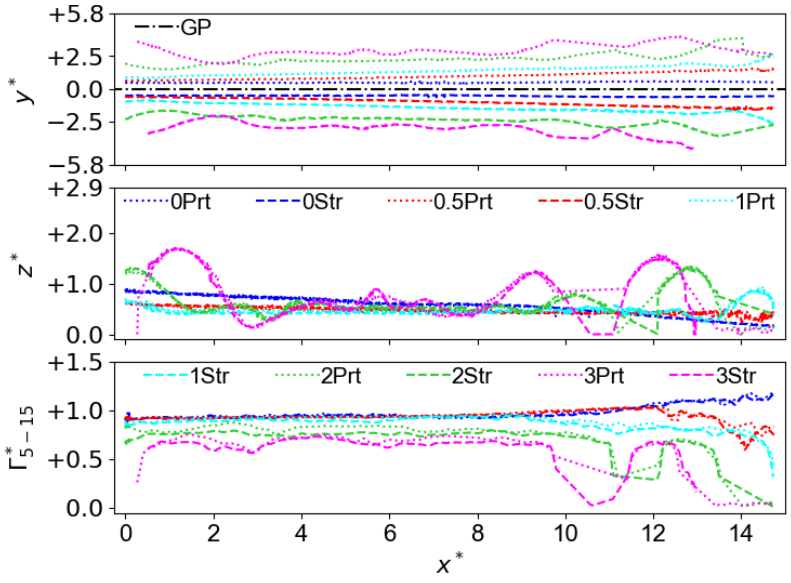

Figure 4.5: Longitudinal evolution of starboard (Str) and port (Prt) vortices, in terms of circulation Γ^*_{5-15}, lateral position y^*_C, and distance above the ground z^*_C, in quiescent atmosphere. Legend numbers refer to simulation times t^*_L. Plot limits represent the computational domain. The glide path (GP) of the aircraft is located at $y^* = 0$. Asynchronous termination of vortex tracking may arise when the tracking failed. (Wartha et al., 2025a) ©

Analyses and further developments in this thesis therefore do not consider data from the immediate touchdown region. For completeness, Stephan et al. (2014) observe a dramatic drop in circulation at touchdown, which they associate with the substantial reduction in lift production by the aircraft wings. Wake vortex trajectories in immediate vicinity to LES domain boundaries other than the ground (bottom) are also not considered further, given potentially unphysical behavior. Consider the pink case i.e., $x^* = 12$ in Fig. 4.4 top. At $t_L^* > 4$ the vortices are very close to the periodic side boundaries of the LES, subjecting them to their counterpart beyond the physical computational domain (due to periodic boundaries). As a result, a stable lateral position is kept by the vortices while mutually inducing upward velocity onto another and therefore rising in altitude (see Fig. 4.4 center).

At a fixed position in space, after wake vortex roll up, first a short period of high circulation follows, after which the magnitude decreases steadily with time. Merely vortices in immediate vicinity to the ground interact with secondary structures and rebound, which may also cause a temporary increase in vortex circulation as visible with Figs. 4.4 center and bottom. The wake vortex decay phases, discussed in Section 2.1.1 with Fig. 2.3, are only subtly discernible in Figs. 4.4 bottom and 4.5 bottom, presumably due to the flaptip and wingtip interaction, as well as the complex three-dimensional dynamics in ground proximity.

The vortex trajectories and strengths for the port crosswind cases are plotted in Figs. 4.6 and 4.7 (analogous legends to Figs. 4.4 and 4.5). The glide path (GP) (dash-dotted line) is no longer located at $y^* = 0$ but further upwind. In general, vortex evolutions exhibit similar trends as described for the quiescent atmosphere case. However, the prevailing crosswinds lead to asymmetric trajectories of the lee and luff wake vortices. Section 2.1.2 claimed that a $0.5w_0$ crosswind should bring the luff vortex to a lateral halt. With the crosswind magnitude specified at altitude b_0 (see Section 3.1.5) and the aircraft descending through the LES domain, negligible lateral vortex movement with a $0.5w_0$ crosswind is only expected at altitude b_0. However, the altitude plot of Fig. 4.6(a) shows most wake vortices located below b_0 (except rebounding vortices). The non-slip conditioned ground in the LES and the resulting logarithmic boundary layer, subject most wake vortices to lower crosswind magnitudes. Furthermore, a low wake vortex altitude leads to a high mutual velocity induction with a strong vorticity layer establishing at the ground surface. As a result, the majority of luff vortices experience unbalanced lateral velocity inductions by the crosswind and vorticity layer, causing lateral transport. On the other hand, the lee vortices do follow the expected behavior, their lateral transport is approximately twice as strong compared to the quiescent case (cf. Fig. 4.4). In Fig. 4.6 dark blue color ($x^* = 0$) represents the vortices generated at the highest altitude and close to $z^* = 1$. For example, Fig. 4.6(a) center shows the luff vortex to hold its lateral position until $t_L^* \approx 2.5$, after which additional effects lead to a slow outward transport. Independently of the crosswind magnitude, the luff secondary vortex, detaching from the boundary layer, must be weaker than the lee secondary vortex as a result of the crosswind-induced shear layer (see Fig. 2.5).

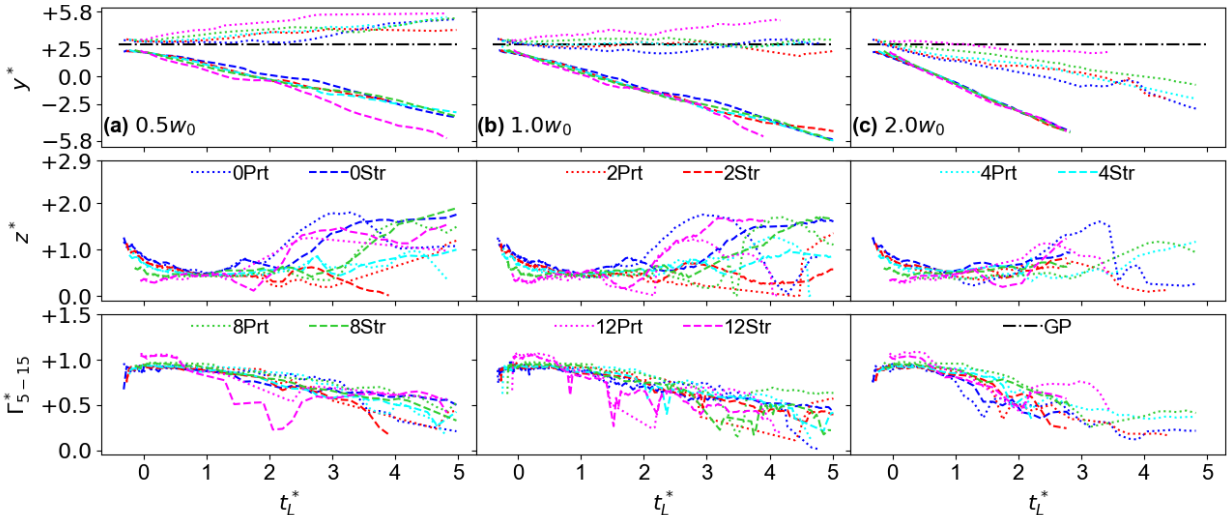

Figure 4.6: Temporal evolution of starboard (Str) and port (Prt) vortices, in terms of circulation Γ^*_{5-15}, lateral position y^*_C, and distance above the ground z^*_C, under various port crosswind strengths (one per column). Legend numbers refer to LES x^* positions. Plot limits represent the computational domain. The glide path (GP) of the aircraft is located at $y^* = 2.8$. Asynchronous termination of vortex tracking may arise when the tracking failed. (Wartha et al., 2025a)©

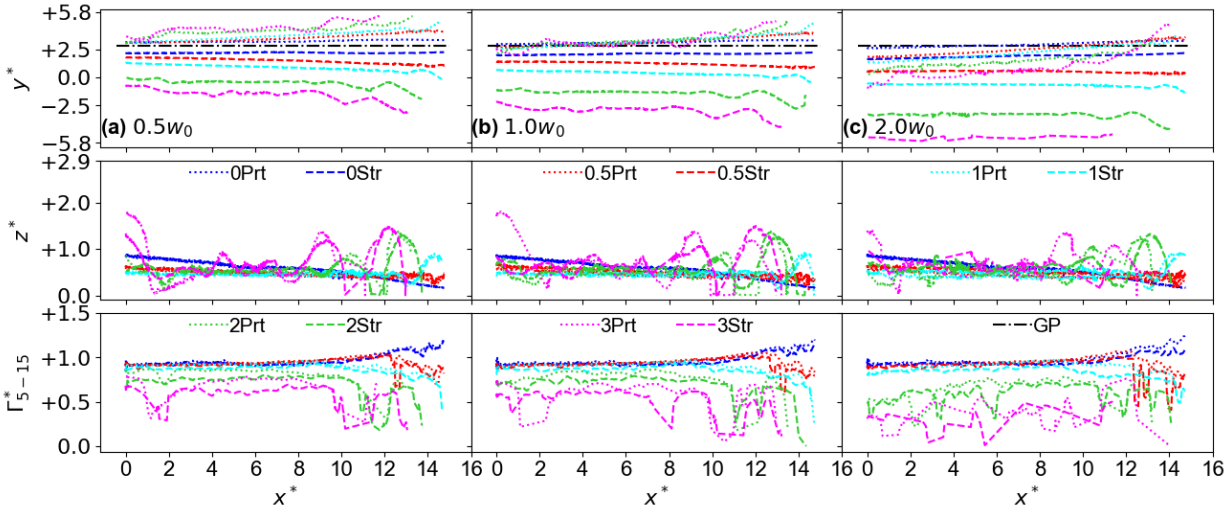

Figure 4.7: Longitudinal evolution of starboard (Str) and port (Prt) vortices, in terms of circulation Γ^*_{5-15}, lateral position y^*_C, and distance above the ground z^*_C. Legend numbers refer to simulation times t^*_L. Plot limits represent the computational domain. The glide path (GP) of the aircraft is located at $y^* = 2.8$. Asynchronous termination of vortex tracking may arise when the tracking failed. (Wartha et al., 2025a)©

This asymmetrical effect is depicted in Fig. 4.8 for a $0.5w_0$ port crosswind, where the aircraft-wake-induced vorticity magnitude is visualized on the ground. In this case, the port (Prt) and starboard (Str) vortices represent the luff and lee vortices, respectively. In the aircraft near-field (right of the boxes) no particular asymmetry is visible in the vorticity layer. At this early stage of vorticity generation, the crosswind shear and secondary vortex structure interaction is not yet fully developed. However, in the extended near-field (the left half of the boxes) the starboard side constitutes higher vorticity content in comparison to the port side. Both a more significant inner vorticity street as well as a stronger and broader outward vorticity street are observed.

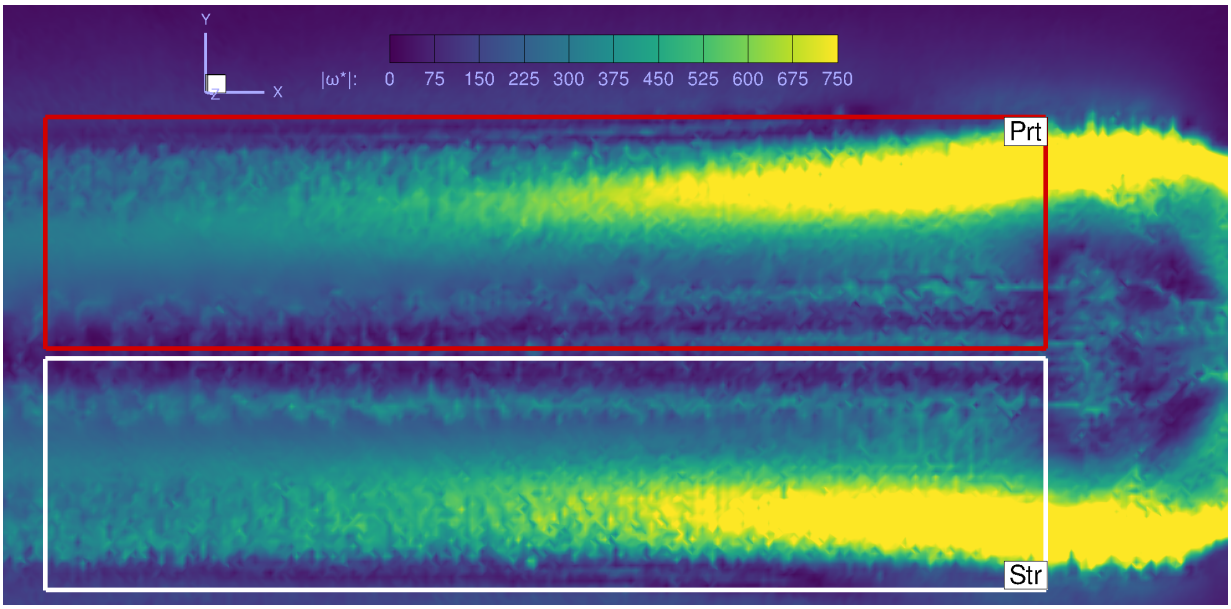

Figure 4.8: Airbus A340 landing at $t_L^* = 0.06$ under a turbulent port crosswind strength of $0.5w_0$ showcasing the asymmetric vorticity layer on the ground as a result of crosswind. The ground is colored by the overall vorticity magnitude $|\omega^*|$. The aircraft flies from the left to the right of the figure.

As a result, the opposite must be true for the wake vortices. Indeed, Figs. 4.6(a) bottom and 4.7(a) bottom confirm the luff wake vortex (here the port vortex) to constitute a higher circulation in most regions. Holzäpfel et al. (2016b) previously studied wake vortex trajectories close to the ground and under the influence of crosswinds. The above trends strongly agree with their findings, although they achieved less noisy vortex tracking by initializing a counter-rotating Lamb-Oseen vortex pair.

Having established that most simulated vortices are subject to crosswind magnitudes below the set strength at altitude b_0, it is unsurprising that the luff vortex-induced lateral propagation speed is matched more frequently with a $1.0w_0$ crosswind [see Figs. 4.6(b) top and 4.7(b) top]. Only towards $t_L^* = 2$ and spatially close to the touchdown point, discernible lateral movement of the luff vortex is visible. Figure 4.9 visualizes the $1.0w_0$ crosswind case, with the logarithmic turbulent boundary layer identifiable using the vertical slice (colored

by the spanwise velocity v). The luff vortex remains laterally stationary. Note that the vortex altitude development is not strongly dependent on the crosswind magnitude until immediate ground vicinity.

With increasing turbulent crosswind magnitude, the tracking of wake vortices proves substantially more challenging. In Fig. 4.6(c) top the $2.0w_0$ crosswind shows vortices to be transported laterally by a distance well over b_0 from the glide path within less than duration t_0 (except in explicit ground vicinity). Gurke and Lafferton (1997); Holzäpfel et al. (2021) have established a 50 m lateral transport as a threshold value beyond which vortices are no longer relevant for hazard analysis. With $b_0 \approx 50$ m for the simulated Airbus A340, tracking of these wake vortices is no longer necessary. In addition to increased lateral transport, increasing the turbulent crosswind magnitude also accelerates the strength reduction of the wake vortices. Figure 4.7 bottom confirms earlier loss of vortex coherency and thus accelerated vortex decay as a result of increased turbulence in the atmosphere with increasing crosswind strength (left to right in the figure).

4.2 LES Lidar Simulations

The purpose of this section is to present and discuss features of the simulated lidar scans with the aim of verifying their appropriateness. First, spatial and temporal factors inherent to lidar measurements are discussed using LLS scans (both lidar simulator types share the same LOS velocity retrieval aspects from the LES). Second, the two LES lidar simulator models, LLS and $\mathrm{LLS_n}$, are compared and their varying validity discussed. Significant parts of this section have previously been presented by Wartha et al. (2025a,c).

4.2.1 Spatial Factors

The impact of spatial averaging i.e., the impact of the RWF, is investigated in Fig. 4.10, where LLS scans (RWF, left) are compared to idealistic point measurements from the LES (no RWF, right) using velocity contour plots for four challenging scenarios, (a) to (d). Point measurements do not deploy a range gate, but directly obtain the LOS velocity at a single point employing Eq. (3.14) and can thus be considered an exact representation of the LES. Note that symbols within the lidar scans are discussed in Section 4.3.1. Point measurement scans contain significantly more detail and visible secondary vortex structures in comparison to LLS scans. Differentiating between wingtip and flaptip vortices is not straightforward in either representation, for example Fig. 4.10(a) right does contain vortices beyond a single counter-rotating pair in the center of the main wake vortex pair. On the other hand, LLS scans regard co-rotating vortex structures as a single vortex even prior to their actual merging. This behavior is common to lidar scans, filtering-out of high velocities and steep velocity gradients. Indeed, the contour plots of Fig. 4.10 right feature at least one further velocity layer. Additionally, the spatial averaging artificially increases the vortex core size. Adulterated LOS velocities and vortex cores may affect the characterization of the wake vortices by lidar processing algorithms (see Fig. 4.19 in Section 4.3.1).

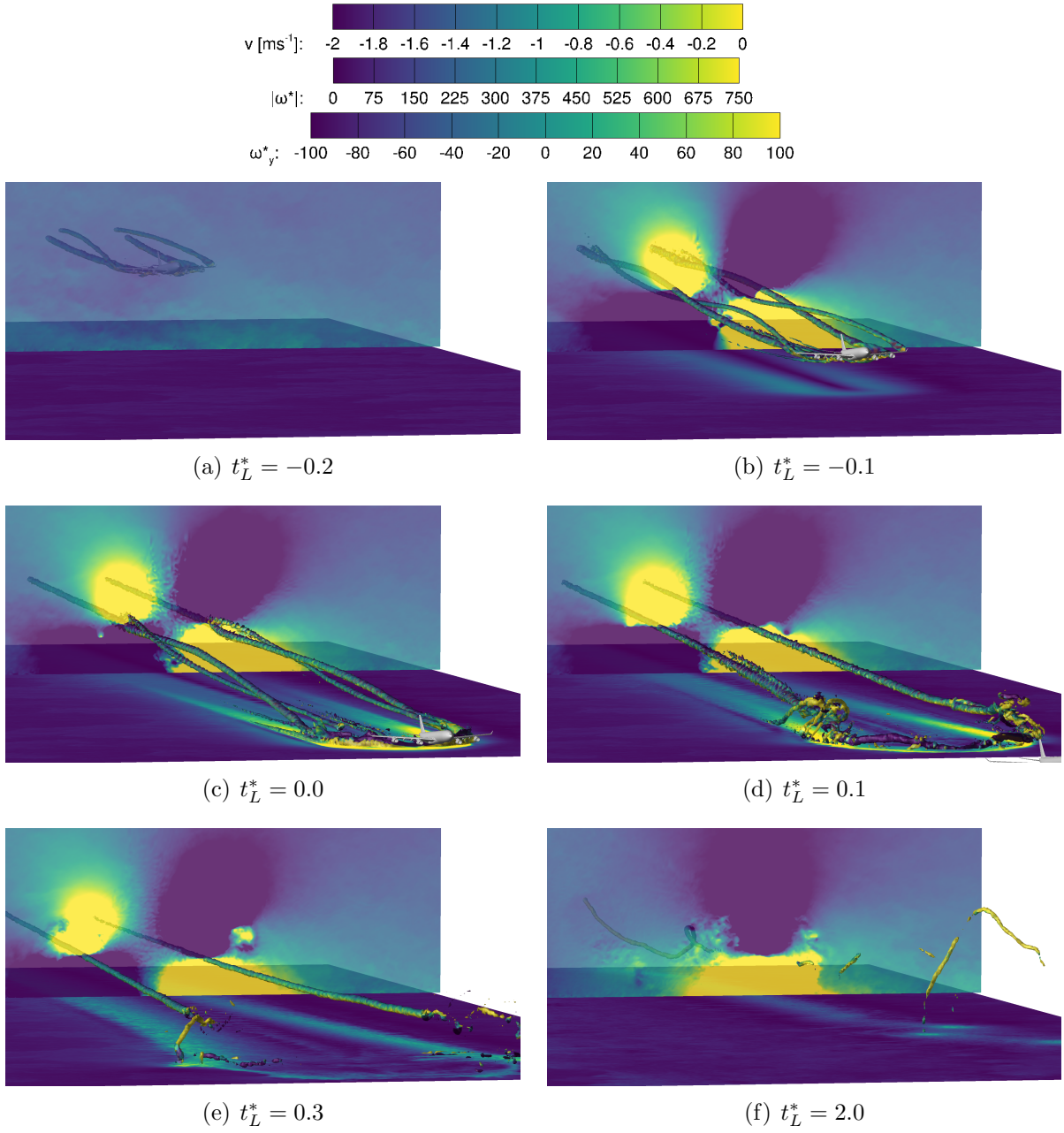

(a) $t_L^* = -0.2$

(b) $t_L^* = -0.1$

(c) $t_L^* = 0.0$

(d) $t_L^* = 0.1$

(e) $t_L^* = 0.3$

(f) $t_L^* = 2.0$

Figure 4.9: Airbus A340 landing simulation with a port $1.0w_0$ crosswind showcasing the complex vortex evolution in time. The iso-surface is given for $|\omega^*| = 300$ and colored by the spanwise vorticity ω_y^* to make vortex deformations apparent. The ground is colored by the overall vorticity magnitude $|\omega^*|$ and the vertical slice is colored by the spanwise velocity v, showcasing the logarithmic crosswind profile.

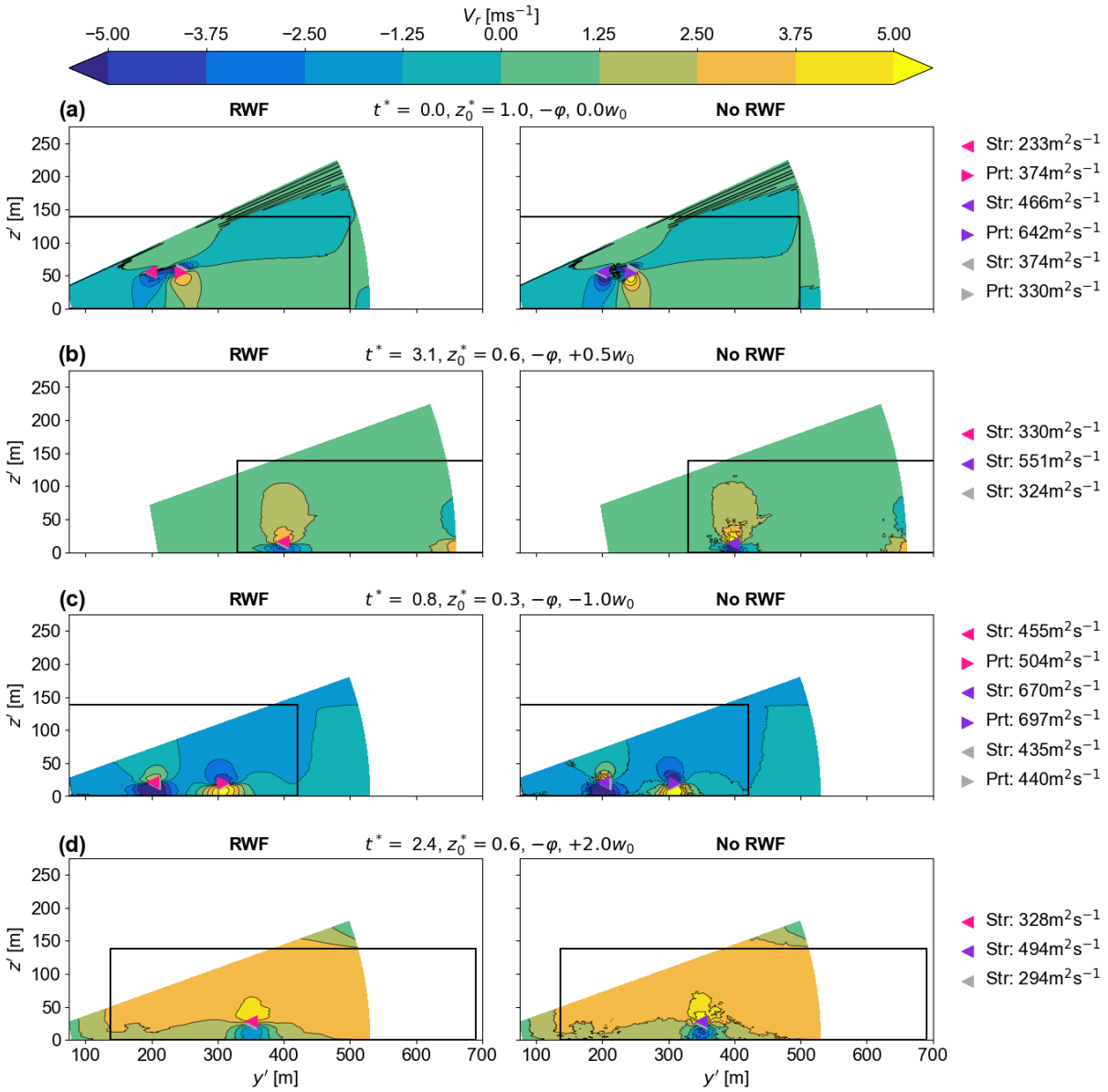

Figure 4.10: Example RV-method-characterized LLS scans in challenging scenarios with (left) and without (right) RWF applied for various crosswinds ($\pm\chi \times w_0$) and directions. Wake vortex position (symbols) and (see legend) and strength characterizations of the simulation truth and the RV method are given. Gray symbols represent the simulation truth, which may be overshadowed by the pink and violet symbols which arise from the RV method with and without the RWF, respectively. The wake vortex age t^*, the aircraft altitude at passage of the lidar measurement plane z_0^*, the scan sense ($+\varphi$ or $-\varphi$), and the crosswind $\chi \times w_0$ are given for each case. The black rectangle represents the LES computational domain. Adapted from Wartha et al. (2025a)©.

Modeling of Wall Effects

All vortices in Fig. 4.10 feature comparably high LOS velocities in their lower half with respect to their upper half. This observation is directly related to the wall proximity (the modeled ground) discussed in Section 2.1.2, the asymmetric velocity distribution of a vortex in wall proximity is caused by the imaginary image vortices below the wall (bottom domain boundary). The image vortices of opposite vorticity model the secondary vorticity induced onto the ground by the descending wake vortices and interact with the flow field. Their presence is further confirmed by vertical velocity contours of the velocity layers close to the ground, where otherwise a non-slip boundary condition would cause a decrease of velocity. Image vortices attenuate opposing velocities inside the computational domain, while superposing velocities of the same sense. With both wake vortex halfs (bottom and top) strictly subject to solely the top half of the image vortex, the wake-vortex-half closer to the ground is strengthened while the upper wake-vortex-half is attenuated in comparison to a vortex flowing in free space.

Modeling of the RHI Scan Geometry

The geometry of RHI scans limits the flow field captured by lidars. Due to convective processes in the atmosphere, it is not always possible to capture the complete aircraft wake - vortices may advect out of the measurement window. For instance, Fig. 4.10(b) includes only parts of the port wake vortex, and Fig. 4.10(c) only includes a single wake vortex. Particularly the former case may cause processing algorithms to adulterate the characteristics of a wake vortex, only part of the port wake vortex is visible in the scans.

Validity of the LLS Padding

A restraint of LLS and LLS_n scans concerns the employed LOS velocity padding beyond the LES domain. In Fig. 4.10 all RHI scans are plotted with respect to the lidar position in the LES domain (black rectangles). Note that the glide path position also changes with respect to the atmospheric condition (see Section 3.1.4). LOS velocity padding typically operates as desired, for example in Fig. 4.10(b) the flow field is extended without introducing unphysical LOS velocity gradients. In other cases, for instance Figs. 4.10(a) and (c), scans are subject to excessive gradient extensions from the LES boundary. Occasionally, unphysical LOS velocity gradients may emerge in the Cartesian coordinate system, such as in Fig. 4.10(d), where the implemented weighting factor forces LOS velocities to zero at great distances from the LES boundary. It can be concluded that the employed padding is most suitable for a quiescent atmosphere in comparison to a crosswind case. Minimal impact on the wake vortex characterization is expected, as vortices are typically not located in the vicinity of the padded scan areas.

4.2.2 Temporal Factors

Lidar scans of RHI format consist of multiple LOSs. The scanning rate determines the time delay between LOSs. Herein, lidar scans may contain temporal differences of up to 7 s between φ_- and φ_+. On the one hand, this may cause rapid phenomena to be only partially captured, for instance see Fig. 4.10(a) where wake vortices are generated during the capture of the RHI lidar scan, and thus only one half of the vortex structures is visible. On the other hand, when wake vortices are in transport, particularly in the vertical direction, their structure may be stretched or compressed in comparison to the actual instantaneous flow field. For instance, a downward moving wake vortex recorded by a lidar with scanning pattern $+\varphi$ will appear compressed. Thus, approximately similar velocities of the vortex are less spread out. The opposite occurs if a lidar with scanning pattern $-\varphi$ meets descending wake vortices. For a specific distance along the LOS from the lidar, the rate of change in the vertical direction due to the scanning rate ω_S is in the same order of magnitude as the initial vortex descend speed w_0. Therefore, this adulteration effect should not be neglected. Indeed, Smalikho (2019) previously showed that lidar processing algorithms may underestimate the circulation of visually compressed wake vortices and overestimate the circulation of visually stretched wake vortices by up to 8 % and 3 % during initial vortex descent, respectively.

4.2.3 Comparison of the Lidar Simulator Types: LLS and $\mathrm{LLS_n}$

Figure 4.11 compares the LES lidar simulator types, LLS and $\mathrm{LLS_n}$, using a zoomed-in representation of a RHI scan. This comparison has previously been discussed by Wartha et al. (2025c). Both LLS types capture the low-pass filter characteristic of lidar instruments well. As expected, the LLS scan (Fig. 4.11 left) represents an idealized scenario, with irregularities observed in field measurement not represented (cf. Fig. 3.14). Instead, the $\mathrm{LLS_n}$ scan (Fig. 4.11 right) produces such irregularities, including:

- LOS streaks from subtracting the same background noise S_N for each range gate along a particular LOS [see Eq. (2.38)].
- Point artifacts from aerosol noise, for instance see $(y', z') = (195\ \mathrm{m}, 20\ \mathrm{m})$.

In comparison to the field measurements, the LES and thus both simulator types lack large-scale turbulence structures occurring in the atmospheric background, which cannot be straightforwardly combined with simulating a turbulent crosswind (generating small-scale turbulence structures).

The main distinctive feature of $\mathrm{LLS_n}$ scans in comparison to LLS scans, is the modeling of individual laser pulses. Figure 4.12 depicts the necessity of multiple pulses when determining the LOS velocity from a Doppler spectrum when modeling pseudo-random background noise and aerosol noise. For the case of a single pulse ($N_a = 1$) the echo signal is too weak in comparison to the noise present in the backscatter signal. The pulses used for accumulation increase in powers of 10 throughout Fig. 4.12, each increase in N_a unveils further flow field information, as pseudo-random signal contributions mutually neutralize.

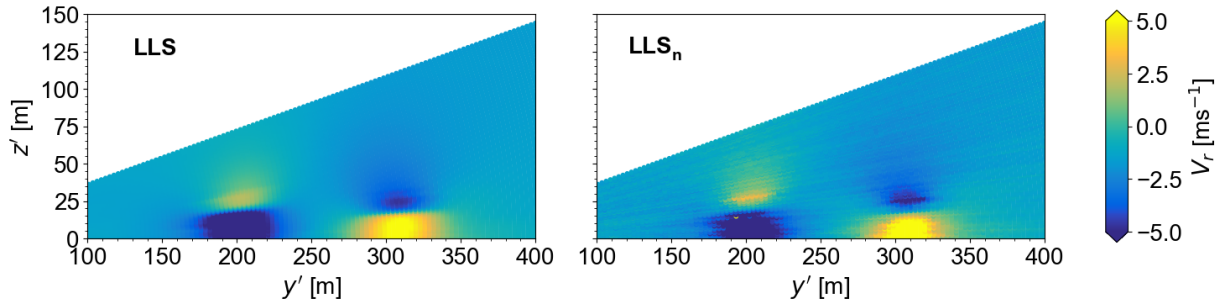

Figure 4.11: Zoomed in example LLS (left) and LLS$_n$ (right) RHI lidar scans at $t^* = 0.5$, with $-\varphi$ scanning sense, and a prevailing port crosswind $-w_0$. Adapted from Wartha et al. (2025c)©.

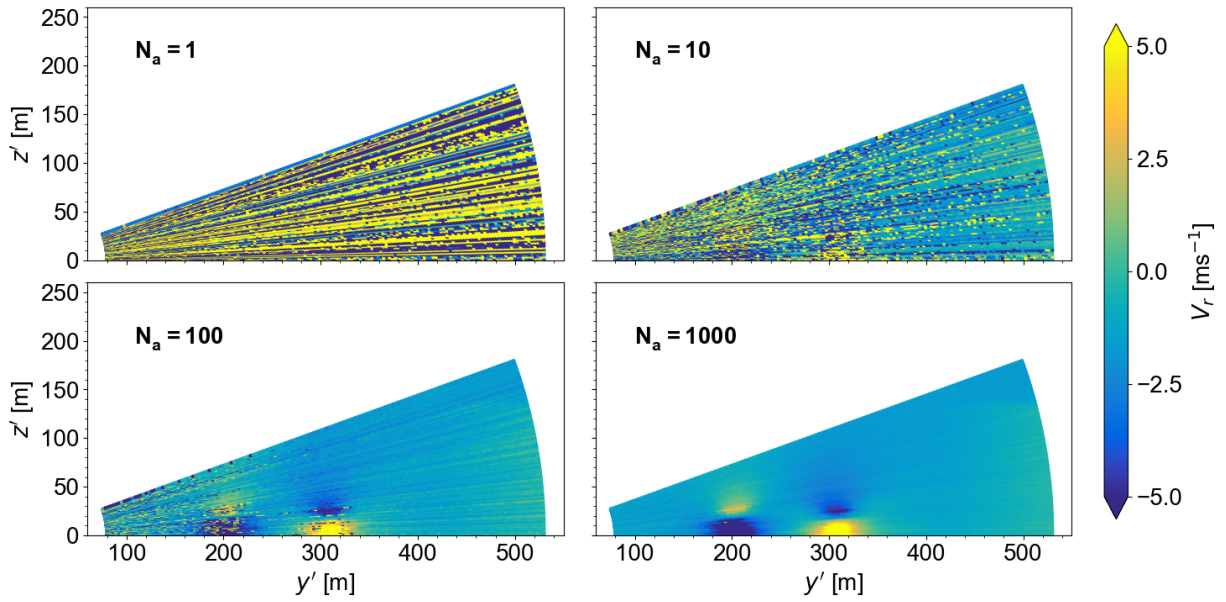

Figure 4.12: Example LLS$_n$ RHI lidar scan (same scenario as Fig. 4.11) for varying pulse accumulation count N_a. Adapted from Wartha et al. (2025c)©.

The LLS allows determining upper accuracy limits of lidar processing algorithms, without dependence on the SNR or other atmospheric/instrument irregularities. Instead, the LLS$_n$ enables precise modeling of real lidar measurements, necessary for data-driven lidar processing algorithms, as they include irregularities observed in field measurements.

4.3 Accuracy of Lidar Processing Algorithms

This part of the thesis aims to answer the first research question, as well as partly the second research question posed in Section 1.3, how reliable and accurate are estimates of the wake vortex position and circulation by lidar processing algorithms. A particular focus is put on the physical RV method (see Section 3.4.2), given its deployment for numerous recent measurement campaigns, including the 2019 Vienna Airport campaign, as well as the novel ML pipeline (see Section 3.4.3). In both cases the LLS dataset family is employed for the accuracy assessment, allowing a comparison to the LES ground truth (using the LES tracking algorithm from Section 3.4.1) and setting an accuracy limit given the assumption of SNR >> 1 for the LLS scans. Note that the datasets of the RV method and ML pipeline analysis are not identical. While the underlying dataset family in both cases is LLS, the partly manual processing of the RV method requires a reduction in scan quantity. Nonetheless, both accuracy evaluations are comparable, given that a statistically relevant quantity and scan diversity is ensured in both cases (for instance atmospheric conditions). The following sections largely cover content previously published by Wartha et al. (2025a,c).

The wake vortex detection is evaluated based on the recall and precision rates, using estimated and missed vortices. For the characterization error, values of the spherical coordinates to a vortex center $\mathrm{E}_{\varphi_C} = \varphi_C^{\mathrm{est}} - \varphi_C^{\mathrm{lbl}}$ and $\mathrm{E}_{R_C} = R_C^{\mathrm{est}} - R_C^{\mathrm{lbl}}$, as well as the Euclidean distance between the estimated and labeled vortex centers D_C [see Eq. (3.49)] and the vortex circulation $\mathrm{E}_{\Gamma_{5-15}} = \Gamma_{5-15}^{\mathrm{est}} - \Gamma_{5-15}^{\mathrm{lbl}}$ are provided.

4.3.1 Radial Velocity Method

The error bounds and further algorithm characteristics are evaluated using a representative subset of all generated LLS scans given in Table 4.1. In total 2142 LLS scans are processed with the RV method. While the number of scans represents all scans attempted to evaluate, Table 4.1 only includes vortices detected both by the RV method and the ground truth. Recall and precision have been defined in Section 3.4.3 using Eq. (3.48) for ML, however these metrics can equally be employed for physical lidar processing algorithms. The recall and precision rates of the RV method are found to be 98.2 % and 99.7 %, respectively. Although the RV method is not split into detection and characterization steps, in some rare cases the RV method entirely fails to characterize wake vortices present in the RHI scan, for example when the vortex core is located too close to a scan boundary, or the vortex coherency is minimal - this can be considered equivalent to an undetected wake vortex. Low vortex coherency is a particular concern for the RV method, as it attempts to fit ideal Burnham-Hallock vortices to the velocity fields. When strong turbulent atmospheric conditions prevail, as for the $2.0w_0$ crosswind case, vortices rapidly break down and lose their coherency quicker than vortices subject to calm atmospheric conditions. Therefore, less wake vortices for the $2.0w_0$ case are analyzed.

Table 4.1: Dataset for assessing the RV method split by wind strength and wake vortex type. Crosswind direction is not considered. (Wartha et al., 2025a)©

Crosswind	No. of port vortices	No. of starboard vortices	No. of LLS scans
$0.0w_0$	528	427	531
$0.5w_0$	510	447	557
$1.0w_0$	543	503	676
$2.0w_0$	298	268	378
Total	1879	1645	2142

Obtained RV method error bounds are documented in Table 4.2. Median (med) error bounds for both the spherical coordinates to a vortex center $\mathrm{E}_{\varphi_C}^{\mathrm{med}}$ and $\mathrm{E}_{R_C}^{\mathrm{med}}$, as well as the normalized two-norm for the Cartesian coordinates to the vortex center $D_C^{\mathrm{med},*}$, and the vortex circulation $\mathrm{E}_{\Gamma_{5-15}^*}^{\mathrm{med}}$ are given, with positive and negative values indicating an over- and underestimation of the RV method with respect to the ground truth, respectively (the LES tracking algorithm). Furthermore, the standard deviation provides the error spread. The position characterization accuracy is also provided for the spherical coordinate system, as the RV method directly computes these. Furthermore, they enable a comparison to theoretical and numerical accuracy estimates by Smalikho et al. (2015); Smalikho (2019).

Table 4.2: RV method characterization accuracy analysis including individual error bounds for starboard and port vortices. The medians (med) of the vortex position characterization errors $\mathrm{E}_{R_C}^{\mathrm{med}}$ and $\mathrm{E}_{\varphi_C}^{\mathrm{med}}$ (in the spherical coordinate system), the normalized circulation characterization error $\mathrm{E}_{\Gamma_{5-15}^*}^{\mathrm{med}}$, and the normalized position two-norm $D_C^{\mathrm{med},*}$ (in the Cartesian coordinate system) are provided. $+/-$ represent a systematic over- and underestimation by the RV method in comparison to the ground truth, respectively. The error spread is given by the standard deviation. (Wartha et al., 2025a)©

Vortex type	$\mathrm{E}_{\varphi_C}^{\mathrm{med}}$ [deg]	$\mathrm{E}_{R_C}^{\mathrm{med}}$ [m]	$D_C^{\mathrm{med},*}$ [-]	$\mathrm{E}_{\Gamma_{5-15}^*}^{\mathrm{med}}$ [-]
Starboard	$+0.47 \pm 0.54$	-0.71 ± 3.95	0.06 ± 0.06	$+0.05 \pm 0.08$
Port	$+0.36 \pm 0.37$	$+0.06 \pm 4.57$	0.07 ± 0.06	$+0.04 \pm 0.07$
Total	$+0.41 \pm 0.46$	-0.31 ± 4.32	0.06 ± 0.06	$+0.04 \pm 0.08$

There is no universally accepted wake vortex circulation below which a wake vortex can be disregarded in glide path hazard analysis, particularly given that the mass and size of the aircraft at risk are vital in the hazard analysis as well. Under all circumstances a wake vortex of strength $\Gamma_{5-15} < 25$ m^2 s^{-1} ($\Gamma_{5-15}^* < 0.06$) can be considered safe for fixed-wing follower aircraft. The vortex position two-norm ($D_C^{\mathrm{med}} \approx 2.8$ m for both vortex types) and the circulation characterization error ($\mathrm{E}_{\Gamma_{5-15}}^{\mathrm{med}} \approx +19.2$ m^2 s^{-1} for both vortex types) are small. No significant difference is evident for the two vortex types (starboard or port) either.

The vortex position characterization error is below the lidar measurement accuracy of $dR = 3$ m and for the circulation characterization accuracy, the error is below the 25 m^2 s^{-1} threshold. However, the error spread reveals a high uncertainty in these values, some vortex characterization errors may substantially exceed or subceed the median errors from Table 4.2. As a result, the RV method circulation characterization accuracy for both vortex types should be quoted as -13.9 m^2 s^{-1} to $+52.3$ m^2 s^{-1}, where the median error is 19.2 m^2 s^{-1} and the bounds arise from addition and subtraction of the respective standard deviation (33.1 m^2 s^{-1}). An analogous error bound can be constructed for the position characterization or a particular vortex type, the standard deviation elevates the precision to nearly twice the measurement accuracy (5.7 m).

Both the vortex position and circulation error spreads are provided in Fig. 4.13 (both vortex rotation senses), with the latter following a Gaussian distribution, while the former is a positively skewed distribution, distinguishing mean and median. Additionally, Fig. 4.14 reveals that the systematic circulation error prevails across the entire magnitude range, the RV method on average overestimates the vortex circulation. Symbols represent individual wake vortices, with the spread in characterization accuracy increasing with weaker wake vortices - a direct and expected result of wake vortex coherency loss during their decay.

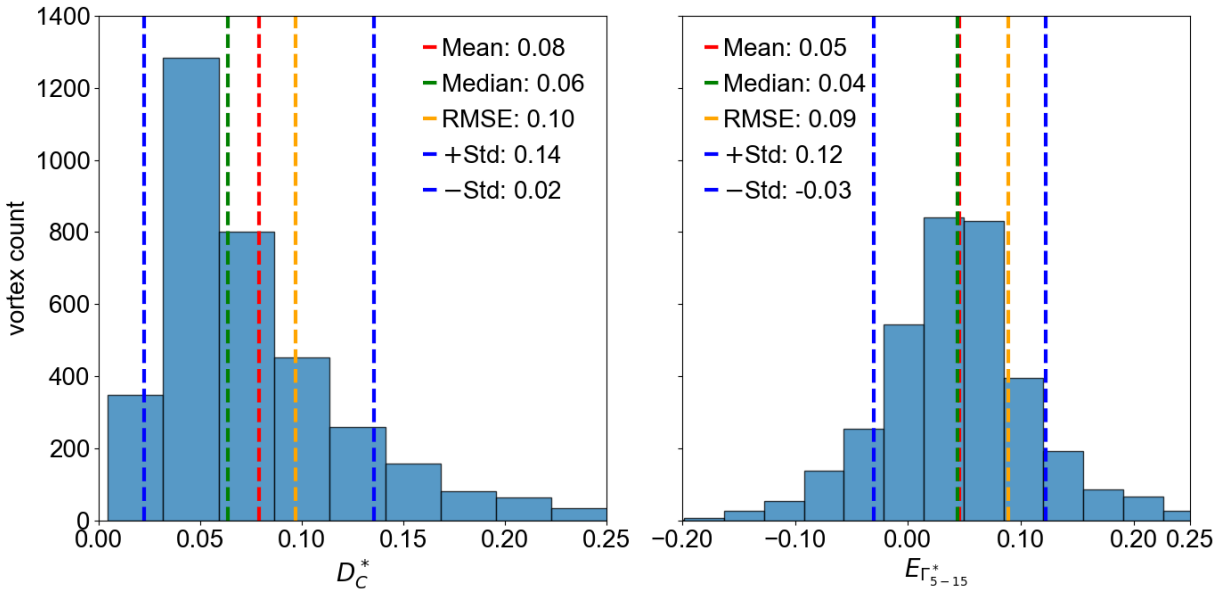

Figure 4.13: RV method accuracy histogram using the two-norm error for the vortex center D_C^* (left) and $E_{\Gamma^*_{5-15}}$ (right) with respect to the vortex count. The mean, median, Root Mean Squared Error (RMSE), and the standard deviation (Std) from the mean are plotted (with the respective error values) for the two cases. Bins with few vortices (belonging to higher errors) are not shown. (Wartha et al., 2025a)©

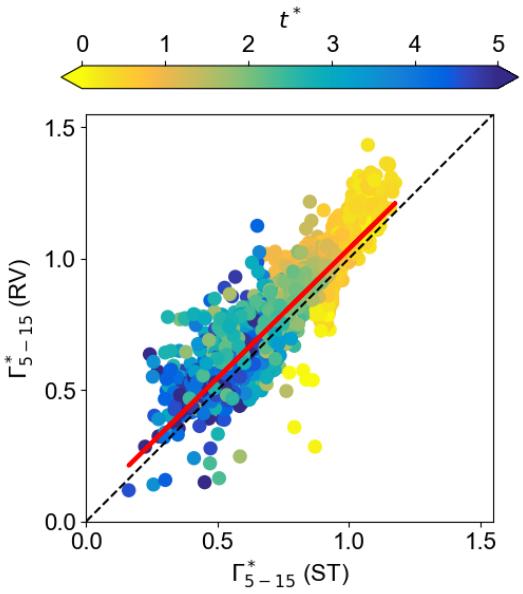

Figure 4.14: Comparison of wake vortex circulation Γ^*_{5-15} estimated by the RV method (RV) and the simulation truth (ST). Wake vortex characterizations (symbols) are colored by the vortex age. (Wartha et al., 2025a)©

Comparison to Theoretical Error Bounds

Table 4.3 compares the herein determined error bounds as RMSE values (for both vortex types, 'Total') to the previously documented theoretical (and numerical) error bounds. RMSE values of both the vortex position and circulation characterizations by the RV method are over triple the values quoted by Smalikho et al. (2015); Smalikho (2019). Presumably, the disparity arises due to the difference between analytical vortex models, lacking both incoherence and unambiguousness of vortices analyzed, in comparison to field measurements and the high-fidelity LES runs in this thesis. Furthermore, previous studies did not investigate common turbulent crosswind conditions for airports. The herein presented practical errors confirm previous campaign observations, suggesting the theoretical errors to underestimate the error bounds of the RV method (Holzäpfel et al., 2022).

It depends on the particular application whether the RV method error bounds presented in this section suffice. Besides the lack of automation and rapid processing speed, the wake vortex position characterization accuracy can be considered satisfactory for a WVAS. However, the error spread suggests to define hazardous areas where the center of a wake vortex may be located (similar to the SHAPe concept) instead of particular points. Characterization of the wake vortex circulation is less acceptable, the uncertainty of 66.2 m^2 s^{-1} (two standard deviations in the case of both vortex types) is significantly larger than the 25 m^2 s^{-1} threshold. Young and strong wake vortices are of most concern for a WVAS, as depicted in Fig. 4.14, the error spread is more narrow for these vortices, implying a high precision and certainty. Overall, the herein assessed RV method constitutes an algorithm with acceptable characterization capabilities, particular for wake vortices at high altitude.

Table 4.3: Comparison of RV method characterization error bounds using the LLS analysis and previous theoretical analysis [by Smalikho et al. (2015); Smalikho (2019)]. The RMSEs of the vortex position characterizations $\mathrm{E}_{R_C}^{\mathrm{RMSE}}$ and $\mathrm{E}_{\varphi_C}^{\mathrm{RMSE}}$ (in the spherical coordinate system), the circulation characterization $\mathrm{E}_{\Gamma}^{\mathrm{RMSE}}$, and the position two-norm D_C^{RMSE} (in the Cartesian coordinate system) are provided. The error spread is given by the standard deviation. $\mathrm{E}_{\Gamma}^{\mathrm{RMSE}}$ for the LLS is assumed comparable to $\mathrm{E}_{\Gamma_{5-15}}^{\mathrm{RMSE}}$ for this comparison. The theoretical $\mathrm{E}_{\varphi_C}^{\mathrm{RMSE}}$, $\mathrm{E}_{R_C}^{\mathrm{RMSE}}$, and lower bound $\mathrm{E}_{\Gamma}^{\mathrm{RMSE}}$ consider a SNR of 0.05 (Smalikho et al., 2015). Theoretical D_C^{RMSE} and the upper bound of $\mathrm{E}_{\Gamma}^{\mathrm{RMSE}}$ consider no instrument noise (Smalikho, 2019). Adapted from Wartha et al. (2025a)©.

Error type	$\mathrm{E}_{\varphi_C}^{\mathrm{RMSE}}$ [deg]	$\mathrm{E}_{R_C}^{\mathrm{RMSE}}$ [m]	D_C^{RMSE} [m]	$\mathrm{E}_{\Gamma}^{\mathrm{RMSE}}$ [$\mathrm{m^2\ s^{-1}}$]
LLS	0.63 ± 0.46	4.3 ± 4.4	4.6 ± 2.7	38.7 ± 33.1
Theoretical	0.21	1.8	1.0	$10.3 - 21.0$

Impact of Turbulent Crosswind

The characterization accuracy of the RV method with respect to varying turbulent crosswinds is provided in Table 4.4. At low crosswind magnitude, the characterization accuracy remains stable, only at a strong $2.0w_0$ turbulent crosswind both the bias and error spread increase by a relevant amount. Applying the same procedure for combining median and standard deviation, results in a vortex circulation uncertainty of -15.3 $\mathrm{m^2\ s^{-1}}$ to $+68.2$ $\mathrm{m^2\ s^{-1}}$ in the case of a $2.0w_0$ crosswind. Similarly, the vortex position error increases to 7.1 m.

Table 4.4: RV method characterization accuracy analysis split by turbulent crosswind strength $\chi \times w_0$. The medians (med) of the vortex normalized circulation characterization error $\mathrm{E}_{\Gamma^*_{5-15}}^{\mathrm{med}}$ and the normalized position two-norm $D_C^{\mathrm{med},*}$ (in the Cartesian coordinate system) are provided. $+/-$ represent an over- and underestimation by the RV method in comparison to the ground truth, respectively. The error spread is given by the standard deviation. (Wartha et al., 2025a)©

Crosswind	$D_C^{\mathrm{med},*}$ [-]	$E_{\Gamma^*_{5-15}}^{\mathrm{med}}$ [-]
$0.0w_0$	0.06 ± 0.04	$+0.04 \pm 0.07$
$0.5w_0$	0.06 ± 0.05	$+0.04 \pm 0.07$
$1.0w_0$	0.06 ± 0.06	$+0.04 \pm 0.07$
$2.0w_0$	0.08 ± 0.07	$+0.06 \pm 0.10$

Table 4.2 established the independence of the wake vortex characterization accuracy with respect to the aircraft-related vortex type: starboard or port. The inclusion of both turbulent port and starboard crosswinds provoked both vortex types to be the luff or lee vortex depending on the crosswind direction. Therefore, Table 4.5 investigates how the vortex characterization accuracy of the RV method is affected by the crosswind direction.

As discussed in Section 2.1.2, the relative position of a vortex belonging to a counter-rotating wake vortex pair, with respect to prevailing wind, plays a significant role in the vortex evolution (due to the circulation sense). Only a marginal difference is found for the wake vortex circulation, with the luff vortex being characterized less accurately. However, the position error of the lee vortex is almost twice as high. The luff wake vortex is expected to remain coherent in the RHI-defined measurement window for a longer period of time, whereas the lee vortex is typically rapidly transported outward. It is presumable that a larger number of lee vortices are chopped-off by the RHI scan boundaries. Furthermore, lee vortices close to the ground interact with a stronger counter-rotating secondary vortex detaching from the boundary layer, causing a premature coherency loss in comparison to their luff counterpart. Fortunately, a rapid vortex decay and swift transport outside of the hazardous region, makes these findings of little operational concern.

Table 4.5: RV method characterization accuracy analysis split by luff and lee vortices. The medians (med) of the vortex normalized circulation characterization error $\mathrm{E}^{\mathrm{med}}_{\Gamma^*_{5-15}}$ and the normalized position two-norm $D_C^{\mathrm{med},*}$ (in the Cartesian coordinate system) are provided. $+/-$ represent an over- and underestimation by the RV method in comparison to the ground truth, respectively. The error spread is given by the standard deviation. (Wartha et al., 2025a)©

Vortex	$D_C^{\mathrm{med},*}$ [-]	$\mathrm{E}^{\mathrm{med}}_{\Gamma^*_{5-15}}$ [-]
Luff	0.05 ± 0.06	0.05 ± 0.08
Lee	0.09 ± 0.06	0.04 ± 0.07

Impact of Spatial Averaging of Lidars

An indirect disadvantage of the RV method is caused by the spatial averaging inherent to lidar measurements. Returning to Fig. 4.10, where the lidar scans on the left consider spatial averaging using the RWF and lidar scans on the right can be considered point measurement, this section analyses the symbols within the individual lidar scans. The LES ground truth is provided by the gray symbols, whereas the pink and violet symbols give the estimates by the RV method in LLS and point measurement scans, respectively. Undoubtedly, the RV method estimates significantly lower vortex circulation values in lidar scans with spatial averaging in comparison to point measurement scans. The smearing-out of the LOS velocity field, causing the vortex core radius to be perceived larger than it is in reality, and the low-pass filtering of LOS velocities and gradients, create this difference. The spatial averaging caused by the RWF reduces the perceived strength of a vortex. The RV method is therefore specifically built for lidar scans, as it very much overestimates the vortex circulations when the RWF is not applied. The spatial averaging creates no noticeable burden for estimating the position of a wake vortex.

Impact of Wake Vortex Position

The position of a vortex relative to the RHI scan geometry exhibits a strong correlation with circulation estimation accuracy. Individual vortices are plotted in Fig. 4.15 within a general RHI lidar scan, they are colored by $E_{\Gamma^*_{5-15}}$. Vortices in the immediate vicinity to the edges of RHI scan geometry produce the most significant circulation characterization outliers, the lidar scan can only see part of the wake vortex, whereas the ground truth can analyze the entire wake vortex.

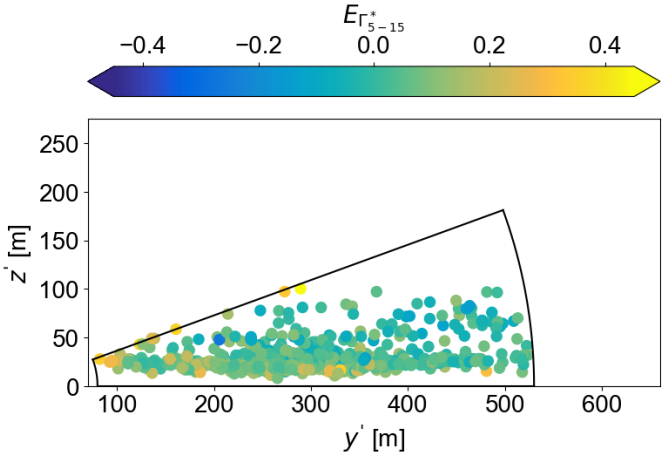

Figure 4.15: RV method circulation characterization errors in an example LLS scan geometry of $[R_-, R_+] = [80, 530]$ and $[\varphi_-, \varphi_+] = [0, 20]$. Symbols of individual wake vortex characterizations are colored by the error between the RV method and the ground truth. $+/-$ represent an over- and underestimation by the RV method in comparison to the ground truth, respectively. Adapted from (Wartha et al., 2025a)©.

Field measurements have previously observed that the characterization of low altitude wake vortices is challenging (Holzäpfel, 2024). Figure 4.16 plots individual wake vortex characterizations with respect to the circulation error and the altitude for starboard vortices (left) and port vortices (right) colored by their circulation magnitude. Sections 2.1.2 and 4.2.1 discussed the presence of image vortices close to walls, as well as the effect on the measured/simulated velocity field with higher magnitude velocities present at the lower half of the wake vortices (the side closer to the bottom wall). A parabolic curve is fit through all symbols (for each vortex type) in Fig. 4.16. Evidently the circulation characterization error of the RV method is highest for low altitude wake vortices.

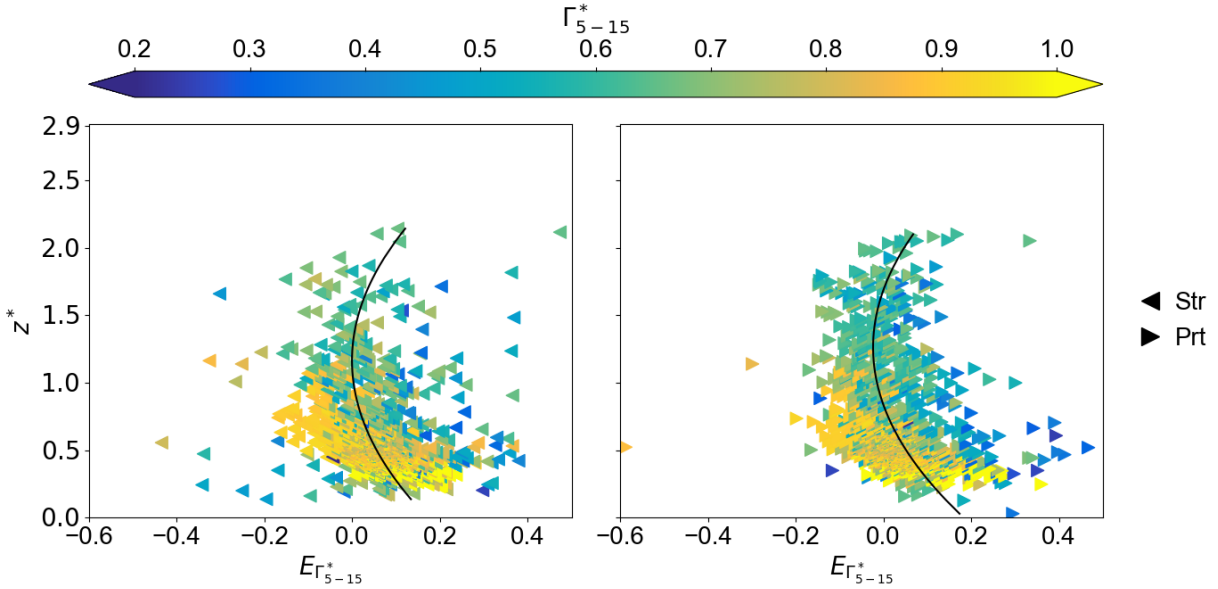

Figure 4.16: RV method circulation characterization error $\mathrm{E}_{\Gamma^*_{5-15}}$ against vortex altitude z^*_C. The z^*-axis is limited by the computational domain height. Individual data points are colored by the ground truth normalized circulation magnitude Γ^*_{5-15}. Vortices are divided into starboard (Str) and port (Prt) (left and right, respectively), for each a second order polynomial is fit to the data in black. Adapted from Wartha et al. (2025a)©.

Depending on the method of vortex circulation determination, the superposed velocity magnitudes of the lower vortex-half may result in an overestimation of circulation magnitude. This thesis focuses on the two most frequently employed methods to compute the circulation of a vortex: using tangential velocities along a line and the vorticity within the enclosed surface [see Eq. (2.2) in Section 2.1]. Holzäpfel et al. (2003) list additional methods. The LES tracking algorithm, considered the ground truth and providing the gray symbols in Fig. 4.10, employs the vorticity (in particular the vorticity in flight direction ω_x) to compute the circulation of a vortex. The integral of the vorticity is not modified by the larger velocities triggered by the image vortices outside the vortex core of the primary vortex. Instead, the RV method fits Burnham-Hallock vortices via few tangential velocities. The considered RV method version furthermore solely fits models to wake vortices within the lidar scan, image vortices are not modeled. As a result, the superposed velocities close to the ground are entirely associated with the wake vortices. Since only few tangential velocities are employed to estimate the vortex circulation and axisymmetric coherent vortices are assumed, the additional velocity from the image vortices is interpreted as genuinely belonging to the primary wake vortices, leading to their overestimation.

An overestimation of the vortex circulation can equally be observed at high altitudes ($1.5 \lesssim z^*$) in Fig. 4.16. The top free-slip LES boundary brings about an analogous mechanism as the bottom non-slip LES boundary, which can analogously be modeled by image vortices (Doligalski et al., 1994). Given that the height of the LES computational domain

is $Z^* = 2.9$ (see Section 3.1.4), the effects at the bottom and top LES boundaries lead to an overall vortex circulation overestimation, with the minimum error expected at the vertical center of the domain i.e., $z^* = 1.45$. Indeed, Fig. 4.16 confirms that at this altitude the wake vortex circulation is just not overestimated on average. However, note that the top image vortices only prevail in the LES, while they are unphysical at field measurements. Given that Fig. 4.16 shows only few vortices located at this altitude, particular in comparison to the number of vortices in ground vicinity, the unphysical effect at the top LES boundary is not considered critical.

On average the circulation of a wake vortex is therefore overestimated by the RV method. Holzäpfel et al. (2021) report the opposite, their Fig. 11 suggests an underestimation on the order of 10 % in field measurements from Vienna Airport (corresponding to the circulation distribution in Fig. 3.16 right). As established in Section 3.3.1, wake vortex heights are on average significantly higher in these field measurements and thus the effect of not considering the ground image vortices with the RV method is marginal. Indeed, also in LLS scans the RV method may underestimate the strength of vortices, particularly when they are strong, coherent, and located within $0.5 \lesssim z^* \lesssim 1.0$. At these altitudes the absent image vortices in the algorithm play a secondary role, with the spatial averaging and low-pass filtering of the velocity field constituting the key adulteration effects. Given that the majority of wake vortices in the LESs are located at a low altitude, the negligence of image vortices by the RV method can be considered the main driver for the overall computed overestimation of wake vortex circulation. As mentioned previously, Smalikho (2019) enhanced the original RV method by considering the ground effect and image vortices. His numerical study demonstrates a significantly reduced wake circulation characterization error in ground proximity. However, the present study aims to assess the original RV method, given its employment for analyzing the field measurements from Vienna Airport, and thus the enhanced RV method is beyond the scope of this thesis.

Impact of Temporal Averaging of Lidars

Section 4.2.2 discussed vortex stretching and compressing as a result of the RHI scanning pattern and vortex descent/ascent. Manually selected wake vortices, where confident educated guesses for their vertical movement were attainable, are plotted in Fig. 4.17. The ground truth circulation (simulation truth, ST) and the circulation estimate by the RV method (RV) are compared. The symbol of each wake vortex indicates whether it appears stretched (Stc) or compressed (Com) in the associated lidar scan. From his numerical studies Smalikho (2019) concluded that stretched vortices have their circulation magnitude overestimated by the RV method. On average this trend is confirmed in Fig. 4.17. On the one hand, this trend is marginal and requires verification in a dedicated study. On the other hand, the marginal difference may suggest the negligible relevance of this effect for characterizing wake vortices in lidar scans in comparison to other uncertainties.

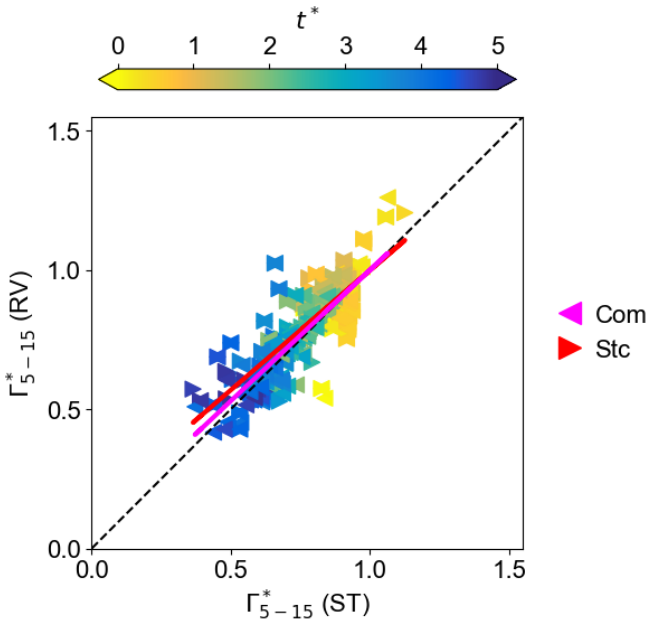

Figure 4.17: Comparison of stretched (Stc) and compressed (Com) wake vortex correlations of the circulation Γ^*_{5-15} estimated by the RV method (RV) and the simulation truth (ST). Wake vortex characterizations (symbols) are colored by the vortex age and limited to the wake vortex simulation with no wind present. Adapted from Wartha et al. (2025a)©.

Impact of the Assumed Vortex Core Radius

The RV method characterizes vortex circulations employing Burnham-Hallock vortices. Section 2.1.3 established that vortex models follow varying notions, leading to different velocity and circulation profiles. Real wake vortices may deviate from the Burnham-Hallock vortex, particularly as they age and lose coherency. Additionally, the core radius of a wake vortex may vary substantially throughout the vortex lifetime, while the RV method assumes a fixed vortex core size for each wake vortex generating aircraft type. A false core radius may adulterate the estimated vortex circulation.

Using Burnham-Hallock vortices, below outlines with a simplified study how a fixed core radius r_c^0 for modeling measured vortices in the RV method can adulterate circulation characterization estimations. A fixed root circulation $\Gamma_0 = 433.9$ m^2 s^{-1} is assumed. For an example case $r_c^0 = r_c^{2\mathrm{m}} = 2$ m, Fig. 4.18 can be plotted with respect to $\Delta r_c = r_c - r_c^0$, where r_c is the core radius of the actual vortex. The vertical axis corresponds to the normalized RV method vortex fitting algorithm [see Eq. (3.26) in Section 3.4.2] with the assumption that close to the vortex $V_\theta \approx V_r$ (the tangential velocities of a vortex are similar to the lidar LOS velocity). For $|\Delta r_c| < 2$, the effect remains in an acceptable range, a parabolic distribution is observed about $\Delta r_c = 0$. A 2-m vortex core radius is rare, particularly older vortices feature higher core radius values (high single digit radii are possible), thus resulting in a significant adulteration of the vortex circulation.

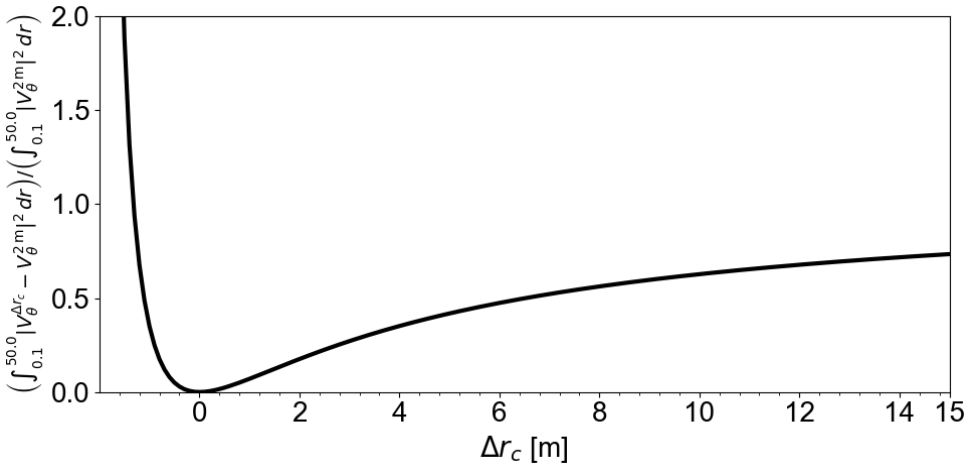

Figure 4.18: Circulation magnitude error for the RV method algorithm based on assuming a wrong core radius, represented by the definite integral of the absolute squared difference of the Burnham-Hallock vortex model with $r_c^0 = r_c^{2m} = 2$ m in comparison to smaller and larger core radii, given by the difference to the reference case Δr_c. Normalization is realized with the definite integral of the absolute and squared reference Burnham-Hallock vortex model. The negative Δr_c is bound by the reference vortex core radius r_c^{2m}.

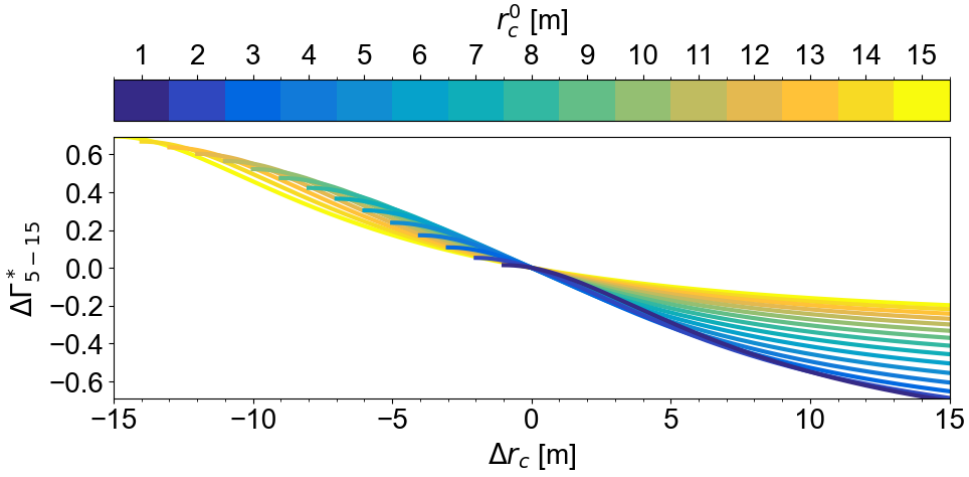

Figure 4.19: Difference in vortex circulation estimation ($\Delta\Gamma^*_{5-15}$) with respect to the difference in core radius of the Burnham-Hallock vortex model. Normalization is realized with $\Gamma_0 = 433.9$ m^2 s^{-1}. Negative Δr_c are bound by the associated reference core radius r_c^0.

By plotting $\Delta\Gamma^*_{5-15} = \Gamma^*_{5-15} - \Gamma^{*,0}_{5-15}$ with respect to Δr_c (superscript 0 refers to the model vortex), Fig. 4.19 suggests that vortices with a larger core radius feature weaker vortex circulations (in the specified regime) than those with a smaller core radius. Although the vortex fitting performed by the RV method is subject to different conditions, it suggests that a circulation under- or overestimation may occur for $\Delta r_c \neq 0$. Further analysis in this matter is beyond the scope of this thesis.

4.3.2 Machine Learning Pipeline

The assessment of the ML pipeline is performed using the ML pipeline case *LLS(LLS)* with labels from the LESs [according to the dataset notation introduced in Section 3.4.3 with Eq. (3.33)]. The test subset of the LLS dataset family equates to 1570 LLS scans, which Table 4.6 divides into the crosswind and vortex types. While the number of scans represents all scans attempted to evaluate, Table 4.6 only includes vortices detected both by the ML pipeline and the ground truth. The overall recall and precision rates are 99.8 % and 97.0 %, respectively, suggesting that the desired conservative approach is fulfilled - almost all present vortices are detected. While the recall rate of the ML pipeline is higher than for the RV method, the precision rate is lower. Most false positives are of weak circulation value, relativizing their false detection for the purpose of a WVAS. Unlike the RV method, the ML pipeline automatically processes single RHI lidar scans within approximately 0.1 s with the hardware described in Section 3.4.3, two orders of magnitude faster than the RV method.

Table 4.6: LLS test subset for assessing the ML pipeline split by wind strength and wake vortex type. Crosswind direction is not considered.

Crosswind	No. of port vortices	No. of starboard vortices	No. of LLS scans
$0.0w_0$	299	248	299
$0.5w_0$	393	381	437
$1.0w_0$	423	419	535
$2.0w_0$	234	230	299
Total	1349	1278	1570

The error bounds of the ML pipeline are given in Table 4.7 using the normalized position two-norm $D_C^{\mathrm{med},*}$ and the vortex circulation $\mathrm{E}^{\mathrm{med}}_{\Gamma^*_{5-15}}$. The ML pipeline determines the position of a wake vortex in Cartesian coordinates, making spherical coordinate accuracies redundant. The systematic error is given by the median and the error spread is given by the standard deviation, combined by the RMSE. Note that by employing same dataset family for all three subsets (training, validation, and test) the present analysis provides ML pipeline accuracy limits. Further studies in this thesis investigate cross evaluations (subsets not belonging to the same dataset family), showing that training subsets which do not perfectly represent the test subset majorly impact the ML pipeline accuracy.

Table 4.7: ML pipeline characterization accuracy analysis with *LLS(LLS)* including individual error bounds for starboard and port vortices. The medians (med) and RMSEs of the normalized circulation characterizations $\mathrm{E}_{\Gamma^*_{5-15}}^{\mathrm{med}}$ and $\mathrm{E}_{\Gamma^*_{5-15}}^{\mathrm{RMSE}}$, as well as the normalized position two-norm $D_C^{\mathrm{med},*}$ and $D_C^{\mathrm{RMSE},*}$ (in the Cartesian coordinate system) are provided. The error spread is given by the standard deviation.

Vortex type	$D_C^{\mathrm{med},*}$	$\mathrm{E}_{\Gamma^*_{5-15}}^{\mathrm{med}}$	$D_C^{\mathrm{RMSE},*}$	$\mathrm{E}_{\Gamma^*_{5-15}}^{\mathrm{RMSE}}$
Starboard	0.04 ± 0.04	0.00 ± 0.06	0.06	0.06
Port	0.05 ± 0.04	0.00 ± 0.05	0.07	0.05
Total	0.04 ± 0.04	0.00 ± 0.05	0.07	0.05

All error bounds are lower compared to the RV method (cf. Table 4.2). Wake vortex circulation characterization bounds can be quoted as -23.2 m^2 s^{-1} to $+24.4$ m^2 s^{-1} (under- and overestimation), where the median error is $+0.6$ m^2 s^{-1} and the bounds arise from addition and subtraction of the respective standard deviation (23.8 m^2 s^{-1}) for both vortex types. An analogous error bound can be constructed for the wake vortex position characterization giving 0.1 m to 3.9 m, where the median error is 2.0 m and the standard deviation is 1.9 m. No significant difference in accuracy between the port and starboard vortex types is observed. The vortex position and circulation error spreads are provided in Fig. 4.20. The latter follows a Gaussian distribution, while the former is characterized by a positively skewed distribution. While the RV method suffered from a systematic vortex strength overestimation (cf. Fig. 4.13), the ML pipeline reduces this systematic error to a minimum ($\mathrm{E}_{\Gamma^*_{5-15}}$ is on average zero).

Impact of Wake Vortex Position

In particular, no systematic overestimation of the vortex circulation close to the ground is observed. Unlike the RV method, the ML pipeline can compensate present image vortices. The fitted parabolas in Fig. 4.21 are of very low curvature, indicating no correlation between the vortex circulation characterization and the vortex altitude. However, seemingly a higher amount of strong vortices at low altitude are underestimated in their circulation magnitude, presumably the vortices are chopped-off by the RHI scan geometry. The RV method produces less of these outliers, as it characterizes the wake vortex circulation with only few tangential velocities in the fitting process. Comparison of the ML pipeline and RV method recall rates (the former is higher than the latter) suggests that the ML pipeline characterizes some vortices with high uncertainties, while the RV method does not detect these same vortices at all.

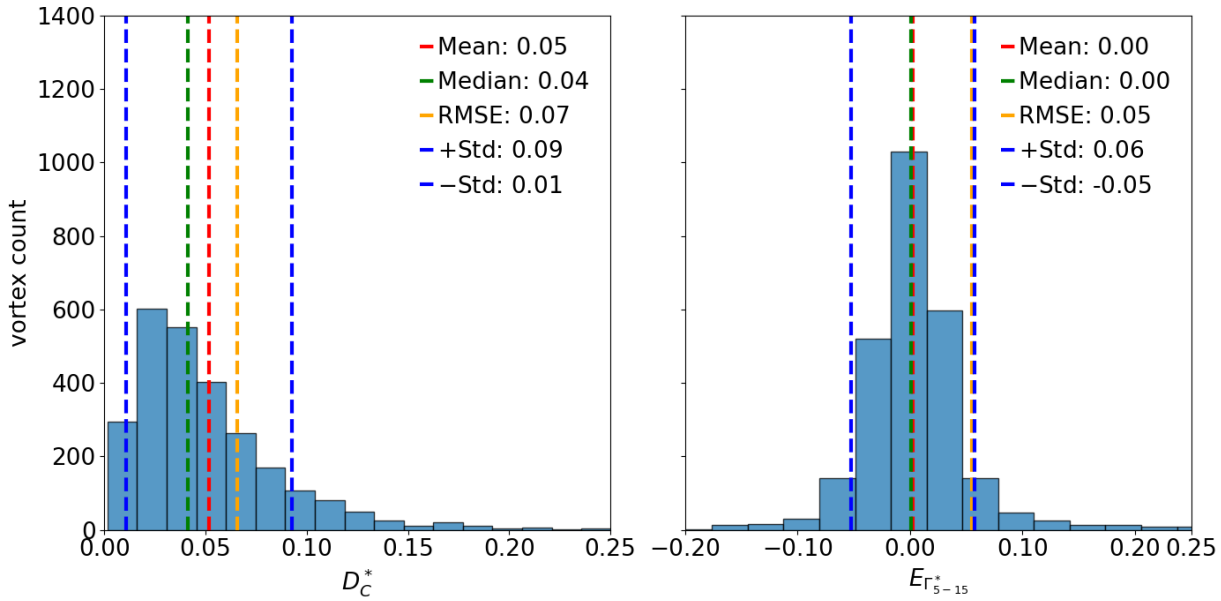

Figure 4.20: ML pipeline accuracy histogram with *LLS(LLS)* using the two-norm error for the vortex center D_C^* (left) and $\mathrm{E}_{\Gamma^*_{5-15}}$ (right) with respect to the vortex count. The mean, median, Root Mean Squared Error (RMSE), and the standard deviation (Std) from the mean are plotted (with the respective error values) for the two cases. Bins with few vortices (belonging to higher errors) are not shown.

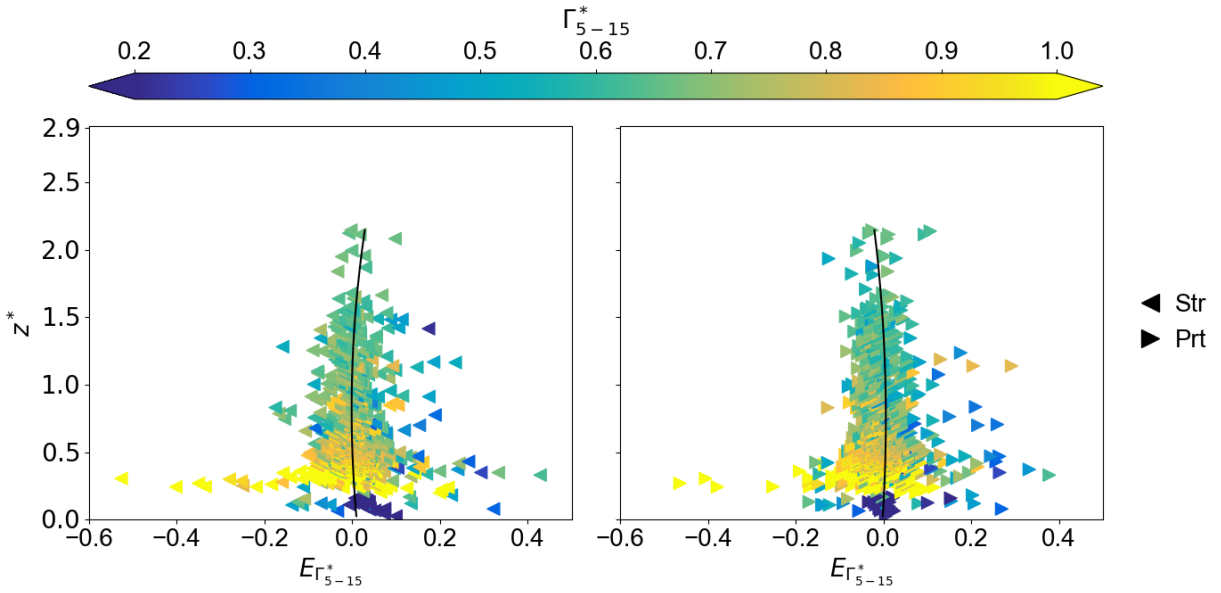

Figure 4.21: ML pipeline circulation characterization error $\mathrm{E}_{\Gamma^*_{5-15}}$ against vortex altitude z^* for *LLS(LLS)*. The z^*-axis is limited by the computational domain height. Individual data points are colored by the ground truth normalized circulation magnitude Γ^*_{5-15}. Vortices are divided into starboard (Str) and port (Prt) (left and right, respectively), for each a second order polynomial is fitted to the data in black.

Impact of Turbulent Crosswind

The characterization accuracy of the ML pipeline with respect to varying turbulent crosswinds is provided in Table 4.8. Regardless of the turbulent crosswind strength, the median position characterization error remains stable; only the error spread marginally increases for stronger turbulent crosswinds. The median circulation characterization error instead decreases (opposite to the RV method), also with an increase in error spread. Overall, the ML pipeline characterization accuracy is affected less by different atmospheric turbulence levels than the RV method (cf. Table 4.4).

Table 4.8: ML pipeline characterization accuracy analysis split by turbulent crosswind strength $\chi \times w_0$. The medians (med) of the vortex normalized circulation characterization error $\mathrm{E}^{\mathrm{med}}_{\Gamma^*_{5-15}}$ and the normalized position two-norm $D_C^{\mathrm{med},*}$ (in the Cartesian coordinate system) are provided. $+/-$ represent an over- and underestimation by the ML pipeline in comparison to the ground truth, respectively. The error spread is given by the standard deviation.

Crosswind	$D_C^{\mathrm{med},*}$ [-]	$\mathrm{E}^{\mathrm{med}}_{\Gamma^*_{5-15}}$ [-]
$0.0w_0$	0.04 ± 0.04	$+0.00 \pm 0.06$
$0.5w_0$	0.04 ± 0.04	$+0.00 \pm 0.06$
$1.0w_0$	0.04 ± 0.05	-0.00 ± 0.07
$2.0w_0$	0.04 ± 0.05	-0.02 ± 0.08

It was found in Table 4.5 that the lee vortex is significantly more difficult to characterize with the RV method than the luff vortex. In contrast, Table 4.9 documents that the ML pipeline characterizes the position and strength of wake vortices completely independent of their rotation sense with respect to the crosswind. This indicates the ability of the ML pipeline to learn vortex coherency effects and scan geometry limitations.

Table 4.9: ML pipeline characterization accuracy analysis with *LLS(LLS)* split by luff and lee vortices. The medians (med) of the vortex normalized circulation characterization error $\mathrm{E}^{\mathrm{med}}_{\Gamma^*_{5-15}}$ and the normalized position two-norm $D_C^{\mathrm{med},*}$ (in the Cartesian coordinate system) are provided. $+/-$ represent an over- and underestimation by the RV method in comparison to the ground truth, respectively. The error spread is given by the standard deviation.

Vortex	$D_C^{\mathrm{med},*}$	$\mathrm{E}^{\mathrm{med}}_{\Gamma^*_{5-15}}$
Luff	0.04 ± 0.04	0.00 ± 0.06
Lee	0.04 ± 0.04	0.00 ± 0.05

4.4 Field Measurement Processing using LES Lidar Simulations and ML

The present section addresses the third research question posed in Section 1.3, to what extent is it possible to train the ML pipeline with simulated lidar scans and thereafter successfully process field measurement lidar scans. Also research question two is partly addressed. This can be considered a necessary generalization approach, given that labeled field measurement datasets might not always be available for every desired setup. The present section explores this possibility using the two lidar simulator types with their respective dataset families introduced in Section 3.3.2: LLS and $\mathrm{LLS_n}$. The testing is performed via the field measurement dataset family from Section 3.3.1. As a reference case, the below analyses are also performed for the ML pipeline trained on the field measurement training subset. Therefore, below primarily considers the following three ML pipelines [dataset notation from Section 3.4.3 with Eq. (3.33)]:

- *FM(FM)*: The reference case. Subsets share the field measurements dataset family.
- *LLS(FM)*: Generalization using idealized lidar simulations (SNR >> 1).
- *LLS_n(FM)*: Generalization using lidar simulations with realistic noise.

Note that the normalization of simulated vortices is performed with Table 3.2, the normalization of field measurement vortices is, where possible, performed with the respective Mode S transponder data (see Section 3.3.1). Significant parts of this section have previously been published by Wartha et al. (2025c).

4.4.1 Wake Vortex Detection

The recall and precision rates with respect to the wake vortex circulation magnitude and age are plotted for the aforementioned ML pipelines in Figs. 4.22 and 4.23, respectively. Uncertainty boundaries emerge from bootstrap resampling with 100 iterations, random selection of vortices from the test subset with return. This allows a particular vortex to be represented multiple times in the subset employed for evaluating the recall and precision.

Section 4.3.2 established the advantage of training, validating, and testing with the same dataset family, the ML pipeline strictly performs best (both in terms of detection and characterization). Subsets within a dataset family only differ in the particular lidar scans, while the setup, data distribution, and scan quality are identical. Thus, as observed for nearly all circulation and age bins, the highest recall and precision rates are expected for *FM(FM)*.

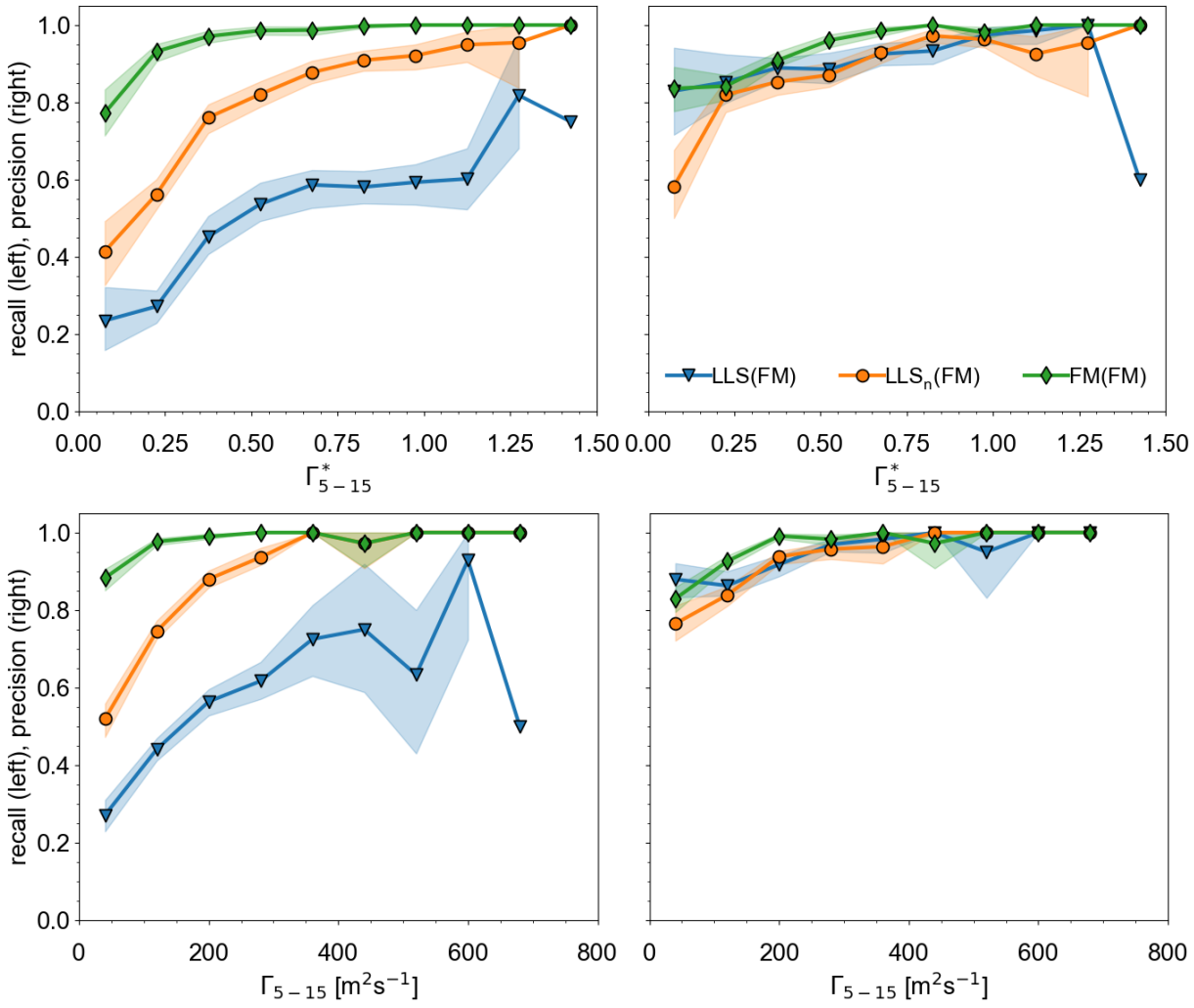

Figure 4.22: Recall (left) and precision (right) for ML pipelines trained on the three different dataset families and tested on field measurements with respect to the normalized/dimensional vortex circulation Γ^*_{5-15} (top) and Γ_{5-15} (bottom). Bootstrap resampling gives the uncertainty. (Wartha et al., 2025c)©

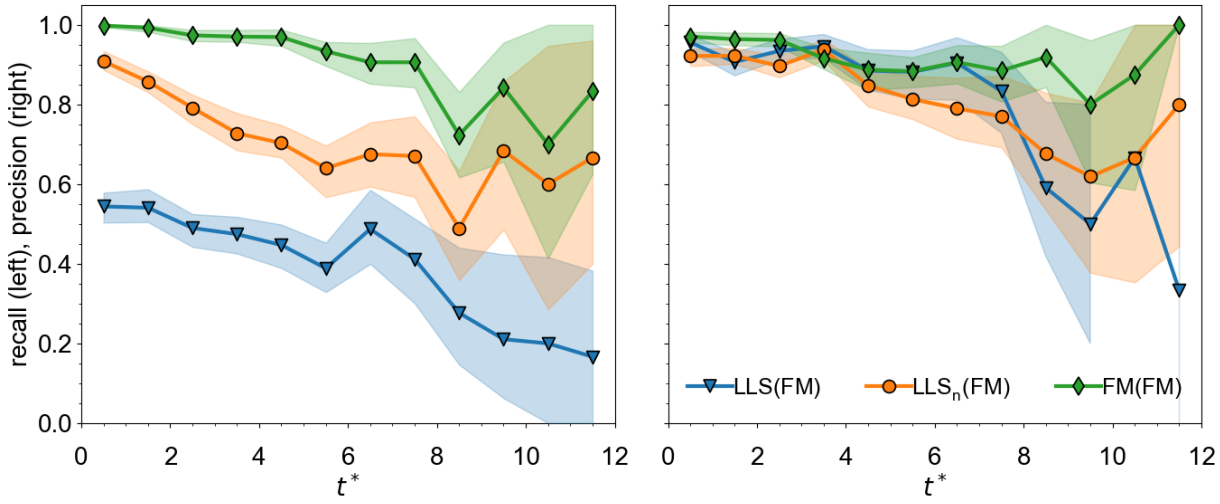

Figure 4.23: Recall (left) and precision (right) for ML pipelines trained on the three different dataset families and tested on field measurements with respect to the normalized vortex age t^*. Bootstrap resampling gives the uncertainty.

The recall rates (Figs. 4.22 left and 4.23 left) are especially satisfactory for vortices of high circulation magnitude and young vortex age. Unsurprisingly, weaker and older wake vortices are more difficult to detect. On the one hand, Fig. 3.16 indicated only the second weakest bin to include a high amount of vortices (significantly above 2000). Therefore, bins with sufficient amounts of wake vortices i.e., $\Gamma^*_{5-15} \geq 0.175$ can attain a recall rate of at least 90 %. On the other hand, weak and incoherent vortices are more diverse than strong and coherent vortices. Very strong vortices (above Γ_0) are also sparse in the dataset, however these can be considered coherent and young, making their characterization less critical.

When training the ML pipeline with LLS or LLS$_n$ scans and evaluating field measurements, the recall rates achieved are expectedly lower. The training and test subsets do not belong to the same dataset family. Moreover, the simulated data contain even less weak vortices than the field measurements (see Figs. 3.17 and 3.16), reasoning the weak circulation bins to result in the largest recall rate differences in comparison to the *FM(FM)* case. Particularly noteworthy is the differing recall rates of cases *LLS(FM)* and *LLS$_n$(FM)*, the latter enables recall rates up to 35 % higher than the former. Figures 4.22 left and 4.23 left thus highlight the importance of modeling aerosol noise and background noise when aiming to simulate realistic lidar measurements. As discussed in Section 4.2.3, the various noise sources alter the lidar scan strongly, hindering idealistic LLS scans to train the ML pipeline sufficiently. Indeed, the characterization of wake vortices in particularly noisy field measurements is only achievable with a LLS$_n$-trained ML pipeline (see Fig. 4.24), instead a LLS-trained ML pipeline is unable to detect wake vortices in very noisy measurements.

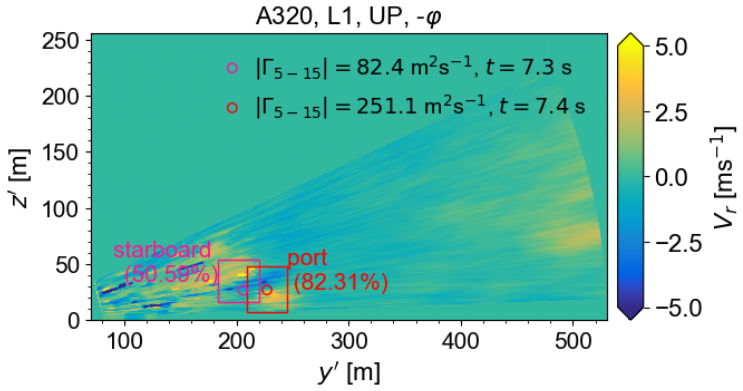

Figure 4.24: Example of a noisy lidar scan processed by ML pipeline case *LLS$_n$(FM)* with bounding boxes, YOLO-confidence, and class given. Circular symbols represent the labels provided by the RV method, with vortex circulation and age.

In general, high recall and low precision rates should not correlate, as this would indicate that the ML pipeline detects vortices everywhere in all lidar scans. While also true vortices would be detected in this way (providing a high recall rate), the majority of detected vortices would be false positives, leading to a low precision rate. Figures 4.22 right and 4.23 right display the precision rates in terms of vortex circulation and age, respectively, showing the opposite trend. Both for circulation and vortex age, low recall rates feature low precision rates, high recall rates feature high precision rates. Thus, the wake vortex signature in lidar scans is properly learned by the ML pipeline. The trends only differ for very strong and old wake vortices, where the fluctuation can be associated with the low vortex count in these bins.

Overall, the precision rates of the three investigated cases are not as distinguishable as the recall rates. For instance, *LLS(FM)* occasionally delivers higher precision rates than *LLS$_n$(FM)* (see Fig. 4.23 right). At the same time, the recall rate of *LLS$_n$(FM)* significantly outperforms *LLS(FM)* (see Fig. 4.23 left). Therefore, LLS$_n$ scans may provide a higher number of number of false positives. At the same time, vortices truly present are more likely to be detected. Thus, a conservative detection approach is ensured.

Regardless, false positives in the field measurement are labeled as such by the error-prone RV method. The significance of this is illustrated using an example case of an Airbus A320 overflight at lidar position L3 at Vienna Airport. Figure 4.25 displays all lidar scans where a difference between the labels and the ML pipeline case *FM(FM)* is noted. Out of 30 lidar scans, the shown 6 differ. Using wake vortex evolution understanding it can be deduced that the majority of the shown scans (4/6) are indeed correct detections by the ML pipeline and labels are missing (green frame). Only 2/6 scans contain actual false negatives (red frame). The missing labels lead to both the recall and particularly the precision to be underestimated [see Eq (3.48)], with actual true positives being flagged as false positives. As a consequence, all displayed recall and precision rates in Figs. 4.22 and 4.23 represent minimum values and higher values can be expected.

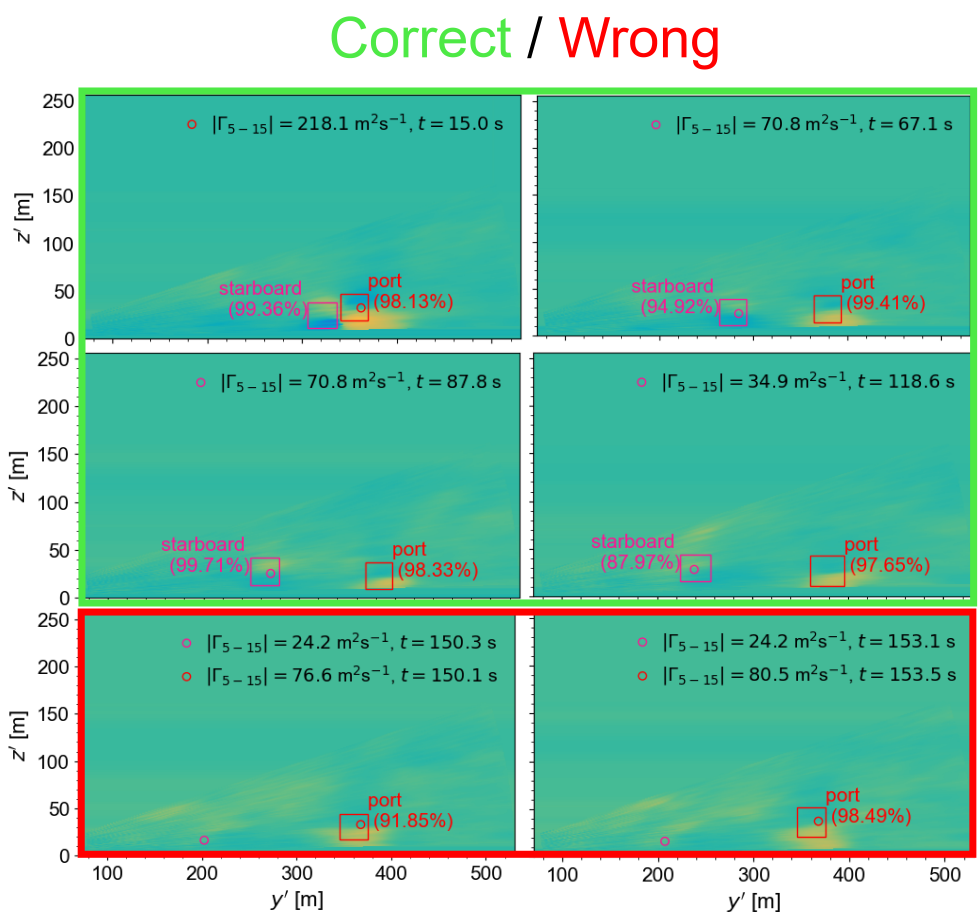

Figure 4.25: Example ML pipeline detections in comparison to available labels. The lidar scans emerge from the Vienna Airport campaign lidar position L3 from an Airbus A320 overflight, where the labels (RV method) and YOLO-detections differ. Green and red lidar scan frames indicate instances where YOLO correctly and incorrectly determined additional wake vortices, respectively (not to be confused with bounding box colors).

Impact of Aircraft Type Diversity

One major difference between the field measurements and the simulated lidar data is the diversity of investigated aircraft types. With the LES runs limited to Airbus A340 aircraft, comprehending the influence on detecting wake vortices generated by other aircraft types is necessary. Field measurements include all RECAT-EU aircraft categories. Figure 4.26 splits the recall rate curves for ML pipeline cases *FM(FM)* (left) and LLS_n*(FM)* (right) into the RECAT-EU aircraft categories. As expected, *FM(FM)* detects vortices generated by all aircraft types similarly well. Only a minor correlation between high recall rates and large/heavy aircraft is observed. Given that the share of wake vortices generated by RECAT-EU CAT-A aircraft (Airbus A380-800) is limited in the dataset, the aforementioned correlation deviates slightly for some circulation bins.

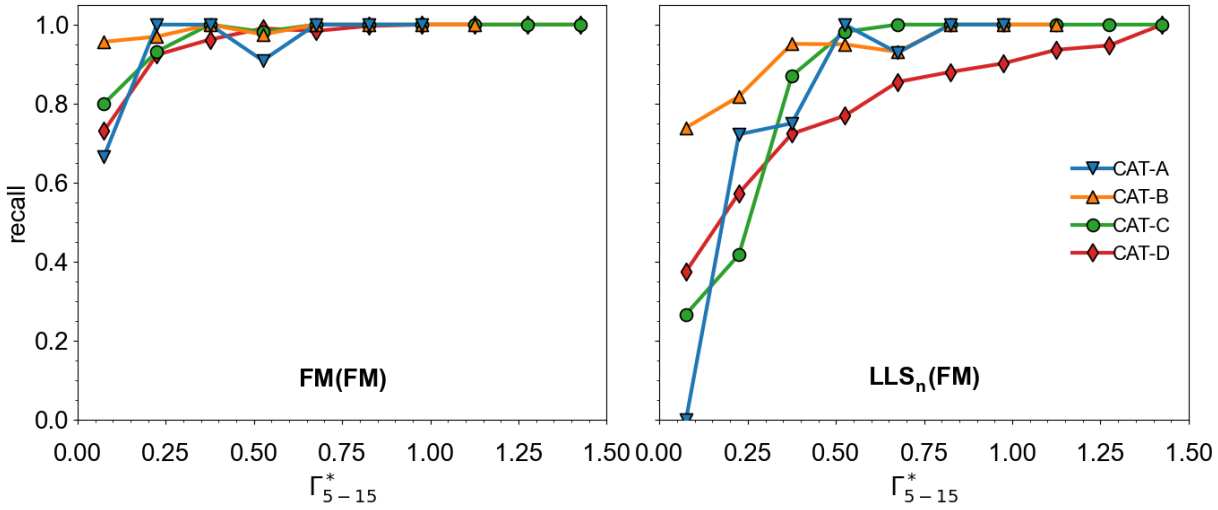

Figure 4.26: Recall split by RECAT-EU aircraft categories for ML pipelines trained using the FM or $\mathrm{LLS_n}$ dataset families and tested on field measurements with respect to normalized vortex circulation. (Wartha et al., 2025c)©

Instead, ML pipeline case *LLS$_n$(FM)* in Fig. 4.26 right indicates significant recall rate differences. The simulated Airbus A340 aircraft belongs to the RECAT-EU CAT-B, for which some of the highest recall rates are observed. RECAT-EU CAT-D contains the aircraft types most different to the Airbus A340 aircraft, leading to the lowest recall rates. It is evident that the detection of wake vortices is most successful when comparable aircraft (in terms of size and mass) are contained in the training subset of the ML pipeline. Note that the vortex amounts for different RECAT-EU aircraft categories differ, which may lead to deviations from the above-detailed trend.

For RECAT-EU CAT-B generated wake vortices of circulation $\Gamma^*_{5-15} \geq 0.375$, the weakest circulation bin in Fig. 3.17 with a respectable amount of wake vortices (more than 2000), recall rates of above 90 % are achieved. Overall, simulated medium to strong wake vortices of RECAT-EU CAT-B aircraft are detected well, whereas weaker vortices and those generated by other aircraft categories are struggled with. Thus, LES-trained ML pipelines may offer serviceable reliability when the field measurement scenario is well represented by the $\mathrm{LLS_n}$ training subset, generalizing the ML pipeline.

This can be investigated further by evaluating the normalized YOLO-estimated bounding box area $A^*_{\mathrm{BB}} = (w_{\mathrm{BB}} \times h_{\mathrm{BB}})\,/b_0^2$, where the normalization uses the bounding box sizing $(b_0 \times b_0)$ from the labeling process described in Section 3.4.3. Example b_0 values for RECAT-EU aircraft categories are provided in Table 4.10. Therefore, if $A^*_{\mathrm{BB}} = 1$, YOLO has learned to differentiate wake vortices generated by different RECAT-EU aircraft categories.

Table 4.10: Initial counter-rotating vortex pair separation b_0 for example aircraft types of each considered RECAT-EU aircraft category. By assuming an elliptic lift distribution, Eq. (2.10) and the respective wingspans B are employed. (Wartha et al., 2025c)©

RECAT-EU aircraft category	Aircraft type	b_0 [m]
CAT-A	Airbus A388	62.7
CAT-B	Airbus A340 (simulated)	47.4
CAT-C	Boeing 763	37.4
CAT-D	Airbus A320	26.8

Figure 4.27 plots the bounding box areas with respect to circulation for each RECAT-EU aircraft category and the two ML pipeline cases *FM(FM)* (left) and *LLS$_n$(FM)* (right). For the former case, all RECAT-EU aircraft categories are close to $A^*_{\mathrm{BB}} = 1$. Thus, the aircraft size can indirectly be determined from the lidar scan. The least reliable bounding boxes are estimated for RECAT-EU CAT-A generated wake vortices, presumably due to their low share in the field measurement training subset. In Fig. 4.27 right, $A^*_{\mathrm{BB}} \approx 1$ is only true for wake vortices generated by RECAT-EU CAT-B aircraft, the aircraft category containing the simulated Airbus A340 aircraft. Wake vortex bounding boxes belonging to alternative aircraft categories are over- or underestimated, neatly corresponding to the factors differentiating b_0 of aircraft types. Note that the minor underestimation of the bounding box size for RECAT-EU CAT-B can be associated with the varying aircraft types in the training and test subsets.

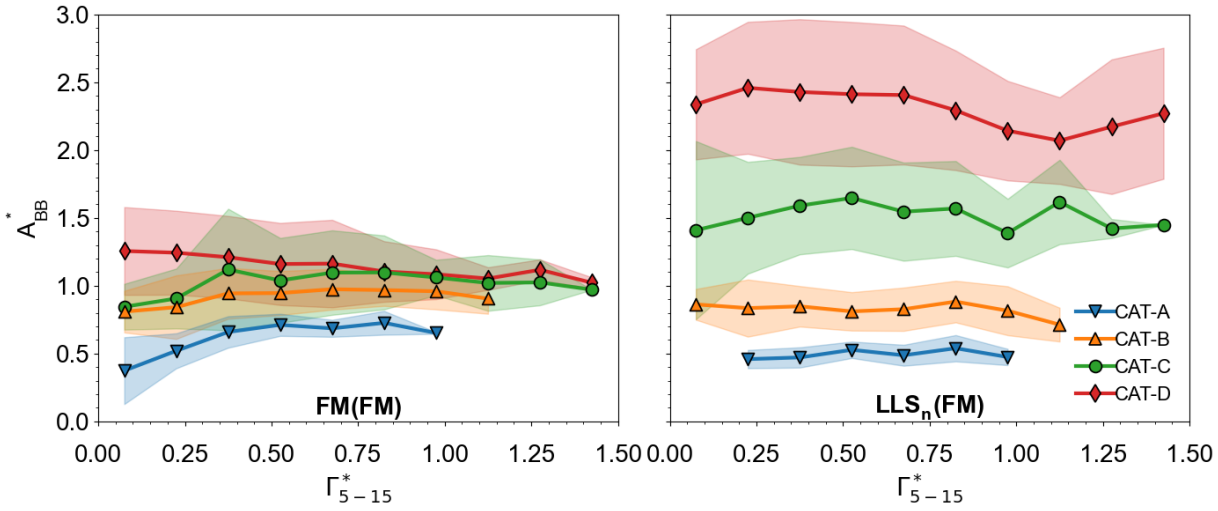

Figure 4.27: Mean normalized YOLO-estimated bounding box area (with the standard deviation giving the uncertainty) with respect to the normalized vortex circulation for FM- and LLS$_n$-trained ML pipelines split into RECAT-EU aircraft categories. (Wartha et al., 2025c)©

4.4.2 Wake Vortex Characterization

Assessment of the ML pipeline characterization for field measurements is conducted using wake vortices detected by both the labels and YOLO i.e., true positive wake vortex detections. Analogously, the ML pipeline cases *FM(FM)* and *LLS$_n$(FM)* are investigated. Table 4.11 documents the obtained wake vortex circulation and position characterization RMSEs. As expected, the reference case *FM(FM)* features lower error bounds than *LLS$_n$(FM)*, manifesting nearly half of the position and circulation RMSEs. The advantage of training, validation, and test subsets emerging from the same dataset family is inevitable. To date, Wartha et al. (2022) provide the only other ML-based lidar processing algorithm for wake vortex characterization employed on the Vienna Airport field measurements. In comparison to ML pipeline case *FM(FM)*, their vortex position and circulation characterization RMSEs are more than double and over 20 % higher, respectively.

Table 4.11: ML pipeline characterization accuracy analysis with cases *FM(FM)* and *LLS$_n$(FM)*. The RMSEs of the vortex dimensional and normalized circulation characterizations $\mathrm{E}_{\Gamma_{5-15}}^{\mathrm{RMSE}}$ and $\mathrm{E}_{\Gamma^*_{5-15}}^{\mathrm{RMSE}}$, as well as the dimensional and normalized position two-norm D_C^{RMSE} and $D_C^{\mathrm{RMSE},*}$ (in the Cartesian coordinate system) are provided. Adapted from Wartha et al. (2025c)©.

ML Pipeline	D_C^{RMSE} [m]	$D_C^{\mathrm{RMSE},*}$ [-]	$\mathrm{E}_{\Gamma_{5-15}}^{\mathrm{RMSE}}$ [m^2 s^{-1}]	$\mathrm{E}_{\Gamma^*_{5-15}}^{\mathrm{RMSE}}$ [-]
FM(FM)	4.4	0.16	29.5	0.10
LLS$_\mathrm{n}$(FM)	7.9	0.28	54.7	0.18

Figures 4.28 top and 4.29 top plot the normalized position characterization error for each vortex with respect to the normalized vortex circulation and age, respectively. For completeness Fig. 4.30 plots the dimensional characterization errors. Symbols are colored by the YOLO-confidence. Figure 4.28 bottom indicates that weak vortices are not only detected worse, but also YOLO is less certain about their detection. Dashed and solid lines represent the position characterization capabilities of YOLO by itself i.e., ML step I only, and the position characterization capabilities of the complete ML pipeline i.e., ML steps I and II. The ML pipeline curves also feature uncertainty boundaries using the error standard deviation. The advantage of fine-tuning the vortex position estimate is apparent particularly for *FM(FM)*, D_C^* is halved across almost the entire vortex strength spectrum. For *LLS$_n$(FM)* the additional regression CNN (ML step II) is only effective for vortices of strength $\Gamma^*_{5-15} > 0.5$ or $t^* < 3$, which are threshold values strongly correlated with the amount of vortices in the training subset (see Fig. 3.17). In other words, particularly ML step II of the ML pipeline (the regression CNN) is reliant on a sufficiently large amount of training data in comparison to ML step I (YOLO). Correlating the vortex share from Fig. 3.17 left and the positional accuracy performance from Fig. 4.28 top right, indicates that at least 2000 samples within a normalized circulation bin width of 0.15 appear sufficient for reasonable position characterization (analogous to the detection task in Section 4.4.1).

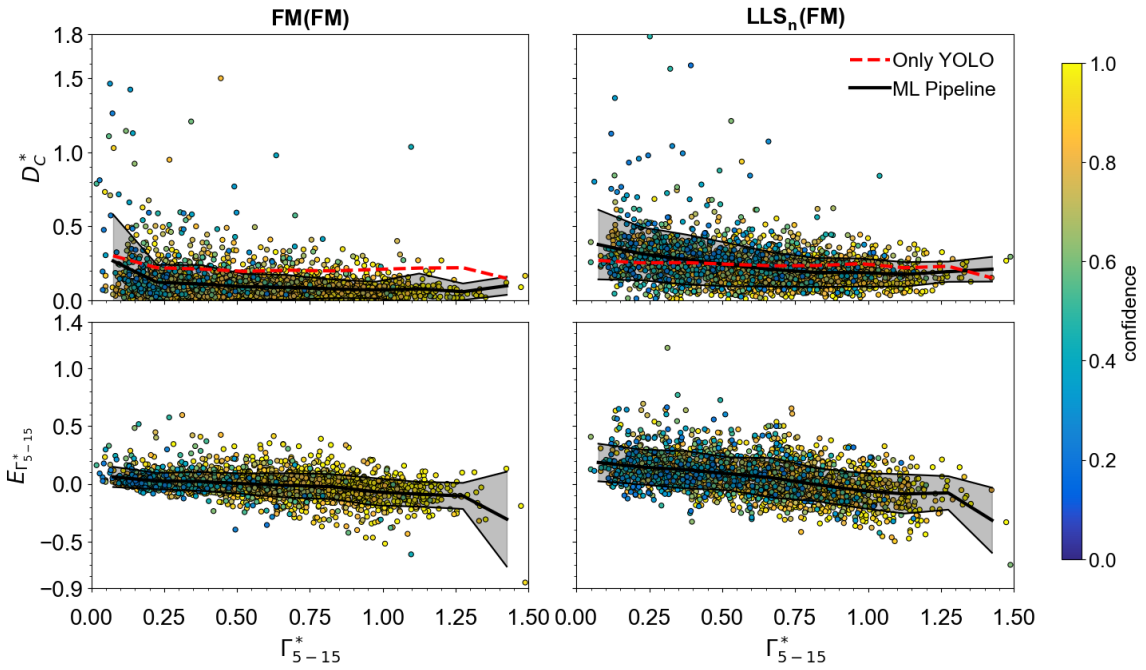

Figure 4.28: ML pipeline normalized vortex position (top) and circulation (bottom) errors with respect to the normalized vortex circulation for *FM(FM)* (left) and *LLS$_n$(FM)* (right). Mean, standard deviation, YOLO-confidence coloring are given. (Wartha et al., 2025c)©

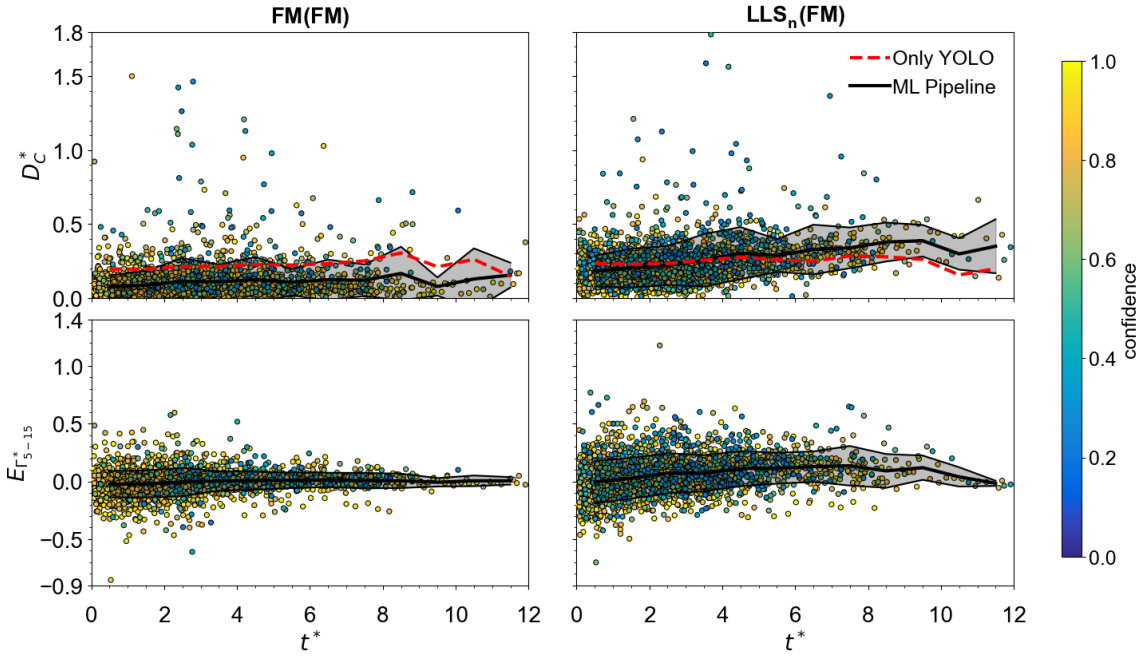

Figure 4.29: ML pipeline normalized vortex position (top) and circulation (bottom) errors with respect to the normalized vortex age for *FM(FM)* (left) and *LLS$_n$(FM)* (right). Mean, standard deviation, YOLO-confidence coloring are given.

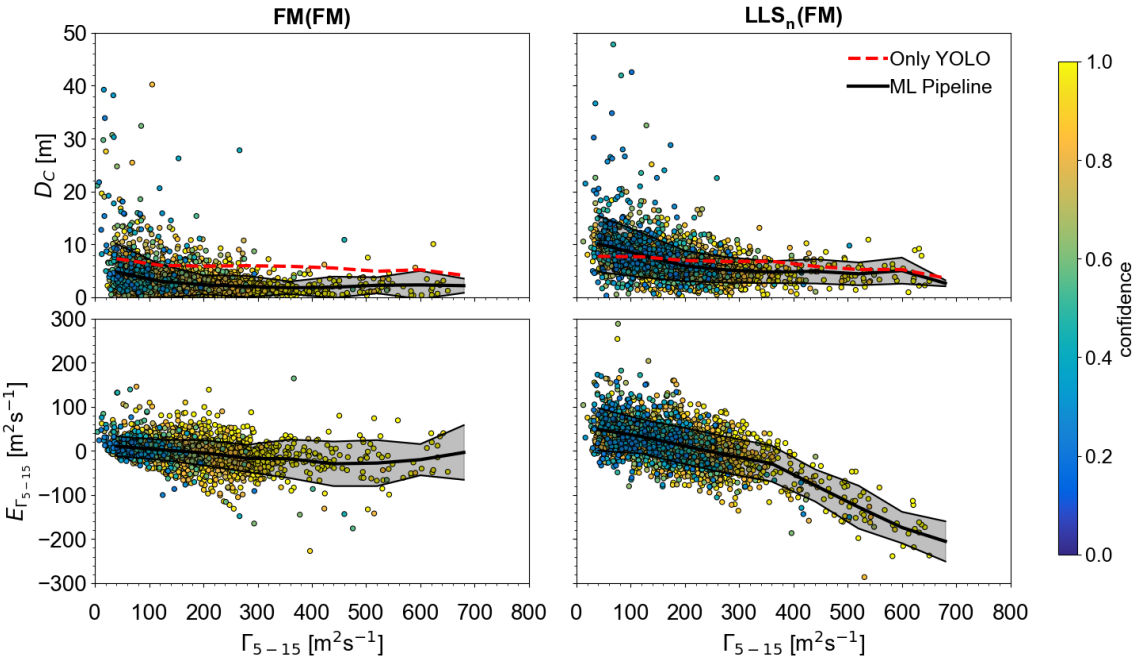

Figure 4.30: ML pipeline vortex position (top) and circulation (bottom) errors with respect to the dimensional vortex circulation for *FM(FM)* (left) and *LLS$_n$(FM)* (right). Mean, standard deviation, YOLO-confidence coloring are given.

Figures 4.28 bottom and 4.29 bottom analogously plot the normalized circulation error. Wake vortex circulations are marginally overestimated for *FM(FM)*, with an intensified overestimation for weak and old wake vortices in comparison to stronger and young vortices. This trend grows further for *LLS$_n$(FM)*, showing a wake vortex circulation magnitude overestimation for nearly all normalized vortex ages and strengths. Approximately above the Airbus A340 root circulation ($\Gamma_0 = 433.9$ m^2 s^{-1}) vortex circulations are severely underestimated, presumably due to the limited number of very strong wake vortices in the LLS$_n$ dataset.

Impact of Aircraft Type Diversity

Wake vortex detection analysis established that the ML pipeline, specifically YOLO, can distinguish RECAT-EU aircraft categories via A^*_{BB}. The third ML pipeline step involves cutting-out LOS velocity data from the pre-processed RHI lidar scan. The cut-out is then padded (or cropped) according to the size of the estimated bounding box. Therefore, Fig. 4.31 left plots the mean D^*_C and $\mathrm{E}_{\Gamma^*_{5-15}}$ with respect to A^*_{BB} bins (bin width 0.25) for the ML pipeline case *LLS$_n$(FM)*. It is investigated whether correct bounding box sizing by YOLO influences the characterization accuracy of the ML pipeline. Since the labeled bounding boxes are sized using the aircraft type dependent b_0, if an estimated bounding box area has an impact on the vortex characterization, it is expected that the lowest characterization errors are obtained at $A^*_{\mathrm{BB}} = 1$.

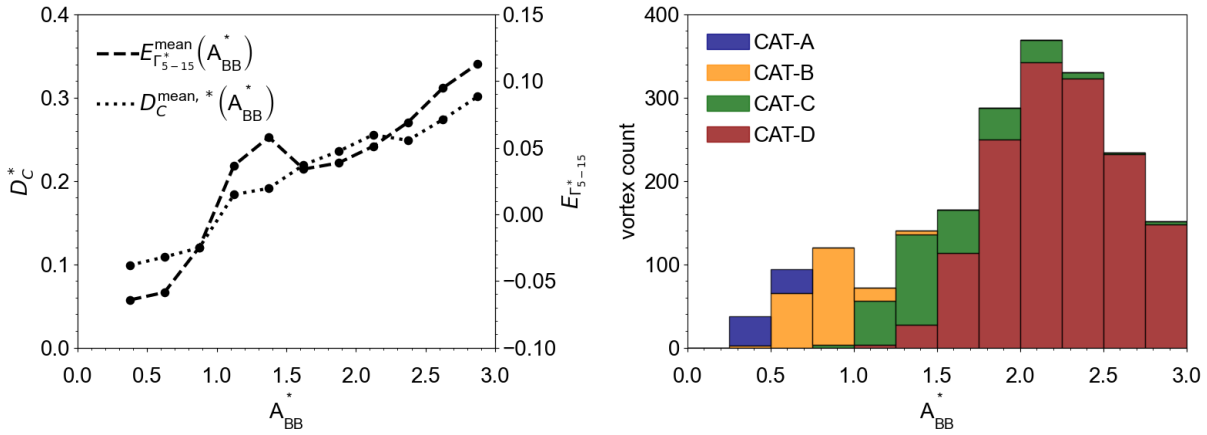

Figure 4.31: Evolution of the mean normalized vortex position and circulation characterization errors with respect to the normalized YOLO-estimated bounding box area for the ML pipeline case *LLS$_n$(FM)* (left) with the associated vortex distribution split by RECAT-EU aircraft categories (right).

The vortex position characterization accuracy (dotted curve) follows this trend for $A^*_{\mathrm{BB}} > 1$, a more significant overestimation in bounding box area results in a higher position characterization error. It would be expected that also a more significant underestimation in bounding box area results in a higher position characterization error, as D^*_C represents a distance, however this is not observed. On the one hand, only a low number of wake vortices are contained in the bounding box area bins $A^*_{\mathrm{BB}} < 1$ (see Fig. 4.31 right). On the other hand, when the size of a bounding box is underestimated, in most cases the wake vortex center used for evaluating D^*_C is still well contained within the bounding box and therefore does not restrict the position characterization.

The vortex circulation characterization follows the expected behavior across all bounding box bins: at $A^*_{\mathrm{BB}} = 1$ the error in vortex circulation is at a minimum. For $A^*_{\mathrm{BB}} < 1$ and $A^*_{\mathrm{BB}} > 1$ the vortex circulation is on average underestimated and overestimated, respectively. Unlike for the vortex position characterization, the circulation characterization builds on the entire LOS velocity field provided by the YOLO-estimated bounding box, thus a bounding box size underestimation also leads to a circulation underestimation.

Ensuring YOLO sizes its estimated bounding boxes according to the wake vortex generating aircraft type is thus a requirement for a high characterization accuracy. Table 4.12 divides the dimensional RMSE values for the ML pipeline case *LLS$_n$(FM)* into the different RECAT-EU aircraft categories, additional mean error values are provided as well. The mean vortex position characterization error strongly correlates with the $D_C^{\mathrm{mean},*}$ in Fig. 4.31 left and the vortex distribution in Fig. 4.31 right. Equally, the mean circulation characterization error correlates well with the $\mathrm{E}^{\mathrm{mean}}_{\Gamma^*_{5-15}}$ curve. The minimum error magnitude is between RECAT-EU CAT-B and CAT-C, as expected from Fig. 4.27 right.

Table 4.12: ML pipeline characterization accuracy analysis with case *LLS$_n$(FM)* split by RECAT-EU aircraft categories. The RMSEs and mean errors of the vortex circulation characterizations $\mathrm{E}_{\Gamma_{5-15}}^{\mathrm{RMSE}}$ and $\mathrm{E}_{\Gamma_{5-15}}^{\mathrm{mean}}$, as well as the position two-norm D_C^{RMSE} and D_C^{mean} (in the Cartesian coordinate system) are provided. +/− represent an over- and underestimation by the ML pipeline in comparison to the ground truth, respectively.

RECAT-EU	D_C^{RMSE} [m]	D_C^{mean} [m]	$\mathrm{E}_{\Gamma_{5-15}}^{\mathrm{RMSE}}$ [m^2 s^{-1}]	$\mathrm{E}_{\Gamma_{5-15}}^{\mathrm{mean}}$ [m^2 s^{-1}]
CAT-A	6.5	5.6	108.2	−63.9
CAT-B	7.0	5.8	74.8	−14.4
CAT-C	7.7	6.6	43.6	+11.24
CAT-D	8.1	7.1	50.2	+19.0

As shown in Fig. 4.31 right, RECAT-EU CAT-B is most prominently located at just under $A_{\mathrm{BB}}^* = 1$. However, note that the $\mathrm{E}_{\Gamma_{5-15}}^{\mathrm{RMSE}}$ values in Table 4.12 are significantly greater for larger and heavier aircraft, even though the simulated Airbus A340 aircraft belongs to RECAT-EU CAT-B. Presumably the strong variation in vortex numbers contained in each RECAT-EU aircraft category has a significant impact. Most vortices are RECAT-EU CAT-D and therefore outliers are suppressed more in this aircraft category. It is known from Figure 3.16 bottom that particularly very strong vortices, beyond the Airbus A340 root circulation of the simulation, are severely underrepresented in the $\mathrm{LLS_n}$ training subset. On the other hand, weaker vortices may be old wake vortices generated by large aircraft or young wake vortices generated by small aircraft. The severe negative bias represented by $\mathrm{E}_{\Gamma_{5-15}}^{\mathrm{mean}}$ for RECAT-EU CAT-A supports this argument and corresponds to Fig. 4.30 bottom right - the strength of very strong wake vortices is significantly underestimated.

In addition to the above-discussed aircraft type dependence, further factors influence D_C^* and $\mathrm{E}_{\Gamma_{5-15}^*}$. Individual vortex characterizations may show a different behavior to the mean trend discussed above. However, it can be concluded that for achieving low characterization errors, the sizing of bounding boxes according to the aircraft type and thus the wake vortex size, does play a role in reducing the error bias. Low systematic characterizations errors can be achieved well when simulating wake vortex $\mathrm{LLS_n}$ scans for the aircraft type wished to evaluate. Random errors may be reduced by increasing the number of wake vortices expected to be evaluated. In all cases it must be remembered that also the RV method has a non-negligible error, and the ML pipeline may indeed provide better characterization estimates.

4.5 Increased ML Pipeline Accuracy with Ground Truth Labels

This section addresses the fourth research question posed in Section 1.3, does the provision of an accurate ground truth enhance the accuracy of the ML pipeline further. Field measurement analyses of this thesis so far focused on data using labels generated by the RV method. It has been established in Section 4.3.1 that the RV method provides error-prone labels for training, validating, and testing of the ML pipeline (see also Fig. 4.25 in Section 4.4.1). By training the ML pipeline with labels including an inherent error component, the ML pipeline output automatically also carries an inherent error component. Note that significant parts of this section have previously been published by Wartha et al. (2025c).

Thus, characterization accuracy discussions for the generalized ML pipeline trained on LES data from Section 4.4.2 do not allow a fair conclusion on whether generalized ML pipelines may enhance the accuracy of lidar processing algorithms. It was established in Section 3.3 that field measurements and lidar simulations (LLS and $\mathrm{LLS_n}$) rely on different labels, the RV method and the LES tracking algorithm, respectively. These distinct label algorithms play a key role in the characterization accuracies obtained for the ML pipeline cases *FM(FM)* and *LLS_n(FM)* in the previous section. Comparison of the solid black lines in Figs. 3.16 top right and 3.17 right shows that the mean vortex circulation throughout the entire wake vortex lifetime is lower for the RV-labels in comparison to the labels from the LESs [also referred to as the Simulation Truth (ST)]. The difference between these two vortex evolutions reads

$$\Delta\Gamma^*_{5-15} = \Gamma^{*,\mathrm{ST}}_{5-15} - \Gamma^{*,\mathrm{FM}}_{5-15}. \tag{4.1}$$

Figure 4.32 compares $\Delta\Gamma^*_{5-15}$ and $\mathrm{E}_{\Gamma^*_{5-15}}$ for *LLS_n(FM)* with respect to the vortex age. Two phases must be separated:

- $0 < t^* < 1$: The roll up phase should be disregarded in this comparison given that here RV-labels strongly vary in their magnitude. The complex vortex structure during roll up does not match the Burnham-Hallock vortices assumed by the RV method well (Hallock and Holzäpfel, 2018).

- $t^* > 1$: A correlation between the input difference ($\Delta\Gamma^*_{5-15}$) and output difference ($\mathrm{E}_{\Gamma^*_{5-15}}$) is evident. Both the simulation labels and the ML-estimates increase their overestimation throughout the vortex lifetime in comparison to the RV-labels.

The above suggests that training with $\mathrm{LLS_n}$ scans and evaluating on field measurements inevitably results in a systematic error. If a ground truth was available for the field measurements, scaling of the circulation values could be undertaken either prior or post ML pipeline training. Therefore, it can be expected that the generalized ML pipeline is capable of higher accuracy on field measurements if the benchmark would rest upon a true basis.

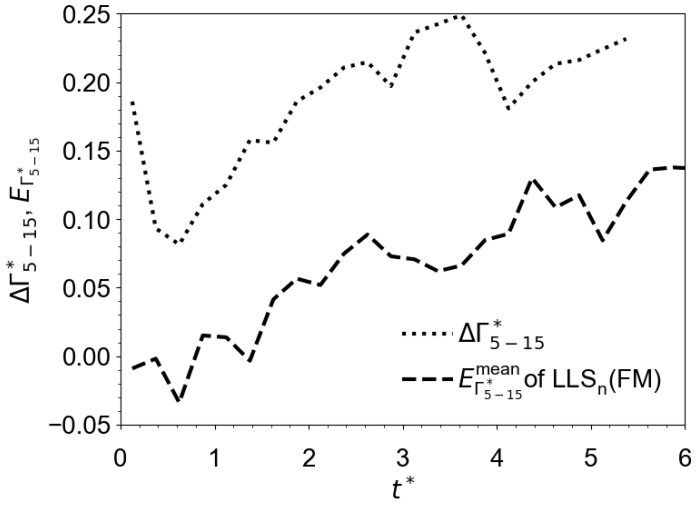

Figure 4.32: Evolutions of the difference between the normalized field measurement (FM) and lidar simulation truth (ST) circulation labels via $\Delta\Gamma^*_{5-15}$ and the error of the normalized vortex circulation characterization $\text{E}^{\text{mean}}_{\Gamma^*_{5-15}}$ for the ML pipeline case *LLS_n(FM)*, with respect to normalized vortex age. Adapted from Wartha et al. (2025c)©.

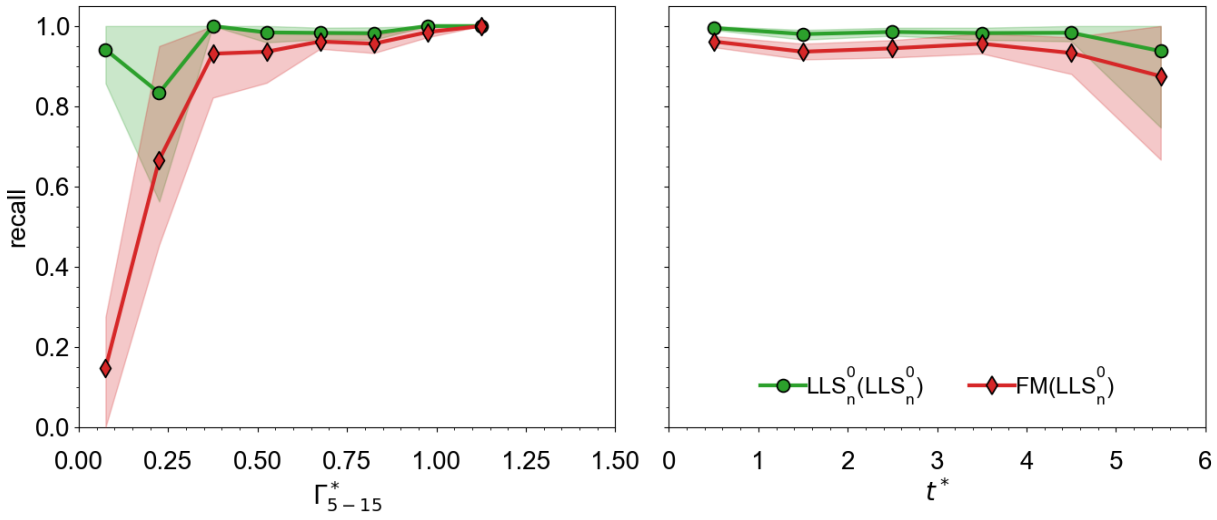

Figure 4.33: Recall for ML pipelines trained using the FM or LLS^0_n dataset families and tested on LLS^0_n scans with respect to normalized vortex circulation (left) and age (right). Bootstrap resampling gives the uncertainty.

Studies with more accurate field measurement labels, provided by another measurement technique like particle image velocimetry or drones, are required to investigate the impact of an accurate ground truth in field measurement lidar scans properly. Techniques for obtaining ground truth labels for field measurements are beyond the scope of this thesis, instead insights and hints for answering the posed research question can be obtained by employing a test subset of $\mathrm{LLS_n}$ scans with near ground truth LES-labels. ML pipelines trained on field measurements (labeled by the RV method) and $\mathrm{LLS_n}$ scans are compared, with the latter also employing the LES-labels. For this study only $\mathrm{LLS_n}$ scans modeling the lidar setup from Vienna Airport are employed, namely $\mathrm{LLS_n^0}$ scans (see Section 3.3.2). For analyzing the wake vortex detection, Fig. 4.33 contains the recall rates with respect to the wake vortex circulation and age. *LLS_n^0(LLS_n^0)* achieves higher recall rates for all circulation and age bins in comparison to *FM(LLS_n^0)*. Thus, the accuracy of the labels has an impact on the wake vortex detection.

The wake vortex position and circulation characterization accuracies are comparable for *FM(LLS_n^0)* and *LLS_n^0(LLS_n^0)*, as plotted with respect to the vortex circulation and age in Figs. 4.34 and 4.35, respectively. Still, *LLS_n^0(LLS_n^0)* provides the smallest mean characterization errors and uncertainty boundaries. Regardless of the trained ML pipeline, individual vortices feature significantly higher YOLO-confidence values when evaluating $\mathrm{LLS_n}$ scans in comparison to evaluating field measurements (cf. Fig. 4.28 and 4.29). Furthermore, the second ML step (II) of the ML pipeline significantly decreases the vortex position characterization error for both ML pipeline cases, with the first ML step (I) also only indicating minor differences between the two cases.

Table 4.13 documents an increase in the characterization error by *FM(LLS_n^0)* compared to *LLS_n^0(LLS_n^0)*. Half the position characterization RMSE and a decrease of the circulation characterization RMSE by 40 % are achieved when training the ML pipeline with $\mathrm{LLS_n}$ scans labeled with a more accurate ground truth than the RV method. Although the advantage of all subsets emerging from the same dataset family must be considered, it can be deduced that the provision of more accurate labels in the training subset may allow higher characterization accuracies, since the ML pipeline case *LLS_n^0(LLS_n^0)* even outperforms the case *FM(FM)*.

4.6 ML Pipeline Dataset Composition Studies

Throughout the previous sections ML pipelines were training subsets were trained with one dataset family only. In each case, the total amount of available training scans was employed, which is expected to deliver the highest possible ML pipeline accuracies. In the interest of practically applying the ML pipeline, this section aims to understand how many lidar scans are required for a successful detection of wake vortices. Furthermore, this section investigates whether complementing an existing field measurement training subset with $\mathrm{LLS_n}$ scans can increase the reliability, accuracy, and generalizability of the ML pipeline.

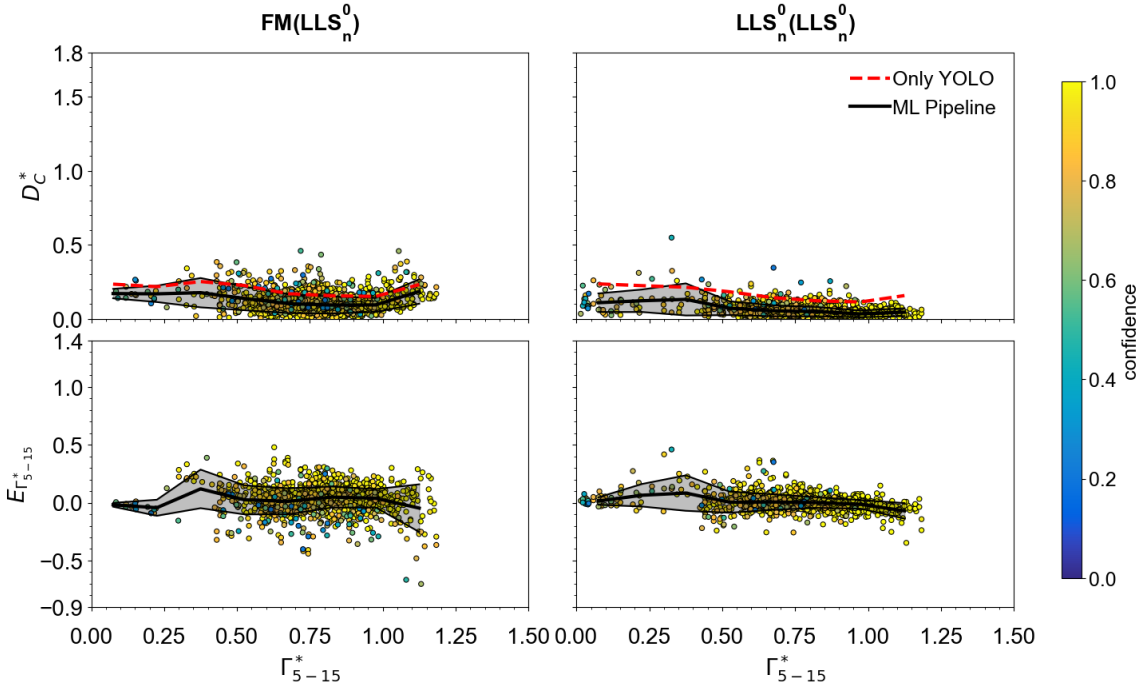

Figure 4.34: ML pipeline normalized vortex position (top) and circulation (bottom) errors with respect to the normalized vortex circulation for $FM(LLS_n^0)$ (left) and $LLS_n^0(LLS_n^0)$ (right). Mean, standard deviation, YOLO-confidence coloring are given.

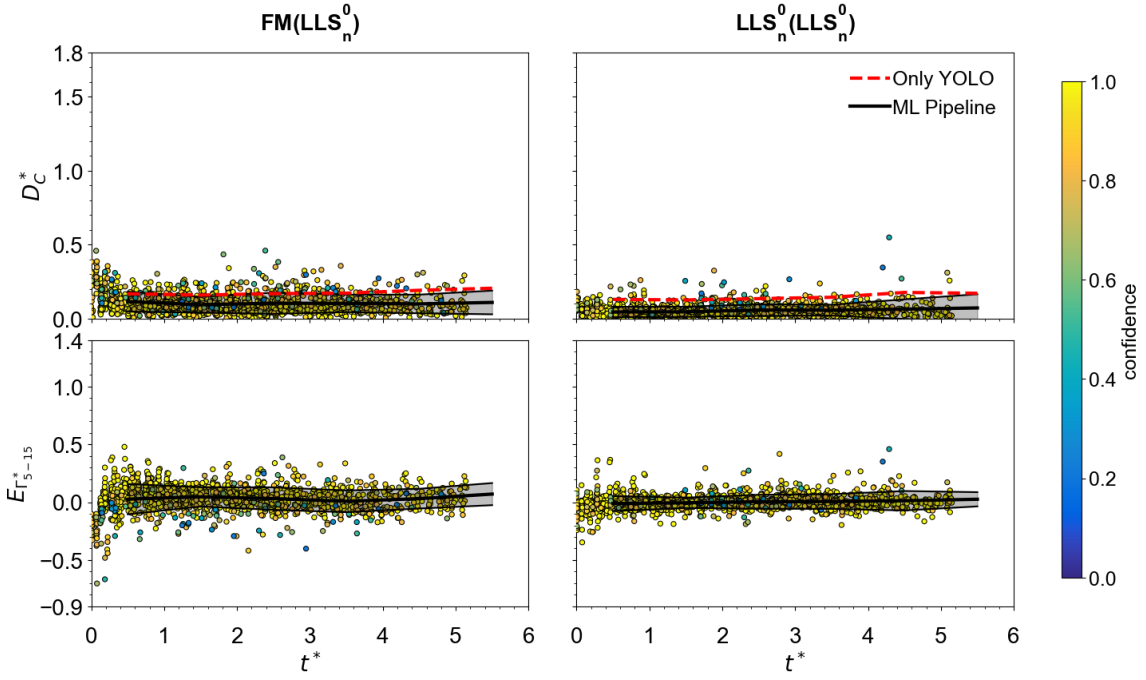

Figure 4.35: ML pipeline normalized vortex position (top) and circulation (bottom) errors with respect to the normalized vortex age for $FM(LLS_n^0)$ (left) and $LLS_n^0(LLS_n^0)$ (right). Mean, standard deviation, YOLO-confidence coloring are given.

Table 4.13: ML pipeline characterization accuracy analysis with cases *FM(LLS$_n^0$)* and *LLS$_n^0$(LLS$_n^0$)*. The RMSEs of the vortex dimensional and normalized circulation characterizations $\mathrm{E}_{\Gamma_{5-15}}^{\mathrm{RMSE}}$ and $\mathrm{E}_{\Gamma_{5-15}^*}^{\mathrm{RMSE}}$, as well as the dimensional and normalized position two-norm D_C^{RMSE} and $D_C^{\mathrm{RMSE},*}$ (in the Cartesian coordinate system) are provided. Adapted from Wartha et al. (2025c)©.

ML Pipeline	D_C^{RMSE} [m]	$D_C^{\mathrm{RMSE},*}$ [-]	$\mathrm{E}_{\Gamma_{5-15}}^{\mathrm{RMSE}}$ [m^2 s^{-1}]	$\mathrm{E}_{\Gamma_{5-15}^*}^{\mathrm{RMSE}}$ [-]
FM(LLS$_\mathrm{n}^0$)	5.8	0.12	48.0	0.11
LLS$_\mathrm{n}^0$(LLS$_\mathrm{n}^0$)	3.1	0.06	26.5	0.06

4.6.1 Number of Training Scans

The effect of the training subset size on the detection reliability of the ML pipeline is studied using the case *FM(FM)*. Figure 4.36 left displays the mAP@25 (see Section 3.4.3) with respect to the epochs and training subset size. The bottom axis represents the percentage of scans used for training out of all 13 618 field measurement scans. The top axis gives the absolute scan count. The epoch count is used to color the individual scatters, allowing an overview of how quickly patterns are learned. Since one epoch signifies having taken the entire training subset into account once, a smaller subset also results in overall less scans being considered. It is evident that already small amounts of labeled lidar data can deliver reasonable mAP@25 values. Indeed, the final epoch mAP@25 is nearly equivalent for all training subset sizes. The positive relationship of the mAP@25 and epoch count signifies proper learning [EASA guideline (Soudain, 2024)]. A major disadvantage of smaller training subsets is the lower diversity in wake vortex and atmospheric scenarios covered by the subset, overfitting may result. Thus, obtained detection rates should be considered with care, a lower generalizability may result.

4.6.2 Hybrid Training Subsets

It may prove beneficial to fill the remaining capacity of the training subset with LLS$_\mathrm{n}$ scans, providing the ML pipeline case *[FM + LLS$_n$](FM)* plotted in Fig. 4.36 right. The plot composition is equivalent to Fig. 4.36 left, except the top axis which now represents the percentage share of LLS$_\mathrm{n}$ with respect to the fixed training subset size of 13 618 scans. The very left case in Fig. 4.36 right constitutes LLS$_\mathrm{n}$ scans only. Undeniably, the inclusion of even only few field measurement lidar scans as part of the training dataset is beneficial and can increase the mAP@25 by up at least 10 % in comparison to purely LLS$_\mathrm{n}$ scans. Increasing the number of field measurements further, while reducing the number of LLS$_\mathrm{n}$ scans, does not lead to a linear increase of mAP@25. Figure 4.37 compares the two cases investigated using the median mAP@25 of the last 10 % of epochs for each subset composition. The green shaded area represents the relative percentage difference ΔmAP@25 of the two ML pipelines. The two curves deliver comparable mAP@25 values, despite the hybrid training subsets holding a significantly greater amount of lidar scans.

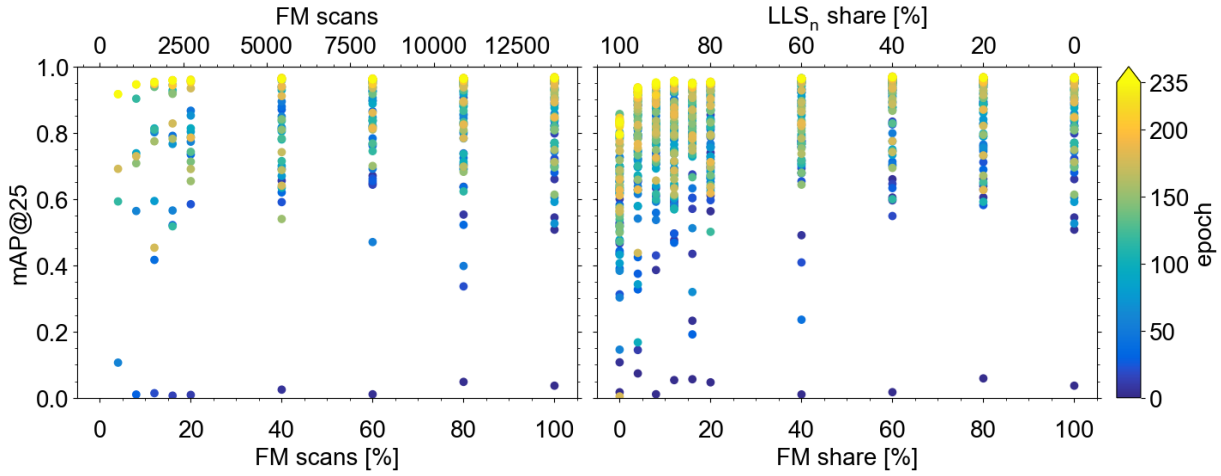

Figure 4.36: Evolution of the vortex detection mAP@25 for the ML pipelines *FM(FM)* (left) and $[FM + LLS_n](FM)$ (right) and varying training subset sizes and hybrid compositions in the former and latter cases, respectively. Percentage values are relative to the maximum amount training field measurement scans available as presented in Section 3.3.1. For each training subset size the mAP@25 is provided for a set of (up to 235) epochs.

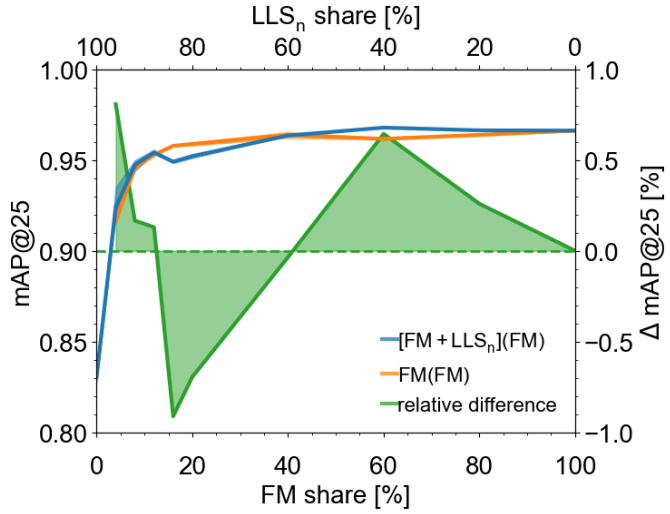

Figure 4.37: Comparison of the median mAP@25 evolutions for the ML pipelines *FM(FM)* and $[FM + LLS_n](FM)$. Green color represents the relative mAP@25 difference.

In the above, the training subset size was limited to 13 618 scans. However, in total 27 868 lidar scans are available for training (field measurements combined with $\mathrm{LLS_n}$). When testing on field measurements the ML pipeline $[FM+LLS_n](FM)$ results in Fig. 4.38, giving the recall rate with respect to the vortex circulation and age. Achieved recall rates are comparable to $FM(FM)$ (replotted for reference). An improvement is achieved for evaluating $\mathrm{LLS_n}$ scans i.e., $[FM + LLS_n](LLS_n)$ compared to $FM(LLS_n^0)$. Thus, the primary advantage of a hybrid training subset is improved generalizability, wake vortices are detected at high recall rates in field measurements and $\mathrm{LLS_n}$ scans. Normalized characterization RMSE values for wake vortex position (D_C^*) and circulation (Γ_{5-15}^*) are 0.15 and 0.11, respectively - comparable and improved significantly compared to the individual field measurement and $\mathrm{LLS_n}$ training subset cases in Table 4.11, respectively.

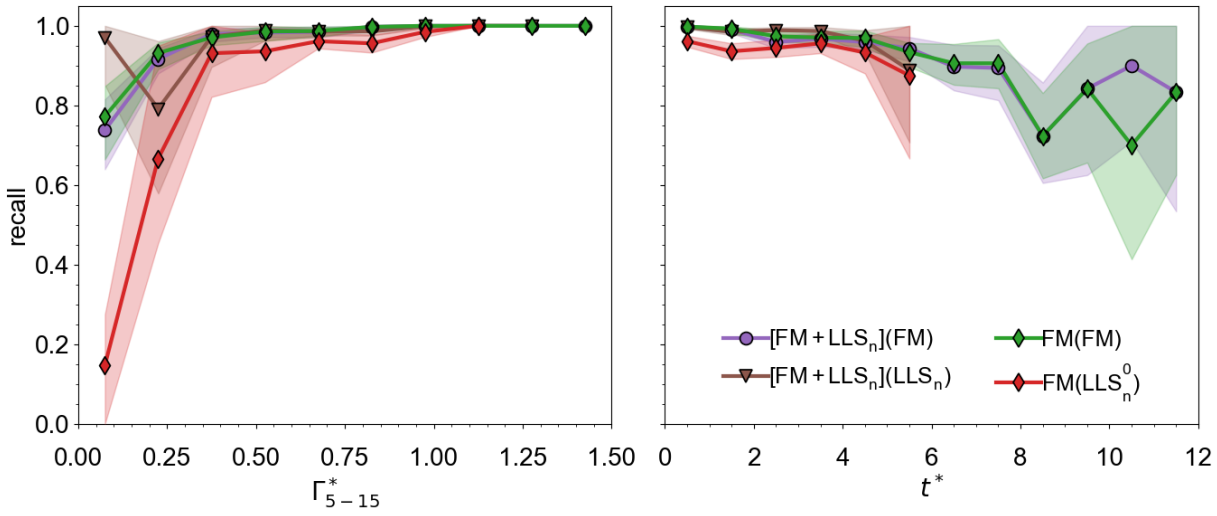

Figure 4.38: Recall for ML pipelines $[FM + LLS_n](FM)$ and $[FM + LLS_n](LLS_n)$ with respect to normalized vortex circulation (left) and age (right) using all available training scans. For reference, cases $FM(FM)$ and $FM(LLS_n^0)$ are also plotted. Bootstrap resampling gives the uncertainty.

4.6.3 Tuning Towards Additional Lidar Setups

A further aspect relevant for practical application of the ML pipeline is its ability to generalize to other lidar setups. The three investigated dataset families greatly share their lidar setup and specifications. The highest wake vortex detection recall rates for the field measurement test subset are achieved using the field measurement training subset, the $\mathrm{LLS_n}$ scans, or the hybrid subset from Section 4.6.2. In this section the ability of these different dataset families to generalize to an alternative lidar setup is investigated. Particularly, it is analyzed whether the provision of few $\mathrm{LLS_n}$ scans of the alternative lidar setup aids the ML pipeline, otherwise trained on the standard lidar setup from Vienna Airport, in detecting wake vortices from the alternative lidar setup.

There is no additional field measurement dataset family available, therefore the LLS_n scans are employed for this investigation. As described in Section 3.3.2, the LLS_n dataset family is divided into scans resembling the Vienna Airport campaign LLS_n^0 and lidar scans from the additional lidar setup LLS_n^+, with example scans given in Figs. 4.39 left and right, respectively. The primary difference between the two lidar setups is that the latter is located significantly further from the aircraft glide path in the lateral direction. Therefore, the SNR is higher throughout the complete RHI scan (see Fig. 3.15). As a reference, wake vortex detection recall rates on LLS_n^0 scans for ML pipelines trained with field measurements and LLS_n^+ scans, or solely field measurements are given by the green and blue curves in Fig. 4.40, respectively. Red and orange curves compare the same ML pipeline models, however testing the vortex detection on lidar scans from the additional lidar setup i.e, LLS_n^+ scans.

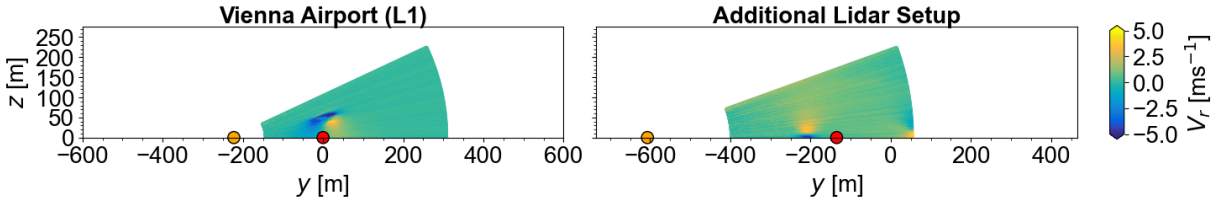

Figure 4.39: Comparison of example LLS_n^0 (left) and LLS_n^+ (right) scans. The red symbols represent the runway centerline and the orange symbols represent the lidar position. The axes correspond to the LES domain.

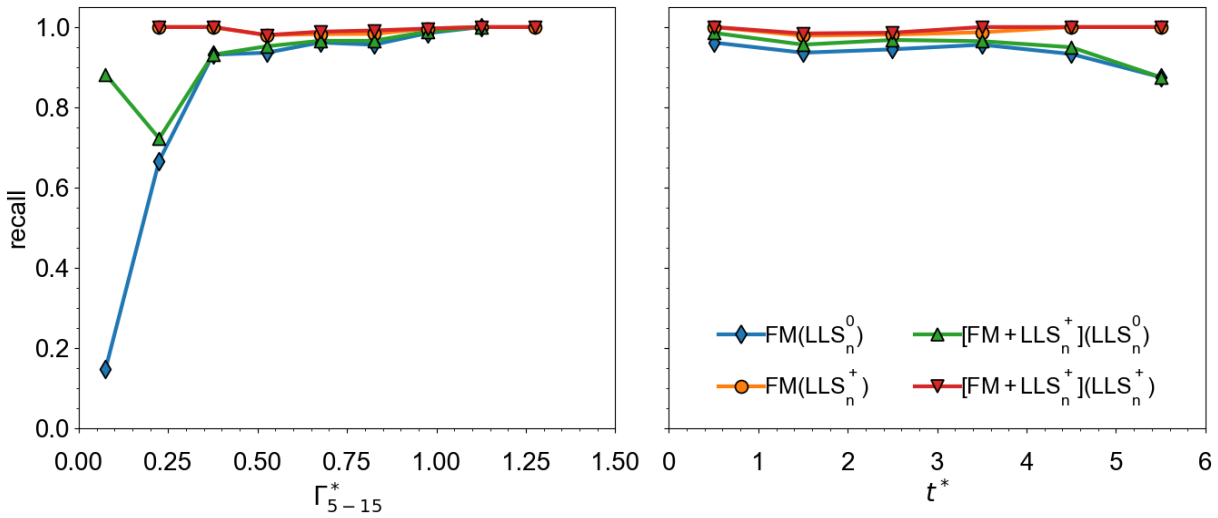

Figure 4.40: Recall for ML pipelines trained with only field measurements or also lidar scans from further setups with respect to normalized vortex circulation (left) and age (right).

Regardless of the ML pipeline, the detection of wake vortices in LLS_n^+ scans is more trivial than detecting wake vortices in LLS_n^0 scans (both the red and orange curves achieve higher recall rates than the green and blue curves). Presumably, the higher SNR of the additional LLS_n^+ scans filters noise as well as secondary vortex structures more strongly. Comparison of the ML pipelines reveals little to no insight regarding the advantage of simulating the additional lidar setup or not. In both cases, evaluating LLS_n^0 or LLS_n^+ scans, the ML pipeline including the LLS_n^+ scans obtains a marginally higher recall rate. It has previously been shown in Fig. 4.38 that ML pipelines trained on field measurements perform well on LLS_n scans, including them in the training subset achieves only minor recall rate improvements. The same is observed in Fig. 4.40.

In order to eliminate the factor of lidar scan structures influencing the comparison (field measurements in comparison to LLS_n scans), Fig. 4.41 compares LLS_n-trained ML pipelines without (LLS_n^0) and with ($[LLS_n^0+LLS_n^+]$) additional lidar setup scans. Trends observed remain minor. Wake vortices in LLS_n^+ scans are detected slightly more often, and the inclusion of LLS_n^+ scans does provide a minor increase in recall rate. Overall, it can nevertheless be concluded that the provision of lidar scans from an additional/alternative lidar setup can improve the detection of wake vortices. However, only for major lidar setup differences a significant detection recall rates improvement is expected. Convolutional layers, which both YOLO and the regression CNN employ, enable translational invariance for detecting wake vortices, furthermore YOLO is largely scale invariant, making the ML pipeline highly generalizable in these regards. Additional factors, such as differences in SNR may alter the pattern of lidar scans, and therefore wake vortex detection success.

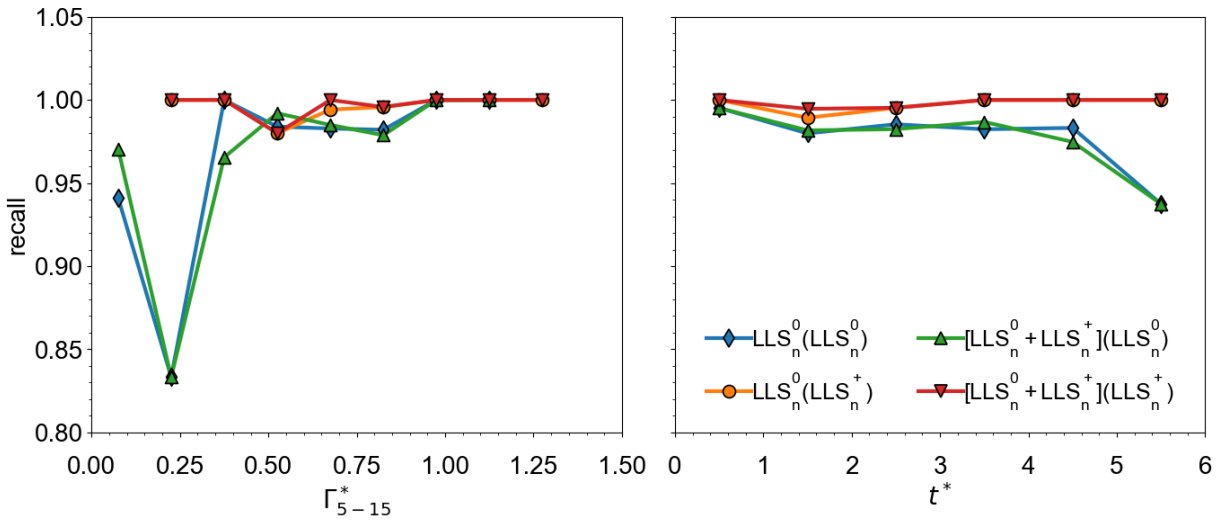

Figure 4.41: Recall for ML pipelines trained with only LLS_n scans or also lidar scans from further setups with respect to normalized vortex circulation (left) and age (right). Note adapted axes in comparison to other recall figures in this thesis.

The wake vortex characterization on the other hand does improve significantly when including lidar scans from the alternative lidar position in the training subset. The RMSE values of the $\mathrm{LLS_n}$ dataset family trained either exclusively on the Vienna Airport lidar positions ($\mathrm{LLS_n^0}$) or on a training subset including scans from the additional lidar position $\left[\mathrm{LLS_n^0} + \mathrm{LLS_n^+}\right]$ are given in Table 4.14. In both cases two test subsets are evaluated, $\mathrm{LLS_n^0}$ and $\mathrm{LLS_n^+}$. First comparing the ML pipelines trained with $\mathrm{LLS_n^0}$ scans only reveals a detrimental vortex position and circulation characterization accuracy on $\mathrm{LLS_n^+}$ scans. However, when additionally including $\mathrm{LLS_n^+}$ scans in the training subset, the RMSE values on $\mathrm{LLS_n^0}$ and $\mathrm{LLS_n^+}$ scans are comparable. While the characterization on $\mathrm{LLS_n^0}$ scans remains similar, the characterization on $\mathrm{LLS_n^+}$ scans is strongly improved. It can thus be concluded that particularly the regression CNN benefits from including lidar scans from the additional lidar setup in the training subset. Instead, the YOLO wake vortex detection is affected less by different lidar positions.

Table 4.14: ML pipeline characterization accuracy analysis for an additional lidar position. The RMSEs of the vortex dimensional and normalized circulation characterizations $\mathrm{E}_{\Gamma_{5-15}}^{\mathrm{RMSE}}$ and $\mathrm{E}_{\Gamma_{5-15}^*}^{\mathrm{RMSE}}$, as well as the dimensional and normalized position two-norm D_C^{RMSE} and $D_C^{\mathrm{RMSE},*}$ (in the Cartesian coordinate system) are provided.

ML Pipeline	D_C^{RMSE} [m]	$D_C^{\mathrm{RMSE},*}$ [-]	$\mathrm{E}_{\Gamma_{5-15}}^{\mathrm{RMSE}}$ [$\mathrm{m^2\ s^{-1}}$]	$\mathrm{E}_{\Gamma_{5-15}^*}^{\mathrm{RMSE}}$ [-]
$\mathrm{LLS_n^0}(\mathrm{LLS_n^0})$	3.2	0.07	29.0	0.07
$\mathrm{LLS_n^0}(\mathrm{LLS_n^+})$	4.2	0.09	42.2	0.10
$\left[\mathrm{LLS_n^0} + \mathrm{LLS_n^+}\right]$ $(\mathrm{LLS_n^0})$	3.1	0.07	27.7	0.06
$\left[\mathrm{LLS_n^0} + \mathrm{LLS_n^+}\right]$ $(\mathrm{LLS_n^+})$	3.3	0.07	32.0	0.07

Chapter 5

Conclusions and Outlook

Wake vortices have in the past and will in the future need to be studied with atmospheric measurement instruments, in order to verify, validate, and conduct postulated theories, mitigation methods, and hazard assessments. Primarily the wake vortex position and strength characterization is required, such that potential rolling moments exerted onto follower aircraft can be quantified and threats assessed. Such wake vortex encounters are particularly of concern along the glide path of aircraft. At airports wake vortices are typically measured employing light detection and ranging (lidar) instruments which deliver high-resolution velocity measurements along the emitted laser beam Line-Of-Sight (LOS). The one-dimensionality of the measurements necessitates dedicated processing algorithms for evaluating the position and strength of the wake vortices accurately. The latter is realized by processing the circulation of wake vortices. Error bounds and limitations of processing algorithms have been documented theoretically and numerically, however their true accuracy is largely unknown, in particular under turbulent atmospheric conditions. Assessment of processing algorithms in the field proves challenging, as no ground truth data are available with conventional atmospheric measurement techniques. Furthermore, although state-of-the-art lidar processing algorithms theoretically deliver high wake vortex characterization accuracies, their deployment for large amounts of data or systems such as a Wake Vortex Advisory System (WVAS) is questionable, given their limited automation or fast-time capabilities. Novel Machine Learning (ML) based processing algorithms have recently been proposed to solve this shortcoming, however these still lack generalizability, reliability, and accuracy. In general, conducting wake vortex measurements is associated with tremendous cost, necessitating efficient and smart planning of the measurement setup as well as processing of the data. Research questions posed by the above scenario were previously given in Section 1.3.

This thesis answers these research questions by performing realistic spatiotemporal lidar simulations within high-fidelity hybrid simulations for a RECAT-EU CAT-B aircraft in the final approach and landing phases using Reynolds-Averaged Navier-Stokes (RANS) and the incompressible Large Eddy Simulation (LES) code Multi Grid Large Eddy Turbulence (MGLET). The initialization of turbulent crosswinds of varying strengths deliver a variety of wake vortex evolutions, due to various interacting physical and atmospheric mechanisms.

The LES runs are performed at realistic scales, enabling comparable dimensions and wind speeds in the simulated lidar scans to field measurements (FMs) from a large-scale wake vortex measurement campaign recently conducted at Vienna Airport. Two types of LES Lidar Simulators (LLSs) are implemented within MGLET. The LLS types differ in the assumed atmospheric noise content and thus assumed Signal-to-Noise Ratio (SNR). An idealized LLS considers no noise, whereas $\mathrm{LLS_n}$ considers low SNR values and aerosol noise similar to measurements from Vienna Airport. Unlike for wake vortices in field measurement data, the ground truth position and strength of wake vortices contained in the simulated lidar scans is accurately known, enabling the assessment of lidar processing algorithms. Herein, three dataset families are employed: FM, LLS, and $\mathrm{LLS_n}$.

This thesis focuses on assessing the legacy Radial Velocity (RV) method for processing wake vortices. Additionally, it provides and assesses a novel two-step ML pipeline, which first employs the popular object detection model You Only Look Once (YOLO) for detecting wake vortices in lidar scans and thereafter individually characterizes the found wake vortices in individual cut-outs, processed bounding boxes, using regression Convolutional Neural Networks (CNNs). The accuracy of supervised ML models strictly depends on the training data they are trained with. Thus, for the first time this thesis evaluates field measurement lidar data employing ML models trained on wake vortex LES data. With this approach inherent errors from the data labeling are reduced and an independence from available labeled field measurements is achieved, promising the applicability of the ML pipeline for any lidar setup.

What are the accuracies and limitations of wake vortex characterization algorithms for lidar measurements?

The first research question posed in this thesis seeks practical error bounds of lidar processing algorithms. The two processing algorithms, the legacy RV method and the novel ML pipeline, are compared based on LLS scans. The practical characterization error bounds of the RV method are found to be at least three times higher in both position (D_C^{RMSE} of 4.6 m rather than 1.0 m) and strength ($\mathrm{E}_{\Gamma_{5-15}}^{\mathrm{RMSE}}$ of 38.7 $\mathrm{m^2\ s^{-1}}$ rather than 10.3 $\mathrm{m^2\ s^{-1}}$) than previously suggested theoretical estimates from analytical means. The recall rate (detected vortices of all available vortices) is above 98 %. While no general wake vortex strength threshold, below which an encounter is considered harmless, is available, the obtained median error bounds may be considered serviceable for most applications. The error spread is more critical, particularly under turbulent atmospheric conditions. This thesis determines the negligence of modeling image vortices for the ground effect as the most significant and consequential assumption of the RV method - wake vortex strengths are severely overestimated near walls. Other effects, such as the low-pass filter characteristic of lidars and assuming a fixed vortex radius for each aircraft type, can lead to strength adulterations as well. With herein simulated wake vortices predominantly located below an altitude of the initial wake vortex separation, a systematic overestimation in vortex strength is found for the RV method.

The characterization error bounds of the ML pipeline, using case *LLS(LLS)* [notation: *training subset(test subset)*], are found to be 39 % lower in position (D_C^{RMSE} of 2.8 m rather than 4.6 m) and 38 % lower in strength ($\mathrm{E}_{\Gamma_{5-15}}^{\mathrm{RMSE}}$ of 23.9 $\mathrm{m^2\ s^{-1}}$ rather than 38.7 $\mathrm{m^2\ s^{-1}}$) compared to estimates by the RV method. The recall rate is above 99 %. The error spread is reduced as well and a systematic strength overestimation is not found. Presumably, the ML pipeline considers the ground (or any wall) during vortex characterization, providing a major advantage for ground-based wake vortex measurements of landing aircraft.

How can ML realize reliable, accurate, and rapid wake vortex characterizations?

The second research question is answered in three parts: wake vortex detection, wake vortex characterization, and the computing time required for the first two steps. The conclusions here refer to ML pipelines where one dataset family builds the training, validation, and test subsets (the third research question covers cross evaluations). The reliability and characterization accuracy of the ML pipeline has largely been covered above (answering the first research question), with the ML pipeline delivering at least comparable results to the valued RV method when employing the LLS dataset family. Also the field measurement dataset family achieves detection recall rates well over 90 % for wake vortices of $\Gamma_{5-15}^{*} \geq 0.175$ (normalized by the root circulation of the wake vortex generating aircraft). Weak wake vortices are naturally more difficult to detect and characterize, given their lower velocity magnitudes and gradients, as well as their weak coherency. The predominant restricting factor for their detection is the low count of wake vortices in the dataset families. Indeed, the above Γ_{5-15}^{*} bound corresponds exactly with strength bins consisting of a sufficient amount of data. While also the highest vortex strength bins include a very low count of vortices, in this regime the vortex velocity magnitudes, gradients, and coherency are stronger and less variable. In comparison to previous data-driven lidar processing algorithms, the vortex position and circulation characterization errors are halved and reduced by a third, respectively.

The size and mass of the wake vortex generating aircraft also impact the ML pipeline detection success. Wake vortices generated by larger and heavier aircraft are more straightforwardly detected in comparison to wake vortices generated by smaller and lighter aircraft. Furthermore, the bounding boxes estimated by YOLO are sized according to the wake vortex generating aircraft, allowing the ML pipeline to estimate RECAT-EU aircraft categories from lidar scans. The regression CNN of the ML pipeline proves not only necessary for the circulation estimation, but also for approximately halving the position estimation error. The computing time required for processing a single lidar scan is approximately two orders of magnitude faster than the RV method, taking less than 0.2 s (considering the ML steps only, the duration of processing steps are assumed negligible for this thesis). Therefore, for the first time fast-time operation, for example for a WVAS monitoring system is possible.

To what extent can simulated data replace measurement data for training ML models?

The third research question posed in this thesis is answered by training the ML pipeline with simulated LES lidar scans in order to process field measurements. Subsets for training, validation, and testing no longer belong to the same dataset family. The detection of wake vortices in field measurements is compared for training subsets from all three dataset families. While the field-measurement-trained ML pipeline detects field measurement wake vortices superiorly to the two ML pipelines, particularly stronger wake vortices are detected respectfully well with the $\mathrm{LLS_n}$-trained ML pipeline. Instead, the LLS-trained ML pipeline delivers poor performance for all vortex strengths. Modeling of atmospheric noise and aerosol noise in $\mathrm{LLS_n}$ scans proves essential for successful wake vortex detection in field measurements, with recall rates differing by up to 35 %.

Since simulations are based on a single RECAT-EU CAT-B aircraft type, other aircraft categories cannot be estimated well from lidar scans. As a result, only wake vortices generated by RECAT-EU CAT-B aircraft obtain recall rates above 90 % for wake vortices of $\Gamma^*_{5-15} \geq 0.375$ (corresponding to the strength threshold with a sufficient amount of wake vortices). The lowest recall rates are obtained for RECAT-EU CAT-D aircraft, the category most different to the simulated aircraft type. Accordingly, YOLO-estimated bounding boxes are only sized correctly for RECAT-EU CAT-B aircraft, impacting the wake vortex position and circulation characterizations by the ML pipeline for the other aircraft categories. Altogether, according to labels by the RV method, the position (D_C^{RMSE}) and circulation ($\mathrm{E}_{\Gamma_{5-15}}^{\mathrm{RMSE}}$) characterization errors are nearly double for *LLS_n(FM)* in comparison to *FM(FM)*. It is thus essential to simulate the aircraft types expected in field measurements in order to achieve serviceable wake vortex processing at airports.

Can the provision of ground truth data help improve the accuracy of lidar processing algorithms?

The fourth research question posed in this thesis addresses the inherent errors of the RV method and the effect on the ML pipeline accuracy. However, the underlying algorithms providing the data labels for the field measurement and $\mathrm{LLS_n}$ dataset families differ. The vortex strength evolution suggests that a permanent offset between the vortex strength determined by the processing algorithms naturally implants a systematic error in the ML pipeline output (when training and test subsets differ). This systematic characterization offset may be lowered employing empirical means. Furthermore, it raises the question of the potential ML pipeline characterization accuracy if the field measurements labels would rest upon a true basis. Two ML pipelines, one trained with field measurements and another trained with $\mathrm{LLS_n}$ scans process test $\mathrm{LLS_n}$ scans. Labels of $\mathrm{LLS_n}$ data represent the ground truth well, hinting at a superior wake vortex detection in comparison to labels by the RV method, particularly evident for weak vortices. However, given the substantial difference in label quality, the satisfactory accuracy by the field-measurement-trained ML pipeline reveals the respectable ability of YOLO to handle imperfect labels. Expectedly, the wake

vortex characterization is also superior when training the ML pipeline with more accurate labels. However, additional factors, such as the advantage of training, validating, and testing the ML pipeline with the same dataset family, as well as the labels originating from the same processing algorithm (unlike for the field measurements) play a role as well. It is nonetheless suggested that the provision of ground truth labels improves the characterization of wake vortices in lidar scans - obtained wake vortex detection and characterization accuracies are superior to a comparable ML pipeline case *FM(FM)*. Undoubtedly, a final verdict may only be given when this study can be repeated with the evaluation of field measurements labeled by more reliable and accurate labels.

On top of answering the posed research question, this thesis also investigates the potential of hybrid datasets, including both field measurements and simulated lidar scans in the training subset, for increased generalizability and tuning the ML pipeline towards new lidar setups. It is established that already few field measurement lidar scans achieve beyond satisfactory wake vortex detection recall and precision rates. Providing additional simulated lidar scans does not obtain higher rates on the field measurement test subset. YOLO also delivers high wake vortex detection recall rates on lidar scans from lidar setups not part of the training subset. However in order to achieve high wake vortex characterization accuracy, including simulated lidar scans in the training subset is beneficial. Thus, tuning the ML pipeline towards an additional lidar position with simulated lidar scans is possible and ensures achieving consistent vortex characterization accuracies across different lidar setups.

Methods developed in this thesis, including high-fidelity LES lidar simulatiors and the ML pipeline, a novel data-driven lidar processing algorithm, shift the state-of-the-art for wake vortex processing of lidar measurements. On the one hand, the most advanced wake vortex lidar simulations are presented in this thesis, offering realistic spatiotemporal averaging, and importantly atmospheric noise as well as aerosol noise modeling, while also simulating physically accurate wake vortex evolutions of landing aircraft. Valuable labeled datasets are produced, with a reliable and accurate ground truth. The presented LES lidar simulators enable realistic simulations of lidar setups and therefore more systematic, efficient, and effectual planning of lidar setups at airports. On the other hand, the generated datasets are employed for two so far unexplored studies. First, lidar processing algorithms are assessed for practical turbulent atmospheric conditions - this puts past and future wake vortex studies relying on these processing algorithms into perspective. Second, LES lidar simulations are used as training data for ML models for processing wake vortices from field measurements. Under the condition that the field measurements are well represented by the $\mathrm{LLS_n}$ scans, i.e., lidar setup, settings, atmospheric conditions, and aircraft types, serviceable wake vortex detection and characterization results are achievable. Alternatively, simulated lidar scans may be employed for tuning the ML pipeline, otherwise trained on field measurements, towards a new lidar setup for added generalizability. Finally, the inability of current state-of-the-art lidar processing algorithms to reliably detect and accurately characterize wake vortices in fast-time is overcome using the ML pipeline.

While the research questions posed in this thesis have been answered to the best extent feasible using the tools and data available, further improvements are expected when

LESs of additional landing aircraft types and RECAT-EU aircraft categories are included in the simulation dataset families. Furthermore, employment of a more sophisticated LES tracking algorithm, for instance considering vortex tilting, may allow tracking weak vortices close to the ground for higher vortex ages. Lastly, the LES runs in this thesis are limited to small-scale turbulent structures owing to the crosswind initialization technique. Field measurements contain large-scale turbulent structures, which if simulated may further improve wake vortex detection and characterization. Ultimately however, the herein presented ML pipeline must be validated on further field measurement campaigns, ideally with labels emerging from accurate measurement techniques, such as particle image velocimetry.

With the overarching goal of studying wake vortices in airport vicinity to construct safe and efficient aircraft throughput, programs such as RECAT-EU build on dynamic aircraft separation schemes requiring methods such as a WVAS to evaluate the hazard of individual situations. Even a WVAS operating in fast-time is presumably not sufficient for enabling dynamic aircraft separations. The ML pipeline only enables the fast-time monitoring within a WVAS. In fact, to dynamically adjust aircraft separations, the evolution of wake vortices must be known well in advance and thus predicted in time. Short-term forecasting may be realized for a WVAS using the introduced LES lidar simulator method, which can provide wake vortex evolutions in varying terrain and atmospheric conditions for different aircraft types. Employing such simulations for training a ML model which is entangled with a physics-based vortex evolution predictor, typically limited by specific terrain and atmospheric setups, may offer the live wake vortex predictions necessary.

Appendix A

Derivation of the Range Gate Weighting Function

This section solves the integral in Eq. (2.34) suggested by Robey and Lundquist (2022),

$$Q_S(s') := \int_{-\infty}^{+\infty} g(s'-s)W(s)ds, \tag{A.1}$$

leading to Eq. (2.35) [Eq. (A.16) below]. First, the non-zero case of Eq. (2.33),

$$W(s) := \begin{cases} 1/\Delta R, & |s| \leq \Delta R/2, \\ 0, & |s| > \Delta R/2, \end{cases} \tag{A.2}$$

and Eq. (2.26),

$$g(s) = \frac{1}{\Delta p\sqrt{\pi}} \exp\left(-\frac{s^2}{\Delta p^2}\right), \tag{A.3}$$

are inserted into Eq. (2.34) [Eq.(A.1) above],

$$Q_S(s') = \int_{-\Delta R/2}^{+\Delta R/2} \frac{1}{\Delta p\sqrt{\pi}} \exp\left[-\frac{(s'-s)^2}{\Delta p^2}\right] \frac{1}{\Delta R} ds. \tag{A.4}$$

Next, parameters are transformed from the spatial domain to the temporal domain i.e., $\Delta p = c\sigma_P/2$ and $\Delta R = cT_W/2$ (including some convenient rearrangements),

$$Q_S(s') = \int_{-\Delta R/2}^{+\Delta R/2} \frac{2}{c\sigma_P\sqrt{\pi}} \frac{2}{cT_W} \exp\left[-\frac{2^2\,(s'-s)^2}{c^2\sigma_P^2}\right] ds. \tag{A.5}$$

The argument of the exponential can be summarized by ξ^2, where

$$\xi = \frac{2\,(s'-s)}{c\sigma_P}, \tag{A.6}$$

enables the derivative with respect to s,

$$\frac{d\xi}{ds} = -\frac{2}{c\sigma_P}. \tag{A.7}$$

Rearranging gives,

$$ds = -\frac{c\sigma_P}{2} d\xi. \tag{A.8}$$

The integration limits therefore become,

$$s = \frac{\Delta R}{2} \rightarrow \xi = \frac{2(s' - \Delta R/2)}{c\sigma_P}, \tag{A.9}$$

$$s = -\frac{\Delta R}{2} \rightarrow \xi = \frac{2(s' + \Delta R/2)}{c\sigma_P}. \tag{A.10}$$

Replacing ds [Eq. (A.8)], the argument of the exponential with ξ^2 [Eq. (A.6)], and the integration limits [Eq. (A.5)] obtains (including some convenient rearrangements),

$$Q_S(s') = -\int_{\frac{2(s'+\Delta R/2)}{c\sigma_P}}^{\frac{2(s'-\Delta R/2)}{c\sigma_P}} \frac{2}{c\sigma_P\sqrt{\pi}} \frac{2}{cT_W} \frac{c\sigma_P}{2} \exp -\xi^2 d\xi, \tag{A.11}$$

$$Q_S(s') = -\frac{1}{cT_W} \frac{2}{\sqrt{\pi}} \int_{\frac{2(s'+\Delta R/2)}{c\sigma_P}}^{\frac{2(s'-\Delta R/2)}{c\sigma_P}} \exp -\xi^2 d\xi, \tag{A.12}$$

$$Q_S(s') = -\frac{1}{cT_W} \left\{ \frac{2}{\sqrt{\pi}} \int_0^{\frac{2(s'-\Delta R/2)}{c\sigma_P}} \exp -\xi^2 d\xi - \frac{2}{\sqrt{\pi}} \int_0^{\frac{2(s'+\Delta R/2)}{c\sigma_P}} \exp -\xi^2 d\xi \right\}. \tag{A.13}$$

With $\mathrm{erf}(x) = (2/\sqrt{\pi}) \int_0^x d\xi \exp(-\xi^2)$, where x is the respective integral limit,

$$Q_S(s') = -\frac{1}{cT_W} \left\{ \mathrm{erf}\left[\frac{2(s' - \Delta R/2)}{c\sigma_P}\right] - \mathrm{erf}\left[\frac{2(s' + \Delta R/2)}{c\sigma_P}\right] \right\}, \tag{A.14}$$

and rearranging gives,

$$Q_S(s') = -\frac{1}{cT_W} \left[\mathrm{erf}\left(\frac{2}{c\sigma_P} s' - \frac{\Delta R}{c\sigma_P}\right) - \mathrm{erf}\left(\frac{2}{c\sigma_P} s' + \frac{\Delta R}{c\sigma_P}\right) \right]. \tag{A.15}$$

Upon replacing $\Delta R = cT_W/2$ and rearranging gives Eq.(2.35),

$$Q_S(s') = \frac{1}{cT_W} \left[\mathrm{erf}\left(\frac{2s'/c + T_W/2}{\sigma_P}\right) - \mathrm{erf}\left(\frac{2s'/c - T_W/2}{\sigma_P}\right) \right]. \tag{A.16}$$

Appendix B

Estimation of the LOS Velocity Without Noise

Banakh and Smalikho (1997) derived the generalized Eq. (2.39),

$$\bar{V}_r(R) = \int_{-\infty}^{+\infty} Q_S(s) V_r(R+s) ds, \tag{B.1}$$

for the rectangular time window and a Gaussian pulse. Below recapitulates their derivation based on the autocorrelation function argument method described by Doviak and Zrnić (1993, chap. 6), which estimates the LOS velocity with

$$\bar{V}_r = \frac{\lambda \arg\left[\bar{B}_z(\delta t)\right]}{4\pi\delta t}, \tag{B.2}$$

where the discrete autocorrelation function is

$$\bar{B}_z(\delta t) = \frac{1}{I-1} \sum_{i=0}^{I-2} \overline{Z(i\delta t)\, Z^*(i\delta t + \delta t)}, \tag{B.3}$$

and the asterisk denotes the complex conjugate. The above can be considered to compute the LOS velocity corresponding to the center of gravity frequency of the echo signal spectrum under the following conditions (Doviak and Zrnić, 1993, chap. 6):

- The Nyquist limits are not exceeded by the spectrum.
- The signal Z is stationary (its statistical properties are constant in time).
- The power spectrum is symmetric or the observed frequency band is smaller than the considered B_0.

With $I >> 2$ and $\sigma_P >> \delta t$, the summation may be transformed to an integration in time,

$$\bar{B}_z(\delta t) = \frac{\mathrm{SNR}}{E_P} \int_{-\infty}^{\infty} P_P(t) \frac{1}{T_W} \int_{-T_W/2}^{T_W/2} \exp\left\{ j \frac{4\pi}{\lambda} \delta t V_r \left[R + \frac{c}{2}(t+t') \right] \right\} dt' dt, \tag{B.4}$$

where the pulse is defined as $P_P(t) = [E_P/(\sigma_P\sqrt{\pi})] \exp(-t^2/\sigma_P^2)$ [equivalent to Eq. (2.26)]. Inserting the above into Eq. (B.2) obtains,

$$\bar{V}_r(R) = \frac{\lambda}{4\pi\delta t} \arctan\left\{ \frac{\int_{-\infty}^{\infty} P_P(t) \frac{1}{T_W} \int_{-T_W/2}^{T_W/2} \sin\left\{\frac{4\pi}{\lambda}\delta t V_r\left[R + \frac{c}{2}(t+t')\right]\right\} dt'dt}{\int_{-\infty}^{\infty} P_P(t) \frac{1}{T_W} \int_{-T_W/2}^{T_W/2} \cos\left\{\frac{4\pi}{\lambda}\delta t V_r\left[R + \frac{c}{2}(t+t')\right]\right\} dt'dt} \right\}. \quad \text{(B.5)}$$

The numerator and denominator can separately be expanded,

$$\int_{-\infty}^{\infty} P_P(t) \frac{1}{T_W} \int_{-T_W/2}^{T_W/2} \sin(\beta + \mu)\, dt'dt \approx$$
$$\int_{-\infty}^{\infty} P_P(t) \frac{1}{T_W} \int_{-T_W/2}^{T_W/2} \left[\sin\beta + \mu\cos\beta - (1/2)\,\mu^2 \sin\beta\right] dt'dt, \quad \text{(B.6)}$$

$$\int_{-\infty}^{\infty} P_P(t) \frac{1}{T_W} \int_{-T_W/2}^{T_W/2} \cos(\beta + \mu)\, dt'dt \approx$$
$$\int_{-\infty}^{\infty} P_P(t) \frac{1}{T_W} \int_{-T_W/2}^{T_W/2} \left[\cos\beta - \mu\sin\beta - (1/2)\,\mu^2 \cos\beta\right] dt'dt, \quad \text{(B.7)}$$

where,

$$\mu(t+t') = \frac{4\pi}{\lambda}\delta t \left\{ V_a\left[R + (t)\frac{c}{2}\right] - V_r(R)\right\}, \quad \text{(B.8)}$$

$$\beta = \frac{4\pi}{\lambda}\delta t V_a(R), \quad \text{(B.9)}$$

and $V_a(R)$ gives the mean velocity of all V_r for that time window T_W i.e., $\bar{V}_r(R)$. Assuming μ is small, allows the following assumptions:

$$\int_{-\infty}^{\infty} P_P(t) \frac{1}{T_W} \int_{-T_W/2}^{T_W/2} \mu(t+t')\, dt'dt \approx 0, \quad \text{(B.10)}$$

$$\int_{-\infty}^{\infty} P_P(t) \frac{1}{T_W} \int_{-T_W/2}^{T_W/2} \mu^2(t+t')\, dt'dt \approx 0. \quad \text{(B.11)}$$

Inserting Eq. (B.8) into Eq. (B.10) and rearranging for $V_a(R)$ i.e., $\bar{V}_r(R)$,

$$\bar{V}_r(R) = \frac{1}{E_P} \int_{-\infty}^{\infty} P_P(t) \frac{1}{T_W} \int_{-T_W/2}^{T_W/2} V_r\left[R + \frac{c}{2}(t+t')\right] dt'dt. \quad \text{(B.12)}$$

The above can be reformulated as the convolution of the range gate profile and the pulse i.e., Eq. (A.1), the Range Gate Weighting Function (RWF) i.e., Eq. (A.16), and finally the cross-correlation of the RWF and the LOS velocity i.e., Eq. (B.1).

Appendix C

Derivation of the Midpoint Rule for the LOS Velocity Estimation

This appendix details the simplified computation of $\bar{V}_r$ for the case SNR >> 1 and no aerosol noise. Robey and Lundquist (2022) previously documented a similar description. The approximation of an one-dimensional integral is referred to as numerical quadrature (Epperson, 2013, chap. 5), where the integral is split into lengths $h_{i'}$, for which the area under the integrand f is approximated. Besides deciding on the magnitude of $h_{i'}$, the approximation of the integrand is a crucial aspect. The midpoint rule is a commonly employed approximation technique due to its accuracy and straightforward implementation; based on the linear Taylor approximation of the integrand it is given by,

$$Q(f;\, a,\, b) := (b-a) f(\frac{a+b}{2}), \tag{C.1}$$

where $b-a$ corresponds to the interval $h_{i'}$ with the midpoint $(a+b)/2$ (Epperson, 2013, chap. 5). For estimating Eq. (2.39) the multiplication of $Q_S \times V_r$ is considered the integrand f. For each $\bar{V}_r$, the midpoint rule is computed I' times, corresponding to the nodes used to approximate the integral. The weighting of each V_r (as a contribution to $\bar{V}_r$) is made up of the typical midpoint rule $h_{i'}$ (contribution to the integral), but equally the RWF $Q_S(s)$ (representing the convolution between the range gate pattern and laser pulse), with s representing the distance along the LOS from the range gate center $R_{j,k}$. Thus, for a single sub-interval

$$Q(V_r;\, h_{i'}) = h_{i'} Q_S(s) V_r(R_{j,k} + s). \tag{C.2}$$

For the complete integral the sum of all Q is computed (Meyer Forsting et al., 2017; Lundquist et al., 2015; Robey and Lundquist, 2022).

Since the contribution of the RWF is bound by $[-\hat{R}, +\hat{R}]$, an under-/overestimation of $\bar{V}_r$ may result. Therefore, the sum of the weights is used as a normalization for each

individual sub-interval contribution,

$$\bar{V}_r(R_{j,k}) \approx \sum_{i'}^{I'} \frac{h_{i'} Q_S(s_{i'})}{\sum_n^{I'} h_n Q_S(s_n)} V_r(R_{j,k} + s_{i'}). \tag{C.3}$$

Note that both sums of the above equation constitute I' components. In the case of equidistant nodes ($h_{i'}$ is constant i.e, h) the general expression reduces to,

$$\bar{V}_r(R_{j,k}) \approx \frac{1}{\sum_n^{I'} h Q_S(s_n)} \sum_{i'}^{I'} h Q_S(s_{i'}) V_r(R_{j,k} + s_{i'}). \tag{C.4}$$

Robey and Lundquist (2022) discuss different patterns for $h_{i'}$, including: equidistant, exponentially spaced, equal RWF area, and equal midpoint area. Below recapitulates some aspects. This thesis employs equidistant aerosols, due to its main two benefits: straightforward implementation and computational efficiency. Particularly with multiple $\bar{V}_r(R_{j,k})$ calculated along a LOS, node overlaps are possible and computations may be reused. On the other hand, high values of Q_S (in other words, the peak of the distribution) are underrepresented by equidistant nodes. Exponentially distributed nodes offer an alternative which takes the aforementioned into account. The equal RWF pattern spacing was first recommended by Meyer Forsting et al. (2017), the area under the RWF curve associated to each individual node is equal. Similarly to the exponential spacing, nodes are more closely spaced at the peak, the contribution by the negligible RWF tails is decreased further. Robey and Lundquist (2022) suggest to keep the midpoint area $h_{i'} Q_S(s_{i'})$ constant which can reduce the error made by the quadrature rule.

List of Acronyms

ANN	Artificial Neural Network
CBL	Convolution Batch Leaky
CBM	Convolution Batch Mish
CDL	Coherent Doppler Lidar
CFL	Courant–Friedrichs–Lewy
CIoU	Complete IoU
CNN	Convolutional Neural Network
COCO	Common Objects in Context
CSP	Cross Stage Partial
cw-CDL	continuous wave CDL
DLR	German Aerospace Center
EASA	European Union Aviation Safety Agency
FAA	Federal Aviation Administration
FM	field measurement
FN	False Negative
FP	False Positive
FWHM	Full-Width at Half Maximum
GP	glide path
GPU	Graphics Processing Unit

ICAO . . . . . International Civil Aviation Organization

IoU . . . . . Intersection over Union

LES . . . . . Large Eddy Simulation

lidar . . . . . light detection and ranging

LLS . . . . . LES Lidar Simulator

LOS . . . . . Line-Of-Sight

LReLu . . . . . Leaky ReLu

LRZ . . . . . Leibniz Rechenzentrum

MAC . . . . . Mean Aerodynamic Chord

mAP . . . . . mean Average Precision

MGLET . . . . . Multi Grid Large Eddy Turbulence

ML . . . . . Machine Learning

MRS . . . . . Minimum Radar Separation

MSE . . . . . Mean Squared Error

MTOM . . . . . Maximum Take-Off Mass

nm . . . . . nautical miles

PAN . . . . . Path Aggregation Network

PCDL . . . . . Pulsed Coherent Doppler Lidar

PM . . . . . Projection Method

PRC . . . . . Precision-Recall Curve

R-CNN . . . . . Region-based CNN

radar . . . . . radio detection and ranging

RANS . . . . . Reynolds-Averaged Navier-Stokes

RCR . . . . . Roll Control Ratio

ReLu . . . . . Rectified Linear unit

RHI . . . . . Range-Height Indicator

RMS . . . . . Root Mean Square

RMSE . . . . . Root Mean Squared Error

RV . . . . . Radial Velocity

RWF . . . . . Range Gate Weighting Function

SHAPe . . . . . Simplified Hazard Area Prediction

SNR . . . . . Signal-to-Noise Ratio

sodar . . . . . sonic detection and ranging

SPP . . . . . Spatial Pyramid Pooling

SSD . . . . . Single Shot Multibox Detector

ST . . . . . Simulation Truth

TAS . . . . . True Air Speed

TN . . . . . True Negative

TP . . . . . True Positive

VE . . . . . Velocity Envelope

WVAS . . . . . Wake Vortex Advisory System

YOLO . . . . . You Only Look Once

List of Abbreviations

Com	compressed
ConvPool	convolutional pooling
DN	down
est	estimate
im	image
lbl	label
lid	lidar
max	maximum
med	median
Prt	port
rec	received
ref	reference
req	required
Stc	stretched
Str	starboard
UP	up

List of Symbols

Symbols

$+\varphi$, $-\varphi$	Positive and negative scanning rate
$[dx, dy, dz]$	Numerical domain resolution, m
$[dyy, dzz]$	Bounding box resolution, m
$[u_{\mathrm{RMS}}, v_{\mathrm{RMS}}, w_{\mathrm{RMS}}]$	RMS velocity fluctuations, m s^{-1}
$[V_x, V_r, V_\theta]$	Cylindrical velocity vector, m s^{-1}
$[x, r, \varphi]$	Cylindrical coordinate vector, m, m, deg
$[X, Y, Z]$	LES domain dimensions, m
$[yy, zz]$	Cartesian bounding box coordinates, m
α, β	Wall switching function parameters
α	Activation function
α	Angle of attack, deg
$\alpha_{i'}$	Amplitude of a sub-signal
β_π	Backscatter coefficient
β_{ss}	Aircraft sideslip angle, deg
$\boldsymbol{\kappa}$, $k \times k$	Convolutional kernel
$\boldsymbol{\omega}$, $[\omega_x, \omega_y, \omega_z]$	Cartesian vorticity vector, s^{-1}
$\boldsymbol{\rho}$, $[x'', y'']$	Laser beam cross-section coordinate vector, m
χ	Wind strength factor
Δf	Frequency resolution, Hz

Δp	Spatial pulse width e^{-1} from peak, m
ΔR	Spatial range gate width, m
Δr	Spatial FWHM pulse width, m
δR	Spatial sampling interval, m
δt	Temporal sampling interval, s
ΔV	Velocity resolution, m s^{-1}
Δz	Sensing volume length, m
Δ	Difference between two quantities
δ	Dirac delta function
δ	Half-channel width, m
δ_c	Control surface deflection, deg
η	Learning rate
η	Quantum efficiency
Γ	Vortex circulation, m^2 s^{-1}
γ	Glide path angle, deg
Γ_0	Initial/root circulation, m^2 s^{-1}
Γ_{5-15}	Averaged vortex circulation (radii 5 to 15 m), m^2 s^{-1}
$\hat{R}$	Maximum midpoint rule interval distance, m
κ	von Kármán constant
Λ	Wing aspect ratio
λ	Laser wavelength, m
λ	YOLO loss function weighting factors
$[r, \varphi, \theta]$	Spherical coordinate vector, m, deg, deg
$\mathbf{e}$	Unit direction vector
$\mathbf{n}$	Normal unit vector to surface, m
$\mathbf{p}$, (w, b)	Trainable parameters

$\mathbf{V}$, $[u, v, w]$	Cartesian velocity vector, m s^{-1}
$\mathbf{x}$, $[x, y, z]$	Cartesian coordinate vector, m
$\mathcal{L}$	Loss
μ	Dynamic viscosity, kg m^{-1} s^{-1}
ν	Photon frequency, Hz
ν	Viscosity, kinematic viscosity, m^2 s^{-1}
ν_t	Eddy viscosity, m^2 s^{-1}
ω_0	Vorticity unit, s^{-1}
ω_S	Scanning rate, deg s^{-1}
Ψ	Power scaling parameter
ρ_∞	Fluid density, kg m^{-3}
σ	Logistic activation function
σ	Standard deviation
σ_P	Temporal pulse width e^{-1} from peak, s
τ_P	Temporal FWHM pulse width, s
τ_w	Wall shear stress, N m^{-2}
E	Error
P	Probability
Re_τ	Intrinsic Reynolds number
T	Threshold
θ	Aircraft pitch angle, deg
ε_1, ε_2, $\varepsilon_3, \varepsilon_4$	Pseudo-random parameters
ζ	Aerosol noise
A	Area, m^2
A	Number of YOLO anchor boxes
a_0	Laser beam radius at intensity level e^{-1}, m

B	Bandwidth, Hz
B	Wingspan, m
b	Bounding box estimate
b	Counter-rotating vortex pair separation, m
b_0	Initial counter-rotating vortex pair separation, m
c, α, v	Loss function parameters
C	Curve, m
C	Dimensionless coefficient
C	Vortex center
C	YOLO-confidence
c	Airfoil chord length, m
c	Speed of light in air, m s^{-1}
c_x, c_y, p_w, p_h	Anchor box coordinates, width, and height, m
C_{L_p}	Roll damping coefficient
$d\varphi$	Elevation angle resolution, deg
D, G	Functionals of the RV method
D	Dataset
D_C	Euclidean distance between vortex centers, m
D_i	Wing induced drag, N
dR	Range gate spacing, m
dt	Timestep, s
E_P	Pulse energy, J
f	Frequency, Hz
f_P	Pulse repetition frequency, Hz
g	Gaussian laser pulse
g	Gravitational acceleration, m s^{-2}

g_t . . . . . Loss function gradient

H . . . . . Lidar scan height, m

h . . . . . Aerosols distribution spacing along a LOS, m

h . . . . . Bounding box height, m

h . . . . . Perpendicular distance from vortex filament, m

h . . . . . Planck's constant, kg m^2 s^{-1}

I' . . . . . Number of modeled aerosols

I . . . . . Sample number

I_{PN} . . . . . Normalized laser beam intensity

L . . . . . Number of spectral channels

L . . . . . Wing lift, N

l . . . . . Airfoil/local lift, N m^{-1}

m, v, η, ϵ, β_1, β_2, g . . . . . Adam optimizer parameters

M . . . . . Aircraft mass, kg

M_L . . . . . Aircraft rolling moment, N m

$N \times M$ . . . . . Grid size of YOLO output

N_a . . . . . Number of pulses for accumulation

N_x . . . . . Number of x cases

O . . . . . Objectness of a bounding box estimate

P . . . . . Laser pulse

p . . . . . Fluid pressure, N m^{-2}

P_P . . . . . Pulse power, W

P_S . . . . . Signal power, W

q . . . . . Convolutional function

Q_S . . . . . Range gate weighting function, m^{-1}

R . . . . . Distance along the LOS from the lidar, m

R_C	Roll control potential
RCR	Roll control ratio
S	Average signal spectrum
S	Strain rate tensor, s^{-1}
S	Wing planform area, m^2
s	Coordinate along a LOS, m
s	Spanwise load factor
T	Computational wall time, s
t	Anchor box to bounding box offset
t	Time, s
t	Vortex age, s
t_0	Characteristic time, s
T_{onset}	Time separating vortex decay phases, s
t_L	Vortex age with respect to aircraft touchdown, s
T_W	Temporal range gate width, s
u_1, u_2, u_3	Cartesian velocity components, m s^{-1}
U_∞	Freestream velocity, True Air Speed, m s^{-1}
u_τ	Wall friction velocity, m s^{-1}
u_{tan}	Tangential velocity to a wall, m s^{-1}
v, c, α	YOLO loss function parameters
W	Lidar scan width, m
W	Range gate indicator function
w	Bounding box width, m
w_0	Initial vortex descend speed, m s^{-1}
x, y	Input and output
x_1, x_2, x_3	Cartesian coordinates, m
Z	Temporal backscatter
V_r	LOS velocity, m s^{-1}

Superscripts

$'$	Alternative, deviation
$'$	Lidar coordinates
$*$	Normalized by wake vortex parameters
$+$	Additional lidar positions
$+$	Normalized by intrinsic channel flow parameters
0	Reference
B	Background lidar scan
V	Wake vortex lidar scan

Subscripts

$-, +$	Minimum, Maximum
0	Initial, Reference
c	Control surface
c	Vortex core
D	Doppler
f	Follower aircraft
f	Frequency band
i	Induced
N	Noise
O	Lidar origin
S	Signal

List of Figures

1.1 Photo of the measuring Vaisala WINDCUBE® 200s lidar at Vienna Airport and animation of a measuring on-ground lidar. 4

2.1 Schematic of the closed vortex ring system for modeling a finite wing. . . . 14
2.2 Schematic of a detaching vortex sheet from the wing and rolling up to trailing wake vortices. 16
2.3 Schematic of the two-phase wake vortex pair decay. 19
2.4 Modeling of a wake vortex induced boundary using image vortices. 20
2.5 Interaction of a wake vortices in ground vicinity with a prevailing crosswind. 21
2.6 Photos of the experimental Plate Line at Vienna Airport and the permanent plate design. 21
2.7 Cylindrical coordinate system of a vortex. 23
2.8 Tangential velocity profiles of different vortex models. 24
2.9 Schematic of a counter-rotating analytical vortex pair. 25
2.10 Schematic of a lidar performing a RHI scan. 29
2.11 Schematic of a RHI scan with LOSs, measurement points, and range gates. 30
2.12 Example Doppler power spectrum of a range gate along a lidar LOS. . . . 33

3.1 Schematic of the hybrid aircraft numerical simulation approach. 36
3.2 The unstructured RANS grid in flow direction. 38
3.3 Axial vorticity distribution around the Airbus A340 in a RANS simulation. 38
3.4 Weighting function combining the RANS and the LES flow fields. 40
3.5 Schematic of a virtual lidar setup with respect to the LES computational domain. 42
3.6 Horseshoe closure of the wake vortex filaments at LES start-up. 44
3.7 Turbulent wind statistics initialized in LESs. 46
3.8 Schematic of the padding method for simulated lidar measurements. 48
3.9 Influence of LLSs on the LES computational time. 49
3.10 Range Gate Weighting Function distribution. 50
3.11 Schematic of an emitted laser pulse traveling through a range gate window. 51
3.12 Vaisala WINDCUBE® 200s at Vienna Airport. 55
3.13 Positioning of lidar instruments at runway 16 of Vienna Airport. 56
3.14 Example RHI lidar scans from Vienna Airport. 57

3.15 Mean SNR distribution of the field measurement dataset family. 58
3.16 Distributions of absolute normalized/dimensional vortex circulation and vortex age of the field measurement training subset. 59
3.17 Distributions of absolute normalized/dimensional vortex circulation and vortex age of the LLS and LLS_n training subsets. 61
3.18 Example SNR distribution of a LLS_n scan. 61
3.19 Example computation of the functional $D(R)$ for all distance from the lidar. 63
3.20 Schematic of the ML pipeline. 66
3.21 Schematic of a simplified universal Cartesian grid in the lidar coordinate system. 69
3.22 Example of the pre-processing performed for RHI lidar scans. 71
3.23 Schematic of the YOLOv4 architecture. 73
3.24 Schematics of individual YOLOv4 blocks. 73
3.25 Schematic of the relationship between an anchor box and a bounding box estimation. 75
3.26 Recall, precision, and mAP with respect to the IoU and YOLO-confidence thresholds. 77
3.27 Example of YOLO-estimated bounding boxes with YOLO-confidence and class. 78
3.28 Regression CNN architecture. 79
3.29 Example of the regression CNN characterizing two wake vortices previously detected by YOLO. 81

4.1 Airbus A340 landing showcasing the complete wake vortex roll up to a counter-rotating pair. 84
4.2 Airbus A340 landing showcasing detaching secondary vortices from the ground. 84
4.3 Airbus A340 landing with interacting secondary and wake vortices. 85
4.4 Temporal evolution of wake vortices, in terms of circulation Γ^*_{5-15}, lateral position y^*_C, and distance above the ground z^*_C, in quiescent atmosphere. . 86
4.5 Longitudinal evolution of wake vortices, in terms of circulation Γ^*_{5-15}, lateral position y^*_C, and distance above the ground z^*_C, in quiescent atmosphere. . 86
4.6 Temporal evolution of wake vortices, in terms of circulation Γ^*_{5-15}, lateral position y^*_C, and distance above the ground z^*_C, under various port crosswind strengths. 88
4.7 Longitudinal evolution of wake vortices, in terms of circulation Γ^*_{5-15}, lateral position y^*_C, and distance above the ground z^*_C, under various port crosswind strengths. 88
4.8 Airbus A340 landing showcasing the asymmetric vorticity layer on the ground as a result of crosswind. 89
4.9 Airbus A340 landing simulation with a port $1.0w_0$ crosswind showcasing the complex vortex evolution in time. 91
4.10 Example RV-method-characterized LLS scans in challenging scenarios with and without RWF. 92

4.11 Zoomed in example LLS and $\mathrm{LLS_n}$ RHI lidar scans. 95
4.12 Example $\mathrm{LLS_n}$ RHI lidar scan for varying pulse accumulation count N_a. . . 95
4.13 RV method accuracy histogram using D_C^* and $\mathrm{E}_{\Gamma^*_{5-15}}$ with respect to the vortex count. 98
4.14 Comparison of the wake vortex circulation Γ^*_{5-15} estimated by the RV method and the simulation truth. 99
4.15 RV method circulation characterization errors in an example LLS scan geometry. 102
4.16 RV method circulation characterization error $\mathrm{E}_{\Gamma^*_{5-15}}$ against vortex altitude z^*_C. 103
4.17 Comparison of stretched and compressed wake vortex correlations of the circulation Γ^*_{5-15} estimated by the RV method and the simulation truth. . 105
4.18 RV method circulation magnitude error based on assuming a wrong core radius. 106
4.19 Difference in vortex circulation estimation with respect to the difference in core radius. 106
4.20 ML pipeline accuracy histogram for *LLS(LLS)* using D_C^* and $\mathrm{E}_{\Gamma^*_{5-15}}$ with respect to the vortex count. 109
4.21 ML pipeline circulation characterization error $\mathrm{E}_{\Gamma^*_{5-15}}$ against vortex altitude z^* for *LLS(LLS)*. 109
4.22 Recall and precision for ML pipelines trained on the three different dataset families and tested on field measurements with respect to vortex circulation. 112
4.23 Recall and precision for ML pipelines trained on the three different dataset families and tested on field measurements with respect to vortex age. . . . 113
4.24 Example of a noisy lidar scan processed by ML pipeline case *LLS$_n$(FM)*. . 114
4.25 Example ML pipeline detections in comparison to available labels. 115
4.26 Recall split by RECAT-EU aircraft categories for ML pipelines trained using the FM or $\mathrm{LLS_n}$ dataset families and tested on field measurements with respect to vortex circulation. 116
4.27 Mean normalized YOLO-estimated bounding box area with respect to the vortex circulation for FM- and $\mathrm{LLS_n}$-trained ML pipelines split into RECAT-EU aircraft categories. 117
4.28 ML pipeline normalized vortex position and circulation characterization errors with respect to the normalized vortex circulation for ML pipelines *FM(FM)* and *LLS$_n$(FM)*. 119
4.29 ML pipeline vortex position and circulation characterization errors with respect to the vortex age for ML pipelines *FM(FM)* and *LLS$_n$(FM)*. 119
4.30 ML pipeline vortex position and circulation characterization errors with respect to the dimensional vortex circulation for ML pipelines *FM(FM)* and *LLS$_n$(FM)*. 120
4.31 Evolution of the vortex position and circulation characterization errors with respect to the normalized YOLO-estimated bounding box area for the ML pipeline case *LLS$_n$(FM)* with the associated vortex distribution. 121

4.32 Evolutions of the difference between the normalized field measurement and lidar simulation truth circulation labels via $\Delta\Gamma^*_{5-15}$ and the error of the normalized vortex circulation characterization $\mathrm{E}^{\mathrm{mean}}_{\Gamma^*_{5-15}}$ for the ML pipeline case *LLS_n(FM)*, with respect to vortex age. 124
4.33 Recall for ML pipelines trained using the FM or $\mathrm{LLS}^0_\mathrm{n}$ dataset families and tested on LLS_n scans with respect to vortex circulation and age. 124
4.34 ML pipeline vortex position and circulation characterization errors with respect to the vortex circulation for ML pipelines *FM(LLS^0_n)* and *LLS^0_n(LLS^0_n)*. 126
4.35 ML pipeline vortex position and circulation characterization errors with respect to the vortex age for ML pipelines *FM(LLS^0_n)* and *LLS^0_n(LLS^0_n)*. . . . 126
4.36 Evolution of the vortex detection mAP@25 for the ML pipelines *FM(FM)* and $[FM + LLS_n](FM)$ and varying training subset compositions. 128
4.37 Comparison of the median mAP@25 evolutions for the ML pipelines *FM(FM)* and $[FM + LLS_n](FM)$. 128
4.38 Recall for ML pipelines *$[FM + LLS_n]$(FM)* and *$[FM + LLS_n]$(LLS_n)* with respect to vortex circulation and age using all available training scans. . . . 129
4.39 Comparison of example $\mathrm{LLS}^0_\mathrm{n}$ and $\mathrm{LLS}^+_\mathrm{n}$ scans. 130
4.40 Recall for ML pipelines trained with only field measurements or also lidar scans from further setups with respect to vortex circulation and age. 130
4.41 Recall for ML pipelines trained with only LLS_n scans or also lidar scans from further setups with respect to vortex circulation and age. 131

List of Tables

1.1 ICAO wake vortex separation minima. 2
1.2 RECAT-EU aircraft categories sorted by aircraft types. 3
1.3 RECAT-EU wake vortex separation minima including aircraft categories relevant for commercial airport operations. 3

3.1 RANS simulation parameters in high-lift configuration. 39
3.2 Normalization parameters for the $1:1$ numerical simulation setup. 39
3.3 Turbulent crosswind specifications in terms of imposed pressure gradient and intrinsic Reynolds number. 46
3.4 Settings of the WINDCUBE® 200s lidar. 54
3.5 Lidar setup at Vienna Airport (field measurements). 57
3.6 Shared LLS and $\mathrm{LLS_n}$ parameters in the LES computational domain. . . . 60

4.1 Dataset for assessing the RV method split by wind strength and wake vortex type. 97
4.2 RV method characterization accuracy analysis including individual error bounds for starboard and port vortices. 97
4.3 Comparison of RV method characterization error bounds using the LLS analysis and previous theoretical analysis. 100
4.4 RV method characterization accuracy analysis split by turbulent crosswind strength. 100
4.5 RV method characterization accuracy analysis split by luff and lee vortices. 101
4.6 LLS test subset for assessing the ML pipeline split by wind strength and wake vortex type. 107
4.7 ML pipeline characterization accuracy analysis with *LLS(LLS)* including individual error bounds for starboard and port vortices. 108
4.8 ML pipeline characterization accuracy analysis split by turbulent crosswind strength. 110
4.9 ML pipeline characterization accuracy analysis with *LLS(LLS)* split by luff and lee vortices. 110
4.10 Initial counter-rotating vortex pair separation for example aircraft types. . 117
4.11 ML pipeline characterization accuracy analysis with cases *FM(FM)* and *LLS_n(FM)*. 118

4.12 ML pipeline characterization accuracy analysis with case $LLS_n(FM)$ split by RECAT-EU aircraft categories. 122
4.13 ML pipeline characterization accuracy analysis with cases $FM(LLS_n^0)$ and $LLS_n^0(LLS_n^0)$. 127
4.14 ML pipeline characterization accuracy analysis for an additional lidar position. 132

Bibliography

Ai, Y., Wang, Y., Pan, W., and Wu, D. (2021). A deep learning framework based on multisensor fusion information to identify the airplane wake vortex. *J. Sens.*, 2021:1–10. DOI: 10.1155/2021/4819254.

Anderson, J. (1984). *Fundamentals of aerodynamics*. McGraw-Hill, 1st edition.

Banakh, V. and Smalikho, I. (1997). Estimation of the turbulence energy dissipation rate from the pulsed Doppler lidar data. *Atmos. Oceanic Opt.*, 10:957–965. [Available from `https://ao.iao.ru/en/content/text?vol=10&issue=12&num=18`].

Banakh, V. and Smalikho, I. (2013). *Coherent Doppler Wind Lidars in a Turbulent Atmosphere*. Artech House.

Bao, F. and Vollmers, H. (2005). Alleviation of end-effect in facilities for far wake investigations. In *43rd AIAA Aerospace Sciences Meeting and Exhibit*. American Institute of Aeronautics and Astronautics. DOI: 10.2514/6.2005-907.

Baranov, N. and Resnick, B. (2021). Wake vortex detection by convolutional neural networks. *Int. J. Electr. Eng. Comput. Sci.*, 3:92–97. [Available from `https://www.wseas.com/journals/eeacs/2021/eeacs2021-015.pdf`].

Baumert, H. (2013). Universal equations and constants of turbulent motion. *Phys. Scr.*, 2013(T155). DOI: 10.1088/0031-8949/2013/T155/014001.

Bishop, C. (2006). *Pattern Recognition and Machine Learning*. Springer.

Bochkovskiy, A. (2021). YOLO v4, v3 and v2 for Windows and Linux. Online. [Available from `https://github.com/AlexeyAB/darknet/`]. Last accessed: 28.02.2025.

Bochkovskiy, A., Wang, C., and Liao, H. (2020). YOLOv4: optimal speed and accuracy of object detection. DOI: 10.48550/ARXIV.2004.10934.

Bodla, N., Singh, B., Chellappa, R., and Davis, L. (2017). Soft-NMS — improving object detection with one line of code. In *IEEE Int. Conf. Comput. Vis.*, pages 5562–5570. DOI: 10.1109/ICCV.2017.593.

Bouraya, S. and Belangour, A. (2021). Deep learning based neck models for object detection: a review and a benchmarking study. *Int. J. Adv. Comput. Sci. Appl.*, 12(11):161–167. DOI: 10.14569/ijacsa.2021.0121119.

Breitsamter, C. (2007). *Nachlaufwirbelsystem großer Transportflugzeuge*. Herbert Utz Verlag.

Breitsamter, C. (2011). Wake vortex characteristics of transport aircraft. *Prog. Aeronaut. Sci.*, 47(2):89–134. DOI: 10.1016/j.paerosci.2010.09.002.

Brockman, P., Barker, B., Koch, G., Nguyen, D., Britt, C., and Petros, M. (1999). Coherent pulsed lidar sensing of wake vortex position and strength, winds and turbulence in the terminal area. In *Tenth Biennial Coherent Laser Radar Technology and Applications Conference*. NASA. 20000012986.

Brown, A. and Holzäpfel, F. (2024). Case studies in modelling cruise-generated trailing vortices. In *AIAA AVIATION FORUM AND ASCEND 2024*. American Institute of Aeronautics and Astronautics. DOI: 10.2514/6.2024-3773.

Brown, A. and Holzäpfel, F. (2025). Case studies in modeling cruise-generated trailing vortices. *J. Airc.*, pages 1–16. DOI: 10.2514/1.c038627.

Burnham, D. and Hallock, J. (1982). Chicago monostatic acoustic vortex sensing system. Technical Report DOT-TSC-FAA-79-103.IV, Federal Aviation Administration. [Available from `https://rosap.ntl.bts.gov/view/dot/9391`].

Burnham, D. and Hallock, J. (2013). Decay characteristics of wake vortices from jet transport aircraft. *J. Aircr.*, 50(1):82–87. DOI: 10.2514/1.c031715.

Cariou, J.-P. and Boquet, M. (2011). Leosphere pulsed lidar principles. Technical report, Leosphere. [Available from `https://www.upwind.eu/images/d6.1.1.pdf`].

Charette, S. (2025). Darknet FAQ. Online. [Available from `https://www.ccoderun.ca/programming/2020-09-25_Darknet_FAQ/`]. Last accessed: 28.02.2025.

Cheng, J., Hoff, A., Tittsworth, J., and Gallo, W. (2016). The development of wake turbulence re-categorization in the United States (invited). In *8th AIAA Atmospheric and Space Environments Conference*. American Institute of Aeronautics and Astronautics. DOI: 10.2514/6.2016-3434.

Chollet, F. (2018). *Deep learning with Python*. Manning Publications Company, Birmingham.

Chollet, F. et al. (2015). Keras. [Available from `https://keras.io`].

Chu, N., Ng, K., Liu, Y., Hon, K., Chan, P., Li, J., and Zhang, X. (2024a). Assessment of approach separation with probabilistic aircraft wake vortex recognition via deep learning. *Transp. Res. E Logist. Transp. Rev.*, 181. DOI: 10.1016/j.tre.2023.103387.

Chu, N., Ng, K., Zhu, X., Liu, Y., Li, L., and Hon, K. (2024b). Towards dynamic flight separation in final approach: a hybrid attention-based deep learning framework for long-term spatiotemporal wake vortex prediction. *Transp. Res. C Emerg. Technol.*, 169. DOI: 10.1016/j.trc.2024.104876.

Constant, G., Foord, R., Forrester, P., and Vaughan, J. (1994). Coherent laser radar and the problem of aircraft wake vortices. *J. Mod. Opt.*, 41(11):2153–2173. DOI: 10.1080/09500349414552021.

Coton, P. (1998). Study of environment effects by means of scale model flight tests in a laboratory. In *21st International Council of the Aeronautical Sciences Congress*. ICAS–98–391.[Available from `https://icas.org/icas_archive/ICAS1998/PAPERS/391.PDF`].

Coustols, E., Stumpf, E., Jacquin, L., Moens, F., Vollmers, H., and Gerz, T. (2003). Minimised wake: a collaborative research programme on aircraft wake vortices. In *41st Aerospace Sciences Meeting and Exhibit*. American Institute of Aeronautics and Astronautics. DOI: 10.2514/6.2003-938.

Critchley, J. and Foot, P. (1991). UK CAA wake vortex database: analysis of incidents reported between 1982 and 1990. Technical Report CAA Paper 91015, Civil Aviation Authority.

Crow, S. (1970). Stability theory for a pair of trailing vortices. *AIAA J.*, 8(12):2172–2179. DOI: 10.2514/3.6083.

Crow, S. and Bate, E. (1976). Lifespan of trailing vortices in a turbulent atmosphere. *J. Aircr.*, 13(7):476–482. DOI: 10.2514/3.44537.

Darracq, D., Corjon, A., Ducros, F., Keane, M., Buckton, D., and Redfern, M. (2000). Simulation of wake vortex detection with airborne Doppler lidar. *J. Aircr.*, 37(6):984–993. DOI: 10.2514/2.c9307-b.

De Visscher, I., Rooseleer, F., and Graham, R. (2020). Time-based separation (TBS) principles as alternative to static distance based separation for final approach. Technical report, EUROCONTROL. [Available from `https://www.eurocontrol.int/publication/eurocontrol-guidelines-time-based-separation-tbs-final-approach`].

Delisi, D., Pruis, M., Wang, F., and Lai, D. (2013). Estimates of the initial vortex separation distance, b_0, of commercial aircraft from pulsed lidar data. In *51st AIAA Aerospace Sciences Meeting including the New Horizons Forum and Aerospace Exposition*. American Institute of Aeronautics and Astronautics. DOI: 10.2514/6.2013-365.

Deng, L., Pan, W., Luan, T., Zhang, C., and Leng, Y. (2024). Rapid aircraft wake vortex identification model based on optimized image object recognition networks. *Aerospace*, 11(10):840. DOI: 10.3390/aerospace11100840.

DLR (2006). Wake vortices – fascination of an invisible phenomenon. DVD.

Dolfi-Bouteyre, A., Augere, B., Besson, C., Canat, G., Fleury, D., Gaudo, T., Goular, D., Lombard, L., Planchat, C., Valla, M., Cariou, J., Petilon, O., and Lawson-Daku, J. (2008). 1.5 µm all fiber pulsed lidar for wake vortex monitoring. In *Conference on Lasers and Electro-Optics*, pages 1–2. Institute of Electrical and Electronics Engineers. DOI: 10.1109/cleo.2008.4551273.

Doligalski, T., Smith, C., and Walker, J. (1994). Vortex interactions with walls. *Annu. Rev. Fluid Mech.*, 26(1):573–616. DOI: 10.1146/annurev.fl.26.010194.003041.

Doviak, R. and Zrnić, D. (1993). *Doppler Radar and Weather Observations*. Academic Press, 2nd edition.

Duan, S., Pan, W., Leng, Y., and Zhang, X. (2023). Two ResNet mini architectures for aircraft wake vortex identification. *IEEE Access*, 11:20515–20523. DOI: 10.1109/access.2023.3249298.

Dufresne, L., Baumann, R., Gerz, T., Winckelmans, G., Moet, H., Capart, R., Cocle, R., and Nybelen, L. (2005). Large eddy simulation of wake vortex flows at very high Reynolds numbers: a comparison of different methodologies. Technical Report AWIATOR D1.14-16, Université Catholique de Louvain.

Ehlers, J., Fischenberg, D., and Niedermeier, D. (2015). Wake impact alleviation control based on wake identification. *J. Airc.*, 52(6):2077–2089. DOI: 10.2514/1.c033157.

Epperson, J. (2013). *An introduction to numerical methods and analysis*. John Wiley & Sons.

Etkin, B. (1972). *Dynamics of Atmospheric Flight*. John Wiley & Sons, 1st edition.

EUROCONTROL (2024). Aviation long-term outlook. Technical report, EUROCONTROL. [Available from `https://www.eurocontrol.int/sites/default/files/2024-12/eurocontrol-aviation-long-term-outlook-flights-co2-forecast-2024-2050.pdf#`].

EUROCONTROL (2025). Seven-year forecast 2025-2031. Technical report, EUROCONTROL. [Available from `https://www.eurocontrol.int/sites/default/files/2025-02/eurocontrol-seven-year-forecast-2025-2031-february-2025.pdf`].

EUROCONTROL and Isambert, E. (2022). Assignment of aircraft types to RECAT-EU wake turbulence categories. Technical report, European Aviation Safety Agency. [Available from `https://www.easa.europa.eu/en/assignment-icao-aircraft-types-recat-eu-wake-turbulence-categories`].

Everingham, M., Van Gool, L., Williams, C., Winn, J., and Zisserman, A. (2009). The PASCAL visual object classes (VOC) challenge. *Int. J. Comput. Vis.*, 88(2):303–338. DOI: 10.1007/s11263-009-0275-4.

FAA (2014). Federal Aviation Administration aircraft wake turbulence re-categorization (RECAT) updates. Technical Report SAFO 14007, FAA. [Available from `https://content.govdelivery.com/attachments/USAFAA/2014/12/17/file_attachments/349722/SAFO14007.pdf`].

FAA (2023). Aeronautical information manual. Online. [Available from `https://www.faa.gov/air_traffic/publications/media/AIM_Bsc_w_Chg_1_2_and_3_dtd_9-5-24.pdf`].

Fezans, N., Schwithal, J., and Fischenberg, D. (2017). In-flight remote sensing and identification of gusts, turbulence, and wake vortices using a Doppler lidar. *CEAS Aeronaut. J.*, 8(2):313–333. DOI: 10.1007/s13272-017-0240-9.

Frehlich, R. (1997). Effects of wind turbulence on coherent Doppler lidar performance. *J. Atmos. Oceanic Technol.*, 14(1):54–75. DOI: 10.1175/1520-0426(1997)014<0054:EOWTOC>2.0.CO;2.

Frehlich, R. and Sharman, R. (2005). Maximum likelihood estimates of vortex parameters from simulated coherent Doppler lidar data. *J. Atmos. Oceanic Technol.*, 22(2):117–130. DOI: 10.1175/JTECH-1695.1.

Fujii, K. (1995). Unified zonal method based on the fortified solution algorithm. *J. Comput. Phys.*, 118(1):92–108. DOI: 10.1006/jcph.1995.1082.

Gao, H., Li, J., Chan, P., and Hon, K. (2019). Parameter retrieval of aircraft wake vortex based on its max–min distribution of Doppler velocities measured by a lidar. *J. Eng.*, 2019(20):6852–6855. DOI: 10.1049/joe.2019.0539.

Gao, H., Li, J., Chan, P., Hon, K., and Wang, X. (2018). Parameter-retrieval of dry-air wake vortices with a scanning Doppler lidar. *Opt. Express*, 26(13):16377–16392. DOI: 10.1364/OE.26.016377.

Gerz, T., Holzäpfel, F., and Darracq, D. (2002). Commercial aircraft wake vortices. *Prog. Aeronaut. Sci.*, 38(3):181–208. DOI: 10.1016/S0376-0421(02)00004-0.

Gimmestag, G. and Roberts, D. (2023). *Lidar Engineering - Introduction to Basic Principles*. Cambridge University Press, 1st edition.

Girshick, R. (2015). Fast R-CNN. In *IEEE Int. Conf. Comput. Vis. Pattern Recognit.*, pages 1440–1448. DOI: 10.1109/ICCV.2015.169.

Girshick, R., Donahue, J., Darrell, T., and Malik, J. (2014). Rich feature hierarchies for accurate object detection and semantic segmentation. In *IEEE Int. Conf. Comput. Vis. Pattern Recognit.*, pages 580–587. DOI: 10.1109/CVPR.2014.81.

Grötzbach, G. (1987). Direct numerical and large eddy simulation of turbulent channel flows. *Encycl. Fluid Mech.*, 6:1337–1391.

Guo, C., Lv, X., Zhang, Y., and Zhang, M. (2021). Improved YOLOv4-tiny network for real-time electronic component detection. *Sci. Rep.*, 11(1). DOI: 10.1038/s41598-021-02225-y.

Gurke, T. and Lafferton, H. (1997). The development of the wake vortices warning system for Frankfurt airport: theory and implementation. *Air Traffic Control Q.*, 5(1):3–29. DOI: 10.2514/atcq.5.1.3.

Géron, A. (2019). *Hands-On Machine Learning with Scikit-Learn, Keras, and TensorFlow*. O'Reilly Media, Inc., 2nd edition.

Hahn, K., Schwarz, C., and Friehmelt, H. (2004). A simplified hazard area prediction (SHAPe) model for wake vortex encounter avoidance. In *24th International Congress of Aeronautical Sciences*, volume 29. ICAS 2004-4.6.4. [Available from `https://icas.org/icas_archive/ICAS2004/PAPERS/070.PDF`].

Hallermeyer, A., Dolfi-Bouteyre, A., Valla, M., Le Brusquet, L., Fleury, G., Thobois, L., Cariou, J., Duponcheel, M., and Winckelmans, G. (2016). Development and assessment of a wake vortex characterization algorithm based on a hybrid lidar signal processing. In *8th AIAA Atmospheric and Space Environments Conference*. American Institute of Aeronautics and Astronautics. DOI: 10.2514/6.2016-3272.

Hallock, J. and Holzäpfel, F. (2018). A review of recent wake vortex research for increasing airport capacity. *Prog. Aeronaut. Sci.*, 98:27–36. DOI: 10.1016/j.paerosci.2018.03.003.

Hannon, S. and Thomson, J. (1994). Aircraft wake vortex detection and measurement with pulsed solid-state coherent laser radar. *J. Mod. Opt.*, 41(11):2175–2196. DOI: 10.1080/09500349414552031.

Hannon, S., Thomson, J., Henderson, S., and Thomson, J. (1997). Real time wake vortex detection, tracking and strength estimation with pulsed coherent lidar. In *Proceedings of the 9th Conference on Coherent Laser Radar*, pages 23–27.

Harvey, J. and Perry, F. (1971). Flowfield produced by trailing vortices in the vicinity of the ground. *AIAA J.*, 9(8):1659–1660. DOI: 10.2514/3.6415.

He, K., Zhang, X., Ren, S., and Sun, J. (2015). Spatial pyramid pooling in deep convolutional networks for visual recognition. *IEEE Trans. Pattern Anal. Mach. Intell.*, 37(9):1904–1916. DOI: 10.1109/tpami.2015.2389824.

He, K., Zhang, X., Ren, S., and Sun, J. (2016). Deep residual learning for image recognition. In *IEEE Conf. Comput. Vis. Pattern Recognit.* [Available from `https://openaccess.thecvf.com/content_cvpr_2016/papers/He_Deep_Residual_Learning_CVPR_2016_paper.pdf`].

Helmholtz, H. (1858). Über Integrale der hydrodynamischen Gleichungen, welche den Wirbelbewegungen entsprechen. *J. Reine Angew. Math.*, 1858(55):25–55. DOI: 10.1515/crll.1858.55.25.

Hennemann, I. (2010). *Deformation und Zerfall von Flugzeugwirbelschleppen in turbulenter und stabil geschichteter Atmosphäre*. PhD thesis, Technische Universität München. [Available from `https://mediatum.ub.tum.de/doc/823304/823304.pdf`].

Hennemann, I. and Holzäpfel, F. (2011). Large-eddy simulation of aircraft wake vortex deformation and topology. *Proc. Inst. Mech. Eng., Part G*, 225(12):1336–1350. DOI: 10.1177/0954410011402257.

Hinton, D. and Tatnall, C. (1997). A candidate wake vortex strength definition for application to the NASA aircraft vortex spacing system (AVOSS). Technical Report NASA TM-110343, NASA, Langley Research Center. [Available from `https://ntrs.nasa.gov/api/citations/19970031683/downloads/19970031683.pdf`].

Hirschberger, M. (2013). *Beiträge zur Erfassung von Wirbelschleppen mit Lidar*. PhD thesis, Ludwig-Maximilians-Universität München. [Available from `https://edoc.ub.uni-muenchen.de/16075/1/Hirschberger_Markus_C.pdf`].

Hirschel, E., Rizzi, A., Breitsamter, C., and Staudacher, W. (2021). *Elements of Vortex Theory*, pages 45–91. Springer Berlin Heidelberg, Berlin, Heidelberg. DOI: 10.1007/978-3-662-61328-3_3.

Hirt, C. and Cook, J. (1972). Calculating three-dimensional flows around structures and over rough terrain. *J. Comput. Phys.*, 10(2):324–340. DOI: 10.1016/0021-9991(72)90070-8.

Hochreiter, S. and Schmidhuber, J. (1997). Long short-term memory. *Neural Comput.*, 9(8):1735–1780. DOI: 10.1162/neco.1997.9.8.1735.

Hokpunna, A. (2009). *Compact fourth-order scheme for numerical simulations of Navier-Stokes equations*. PhD thesis, Technische Universität München. [Available from `https://mediatum.ub.tum.de/doc/813362/file.pdf`].

Hokpunna, A. and Manhart, M. (2010). Compact fourth-order finite volume method for numerical solutions of Navier-Stokes equations on staggered grids. *J. Comput. Phys.*, 229(20):7545–7570. DOI: 10.1016/j.jcp.2010.05.042.

Holzäpfel, F. (2003). Probabilistic two-phase wake vortex decay and transport model. *J. Aircr.*, 40(2):323–331. DOI: 10.2514/2.3096.

Holzäpfel, F. (2024). Personal communication.

Holzäpfel, F. and Gerz, T. (1999). Two-dimensional wake vortex physics in the stably stratified atmosphere. *Aerosp. Sci. Technol.*, 3(5):261–270. DOI: 10.1016/s1270-9638(00)86962-x.

Holzäpfel, F., Gerz, T., and Baumann, R. (2001). The turbulent decay of trailing vortex pairs in stably stratified environments. *Aerosp. Sci. Technol.*, 5(2):95–108. DOI: 10.1016/S1270-9638(00)01090-7.

Holzäpfel, F., Gerz, T., Frech, M., Tafferner, A., Köpp, F., Smalikho, I., Rahm, S., Hahn, K., and Schwarz, C. (2009a). The wake vortex prediction and monitoring system WSVBS part I: design. *Air Traffic Control Q.*, 17(4):301–322. DOI: 10.2514/atcq.17.4.301.

Holzäpfel, F., Gerz, T., Köpp, F., Stumpf, E., Harris, M., Young, R., and Dolfi-Bouteyre, A. (2003). Strategies for circulation evaluation of aircraft wake vortices measured by lidar. *J. Atmos. Oceanic Technol.*, 20(8):1183–1195. DOI: 10.1175/1520-0426(2003)020<1183:SFCEOA>2.0.CO;2.

Holzäpfel, F., Hofbauer, T., Gerz, T., and Schumann, U. (2002). *Aircraft Wake Vortex Evolution and Decay in Idealized and Real Environments: Methodologies, Benefits and Limitations*, pages 293–309. Springer Netherlands. DOI: 10.1007/0-306-48383-1_19.

Holzäpfel, F. and Kladetzke, J. (2011). Assessment of wake-vortex encounter probabilities for crosswind departure scenarios. *J. Airc.*, 48(3):812–822. DOI: 10.2514/1.c000236.

Holzäpfel, F., Kladetzke, J., Amelsberg, S., Lenz, H., Schwarz, C., and De Visscher, I. (2009b). Aircraft wake vortex scenarios simulation package for takeoff and departure. *J. Aircr.*, 46(2):713–717. DOI: 10.2514/1.39346.

Holzäpfel, F., Misaka, T., and Hennemann, I. (2010). Wake-vortex topology, circulation, and turbulent exchange processes. In *AIAA Atmospheric and Space Environments Conference*. American Institute of Aeronautics and Astronautics. DOI: 10.2514/6.2010-7992.

Holzäpfel, F. and Rotshteyn, G. (2023). Estimating aircraft landing weights from Mode S data. *J. Aircr.*, 60(2):589–593. DOI: 10.2514/1.c036689.

Holzäpfel, F. and Steen, M. (2007). Aircraft wake-vortex evolution in ground proximity: analysis and parameterization. *AIAA J.*, 45(1):218–227. DOI: 10.2514/1.23917.

Holzäpfel, F., Stephan, A., Heel, T., and Körner, S. (2016a). Enhanced wake vortex decay in ground proximity triggered by Plate Lines. *Aircr. Eng.*, 88(2):206–214. DOI: 10.1108/aeat-02-2015-0045.

Holzäpfel, F., Stephan, A., Rotshteyn, G., Körner, S., Wildmann, N., Oswald, L., Gerz, T., Borek, G., Floh, A., Kern, C., Kerschbaum, M., Nossal, R., Schwarzenbacher, J., Strobel, M., Strauss, L., Weiß, C., Kauczok, S., Schiefer, C., Czekala, H., Maschwitz,

G., and Smalikho, I. (2021). Mitigating wake turbulence risk during final approach via Plate Lines. *AIAA J.*, 59(11):4626–4641. DOI: 10.2514/1.J060025.

Holzäpfel, F., Tchipev, N., and Stephan, A. (2016b). Wind impact on single vortices and counterrotating vortex pairs in ground proximity. *Flow, Turbul. Combust.*, 97:829–848. DOI: 10.1007/s10494-016-9729-2.

Holzäpfel, F., Vechtel, D., Rotshteyn, G., and Stephan, A. (2022). Plate Lines to enhance wake vortex decay for reduced separations between landing aircraft. *Flow*, 2. DOI: 10.1017/flo.2021.16.

Hoogstraten, M., Visser, H., Hart, D., Treve, V., and Rooseleer, F. (2015). Improved understanding of en route wake-vortex encounters. *J. Aircr.*, 52(3):981–989. DOI: 10.2514/1.C032858.

Huler, S. (2007). *Defining the Wind: the Beaufort Scale and How a 19th-Century Admiral Turned Science into Poetry*, volume 226. The Crown Publishing Group.

ICAO (2004). Manual on Mode S specific services. Technical Report Doc 9688, AN/952, ICAO. [Available from `https://www.anteni.net/adsb/Doc/9688_cons_en.pdf`].

ICAO (2008). Guidance on A380-800 wake vortex aspects. Technical Report TEC/OPS/SEP—08-0294.SLG, ICAO.

Ioffe, S. and Szegedy, C. (2015). Batch normalization: accelerating deep network training by reducing internal covariate shift. In *Proceedings of the 32nd International Conference on Machine Learning*, volume 37, pages 448–456. PMLR. [Available from `http://proceedings.mlr.press/v37/ioffe15.pdf`].

Jacob, D., Lai, D., and Delisi, D. (2013). Development of an improved pulsed lidar circulation estimation algorithm and performance results for Denver OGE data. In *51st AIAA Aerospace Sciences Meeting including the New Horizons Forum and Aerospace Exposition*. American Institute of Aeronautics and Astronautics. DOI: 10.2514/6.2013-509.

Jacob, D., Lai, D., Delisi, D., Hutton, D., Barr, K., Shald, S., Hannon, S., and Gatt, P. (2011). Assessment of Lockheed Martin's aircraft wake vortex circulation estimation algorithms using simulated lidar data. In *3rd AIAA Atmospheric Space Environments Conference*. American Institute of Aeronautics and Astronautics. DOI: 10.2514/6.2011-3196.

Jacob, D., Lai, D., Pruis, M., and Delisi, D. (2015). Assessment of WakeMod 4: a new standalone wake vortex algorithm for estimating circulation strength and position (invited). In *7th AIAA Atmospheric and Space Environments Conference*. American Institute of Aeronautics and Astronautics. DOI: 10.2514/6.2015-3176.

Jarrett, K., Kavukcuoglu, K., Ranzato, M., and LeCun, Y. (2009). What is the best multi-stage architecture for object recognition? In *IEEE 12th Int. Conf. Comput. Vis.*, pages 2146–2153. Institute of Electrical and Electronics Engineers. DOI: 10.1109/iccv.2009.5459469.

Jeong, J. and Hussain, F. (1995). On the identification of a vortex. *J. Fluid Mech.*, 285:69–94. DOI: 10.1017/S0022112095000462.

Jocher, G., A. Chaurasia, Stoken, A., Borovec, J., NanoCode012, Y. Kwon, K. Michael, TaoXie, J. Fang, Imyhxy, Lorna, Z. Yifu, Wong, C., V. Abhiram, Montes, D., Z. Wang, Fati, C., J. Nadar, Laughing, UnglvKitDe, Sonck, V., Tkianai, YxNONG, Skalski, P., Hogan, A., D. Nair, Strobel, M., and Jain, M. (2022). ultralytics/yolov5: v7.0 - YOLOv5 SOTA realtime instance segmentation. DOI: 10.5281/ZENODO.3908559.

Joukowski, N. (1906). On annexed [bounded] vortices. *Trudy Otdeleniya Fiziches-kikh Nauk Obshchestva Lubitelei Estestvoznaniya*, 13:12–25. Published in Russian.

Jung, B. (2023). Plate Lines entschärfen Wirbelschleppen. Online. [Available from `https://www.dlr.de/de/aktuelles/nachrichten/2023/02/plate-lines-entschaerfen-wirbelschleppen`]. Last accessed: 14.02.2025.

Kaikwong, H. and Pakwai, C. (2017). Aircraft wake vortex observations in Hong Kong. *J. Radars*, 6(6):709–718. DOI: 10.12000/JR17072.

Kalnay, E. (2003). *Atmospheric Modeling, Data Assimilation and Predictability*, volume 341. Cambridge University Press.

Keye, S. (2011). Fluid-structure coupled analysis of a transport aircraft and flight-test validation. *J. Airc.*, 48(2):381–390. DOI: 10.2514/1.C000235.

Kingma, D. and Ba, J. (2014). Adam: a method for stochastic optimization. DOI: 10.48550/ARXIV.1412.6980.

Kingston, R. (1977). Coherent optical radar. *Opt. News*, 3(2). DOI: 10.1364/on.3.2.000027.

Kobayashi, M. (1999). On a class of Padé finite volume methods. *J. Comput. Phys.*, 156(1):137–180. DOI: 10.1006/jcph.1999.6376.

Koloschin, A., Vechtel, D., Holzäpfel, F., and Rotshteyn, G. (2025). Improved pairwise aircraft separation minima applying Plate Lines. *CEAS Aeronaut. J.*, 16(2):525–536. DOI: 10.1007/s13272-025-00814-5.

Köpp, F. (1994). Doppler lidar investigation of wake vortex transport between closely spaced parallel runways. *AIAA J.*, 32(4):805–810. DOI: 10.2514/3.12057.

Köpp, F., Franke, J., and Tetzlaff, G. (1991). Untersuchungen der Wirbelschleppen landender Flugzeuge am Flughafen Frankfurt/Main, Abschlussbericht Teil 1. Technical report, Institut für Optoelektronik, Deutsches Zentrum für Luft- und Raumfahrt.

Köpp, F., Rahm, S., and Smalikho, I. (2004). Characterization of aircraft wake vortices by 2-µm pulsed Doppler lidar. *J. Atmos. Oceanic Technol.*, 21(2):194–206. DOI: 10.1175/1520-0426(2004)021<0194:coawvb>2.0.co;2.

Köpp, F., Rahm, S., Smalikho, I., Dolfi-Bouteyre, A., Cariou, J., Harris, M., and Young, R. (2005). Comparison of wake-vortex parameters measured by pulsed and continuous-wave lidars. *J. Aircr.*, 42(4):916–923. DOI: 10.2514/1.8177.

Kovalev, D. (2019). *Radar Signature Simulator Based on Large Eddy Simulation of Wake Vortices in Turbulent and Stratified Atmospheres*. PhD thesis, Universite catholique de Louvain. [Available from `https://dial.uclouvain.be/pr/boreal/object/boreal%3A215227/datastream/PDF_01/view`].

Kundu, P. and Cohen, I. (2002). *Fluid Mechanics*. Academic Press, 2nd edition.

Kutta, M. (1902). Auftriebskräfte in strömenden Flüssigkeiten. *Ill. Aër. Mitt.*, 6(133):133–135.

Lai, D., Jacob, D., and Delisi, D. (2010). Assessment of pulsed lidar measurements of aircraft wake vortex positions using a lidar simulator. In *AIAA Atmospheric and Space Environments Conference*. American Institute of Aeronautics and Astronautics. DOI: 10.2514/6.2010-7988.

Lai, D., Jacob, D., Lo, F., and Delisi, D. (2011). Assessment of pulsed lidar measurements of aircraft wakes using a lidar simulator: vortex position estimates for IGE, linking, and oblique viewing, and dependence of vortex lifetime on SNR. In *3rd AIAA Atmospheric Space Environments Conference*. American Institute of Aeronautics and Astronautics. DOI: 10.2514/6.2011-3197.

Lamb, H. (1932). *Hydrodynamics*. Dover Publications Inc., 6th edition.

Lanchester, F. (1907). *Aerodynamics*. Archibald Constable & Co.

Lange, R. and Moore, J. (1980). Large wing-in-ground effect transport aircraft. *J. Aircr.*, 17(4):260–266. DOI: 10.2514/3.57898.

LeCun, Y. (1989). Generalization and network design strategies. Technical report, University of Toronto Connectionist Research Group. CRG-TR-89-4.

Leng, Y., Pan, W., Yin, H., Luo, Y., Xu, Y., and J., W. (2021). Random forest aircraft wake recognition based on feature fusion. *J. Xihua Univ. Nat. Sci.*, 40(6):22–26. DOI: 10.12198/j.issn.1673-159X.4137.

Li, C., Li, L., Jiang, H., Weng, K., Geng, Y., Li, L., Ke, Z., Li, Q., Cheng, M., Nie, W., Li, Y., Zhang, B., Liang, Y., Zhou, L., Xu, X., Chu, X., Wei, X., and Wei, X. (2022). YOLOv6: a single-stage object detection framework for industrial applications. DOI: 10.48550/ARXIV.2209.02976.

Li, J., Shen, C., Gao, H., Chan, P., Hon, K., and Wang, X. (2020). Path integration (PI) method for the parameter-retrieval of aircraft wake vortex by lidar. *Opt. Express*, 28(3):4286–4306. DOI: 10.1364/OE.382968.

Lin, T., Goyal, P., Girshick, R., He, K., and Dollár, P. (2017). Focal loss for dense object detection. DOI: 10.48550/ARXIV.1708.02002.

Lin, T., Maire, M., Belongie, S., Bourdev, L., Girshick, R., Hays, J., Perona, P., Ramanan, D., Zitnick, C., and Dollár, P. (2014). Microsoft COCO: common objects in context. DOI: 10.48550/ARXIV.1405.0312.

Lindholm, A., Wahlström, N., Lindsten, F., and Schön, T. (2022). *Machine Learning - A First Course for Engineers and Scientists*. Cambridge University Press.

Liu, S., Qi, L., Qin, H., Shi, J., and Jia, J. (2018). Path aggregation network for instance segmentation. In *IEEE Conf. Comput. Vis. Pattern Recognit.*, pages 8759–8768. DOI: 10.1109/CVPR.2018.00913.

Liu, W., Anguelov, D., Erhan, D., Szegedy, C., Reed, S., Fu, C., and Berg, A. (2016). *SSD: Single Shot MultiBox Detector*, pages 21–37. Springer International Publishing. DOI: 10.1007/978-3-319-46448-0_2.

Lugan, S. (2016). *Geometry-based simulations for detection of wake vortices using a pulsed Doppler lidar*. PhD thesis, Université Catholique de Louvain. [Available from `http://hdl.handle.net/2078.1/178073`].

Lugt, H. (1983). *Vortex Flow in Nature and Technology*. John Wiley & Sons, 1st edition.

Lundquist, J., Churchfield, M., Lee, S., and Clifton, A. (2015). Quantifying error of lidar and sodar Doppler beam swinging measurements of wind turbine wakes using computational fluid dynamics. *Atmos. Meas. Tech.*, 8(2):907–920. DOI: 10.5194/amt-8-907-2015.

Maas, A., Hannun, A., and Ng, A. (2013). Rectifier nonlinearities improve neural network acoustic models. In *Proceedings of the 30th International Conference on Machine Learning*, volume 28, pages 8759–8768. [Available from `https://robotics.stanford.edu/~amaas/papers/relu_hybrid_icml2013_final.pdf`].

Manhart, M. (2004). A zonal grid algorithm for DNS of turbulent boundary layers. *Comput. Fluids*, 33(3):435–461. DOI: 10.1016/S0045-7930(03)00061-6.

McCulloch, W. and Pitts, W. (1943). A logical calculus of the ideas immanent in nervous activity. *Bull. Math. Biophys.*, 5(4):115–133. DOI: 10.1007/bf02478259.

Meneveau, C., Lund, T., and Cabot, W. (1996). A Lagrangian dynamic subgrid-scale model of turbulence. *J. Fluid Mech.*, 319:353–385. DOI: 10.1017/S0022112096007379.

Menzies, R. and Hardesty, R. (1989). Coherent Doppler lidar for measurements of wind fields. *Proc. IEEE*, 77(3):449–462. DOI: 10.1109/5.24130.

Meyer Forsting, A., Troldborg, N., and Borraccino, A. (2017). Modelling lidar volume-averaging and its significance to wind turbine wake measurements. *J. Phys.: Conf. Ser.*, 854. DOI: 10.1088/1742-6596/854/1/012014.

Mikkelsen, T. (2009). On mean wind and turbulence profile measurements from ground-based wind lidars - limitations in time and space resolution with continuous wave and pulsed lidar systems. In *European Wind Energy Conference and Exhibition*. European Wind Energy Conference. [Available from `https://backend.orbit.dtu.dk/ws/portalfiles/portal/3746226/2009_11.pdf`].

Ministère de la Transition Écologique et Solidaire, R. F. (2018). RECAT-EU for Paris-CDG & Le Bourge. Technical report, EUROCONTROL. [Available from `https://www.ecologie.gouv.fr/sites/default/files/documents/RECAT_EU.pdf`].

Misaka, T., Holzäpfel, F., and Gerz, T. (2010). Large eddy simulation of wake vortex flows: a comparison of EULAG and MGLET. Technical report, Institut für Physik der Atmosphäre, Deutsches Zentrum für Luft- und Raumfahrt.

Misaka, T., Holzäpfel, F., and Gerz, T. (2012a). Wake evolution of wing-body configuration from roll-up to vortex decay. In *50th AIAA Aerospace Sciences Meeting including the New Horizons Forum and Aerospace Exposition*. American Institute of Aeronautics and Astronautics. DOI: 10.2514/6.2012-428.

Misaka, T., Holzäpfel, F., and Gerz, T. (2013). Wake evolution of high-lift configuration from roll-up to vortex decay. In *51st AIAA Aerospace Sciences Meeting including the New Horizons Forum and Aerospace Exposition*. American Institute of Aeronautics and Astronautics. DOI: 10.2514/6.2013-362.

Misaka, T., Holzäpfel, F., and Gerz, T. (2015). Large-eddy simulation of aircraft wake evolution from roll-up until vortex decay. *AIAA J.*, 53(9):2646–2670. DOI: 10.2514/1.j053671.

Misaka, T., Holzäpfel, F., Hennemann, I., Gerz, T., Manhart, M., and Schwertfirm, F. (2012b). Vortex bursting and tracer transport of a counter-rotating vortex pair. *Phys. Fluids*, 24(2). DOI: 10.1063/1.3684990.

Misra, D. (2019). Mish: a self regularized non-monotonic activation function. DOI: 10.48550/ARXIV.1908.08681.

Moet, H., Laporte, F., Chevalier, G., and Poinsot, T. (2005). Wave propagation in vortices and vortex bursting. *Phys. Fluids*, 17(5). DOI: 10.1063/1.1896937.

Morris, C., Peters, J., and Choroba, P. (2013). Validation of the time based separation concept at London Heathrow Airport. In *Tenth USA/Europe Air Traffic Management Research and Development Seminar*. National Air Traffic Services and EUROCONTROL. [Available from `https://www.researchgate.net/publication/327466692_Validation_of_the_Time_Based_Separation_concept_at_London_Heathrow_Airport`].

Moser, R., Kim, J., and Mansour, N. (1999). Direct numerical simulation of turbulent channel flow up to Re_τ=590. *Phys. Fluids*, 11(4):943–945. DOI: 10.1063/1.869966.

Nair, V. and Hinton, G. (2010). Rectified linear units improve restricted Boltzmann machines. In *Proceedings of the 27th international conference on machine learning*, pages 807–814. [Available from `https://www.cs.toronto.edu/~hinton/absps/reluICML.pdf`].

NATS (2018). Enhanced time based separation for Heathrow arrivals & RECAT EU for arrivals and departures. Technical report, NATS. [Available from `https://www.nats.aero/wp-content/uploads/2018/01/ETBSFactsheet_Jan2018V3.pdf`].

Pan, W., Duan, Y., Zhang, Q., Tang, J., and Zhou, J. (2019a). Deep learning for aircraft wake vortex identification. *IOP Conf. Ser.: Mater. Sci. Eng.*, 685(1). DOI: 10.1088/1757-899x/685/1/012015.

Pan, W., Duan, Y., Zhang, Q., Wu, Z., and Liu, H. (2019b). Research on aircraft wake vortex recognition using AlexNet. *Opto-Electr. Eng.*, 46(7). [Available from `https://www.researching.cn/ArticlePdf/m00029/2019/46/7/190082.pdf`].

Pan, W., Leng, Y., Wu, T., Xu, Y., and Zhang, X. (2022a). Conv-Wake: a lightweight framework for aircraft wake recognition. *J. Sens.*, 2022. DOI: 10.1155/2022/3050507.

Pan, W., Leng, Y., Yin, H., and Zhang, X. (2022b). Identification of aircraft wake vortex based on VGGNet. *Wirel. Commun. Mob. Comput.*, 2022:1–10. DOI: 10.1155/2022/1487854.

Pan, W., Wu, Z., and Zhang, X. (2020). Identification of aircraft wake vortex based on SVM. *Math. Probl. Eng.*, 2020. DOI: 10.1155/2020/9314164.

Pan, W., Yin, H., Leng, Y., and Zhang, X. (2022c). Recognition of aircraft wake vortex based on random forest. *IEEE Access*, 10:8916–8923. DOI: 10.1109/access.2022.3141595.

Prandtl, L. (1918a). Der induzierte Widerstand von Mehrdeckern. Technical report, Flugzeugmeisterei der Inspektion der Fliegertruppen. Technische Berichte Band III.

Prandtl, L. (1918b). Tragflügeltheorie I Mitteilung. Technical report, Nachrichten der K. Gesellschaft der Wissenschaften zu Göttingen. Math-Phys. Kl. 151-77.

Prandtl, L. (1919). Tragflügeltheorie II Mitteilung. Technical report, Nachrichten der K. Gesellschaft der Wissenschaften zu Göttingen. Math-Phys. Kl. 107-37.

Proctor, F., Ahmad, N., Switzer, G., and Limon Duparcmeur, F. (2010). Three-phased wake vortex decay. In *AIAA Atmospheric and Space Environments Conference*. American Institute of Aeronautics and Astronautics. DOI: 10.2514/6.2010-7991.

Proctor, F., Hamilton, D., and Han, J. (2000). Wake vortex transport and decay in ground effect - vortex linking with the ground. In *38th Aerospace Sciences Meeting and Exhibit*. American Institute of Aeronautics and Astronautics. DOI: 10.2514/6.2000-757.

Qu, Z., Yuan, S., Färber, M., Brennfleck, M., Wartha, N., and Stephan, A. (2025). Explainable lidar 3D point cloud segmentation and clustering for detecting airplane-generated wind turbulence. In *Proceedings of the 31st ACM SIGKDD Conference on Knowledge Discovery and Data Mining V.1*, KDD '25, pages 2504–2513. ACM. DOI: 10.1145/3690624.3709436.

Redmon, J., Divvala, S., Girshick, R., and Farhadi, A. (2016). You only look once: unified, real-time object detection. In *IEEE Conf. Comput. Vis. Pattern Recognit.*, pages 779–788. DOI: 10.1109/CVPR.2016.91.

Redmon, J. and Farhadi, A. (2017). YOLO9000: better, faster, stronger. In *IEEE Conf. Comput. Vis. Pattern Recognit.*, pages 6517–6525. DOI: 10.1109/CVPR.2017.690.

Redmon, J. and Farhadi, A. (2018). YOLOv3: an incremental improvement. DOI: 10.48550/ARXIV.1804.02767.

Ren, S., He, K., Girshick, R., and Sun, J. (2017). Faster R-CNN: towards real-time object detection with region proposal networks. *IEEE Trans. Pattern Anal. Mach. Intell.*, 39(6):1137–1149. DOI: 10.1109/TPAMI.2016.2577031.

Robey, R. and Lundquist, J. (2022). Behavior and mechanisms of Doppler wind lidar error in varying stability regimes. *Atmos. Meas. Tech.*, 15(15):4585–4622. DOI: 10.5194/amt-15-4585-2022.

Robins, R., Delisi, D., and Greene, G. (2001). Algorithm for prediction of trailing vortex evolution. *J. Airc.*, 38(5):911–917. DOI: 10.2514/2.2851.

Rooseleer, F. (2024). RECAT-EU European wake turbulence categorisation and separation minima on approach and departure. Technical report, EUROCONTROL. [Available from `https://www.eurocontrol.int/publication/european-wake-turbulence-categorisation-and-separation-minima-approach-and-departure`].

Rossow, V. and James, K. (2000). Overview of wake-vortex hazards during cruise. *J. Aircr.*, 37(6):960–975. DOI: 10.2514/2.2723.

Rumelhart, D., Hinton, G., and Williams, R. (1985). Learning internal representations by error propagation. Technical report, Defense Technical Information Center. [Available from `https://www.cs.toronto.edu/~hinton/absps/pdp8.pdf`].

Rye, B. (1990). Spectral correlation of atmospheric lidar returns with range-dependent backscatter. *J. Opt. Soc. Amer. A*, 7(12):2199–2207. DOI: 10.1364/josaa.7.002199.

Rye, B. and Hardesty, R. (1994). Spectral matched filters in coherent laser radar. *J. Mod. Opt.*, 41(11):2131–2144. DOI: 10.1080/09500349414552001.

Saffman, P. (1992). *Vortex Dynamics*. Cambridge University Press.

Sagaut, P. (2001). *Large Eddy Simulation for Incompressible Flows*. Springer, 1st edition.

Salamitou, P., Dabas, A., and Flamant, P. (1995). Simulation in the time domain for heterodyne coherent laser radar. *Appl. Opt.*, 34(3):499–506. DOI: 10.1364/AO.34.000499.

Schmitt, N., Rehm, W., Pistner, T., Zeller, P., Diehl, H., and Navé, P. (2007). The AWIATOR airborne lidar turbulence sensor. *Aerosp. Sci. Technol.*, 11(7–8):546–552. DOI: 10.1016/j.ast.2007.03.006.

Schwamborn, D., Gerhold, T., and Heinrich, R. (2006). The DLR TAU-code: recent applications in research and industry. In *Proceedings of the European Conference on Computational Fluid Dynamics*, Egmond aan Zee, The Netherlands. Delft University of Technology. [Available from `https://www.researchgate.net/profile/Dieter-Schwamborn/publication/224798567_The_DLR_TAU-code_Recent_applications_in_research_and_industry/links/593a8635aca2723334064aec/The-DLR-TAU-code-Recent-applications-in-research-and-industry.pdf`].

Shen, C., Li, J., Zhang, F., Chan, P., Hon, K., and Wang, X. (2020). Two-step locating method for aircraft wake vortices based on Gabor filter and velocity range distribution. *IET Radar Sonar Navig.*, 14(12):1958–1967. DOI: 10.1049/iet-rsn.2020.0319.

Shen, C., Tang, W., Gao, H., Wang, X., Chan, P., Hon, K., and Li, J. (2023). Aircraft wake recognition and strength classification based on deep learning. *IEEE J. Sel. Top. Appl. Earth Obs. Remote Sens.*, 16:2237–2249. DOI: 10.1109/jstars.2023.3243941.

Simonyan, K. and Zisserman, A. (2014). Very deep convolutional networks for large-scale image recognition. DOI: 10.48550/ARXIV.1409.1556.

Smalikho, I. (2019). Taking into account the ground effect on aircraft wake vortices when estimating their circulation from lidar measurements. *Atmos. Oceanic Opt.*, 32:686–700. DOI: 10.1134/S1024856019060149.

Smalikho, I., Banakh, V., Holzäpfel, F., and Rahm, S. (2015). Method of radial velocities for the estimation of aircraft wake vortex parameters from data measured by coherent Doppler lidar. *Opt. Express*, 23(19):A1194–A1207. DOI: 10.1364/OE.23.0A1194.

Soudain, G. (2024). Artificial intelligence concept paper issue 2. Technical report, EASA. [Available from `https://www.easa.europa.eu/en/document-library/general-publications/easa-artificial-intelligence-concept-paper-issue-2`].

Staufenbiel, R. and Schlichting, U. (1988). Stability of airplanes in ground effect. *J. Aircr.*, 25(4):289–294. DOI: 10.2514/3.45562.

Stephan, A. (2014). *Wake Vortices of Landing Aircraft*. PhD thesis, Ludwig-Maximilians-Universität München. [Available from `https://edoc.ub.uni-muenchen.de/16756/1/Stephan_Anton.pdf`].

Stephan, A., Holzäpfel, F., and Misaka, T. (2013a). Aircraft wake-vortex decay in ground proximity — physical mechanisms and artificial enhancement. *J. Airc.*, 50(4):1250–1260. DOI: 10.2514/1.C032179.

Stephan, A., Holzäpfel, F., and Misaka, T. (2014). Hybrid simulation of wake-vortex evolution during landing on flat terrain and with Plate Line. *Int. J. Heat Fluid Flow*, 49:18–27. DOI: 10.1016/j.ijheatfluidflow.2014.05.004.

Stephan, A., Holzäpfel, F., Misaka, T., Geisler, R., and Konrath, R. (2013b). Enhancement of aircraft wake vortex decay in ground proximity: experiment versus simulation. *CEAS Aeronaut. J.*, 5(2):109–125. DOI: 10.1007/s13272-013-0094-8.

Stephan, A., Holzäpfel, F., and Zholtovski, S. (2017). The effect of gusts on aircraft wake vortices. *Aircr. Eng.*, 89(5):692–702. DOI: 10.1108/AEAT-01-2017-0032.

Stephan, A., Rohlmann, D., Holzäpfel, F., and Rudnik, R. (2018). Hybrid numerical simulation of the jet-wake-vortex interaction of a cruising aircraft. In *2018 Atmospheric and Space Environments Conference*. American Institute of Aeronautics and Astronautics. DOI: 10.2514/6.2018-2865.

Stephan, A., Rohlmann, D., Holzäpfel, F., and Rudnik, R. (2019a). Effects of detailed aircraft geometry on wake vortex dynamics during landing. *J. Airc.*, 56(3):974–989. DOI: 10.2514/1.C034961.

Stephan, A., Rotshteyn, G., Wartha, N., Holzäpfel, F., Petross, N., and Stietz, L. (2023). Artificial neural networks for individual tracking and characterization of wake vortices in lidar measurements. In *AIAA AVIATION 2023 Forum*. American Institute of Aeronautics and Astronautics. DOI: 10.2514/6.2023-3682.

Stephan, A., Wildmann, N., and Smalikho, I. (2019b). Effectiveness of the MFAS method for determining the wind velocity vector from Windcube 200s lidar measurements. *Atmos. Oceanic Opt.*, 32(5):555–563. DOI: 10.1134/s1024856019050166.

Stietz, L. (2022). Artificial neural networks for individual tracking and characterization of wake vortices in lidar measurements. Master's thesis, Universität Hamburg. [Available from `https://elib.dlr.de/189820/1/Masterthesis-Stietz.pdf`].

Stumpf, E. (2003). *Untersuchung von 4-Wirbelsystemen zur Minimierung von Wirbelschleppen und ihre Realisierung an Transportflugzeugen*. PhD thesis, Rheinisch-Westfälische Technische Hochschule Aachen, Aachen. DOI: 10.18154/RWTH-CONV-121073.

Stumpf, E. (2005). Study of four-vortex aircraft wakes and layout of corresponding aircraft configurations. *J. Aircr.*, 42(3):722–730. DOI: 10.2514/1.7806.

Thobois, L. and Cariou, J. (2017). Next generation scanning lidar systems for optimizing wake turbulence separation minima. *J. Radars*, 6(6):689–698. DOI: 10.12000/JR17056.

Thomson, J. and Meng, J. (1976). Scanning laser Doppler velocimeter system simulation for sensing aircraft wake vortices. *J. Airc.*, 13(8):605–613. DOI: 10.2514/3.44549.

von Kármán, T. (1937). On the statistical theory of turbulence. *Proceedings of the National Academy of Sciences*, 23(2):98–105. DOI: 10.1073/pnas.23.2.98.

Wang, C., Liao, H., Wu, Y., Chen, P., Hsieh, J., and Yeh, I. (2020). CSPNet: a new backbone that can enhance learning capability of CNN. In *IEEE Conf. Comput. Vis. Pattern Recognit. Workshops*. DOI: 10.1109/CVPRW50498.2020.00203.

Wartha, N., Stephan, A., and Holzäpfel, F. (2025a). Assessment of a wake vortex retrieval method using large-eddy simulations and a lidar simulator. *J. Atmos. Oceanic Technol.*, 42(3):233–251. DOI: 10.1175/jtech-d-24-0093.1.

Wartha, N., Stephan, A., and Holzäpfel, F. (2025b). Virtual RHI lidar scans retrieved in high-fidelity wake vortex simulations of landing aircraft under turbulent crosswind conditions - LES Lidar Simulator (LLS). DOI: 10.5281/zenodo.12085034.

Wartha, N., Stephan, A., and Holzäpfel, F. (2025c). Wake vortex lidar measurement processing with large-eddy simulations and machine learning. *Opt. Express*, 33(12):26473–26498. DOI: 10.1364/oe.562553.

Wartha, N., Stephan, A., Holzäpfel, F., and Rothsteyn, G. (2023). Investigating errors of wake vortex retrievals using high fidelity lidar simulations. In *AIAA AVIATION 2023 Forum*. American Institute of Aeronautics and Astronautics. DOI: 10.2514/6.2023-3679.

Wartha, N., Stephan, A., Holzäpfel, F., and Rotshteyn, G. (2022). Characterizing aircraft wake vortex position and strength using lidar measurements processed with artificial neural networks. *Opt. Express*, 30(8):13197. DOI: 10.1364/oe.454525.

Wassaf, H., Burnham, D., and Wang, F. (2011). Wake vortex tangential velocity adaptive spectral (TVAS) algorithm for pulsed lidar systems. In *16th Coherent Laser Radar Conference*. Universities Space Research Association. [Available from `https://rosap.ntl.bts.gov/view/dot/9150/dot_9150_DS1.pdf`].

Wei, Z., Lu, T., Gu, R., and Liu, F. (2024). DBN-GABP model for estimation of aircraft wake vortex parameters using lidar data. *Chin. J. Aeronaut.*, 37(9):347–368. DOI: 10.1016/j.cja.2024.05.011.

Wieselberger, C. (1922). Wing resistance near the ground. Technical Report NACA TM-77, NASA. [Available from `https://ntrs.nasa.gov/api/citations/19930081293/downloads/19930081293.pdf`].

Williamson, J. (1980). Low-storage Runge-Kutta schemes. *J. Comput. Phys.*, 35(1):48–56. DOI: 10.1016/0021-9991(80)90033-9.

Wu, S., Zhai, X., and Liu, B. (2019). Aircraft wake vortex and turbulence measurement under near-ground effect using coherent Doppler lidar. *Opt. Express*, 27(2). DOI: 10.1364/oe.27.001142.

Yoshikawa, E. and Matayoshi, N. (2017). Aircraft wake vortex retrieval method on lidar lateral range–height indicator observation. *AIAA J.*, 55(7):2269–2278. DOI: 10.2514/1.j055224.

Zhang, X., Zhang, H., Wang, Q., Liu, X., Liu, S., Zhang, R., Li, R., and Wu, S. (2024). Locating and grading of lidar-observed aircraft wake vortex based on convolutional neural networks. *Remote Sens.*, 16(8). DOI: 10.3390/rs16081463.

Zhao, Z., Zheng, P., Xu, S., and Wu, X. (2019). Object detection with deep learning: a review. *IEEE Trans. Neural Netw. Learn. Syst.*, 30(11):3212–3232. DOI: 10.1109/tnnls.2018.2876865.

Zheng, Z., Wang, P., Liu, W., Li, J., Ye, R., and Ren, D. (2020). Distance-IoU loss: faster and better learning for bounding box regression. *Proc. AAAI Conf. Artif. Intell.*, 34(07):12993–13000. DOI: 10.1609/aaai.v34i07.6999.

Zierep, J. (1992). *Ähnlichkeitsgesetze und Modellregeln der Strömungslehre*. Springer-Verlag.

Acknowledgments

Completion of this thesis would not have been possible without the encouragement, guidance, consultation, and supervision I have received. First I would like to thank my PhD supervisor, the chair of the Institute of Aerospace Systems at RWTH Aachen University, Prof. Eike Stumpf. Thank you Eike, for your valuable supervision, feedback, and time. Many thanks also to Prof. Christian Breitsamter from the Technical University of Munich for discussions and comments we have exchanged.

I owe deep gratitude to Anton Stephan and Frank Holzäpfel, my two technical supervisors from the applied meteorology (MET) department at the Institute of Atmospheric Physics (IPA) of the German Aerospace Center (DLR). Without your commitment after completing my master's thesis at the MET department in 2020 it is uncertain whether I would have continued my academic career. Anton, we both know how many long, short, tough, casual, technical, nontechnical, and other kinds of conversations we have had. I am immensely proud of the outcome and your support allowed me to achieve this. Equally Frank, the amount of times I came up to you, called you, or messaged you regarding all kinds of wake vortex topics cannot be counted - your input has proven indispensable throughout the years. Throughout my time as a PhD the MET department was first chaired by Thomas Gerz, followed by Norman Wildmann. Thomas, Norman, thank you both for your trust, goodwill, and consideration throughout the past years. I also want to thank my former colleague Grigory Rotshteyn. Gregor, your assistance in a multitude of activities has been a major contribution. At the beginning of my PhD I had the pleasure of supervising the master's thesis of Lars Stietz. Lars, thank you for your dedication and valuable work on the ML pipeline.

Further colleagues, who I am thankful for include: the IT team of the IPA and Lars Kühne from the Institute of Data Science at DLR. Furthermore, Brigitte Ziegele was a major help with any administrative task. I also appreciated the mentoring I have received by Klaus Gierens. Thank you to the internal reviewers of my publications: Oliver Reitebuch and Dennis Piontek. Particularly, I am grateful for my fellow IPA PhDs for the many conversations, including my friends Moritz Spraul, Kianusch Vahid Yousefnia, Johannes Kistner, Sirine Gharbi, Annemarie Lottermoser, Linus Wrba, and Manuel Moser.

Thank you to my family and friends for their understanding of my regular absence. Mama, Papa, Lissi, you took so much of your time to support me with technical discussions, emotional hardships, and distractions, all whilst going through troubling times yourselves. To my friends, who were an immense backing throughout the past years, thank you for

finding the right words of encouragement or necessary banter during my lows, but also for celebrating achievements with me.

I would like to acknowledge the necessary infrastructure and data, which this thesis relied on and without which it could not have been realized. Thank you to: the Technical University of Munich, Hydromechanics, for the kind provision of the original MGLET code, the Gauss Centre for Supercomputing e.V. (`www.gauss-centre.eu`) for funding this project by providing computing time on the GCS Supercomputer SuperMUC-NG at Leibniz Supercomputing Centre (`www.lrz.de`), DLR's Institute of Data Science for providing GPU computing time on the High-Performance-Data Analysis cluster KRATOS, Stefan Melber from DLR's Institute of Aerodynamics and Flow Technology for providing the results of the RANS simulations from the EU-funded AWIATOR project and Airbus for the allowance to use them, Wolfgang Wurzinger for providing the exact gross mass of Austrian Airlines aircraft during the 2019 Vienna Airport campaign.

Finally, the work contained in this thesis was partially funded by the German Federal Ministry for Digital and Transport within the mFUND project 'KIWI'.

Curriculum Vitae

Niklas Louis Wartha

(* 18.10.1997, Darmstadt, Germany)

2014-2016	**International Baccalaureate:** International School of Turin, Chieri, Italy
2016-2021	**Master of Engineering:** University of Glasgow, Glasgow, United Kingdom
2018-2019	**Study Abroad:** Delft University of Technology, Delft, The Netherlands
2020	**Master's Student:** Institute of Atmospheric Physics, DLR, Oberpfaffenhofen, Germany
2021-2025	**PhD Student:** Institute of Atmospheric Physics, DLR, Oberpfaffenhofen, Germany
2025-present	**Research Associate:** Institute of Atmospheric Physics, DLR, Oberpfaffenhofen, Germany